

# **Research Experience for Undergraduates**

## **1996 Program Report**

**The National Radio Astronomy Observatory is a facility of the National Science Foundation operated under cooperative agreement by Associated Universities, Inc.**



# 1996 Research Experiences for Undergraduates Program

Program Report

December 6, 1996

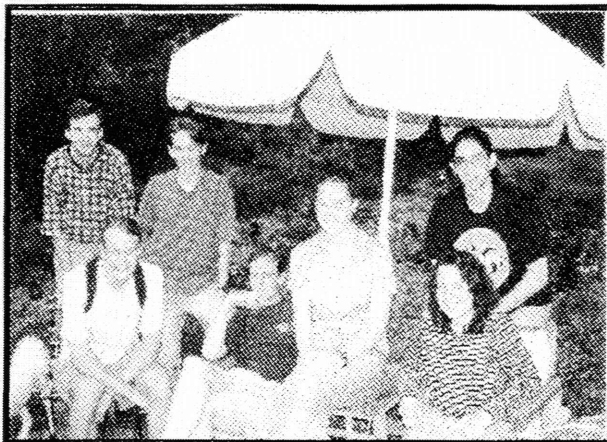


**Figure 1** Charlottesville Summer Students meet the Green Bank Summer Students.



**Figure 2** AOC Summer Students at the V.I.A.



# National Radio Astronomy Observatory REU Program Report

## Overview

Twenty undergraduates participated in the 1996 Research Experiences for Undergraduates program sponsored by the National Science Foundation, at the NRAO. Many students from previous years also keep in contact with their mentors, hence a report on 1996 alone misses some of the program's impact. In this report we divide the report into four main sections, each of which covers activities in the program and research conducted at one of the four main NRAO sites: Charlottesville, Socorro, Green Bank, and Tucson. In an Appendix, we include the reports which fourteen of the students wrote as part of their experience. Five of the research projects will be presented at the 178<sup>th</sup> meeting of the American Astronomical Society in January 1997, four of them by the students themselves. One project, with student Daniel Larson as first author, will be published in the *Astronomical Journal* early in 1997; his preprint is attached in lieu of a report. Two students from former years--David Copeland (REU '95 from Reed College) and Jake Callcut (REU '94 from Michigan State University) turned in senior theses based upon research they had begun during their REU years. Copeland turned in a thesis on the structure of molecular gas in a cloud slowly being destroyed by Rho Ophiuchi, working with Wootten as an external advisor (while Reed has faculty in Physics, it has none in astronomy). Callcut presented his thesis on VLA observations of water masers near the young S106IR region. Callcut and Winfrey (REU 94 University of Michigan) submitted their own VLA proposal for this project, received time and obtained the observations for the research. Callcut then reduced the data, working with Wootten through the internet, and incorporated it into his senior thesis.

## NRAO/Charlottesville 1996 Research Experience for Undergraduates (REU) Program

There were four students in the 1996 NSF Research Experience for Undergraduates (REU) program at NRAO-Charlottesville. Highlights of the program included a series of introductory level lectures on aspects of astronomy, particularly radio astronomy, spread over a few weeks. These lectures were intended to acquaint the students with the research which various staff members carry out.

Many of the students in the NRAO-Green Bank program visited Charlottesville for a tour of the

Central Development Laboratory , and of the University of Virginia's facility for the fabrication of the Semiconductor-Insulator-Semiconductor detectors used in millimeter wave receivers, the Semiconductor Device Laboratory. The Cover photo shows the students at a backyard barbecue get-together in Charlottesville. Left to right: Matthew Weatherly (GB), Daniel Larson. Gregory Holsclaw (GB) John Armstrong, Julianne Zuber (GB), Mary Putman, and Brian Wang.

The students had an informal get-together with astronomers from the University of Virginia at lunch, and from NRAO in the evening, followed by a visit with graduate students from the University's Astronomy Department.

In August, the Charlottesville students visited Green Bank to see the NRAO telescopes located there, to meet members of the Green Bank staff, and to attend the annual picnic. The students gave a series of 15 minute talks on their projects during a lunch symposium in Charlottesville before they began leaving for the summer. They produced short reports describing their summer research. Written reports are given in an appendix to this document.

The students traveled to Green Bank for a session of observations on the 43m telescope. This involved observations of OH emission from C/1995 O1 Hale-Bopp, peaking in intensity near this time. The students also toured the grounds of the Green Bank Telescope.

### CV Summer Student Schedule, Summer 1996

Date	Person	Item	Location	Time
19 Jun	Wooten	Orientation	Rm 317 ER	0900
19 Jun	Weatherly	Visit of Green Bank Summer Students	Alden House	pm
20 Jun	Bradley	Central Development Lab Introduction	Rm 228 Ivy Road	9am
20 Jun	Bradley	Tour of Central Development Lab	Rm 228 Ivy Road	10 am
20 Jun	Wooten	Pizza Lunch at Anna's No. 5	115 Maury Ave 977-6228	12 noon
20 Jun	Bradley	Tour of U. Va. Device Fabrication Facility	U. Va.	1:30 pm - 3:30 pm
20 Jun	Wooten	BBQ in the Wooten's backyard,	1714 Solomon Rd. Ch'ville 971-6518	6pm - 8 pm
21 Jun	Uson	Radiotelescopes and Interferometry	Rm 317,	9am
21 Jun	open	Public Night at McCormick Observatory	at the Observatory	9pm
24 Jun	open	Open	...	...
26 Jun	Condon	Radio Sources	Rm 317,	9am
28 Jun	Nice	Pulsars	Rm 317,	*9am*

1 Jul	Bridle	Jets, Radio Galaxies and Quasars	Rm 317,	9am
3 Jul	D. Hogg	The Interstellar Medium in Galaxies	Rm 317,	9am
5 Jul	open	Public Night at McCormick Observatory	at the Observatory	9pm
8 Jul	Zensus	The VLBA: Nuclear Jets and Compact Structures	Rm 317,	9am
10 Jul	Turner	Interstellar Molecules and Their Chemistry	Rm 317,	10am
11 Jul	Rood	Helium-3,	University of Virginia	TBA
15 Jul	Simon	Extrasolar Planets and the Millimeter Array	Rm 317,	9am
17 Jul	Desai	Radiowave Scattering	Rm 317,	9am
19 Jul	Barnbaum	Evolved Stars	Rm 317,	9am
19 Jul	open	Public Night at McCormick Observatory	at the Observatory	9pm
22 Jul	Uson	Cosmology	Rm 317,	9am
24 Jul	Schulman	X-Ray Astronomy	Rm 317,	9am
26 Jul	Uson	To Be Announced	Rm 317,	9am
31 Jul	Wootten	Comets	Rm 317,	9am
2 Aug	Wiseman	Molecular Clouds	Rm 317,	9am
2 Aug	open	Public Night at McCormick Observatory	at the Observatory	9pm
3 Aug	Wiseman	Travel to Green Bank for Observatory picnic, tours, etc.	...	...
3 Aug	Wiseman	CV students overnight Green Bank	GB	...
3 Aug	Wiseman	GB Picnic	GB	...
4 Aug	Wiseman	Return from Green Bank after lunch.	GB	...
6 Aug	Wootten	Summer students present their research (lunch)	Rm 317	12:05
13 Aug	Wootten	Travel to Green Bank for Observations of OH in C/Hale Bopp	43m	8am
13 Aug	Wootten	Overnight GB.	Dorms	am
14 Aug	Wootten	Submit OH paper, tour site, return to CV.	GB	pm
16 Aug	open	Public Night at McCormick Observatory	at the Observatory	9pm

The Charlottesville students achieved an impressive research record. Each of the students wrote a short description of their research, which is appended to this report. Here we give a paragraph summarizing each student's research.

### Daniel Larson, of Harvard University

worked with Eric Schulman

on

Analysis of X-Ray Observations of M33

Daniel Larson worked with Eric Schulman in analyzing the variability of X-ray sources in M33, using data from the ROSAT and ASCA satellites. In particular, he will precisely determine the period of an eclipsing binary X-ray source in M33 and attempt to determine whether its orbital period is changing. A paper, 'A Revised Orbital Period for M33 X-7' by Larson and Schulman, will appear in the February 1997 issue of The Astronomical Journal.

### Bryan Wang, of the University of Virginia

worked with Richard F. Bradley

on

An Adaptive Interference-Cancelling Receiver

Radio emission near 94 MHz from C60 molecules, or 'Bucky Balls', might be detected in the interstellar medium with a sensitive telescope such as the NRAO 140' telescope in Green Bank. However, local FM radio interferes at or near the frequency of emission, obscuring the incredibly weak interstellar signal. Bryan worked with Richard to design a receiver capable of canceling the undesired radio interference, using an adaptive Least-Mean-Squared cancellation algorithm.

### John Armstrong, of the University of Iowa

worked with A. Zensus and K. Kellerman

on

A 2cm VLBI Survey

Zensus and Kellerman are conducting the survey using the VLBA at 2cm to investigate the properties of compact extragalactic radio sources. The survey is aimed at morphological source classification, the physics of parsec-scale jet sources, and determination of parameters used in cosmology. The summer project included the complete analysis of a 2 day observing run in April. This included data calibration, image analysis, classification, and search for superluminal motion. The results will be compared to 4 runs we have had in 1994/1995. The summer project was a good opportunity for John to learn about VLBI, and to get a detailed training on VLBA data analysis. His experience with AIPS was useful and gave him a head start towards working on interesting aspects of the project. Besides the work on the data, John was involved in literature research to collect information about the survey sources. Finally, we are also planning to make part of the project results available on the World-Wide Web, which he was involved in as well.

**Mary Putman, of the University of Wisconsin**

worked with Jennifer Wiseman

on

**Studies of Stellar Outflows**

Putman and Wiseman studied high velocity molecular gas outflows from young stellar objects in the Orion Molecular Cloud, using data from the VLA.

Putman attended the Wellesley Star Formation Meeting, where she presented her work in a poster. Wiseman will present work they did at the 189<sup>th</sup> AAS meeting in session 53.06.

**Will Morrison, of Western Albemarle High School**

worked with Paul Shannon

on

**The CO Distribution in C/1996 B2 (Hyakutake)**

An image of the carbon monoxide distribution in C/1996 B2 (Hyakutake) taken by Jeff Mangum with the NRAO 12m radiotelescope will be analyzed. The primary goal of the project is to determine whether the azimuthally averaged image shows evidence for a second source of CO located within the coma. Such a second source, arising from photodissociation of more complex molecules, has been hypothesized. A measurement of its location could offer clues to the identity of the parent molecule. Will was not employed by the REU program.

**NRAO/Socorro 1996 Research  
Experience for  
Undergraduates (REU) Program**

The second cover photo shows the NRAO/Socorro 1996 REU summer students (+ Anuj), visiting the VLA on the plains of San Augustin. From left to right, they are:

1 - Lauren Herold , 2 - Craig Heinke , 3 - Olivia Johnson , 4 - Todd Konkel , 5 - Lon Freeman , 6 - Gus Tucker , 7 - Pat Udomprasert , 8 - Andrew Kerr , 9 - Anuj Sarma (non-REU summer student)

The summer REU program at NRAO/Socorro in 1996 consisted of 4 main categories of activity:

- 1 - student research projects, in collaboration with an NRAO advisor
- 2 - lectures to the students by NRAO staff members
- 3 - a joint student project, involving observations with the Very Large Array (VLA)
- 4 - guided tours of the VLA, given by the students on weekends

The 1996 REU program at NRAO/Socorro was under the direction of Bryan Butler, assisted by Min Yun, both of whom are Jansky Postdoctoral Researchers at NRAO/Socorro.

## Student Research Projects

Each of the REU students worked with one or more advisors on one or more projects throughout the summer. This was the main focus of the program, and the majority of the students' time was spent on these research endeavors. These projects involved observing, data reduction and analysis, equipment development, and theoretical studies. At the end of the program, each student gave a lunch talk explaining the main project(s) he or she worked on during the summer. The possibility exists for the students to present their original research at scientific meetings deemed appropriate by their advisor(s). Three of the NRAO-AOC students will be presenting posters at the 189<sup>th</sup> Meeting of the American Astronomical Society in Toronto in January, 1987. Following is a summary of the specific projects carried out by the NRAO/Socorro REU students. More complete written descriptions, by the students, can be found in the appendix to this report.

**Robert (Lon) Freeman, of Princeton University**

Advisor: Jim Ruff

Project: Vectorization of VLA Drawings

Freeman worked on converting rasterized antenna drawings (obtained by scanning in old VLA blueprints) into vectorized drawings. He did this through the use of CAD software. The vectorized drawings are much simpler to work with, and will be used by the engineers in the future. He also created a finite element model of the pedestal of the VLA antennas. This model will be used to do structural studies pertaining to the VLA upgrade.

## Catharine (Olivia) Johnson, of Vassar College

Advisors: Miller Goss and Chris DePree

Project: Recombination Line Observations of UltraCompact HII Regions

Olivia worked on H66alpha observations of M17-UC1, an UltraCompact HII region which is also a Broad Line source. She looked at 1.35-cm (K-band) spectral line data taken at the VLA. The conclusions are that the arc of material near UC1 is an ionization front, which somehow focuses a shock which is propagating from the other side of the arc. This shock has then induced star formation, and UC1 is a photoionized shell from a B0 star. All BL sources may be formed in a similar fashion. The results seem to support the data, model and conclusions of earlier workers (Felli et al.).

Johnson will be presenting her results at the 189<sup>th</sup> AAS Meeting, Session 106.04.

## Andrew Kerr, of Bradley University

Advisor: Paul Lilie

Project: Characterization of the 43 Ghz Receiver System

Andrew worked on investigating the behavior of the 43 GHz receiver system. The 43 GHz system is the newest receiver system at the VLA, and is the highest operating frequency of the antenna. As such, calibration is as challenging as the science the array produces is exciting. Accurate values for the calibration temperature values (Tcal's) for each of the 13 Q-band antennas are an important step towards making the 43 GHz system more usable. The Tcal's (and fluctuations in them) were accurately determined by using hot, sky, and liquid nitrogen loads in conjunction with manual tipping scans throughout the summer. Although the system showed some problems associated with cloud cover and ambient temperature, the determination of the Tcal values was quite successful.

## Lauren Herold, of Princeton University

Advisor: Min Yun

Project: Perturbed HI in Interacting Galaxies

Lauren worked on debugging and providing a user friendly graphical interface for software which maps the perturbation of HI in interacting galaxies using 3-body simulations. She modified existing software in order to create a program with a good graphics display and versatility so that it may in the future be used to examine the orbital details of two or more interacting galaxies quickly and easily, without having to do any full N-body calculation. The M81-M82-NGC3077 interacting system was examined, showing that most of the morphology may be reproduced (and displayed) with this technique.

## Todd Konkel , of Rice University

Advisor: Bryan Butler

Project: VLA Observations of Uranus and Neptune

Todd worked on L-band (21.4 cm) data from Uranus and Neptune, taken with the VLA during 1995 and 1996 (using the outer array during Q-band tests). The data from several different runs were calibrated, and added together. The estimated value of the received flux density was then used to calculate the disk-averaged brightness temperature of the two bodies. These numbers were:  $T_b(\text{Uranus}) = 250 \pm 9$  K;  $T_b(\text{Neptune}) = 307 \pm 12$  K. These numbers are similar to previous measurements, but with smaller uncertainties. These brightness temperatures seem to indicate some difference in the opacity sources of the two bodies at great depth (10's of bars).

## Craig Heinke , of Carleton College

Advisor: Dale Frail

Project: Gamma Ray Bursters and Pulsar Motion

Craig worked on two projects this summer: the first involving positions of Gamma Ray Bursters (GRB's), and the second involving measuring the motion of the Pulsar 1257+12. The GRB project involved the reduction and analysis of VLA data from a long-term monitoring effort on GRB's. The objective was to try to find any indication of variable radio sources within the error boxes of GRB sources. No such sources were found, and a tight upper limit on the maximum flux density of any such source was found. The pulsar project involved taking several epochs of VLA data and measuring the position and motion of the pulsar, relative to many other radio sources in the field. A proper motion which agrees well with that obtained from accurate timing measurements was measured.

Heinke will present his research at the 189<sup>th</sup> meeting of the AAS in posters 74.04 and 101.03.

## Patricia Udomprasert , of Princeton University

Advisor: Greg Taylor

Project: VLBA Observations of Compact Steep Spectrum Sources

Pat worked on multi-frequency VLBA observations of the Compact Steep Spectrum (CSS) sources 3C318 and OQ172. Taking into account the redshift of OQ172, it has the highest Rotation Measure (RM) ever seen in any source ( $RM \gtrsim 10000$ ). The RM structure was also mapped with 2 msec resolution in OQ172.

Udomprasert will present some results of her research at the 189<sup>th</sup> meeting of the AAS in session 10.08.

## Gus Tucker, of Athens State College

Advisor: Clint Janes

Project:Radio Frequency Interference at the VLA

Gus worked with on ways to monitor Radio Frequency Interference (RFI) , worked on developing RFI Bulletins for the Very Large Array (VLA) and Very Long Baseline Array (VLBA) homepages, and worked with interference data taken at VLBA sites. He used the Spectrum Analyzer software package SPAN to take in and analyze the RFI data.

### Lectures and Other Activities

Several lectures about radio astronomy and interferometry were presented, allowing the students to obtain a good understanding of the technique. Talks were also given on general topics in astronomy, presented by members of the scientific staff. The astronomy talks were designed to give the students an understanding of what sort of research goes on at NRAO, and in radio astronomy in general. The detailed list of lectures and events for the summer is in the following table.

#### NRAO/Socorro Summer Student Schedule, 1996

Date	Time	Location	Item
6/11	1400	CON3	Discussion of this list - Min Yun
6/12	1400	CON1	Safety Lecture - Jon Spargo
6/13	0930	CON3	Telescopes - Peter Napier
6/17	1400	CON3	Fourier Transforms - Bryan Butler
6/19	1400	CON3	Basic Interferometry - Tony Beasley
6/20	0930	AUD	PR for the VLA - Dave Finley
6/20	1100	Lobby	Leave for VLA site/Datil
6/20	1230	Datil	Lunch at Eagle Guest Ranch
6/20	1400	Site	Guided Tour of VLA - Dave Finley
6/21	1300	CON3	Imaging/Deconvolution - Tim Cornwell
6/22	1030	Site	Tours of VLA - summer students

6/23	1030	Site	Tours of VLA - summer students
6/24	1400	AUD	VLBI - Craig Walker
6/26	1400	AUD	VLA Observations (1) - Bryan Butler
6/28	1400	AUD	VLA Observations (2) - Bryan Butler
6/29	1030	Site	Tours of VLA - summer students
6/30	1030	Site	Tours of VLA - summer students
7/01	1400	CON3	Radiative Transfer & Continuum Emission Processes - Bryan Butler
7/03	1400	CON3	Spectral Lines - Min Yun
7/06	0900	Site	Tours of VLA - summer students
7/07	0900	Site	Tours of VLA - summer students
7/08	0500	Site	Observing Time
7/08	1700	Site	Observing Time
7/09-7/11			Tucson Trip
7/13	0900	Site	Tours of VLA - summer students
7/14	0900	Site	Tours of VLA - summer students
7/16	1400	AUD	Planets & Sun - Bryan Butler & Tim Bastian
7/18	1300	CON3	Radio Stars, SN/SNR, masers - Michael Rupen
7/20	0900	Site	Tours of VLA - summer students
7/21	0900	Site	Tours of VLA - summer students
7/22	1430	CON3	Milky Way - Mark Claussen
7/24	1400	CON3	Other Galaxies (HI) - Dave Westpfahl
7/27	0900	Site	Tours of VLA - summer students
7/28	0900	Site	Tours of VLA - summer students

8/01	1200	AUD	lunch talks - Olivia Johnson & Lon Freeman
8/03	0900	Site	Tours of VLA - summer students
8/04	0900	Site	Tours of VLA - summer students
8/06	1400	CON3	Radio Galaxies - Greg Taylor
8/08	1300	CON3	High-z Objects - Chris Carilli
8/10	0900	Site	Tours of VLA - summer students
8/11	0900	Site	Tours of VLA - summer students
8/13	1200	AUD	lunch talks - Todd Konkel, Lauren Herold & Andrew Kerr
8/15	1200	AUD	lunch talks - Pat Udomprasert, Craig Heinke & Gus Tucker
AUD = Auditorium			
CON3 = 3rd Floor Conference Room			
CON1 = 1st Floor Conference Room			

### Joint Student Research Project

The students were given 2 hours of their own VLA time, which they used to observe a very high redshift galaxy ( $z=4.7$ ) at 2-cm, and NGC253 at 1.3 and 0.7-cm.

### NRAO/Green Bank 1996 Research Experience for Undergraduates (REU) Program

Students conducting their research at the NRAO Green Bank Site in West Virginia included the following. The program at Green Bank is under the direction of Dr. Ron Maddalena.

The Green Bank students arrived early, in mid-May. As soon as the Charlottesville students had arrived (most of them came in mid-June), they visited Charlottesville for the tour of the Central Development Lab, Headquarters, and the University of Virginia mentioned earlier.

The introduction to radio astronomy for most Green Bank REU students comes with attendance at lectures in the Institute for High School Teacher Enhancement. In these and other activities,

the Green Bank REU students were joined by the four Green Bank Co-op students, Christopher Norris, Samantha Fore, Amy Petticrew and David Bradley, as well as two non-REU students, Naomi Bates and Justin Jesselli. The Co-op students and the REU students also gave talks as described in the following table.

## Student Lectures in Green Bank

David Bradley	June 6	Methodology in Experimentation
Amy L. Petticrew	June 6	Laser Ranging Fundamentals
Samantha Fore and Christopher Norris	June 27	Radio Frequency Interference
REU Students	July 22	Summer Research Talks

Several additional lectures were also given for the summer students.

J. Lockman	July 16	Radio Telescope Basics
R. Maddalena	July 18	The Surface Accuracy of Radiotelescopes
R. Norrod	July 23	Radio Telescope Electronics
L. D'Addario	July 25	Interferometry
F. Ghigo	July 30	Earth Orientation from VLBI
D. Balsler	Aug 1	Radio Science

Maddalena composed a questionnaire to provide feedback so that we might improve the program in 1997. I attach a copy of the questionnaire and summarize the responses here. Most of the students found out about the program through word of mouth, rather than by postings on real or electronic bulletin boards or other means. The students all responded that their work seemed to be very much a 'real world' experience, and that they thought they had gained a lot from the research which they had done. All of the students responding stated that the summer had reinforced their career plans; none had previous REU experiences. Some students asked for more intensive lectures, more money, or a more comprehensive introduction to who was doing what at the observatory. One student wished for more interaction between the sites (all students were given all other students' email addresses before arrival at NRAO, and students from the western sites were able to get together once in Tucson, and at the eastern sites once in Charlottesville and twice in Green Bank).

Short summaries of the research performed by the students and their mentors follow.

## **Matthew Weatherly, of West Virginia University**

**worked with John Ford**

**on**

**Remote Reset and SBC Control box**

Matthew worked on 3 projects.

### **(1) Single-Board Control and Reset Box**

For his first project, he designed a "Single-Board Control and Reset Box" that allows an engineer or telescope operator to connect to the console port of a single-board embedded controller, and perform a hardware reset of the board. This box is capable of handling up to 15 embedded computers at a time. There will be 4 of these boxes built for the GBT, and installed in the Receiver room, the Active Surface Room, the Alidade Servo Room, and in the Equipment Room. The box consists of a terminal server for connecting it to the network, a digital I/O interface for handling the reset bits, and 15 serial interface ports to the various embedded computers. The whole thing is built into an EMI/RFI shielded rack-mountable enclosure. Matthew built a prototype, and wrote software to control it. The results of his efforts are available on the Web. We are releasing the production version for 4 copies later this month.

### **(2) SIB Reliability enhancement**

He then designed and tested a reliability enhancement for the VLBA Standard Interface Board that we are using in most of the GBT systems for communication with the telescope control system. The modification consisted of designing a PC board and picking out components for a power supply monitor and watchdog timer to be retrofitted to the existing design. He built a breadboard prototype of the PC board he designed, and figured out the necessary firmware changes to be made to the VLBA firmware, and tested these in our lab. We have a package ready to be released for production if the decision is made to do it. This project's design is also available via WWW.

### **(3) GBT Alidade Room Monitor & Control Equipment Rack design**

For his 3rd project, Matthew gathered data and laid out the equipment racks for the Alidade room, figured out the interconnections between devices in the racks, and made tables showing these interconnections. These racks will be assembled later this winter and will be eventually installed in the GBT.

## **Julianne Zuber of Denison University**

**worked with Glen Langston and Frank Ghigo**

**on**

**Survey of the Northern Sky**

Zuber took charge of the 45' all northern sky survey at 8.35 and 14.35 GHz. produced a source identification list and check calibration. For a full description of Julianne's project, see the

Appendix.

**Gregory Holsclaw, of West Virginia University**  
worked with Sue Ann Heatherly  
on  
The 40ft Radiotelescope

**Jason Ray, of The West Virginia Institute of Technology**  
worked with Wes Grammer  
on  
IF System Hardware for the Green Bank Telescope

Jason Ray, a sophomore at West Virginia Tech, worked to modify a fairly large and sophisticated diagnostic program, used for tests of GBT receivers, LO, and IF system hardware in the lab. The program allows the user control of MCB and HPIB devices via a friendly, mouse-driven graphical user interface (GUI), and runs under MS-DOS on a PC. It is written in C++, and is highly structured and modular, with good internal documentation. However, the author of the program had not time to generate any formal documentation on it, and has since left NRAO. Jason had the formidable task of learning how the program worked, and then make significant modifications/additions to it, adding new menus and graphical screens to implement a new control/monitor interface for the GBT Converter Rack. In this task he was almost entirely on his own. Jason completed the above tasks in only 10 weeks, demonstrating the program's new capabilities with actual GBT hardware in his project presentation. In addition, he solved a memory allocation problem that placed limitations on the number of interface screens that could be open at one time. The remaining week he spent helping Holsclaw with hardware problems at the 40' telescope.

**Ryan McCowan, of Tennessee Technological University**  
worked with David Parker  
on  
Pointing the Green Bank Telescope

Mr. McCowan worked with the Green Bank Telescope Antenna Metrology group, performing tasks such as; experimental data analysis, conduction of experiments, electronics assembly and testing, software testing, and metrology laboratory assistance.

McCowan's work is described further in a report in the appendix.

## NRAO/Tucson 1996 Research Experience for Undergraduates (REU) Program

Students conducting their research at the NRAO Tucson Site in Arizona included . The program in Tucson is under the direction of Jeff Hagen. As the NRAO offices are across the street from KPNO/NOAO offices, the REU group shares in the activities of the NOAO REU program there.

**Ethan Schartman, of Carnegie-Mellon University**  
Worked with Simon Radford  
on  
MMA Submillimeter Tipping Radiometer

For MMA site testing, Dr. Radford is developing a submm tipper in collaboration with Jeff Peterson at Carnegie Mellon University. This device will use an ambient temperature, broad band pyroelectric detector with bands defined by resonant mesh filters. Initially, the instrument will be operated at a wavelength of 350 um, and then the operation will be extended to both shorter (200 um) and longer (800 and 1100 um) wavelengths. Assembly, testing, and deployment of these instruments will require a broad range of technical skills, including optics, electronics, mechanics, and software. Initial development will be two units, one for the MMA site in Chile (NRAO) and one for the South Pole (CMU/CARA). Several groups are interested in further units once they are developed.

**Clair Branch, of University of Michigan**  
Worked with Jeff Mangum  
on  
Visualization of Millimeter Images of the Sky

Ms. Branch will work on coupling OTF data to the PVWave visualization package. In particular, she will build program interfaces to three dimensional data images taken in the 'on-the-fly' mode with the 12m, in FITS format and, possibly, AIPS image files. This work will partially build upon the work done by Phil's student of last summer Jim Wren REU95 .

A report on Branch's work may be found in the appendix.

# **Raymond Kennedy, of Cameron University**

**Worked with Matt Waddel**

**on**

## **Analysis of Thermal Characteristics of the 12m Radiotelescope**

**Raymond Kennedy was hired to integrate a temperature monitoring system for the backup structure of the 12m telescope. The hardware portion of this project was designed and built last summer by another summer intern. Raymond's task this summer was to write the software that would display the thermal data visually. A visual display has been installed at Kitt Peak.**

**Gregory Holsclaw, of West Virginia University**  
worked with Sue Ann Heatherly  
on  
**The 40 foot Radiotelescope**

Greg was to learn all he could about the computer interface hardware for the forty foot, the computer control software for the forty foot telescope and the work done by a former summer student to improve these systems, then to build on those improvements - The ultimate outcome is to have a reliable computer control system for the forty foot telescope; one that is easier for the observer to use.

Greg first learned the basics about radio astronomy instrumentation by using the forty foot. Since there were discrepancies between computer controlled pointing of the telescope and manual pointing of the telescope, Greg was asked to create and conduct pointing experiments with the forty foot telescope.

He also improved the motor control hardware. For years we have been blowing relays in the circuit due to power surges when you change the direction in which the telescope is moving.

Greg made some changes to the computer interface hardware and worked with the software that had been partially developed by a former summer student. He also analyzed the system as it currently stands and made an instructive report about what needs to be done. He documented previously undocumented hardware and software.

Greg wrote a report on his upgrades to the telescope. A copy of this report may be found in the Appendix.

# Appendix I

## Example of Student Questionnaire



# NATIONAL RADIO ASTRONOMY OBSERVATORY MEMORANDUM

**DATE:** August 1, 1996  
**TO:** Summer Students  
**FROM:** Ron Maddalena  
**SUBJECT:** Questionnaire

Before you leave us we would appreciate you filling out and returning to me the following questionnaire. We will use your responses to improve the program for next year. Feel free to use the back of this sheet if you need more room for your responses. Thanks!

- How did you find out about the NRAO-REU program?
  
- What is your overall reaction to the program?
  
- How have your career decisions been influenced by you experiences at NRAO?
  
- Have you previously been an REU student at another institution? If so, how do your NRAO experiences compare with your experiences elsewhere?
  
- In what ways could we improve your stay at NRAO?
  
- What changes would you like to see in the NRAO-REU program?
  
- Do you and your mentor plan to publish results of your summer research, or to present the results at a professional meeting (the REU program can pay most of your costs)?

## Appendix II

Abstracts of 1996 NRAO REU Students to be presented at the Toronto AAS Meeting.



Previous abstract



Next abstract

**Session 74 - Pulsars.**

*Display session, Wednesday, January 15*

*Metropolitan Ballroom,*

## **[74.04] The Position and Proper Motion of PSR 1257+12**

*C. O. Heinke (Carleton College), D. A. Frail (NRAO), A. Wolszczan (Penn State)*

We have performed accurate astrometric observations of the planet pulsar PSR 1257+12 with the VLA on two epochs separated by approximately one year. These observations have resulted in measurements of the absolute position and a preliminary proper motion of PSR 1257+12 with typical accuracies of 100 mas and 30 mas year<sup>-1</sup>, respectively. These results are compared to independently-determined values from a pulsar timing analysis. The proper motion measurements agree within the errors, and a discrepancy which existed between the earlier timing and interferometric absolute positions (Wolszczan & Frail 1992) has now been resolved.

---



**Previous abstract**



**Next abstract**

**Session 101 - X-rays and X-ray Bursts.**

*Display session, Thursday, January 16*

*Metropolitan Ballroom,*

## **[101.03] VLA Searches for the Radio Counterparts of Gamma-ray Bursters**

*D. A. Frail (NRAO), S. R. Kulkarni (Caltech), C. O. Heinke (Carleton College), C. Carpenter (Harvard), Beppo-SAX GRB Team*

We report on the results of a radio monitoring campaign of the arcminute-sized error boxes toward several gamma-ray bursts. The fields of 11 well-localized gamma-ray bursts were observed with the Very Large Array (VLA), mostly at 20-cm, over a period of several years. Examples include the May 1, 1992 burst, localized with the Third Interplanetary Network, and the recent Beppo-SAX burst GRB 960720. These observations sample a range of postburst timescales and allow us to constrain the parameter space in which predictions of a long-lived, time-variable radio counterpart can be applied.

---



[Previous abstract](#)



[Next abstract](#)

**Session 106 - HII Regions and Ultracompact HII Regions.**

*Display session, Thursday, January 16*

*Metropolitan Ballroom,*

## **[106.04] A High Resolution VLA Study of M17-UC1**

*C. O. Johnson (Vassar College), C. G. DePree (Agnes Scott College), W. M. Goss (NRAO)*

We have observed the H66-alpha radio recombination line (RRL) emission at 1.3cm and the H52-alpha RRL emission at 7mm towards the ultracompact HII region M17-UC1 and the nearby arc-shaped structure. The angular resolution of the H66-alpha data, obtained using the Very Large Array in the C and DnC arrays, is 1"; the H52-alpha observations, taken in the D array, have an angular resolution of 2.3" by 1.5". H<sub>2</sub>O maser emission, at 1.3 cm, from the region of M17-UC1 was also observed in the D array with a beam of 4". We present these observations, derive the physical parameters of UC1 and the arc-shaped structure, and compare them with the values of Felli, Churchwell, and Massi(1984). We discuss the source as an example of shock induced star formation consisting of a hot, young, massive star surrounded by ionized material resulting from a stellar wind outflow. We compare M17-UC1 with six other sources known to have unusually broad RRL emission. The compact HII region (size 0.6" or 0.006 pc) is one of a growing number of HII regions with broad (>35 km/s) RRLs. M17-UC1 has an H66alpha line width (FWHM) of 47 km/s and an H52alpha line width of 41 km/s. Both lines have a central velocity of +19 km/s. The line parameters of the arc, about 1" or 0.01 pc to the east of UC1, are remarkably constant over an area extending 16.5" by 3" (0.165 pc by 0.03 pc), with a line width of 36 km/s and a central velocity of +16 km/s. The derived LTE electron temperature is 6600 K in UC1 and 8200 K in the arc region. Observations of the H<sub>2</sub>O maser emission toward UC1 reveals four masers within .5' of UC1. Of these, two are newly detected. The maser emission is near, but not coincident with, the position of the ultracompact source. Recent studies of the relation between water masers and ultracompact HII regions (Codella et al, 1996; Hofner and Churchwell, in press) suggest that such masers are among the earliest indicators of young stellar evolution, coincident with hot, dense, molecular clumps and molecular outflows in post-shock regions even before the development of an ionized region.



[Program listing for Thursday](#)



[Previous abstract](#)



[Next abstract](#)

**Session 53 - Circumstellar Disks & Outflows Associated with YSOs.**

*Oral session, Tuesday, January 14*

*Piers 4/5,*

## **[53.06] Outflows and Their Effects in Regions of High Mass Star Formation**

*J. Wiseman, R. Brown (NRAO), M. Putman (NRAO, Univ. Wisconsin), P. T. P. Ho (CFA)*

Bipolar outflows from young stars impact the surrounding molecular cloud core through shock heating, turbulence, and shearing. Energy is transported across large distances, affecting the character of future star formation. Some models of outflow structure include an ionized inner region, with lower velocity and less collimated neutral gas making up the outflow further from the central source. However, the exact nature of the structure and effects of outflows have been difficult to observationally confirm until recently because of instrumental sensitivity and resolution limitations.

Here we present new VLA detections of both the structure and the large scale effects of outflows in two regions of high mass star formation. One such source, DR 21, contains at least one vigorous bipolar outflow. Recent single-dish observations revealed evidence for very high velocity ionized gas in the region, with line wings of recombination line spectra extending several hundreds of kilometers per second from the central line peak. We have mapped this ionized gas with the VLA, revealing the spatial relationship of the high velocity ionized gas with the bipolar lobes of the previously detected molecular outflow in the region. High spectral dynamic range imaging techniques allow the possibility of detecting an inner ionized high velocity component within this powerful outflow.

We also present a high resolution mosaic of high velocity heated gas in the Orion OMC-1 outflow region. Emission from the ammonia (3,3) inversion transition was observed, which is sensitive to gas heated within the outflow or in regions heated as the outflow shocks and shears the surrounding filamentary molecular gas environment. Several fields were combined to create a linear mosaic covering a 3' x 3' region. We present maps which reveal dense molecular gas blueshifted to high velocities from a central region near the "hot core". Temperatures derived from the region show a direct relation between the spatial paths where the outflow lobes escape from the central core, and "hot spots" where the heated gas shears past the surroundings. These results show dynamic and far reaching effects of outflows on their environment.



[Program listing for Tuesday](#)



**Previous abstract**



**Next abstract**

**Session 10 - AGN - Host Galaxies & Environment.**

*Display session, Monday, January 13*

*Metropolitan Ballroom,*

## **[10.08] Probing the AGN Environment - The rotation measure structure of the quasar OQ 172 at milliarcsecond resolution**

*P. Udomprasert (Princeton), G. B. Taylor (NRAO), T. J. Pearson (Caltech, Radio Astronomy), D. H. Roberts (Brandeis)*

We present multi-frequency VLBA polarimetric observations of the Compact Steep Spectrum (CSS) quasar OQ 172 in the 6 and 18 cm bands. This object was previously known to have anomalously high Faraday rotation measures (RMs) -- in excess of  $20,000 \text{ rad m}^{-2}$  in the rest frame of the source. With a resolution of 2 mas, we confirm the high RMs seen at lower resolution and further find that the high RMs are associated with the nuclear component. Only 10 mas from the nucleus the jet IRMIs fall to less than  $100 \text{ rad m}^{-2}$  -- low enough to be produced entirely by the passage of the radiation through the interstellar medium of our galaxy. Such differences in the RM structure on scales of 50 parsecs rule out a cluster magnetic field Faraday screen thought to be the dominant mechanism for producing the high RM objects seen at lower redshift. We suggest that the high RMs seen in OQ 172, and perhaps in other CSS quasars as well, originate in the nuclear environment.

---

The author(s) of this abstract have provided an email address for comments about the abstract:  
[psu@astro.princeton.edu](mailto:psu@astro.princeton.edu)



**Program listing for Monday**

## Appendix III

Reports of Summer Students on Research, including articles in press or memos published.

# **A Revised Orbital Period for M33 X-7**

**Daniel T. Larson and Eric Schulman**

National Radio Astronomy Observatory  
520 Edgemont Road  
Charlottesville, Virginia 22903-2475  
dlarson@nrao.edu, eschulma@nrao.edu

Submitted to  
*The Astrophysical Journal (Letters)*

# A Revised Orbital Period for M33 X-7

Daniel T. Larson<sup>1</sup> and Eric Schulman<sup>2</sup>

*National Radio Astronomy Observatory*<sup>3</sup>, 520 Edgemont Road, Charlottesville, VA 22903-2475;  
dlarson@nrao.edu, eschulma@nrao.edu

## ABSTRACT

We analyzed the X-ray light curve of M33 X-7 using observations made by the *Einstein Observatory*, *ROSAT*, and *ASCA* satellites. Based on the high and low states characteristic of an eclipsing X-ray binary, we find evidence for a constant orbital period of  $P_{\text{orb}} = 3.4531$  days and a trapezoidal light curve with a fall time of 0.6 days, a total eclipse lasting 0.3 days, and a rise time of 0.2 days. The current data cannot exclude a constant rate of change of the orbital period. The source exhibits steep-sided total eclipses, suggesting that M33 X-7 is a high-mass X-ray binary.

*Subject headings:* binaries: eclipsing — galaxies: individual (M33) — stars: individual (M33 X-7) — X-rays: galaxies — X-rays: stars

---

<sup>1</sup>Current address: Physics Department, Harvard University, Cambridge, Massachusetts, 02138; dtlarson@husc.harvard.edu.

<sup>2</sup>Jansky Fellow.

<sup>3</sup>The National Radio Astronomy Observatory is a facility of the National Science Foundation operated under cooperative agreement by Associated Universities, Inc.

## 1. Introduction

M33 is at a distance of 795 kpc (van den Bergh 1991) and has an inclination of  $56^\circ$  (Zaritsky, Elston & Hill 1989). Because of its relatively low internal extinction and known distance, it is the most suitable spiral galaxy in which to obtain a complete sample of X-ray sources. This *Letter* describes a study of eclipse patterns in the X-ray source M33 X-7.

Previous variability studies of M33 X-7 were conducted by Long et al. (1981), Markert & Rallis (1983), Peres et al. (1989; hereafter PRCF), and Schulman et al. (1993, 1994; hereafter SBCRP). PRCF proposed that the source is an eclipsing X-ray binary with an orbital period of  $1^d7857$ , and commented that a period twice as long could not be excluded. SBCRP used the 12-year interval between the *Einstein Observatory* observations and the first *ROSAT* HRI observations to more precisely determine the period, and found  $P_{\text{orb}} = 1^d78586$ . We have reanalyzed the data used in the previous studies in addition to making use of new *ROSAT* (Long et al. 1996; Schulman & Bregman 1997) and *ASCA* (Takano et al. 1994) observations that have increased the size and time range of our data set. The analysis presented here suggest that the orbital period is  $3^d4531$ .

## 2. Observations

M33 has been the target of pointed X-ray observations over a 15 year timescale, as shown in Table 1. There were five observations by the *Einstein Observatory*: three with the High-Resolution Imager (HRI), denoted by the prefix “EH” in Table 1, and two with the Imaging Proportional Counter (IPC), labeled “EI.” M33 has been observed multiple times by the *ROSAT* High-Resolution Imager

(HRI), labeled “RH,” and Position Sensitive Proportional Counter (PSPC), labeled “RP” or “WP,” and has been the subject of two pointed observations with the *ASCA* satellite, labeled “AD.” *ASCA* has four instruments that observe simultaneously: two Gas Imaging Spectrometers (GIS) and two Solid-State Imaging Spectrometers (SIS). A summary of the X-ray observations that we examined is presented in Table 1, along with the pointing centers, dates of observation, live times (the amount of time during which the telescope could detect photons), and the average count rates for M33 X-7 (excluding eclipses). Six of the observations could not be used to study the source: M33 X-7 was out of the field of view during three of the *ROSAT* HRI observations and the first *ASCA* SIS observation, at the edge of the field of view during the first *ASCA* GIS observation, and behind the support ring during two of the *ROSAT* PSPC observations.

Detailed information about each of the satellites and their respective instruments can be found in Giacconi et al. (1979) for the *Einstein Observatory*, Trümper (1984) for *ROSAT*, and Tanaka et al. (1994) for *ASCA*.

## 3. Analysis and Results

The 16 observations used for our study were reduced using IRAF Version 2.10.4 and PROS Version 2.3.1. The parameters for extracting the count rate of M33 X-7 (via the PROS task *imcnts*) appear in Table 2. For most of the *Einstein Observatory* and *ROSAT* observations, the aperture was centered on the position of M33 X-7 as determined by the PROS task *ldetect*. For the *ASCA* observations and the observations during which the source was always in eclipse or had a large off-axis angle, the aperture center was deter-

mined by using an offset from M33 X-8 (the strong nuclear source in M33). The nominal coordinates of M33 X-7 are  $\alpha = 1^{\text{h}} 30^{\text{m}} 44^{\text{s}}.9$ ,  $\delta = +30^{\circ} 16' 49''$  (B1950).

Each observation was composed of contiguous data sections separated by gaps during which useful data could not be obtained. The contiguous data sections can be extremely short, so we combined consecutive sections so as to decrease the count rate errors while keeping the fraction of live time as large as possible. The resulting data points are composed of 400 to 4000 seconds of observing time, with a typical length of  $\sim 1500$  s. About 90% of the points had a live time fraction of 90% or larger, and only 1% of the points had live time fractions below 70%. Our time intervals are significantly shorter than those used by PRCF and SBCRP so that we could obtain the good time resolution necessary for precise timing of the eclipses. One disadvantage of shorter time intervals is the larger count rate error per point. Another disadvantage is that any short time intervals separated by more than a few hundred seconds from longer intervals must be discarded. We used between 91% and 100% of the live time for all the instruments except for the *ASCA* GIS, for which only 50% of the time was in sufficiently long time intervals. The error bars on each point were determined using Poisson statistics, following the method of Gehrels (1986). About 6000 photons were detected during the 354 ks of live observing time (approximately 1000 of these photons were attributed to the background).

We are interested specifically in the timing of the eclipses and not in the absolute X-ray flux, so we did not directly compare the X-ray fluxes determined by the various instruments. Instead, the count rate for each

data point was normalized by the average of the “high” state for that instrument, shown in column 6 of Table 1. Because the *ROSAT* HRI observations had different pointing centers, these data were corrected for the fraction of photons that were scattered outside of the aperture at different off-axis angles (David et al. 1993). For the *Einstein Observatory* HRI observations we used an aperture that is large compared to the resolution of the instrument in order to minimize scattering effects. The multiple observations by the other instruments all had the same off-axis angles (Table 1), except for *ROSAT* PSPC observation WP600407, for which we determined a count rate normalization independent of the other PSPC observations.

We tested the 194 normalized data points against a simple model of periodic on and off states using chi-squared analysis. Three parameters were varied initially: the orbital period, the eclipse duration, and the midpoint of the first eclipse observed by the *Einstein Observatory*, also called the zero point. We tested periods between 100 and 700 ks ( $\sim 1$ -8 days) and eclipse durations between 10 and 60 ks (roughly 2% to 40% of the various period lengths). We also tested periods in the range 1-46 days using a constant eclipse duration of 0.7. Rows 2 through 15 of Table 3 display the fourteen sets of parameters we found that yield  $\chi^2_{\nu} < 3.75$  using this simple analysis. To investigate the robustness of the best orbital period we ran a phase space search over a broad region centered on the optimal parameters, alternately eliminating one of the 16 sets of data. In each case the best-fit period was within 4 s of the nominal value (298348 s), demonstrating that this orbital period is not an artifact of any one particular observation.

We then modeled the eclipse pattern with

an asymmetric trapezoid by adding parameters for the fall time (the transition time between the high state and total eclipse) and the rise time (the transition time between total eclipse and the high state). Chi-square analysis with five free parameters demonstrated that  $\chi^2_\nu$  could be reduced significantly by using the parameters shown in the first row of Table 3. The quality of this fit can be seen in Figure 1, which shows the 194 data points folded by a period of 298345<sup>s</sup>.6 (3<sup>d</sup>.45307) with a 53.4 ks (0<sup>d</sup>.62) fall time, 28.7 ks (0<sup>d</sup>.33) duration of total eclipse, and 18.5 ks (0<sup>d</sup>.21) rise time. The rise time is well constrained, but there are too few points with phases between 0.6 and 0.9 to constrain the fall time very well. Note that the six instruments have different spectral responses, and that the fall and rise times could be different for different energy ranges.

We performed similar chi-squared tests that included a constant rate of period change as a sixth parameter with the fall and rise times fixed at the optimal values,  $f = 53.4$  ks and  $r = 18.5$  ks (Table 3, row 1). We focused especially on the region of the best fit for a constant period. The period changes tested ranged from  $-5$  to  $5$  seconds per year, corresponding to  $-2 \times 10^{-5} \leq \dot{P}_{\text{orb}}/P_{\text{orb}} \leq 2 \times 10^{-5} \text{ yr}^{-1}$ . These extremes represent rates of period change that are larger than any so far observed in X-ray binaries (White, Nagase & Parmar 1995). SMC X-1 has the largest orbital decay yet measured, at  $\dot{P}_{\text{orb}}/P_{\text{orb}} = -3 \times 10^{-6} \text{ yr}^{-1}$  (Levine et al. 1993), while X 1822–371 has the largest known period increase rate, at  $\dot{P}_{\text{orb}}/P_{\text{orb}} = 3 \times 10^{-7} \text{ yr}^{-1}$  (Hellier et al. 1990). We found no combination of parameters that lowered  $\chi^2_\nu$  below the minimum found without a period change, but there was a wide range of period changes

that preserved the minimum value with modifications in the other free parameters. The 68%, 90%, and 99% confidence level contours (Avni 1976) around the minimum are shown in Figure 2, where the period change is plotted against the orbital period. The above confidence levels assume that our simple trapezoidal model is a valid representation of the X-ray light curve, and are therefore upper limits to the true confidence levels. The 99% confidence interval for the rate of period change is  $-5 \times 10^{-6} \leq \dot{P}_{\text{orb}}/P_{\text{orb}} \leq 9 \times 10^{-6} \text{ yr}^{-1}$ , so further observations are necessary to obtain stricter constraints on the rate of orbital period change.

#### 4. Discussion and Conclusions

M33 X-7 was first found to be variable in *Einstein Observatory* IPC (Long et al. 1981) and HRI (Markert & Rallis 1983) observations. PRCF reanalyzed these observations and proposed that an orbital period of 1<sup>d</sup>.7857 could account for all the minima, assuming an eclipse duration of 0<sup>d</sup>.4. The eclipse during observation EH7577 lasted at least 0<sup>d</sup>.9, but PRCF suggested that this could have been produced by a depressed maximum, similar to those observed in the light curve of Cen X-3 (Schreier et al. 1976). They pointed out that a period twice as long ( $P_{\text{orb}} = 3^{\text{d}}.5714$ ) could account for most of the minima. SBCRP used the one eclipse during *ROSAT* HRI observation RH600020 to more precisely determine the period, and found that  $P_{\text{orb}} = 1^{\text{d}}.78586$  fit most of the observations. SBCRP noted that it was unlikely for the orbital period to be exactly twice this value. Because the analysis of our entire dataset determined that an orbital period of 1<sup>d</sup>.8 was unlikely (see Table 3 and Figure 3), we performed chi-squared analysis on our data for just the *Einstein Obser-*

vatory observations and *ROSAT* HRI observation RH600020. We found that an orbital period of 1<sup>d</sup>.786 with an eclipse duration of 0<sup>d</sup>.6 has  $\chi^2_\nu = 1.8$  (85 points and 3 free parameters), while an orbital period of 3<sup>d</sup>.453 with an eclipse duration of 0<sup>d</sup>.7 has  $\chi^2_\nu = 1.7$  (85 points and 3 free parameters). The fact that the 3<sup>d</sup>.453 period is marginally better than the best period found by PRCF and SBCRP can be accounted for in the improved time resolution and decreased sensitivity of our reanalyzed data.

The analysis presented here shows that an orbital period of 3<sup>d</sup>.4531, fall time of 0<sup>d</sup>.6, duration of total eclipse of 0<sup>d</sup>.3, and rise time of 0<sup>d</sup>.2 fit the data fairly well ( $\chi^2_\nu = 1.55$  with 194 data points and 5 free parameters; Figure 1), significantly better than the orbital parameters proposed previously (see Figure 3). The relatively large value of  $\chi^2_\nu$  is not unexpected since X-ray binaries have fluxes and light curve shapes that can vary from cycle to cycle (see Schreier et al. 1976 for an excellent example of this phenomenon). Future X-ray observations will increase the constraints on the orbital parameters as well as on the shape of the light curve.

M33 X-7 is likely a high-mass X-ray binary (HMXRB) with an O or B giant or supergiant companion. It has an X-ray luminosity of about  $10^{38}$  erg s<sup>-1</sup> (Schulman & Bregman 1995; Long et al. 1996), similar to that of other HMXRBs. Steep-sided total eclipses, such as those exhibited by M33 X-7, are rare both in low-mass X-ray binaries (Parmar & White 1988) and in HMXRBs with Be companions (Verbunt & van den Heuvel 1995). If the companion is an O or B giant or supergiant then it should be bright enough to be observed with optical spectroscopy. Such observations would determine the orbital ve-

locity and constrain the size of the orbit and masses of the stars. Because many HMXRBs with giant or supergiant companions show optical brightness variations of  $\sim 10\%$  as a function of orbital phase (van Paradijs & McClintock 1995), the companion to M33 X-7 could be found by searching for such variability in optical images taken over the span of a week or so.

M33 X-7 is an eclipsing binary with orbital period of 3<sup>d</sup>.4531, fall time of  $\sim 0^d.6$ , total eclipse duration of  $\sim 0^d.3$ , and rise time of  $\sim 0^d.2$ . We are unable to place strong constraints on the rate of orbital period change using the present observations.

We thank Phil Charles and Giovanni Peres for valuable discussions, and John Armstrong, Knox Long, Mary Putman, and Jennifer Wiseman for careful readings of the manuscript. We also thank Ellen Bouton and Mary Jo Hendricks for helping us find important articles in obscure places. We gratefully acknowledge support from the National Science Foundation's Research Experiences for Undergraduates program. Most of the data used in this research were obtained through the High Energy Astrophysics Science Archive Research Center Online Service, provided by the NASA/Goddard Space Flight Center. This research has made extensive use of NASA's Astrophysics Data System Abstract Service.

## REFERENCES

- Avni, Y. 1976, *ApJ*, 210, 642
- David, L. P., Harnden, F. R., Jr., Kearns, K. E., & Zombeck, M. V. 1993, The *ROSAT* High Resolution Imager (HRI), Technical Report (US *ROSAT* Science Data Center/SAO)
- Gehrels, N. 1986, *ApJ*, 303, 336
- Giacconi, R., et al. 1979, *ApJ*, 325, 544
- Hellier, C., Mason, K. O., Smale, A. P., & Kilkenny, D. 1990, *MNRAS*, 244, 39p
- Levine, A., Rappaport, S., Deeter, J. E., Boynton, P. E., & Nagase, F. 1993, *ApJ*, 410, 328
- Long, K. S., Charles, P. A., Blair, W. P., & Gordon, S. M. 1996, *ApJ*, 466, 750
- Long, K. S., D'Odorico, S., Charles, P. A., & Dopita, M. A. 1981, *ApJ*, 246, L61
- Markert, T. H., & Rallis, A. D. 1983, *ApJ*, 275, 571
- Parmar, A. N., & White, N. E. 1988, *Mem. Soc. Astro. Ital.*, 59, 147
- Peres, G., Reale, F., Collura, A., & Fabbiano, G. 1989, *ApJ*, 336, 140 (PRCF)
- Schreier, E. J., Swartz, K., Giacconi, R., Fabbiano, G., & Morin, J. 1976, *ApJ*, 204, 539
- Schulman, E., & Bregman, J. N. 1995, *ApJ*, 441, 568
- . 1997, in preparation
- Schulman, E., Bregman, J. N., Collura, A., Reale, F., & Peres, G. 1993, *ApJ*, 418, L67 (SBCRP)
- . 1994, *ApJ*, 426, L55
- Takano, M., Mitsuda, K., Fukazawa, Y., & Nagase, F. 1994, *ApJ*, 436, L47
- Tanaka, Y., et al. 1994, *PASJ*, 46, L37
- Trümper, J. 1984, *Phys. Scripta*, T7, 209
- van den Bergh, S. 1991, *PASP*, 103, 609
- van Paradijs, J., & McClintock, J. E. 1995, in *X-Ray Binaries*, ed. W. H. G. Lewin, J. van Paradijs, & E. P. J. van den Heuvel (Cambridge: Cambridge Univ. Press), 58
- Verbunt, F., & van den Heuvel, E. P. J. 1995, in *X-Ray Binaries*, ed. W. H. G. Lewin, J. van Paradijs, & E. P. J. van den Heuvel (Cambridge: Cambridge Univ. Press), 457
- White, N. E., Nagase, F., & Parmar A. N. 1995, in *X-Ray Binaries*, ed. W. H. G. Lewin, J. van Paradijs, & E. P. J. van den Heuvel (Cambridge: Cambridge Univ. Press), 1
- Zaritsky, D., Elston, R., & Hill, J. M. 1989, *AJ*, 97, 97

---

This 2-column preprint was prepared with the AAS L<sup>A</sup>T<sub>E</sub>X macros v4.0.

Fig. 1.— The X-ray light curve of M33 X-7 folded with a period of 298345.6 s. The data are plotted twice to show two cycles, and the *heavy dotted line* sketches an average trapezoidal light curve. *Einstein Observatory* observations are denoted by *circles*, *ROSAT* observations by *squares*, and *ASCA* observations by *triangles*.

Fig. 2.— The 68% (*inner*), 90% (*middle*), and 99% (*outer*) confidence level contours around the  $\chi^2$  minimum for the best orbital period and rate of period change calculated with a zero point offset= -29.9 ks, fall time= 53.4 ks, duration of total eclipse= 28.7 ks, and rise time= 18.5 ks.

Fig. 3.— The X-ray light curve of M33 X-7 folded with a period of 154227 s. The data are plotted twice to show two cycles, and the *heavy dotted line* sketches an average light curve. *Einstein Observatory* observations are denoted by *circles*, *ROSAT* observations by *squares*, and *ASCA* observations by *triangles*.

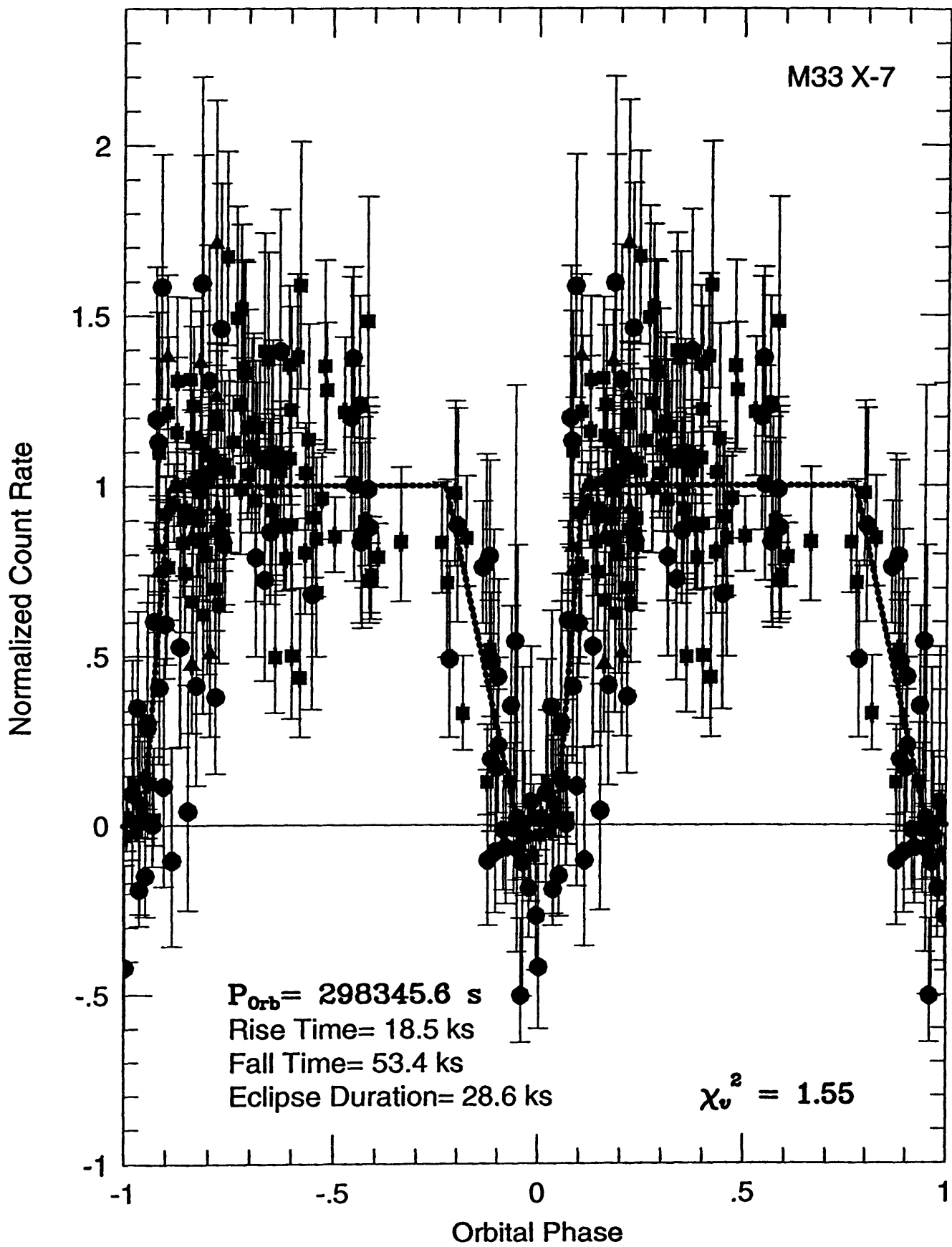


Figure 1

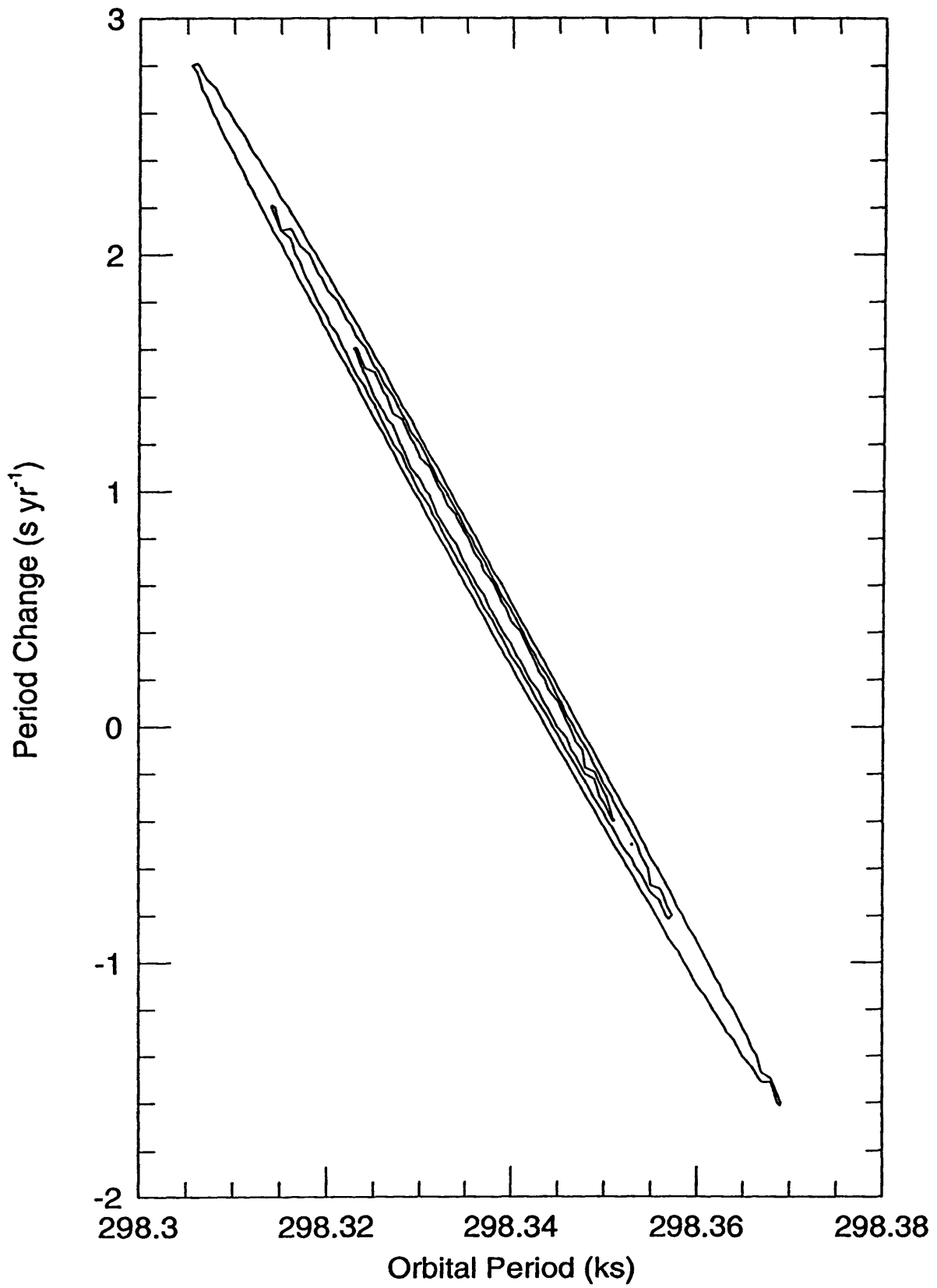


Figure 2

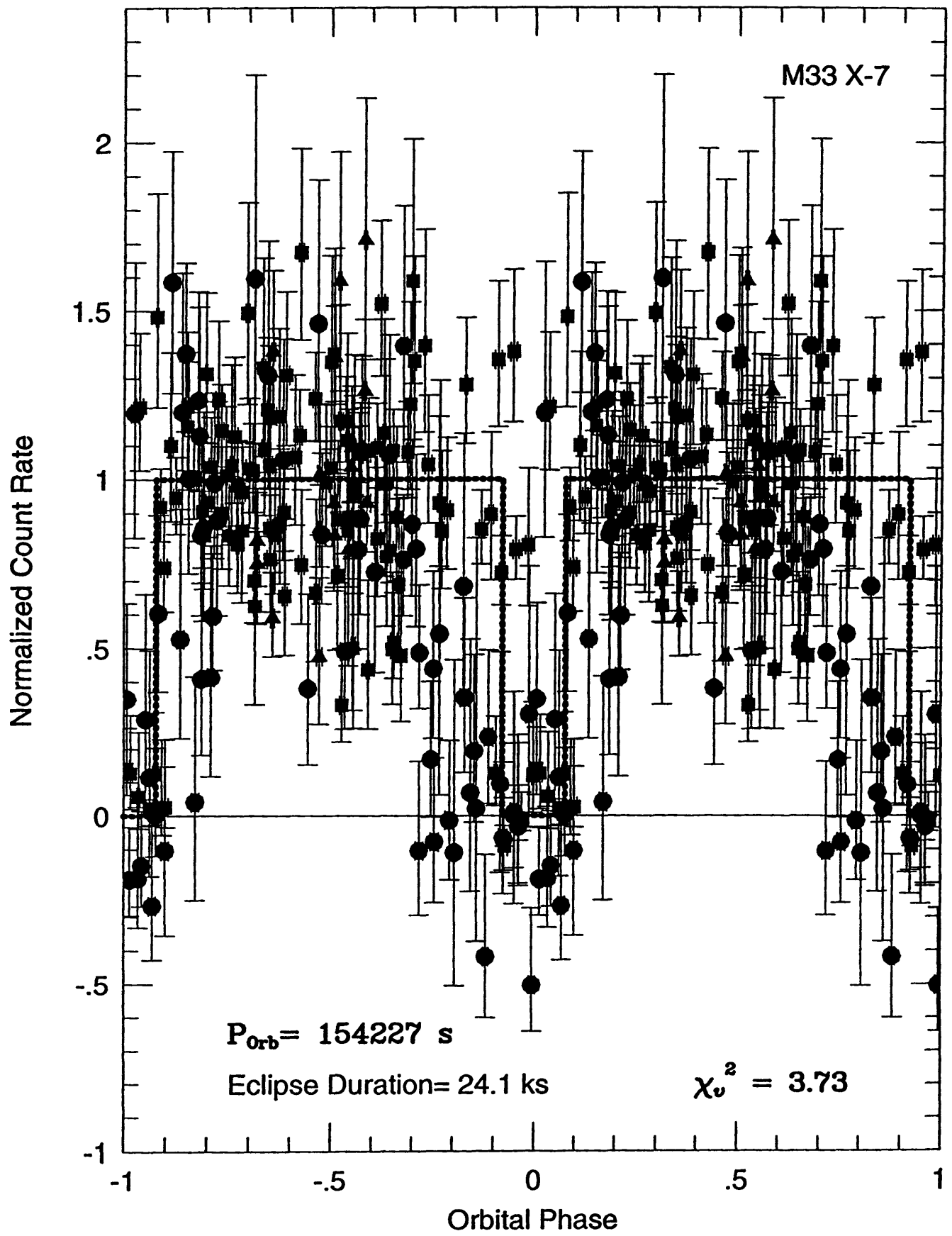


Figure 3

TABLE 1  
*Einstein Observatory, ROSAT, AND ASCA OBSERVATIONS OF M33*

Sequence Number	Pointing Center (B1950)		Observing Dates	Live Time (ks)	Count Rate (counts ks <sup>-1</sup> )
	$\alpha$	$\delta$			
EI2090	1:31:04.8	30:24:00	1979 Jul 31 - Aug 3	19.8	19.2
EH2724	1:31:04.8	30:24:00	1979 Aug 5 - Aug 7	39.7	5.6
EI2091	1:31:04.8	30:24:00	1980 Jan 11 - Jan 12	13.1	19.2
EH7577	1:31:26.4	30:24:36	1980 Jan 14 - Jan 15	26.4	5.6
EH9907	1:30:33.6	30:26:24	1980 Aug 2 - Aug 2	20.9	5.6
RP600023a	1:31:01.2	30:24:14	1991 Jul 29 - Jul 30	29.1	46.2
RH600020a	1:31:03.6	30:23:02	1992 Jan 8 - Jan 12	19.1	12.6
RH600020b	1:31:03.6	30:23:02	1992 Aug 1 - Aug 3	15.8	12.6
RP600023b	1:31:01.2	30:24:14	1992 Aug 10 - Aug 10	5.0	46.2
RP600023c	1:31:01.2	30:24:14	1993 Jan 7 - Jan 9	16.3	46.2
WP600407	1:29:46.9	30:30:12	1993 Feb 5 - Feb 5	3.7	37.8
WP600410	1:30:30.0	30:37:25	1993 Feb 5 - Feb 6	3.5	... <sup>a</sup>
WP600389	1:31:22.6	30:35:39	1993 Feb 6 - Feb 7	4.5	... <sup>a</sup>
AD60036000	1:31:15.5	30:30:43	1993 Jul 22 - Jul 23	17.4	... <sup>a</sup>
AD60036010	1:30:49.1	30:17:41	1993 Jul 23 - Jul 23	18.2	various <sup>b</sup>
RH600487	1:30:32.6	30:09:13	1994 Jul 27 - Aug 7	30.5	12.6
RH600488	1:30:18.2	30:15:13	1994 Jul 27 - Aug 7	24.5	12.6
RH600486	1:30:37.2	30:29:37	1994 Aug 1 - Aug 11	16.4	12.6
RH600489	1:30:18.1	30:23:01	1994 Aug 6 - Aug 8	20.3	12.6
RH600485	1:30:49.1	30:39:40	1994 Aug 6 - Aug 8	17.1	... <sup>a</sup>
RH600483	1:31:46.6	30:33:51	1994 Aug 6 - Aug 9	25.9	... <sup>a</sup>
RH600484	1:31:08.3	30:37:26	1994 Aug 8 - Aug 9	18.7	... <sup>a</sup>

<sup>a</sup>M33 X-7 was outside the effective field of view of these observations.

<sup>b</sup>Count rates varied by instrument: GIS= 7.8 counts ks<sup>-1</sup>, SIS0= 20.0 counts ks<sup>-1</sup>, SIS1= 13.7 counts ks<sup>-1</sup>.

TABLE 2  
COUNT RATE EXTRACTION PARAMETERS

Sequence Number	Aperture Radius (")	Background Annulus		Position
		inner	outer	
EI2090	80	140	180	centered on X-7
EH2724	30	60	80	centered on X-7
EI2091	80	140	180	centered on X-7
EH7577	30	60	80	offset from X-8
EH9907	30	60	80	offset from X-8
RP600023a	50	150	220	centered on X-7
RH600020a	15	150	240	centered on X-7
RH600020b	15	150	240	centered on X-7
RP600023b	50	150	220	centered on X-7
RP600023c	50	150	220	centered on X-7
WP600407	60	150	200	offset from X-8
AD60036010 (GIS)	90	120	150	offset from X-8
AD60036010 (SIS)	60	0	120 <sup>a</sup>	offset from X-8
RH600487	15	150	240	centered on X-7
RH600488	15	150	240	centered on X-7
RH600486	15	150	240	centered on X-7
RH600489	15	150	240	centered on X-7

<sup>a</sup>Background aperture centered at  $\alpha = 1^{\text{h}} 31^{\text{m}} 18^{\text{s}}.6$ ,  $\delta = +30^{\circ} 15' 35''$  (B1950).

TABLE 3  
RESULTS OF CHI-SQUARED ANALYSIS

Period Range (s)	Eclipse Duration (ks)	Zero Point Offset <sup>a</sup> (ks)	$\chi^2$ <sup>b</sup>
298345 to 298347	trapezoid <sup>c</sup>	-31.0 to -29.0	1.55 <sup>d</sup>
298347 to 298348	59.0 to 62.2	-21.9 to -20.2	1.76
319499	57.0 to 57.8	-6.4 to -6.0	2.31
326090	64.2 to 64.6	-22.1 to -21.9	2.60
304094 to 304096	59.8 to 63.4	-19.2 to -15.8	2.67
310066 to 310067	71.4 to 75.4	-18.0 to -15.3	2.71
316306	50.0 to 57.6	-3.2 to 0.7	2.93
311491	45.4 to 49.8	-34.0 to -31.8	3.00
325835 to 325837	53.4 to 55.4	-35.7 to -34.6	3.15
292991 to 292995	68.4 to 75.2	-14.8 to -10.8	3.42
305480 to 305483	40.0 to 47.6	- 4.4 to 0.8	3.50
351232 to 351234	97.6 to 100.8	6.0 to 7.6	3.54
147782	27.0 to 28.2	-15.6 to -15.0	3.67
302550 to 302552	37.8 to 50.6	- 5.4 to 3.9	3.68
154227	23.6 to 24.6	-26.9 to -26.4	3.73 <sup>e</sup>

<sup>a</sup>The center of the first eclipse is J.D. 2,444,087.606 + Zero Point Offset.

<sup>b</sup>Calculated with 194 points and 3 free parameters. Row 1 used 5 free parameters.

<sup>c</sup>Trapezoidal model with fall time= 46 to 62 ks, duration of total eclipse= 26 to 30 ks, and rise time= 16 to 21 ks.

<sup>d</sup>See Figure 1.

<sup>e</sup>See Figure 3.

**NATIONAL RADIO ASTRONOMY OBSERVATORY  
Charlottesville, Virginia**

**ELECTRONICS DIVISION INTERNAL REPORT NO. 305**

**AN ADAPTIVE INTERFERENCE CANCELING RECEIVER  
FOR RADIO ASTRONOMY - THEORY**

**R. Bradley, S. Wilson\*, C. Barnbaum and B. Wang\*\***

November 1, 1996

---

\*University of Virginia, Electrical Engineering

\*\*NSF REU Student

## Table of Contents

<b>1.0</b>	<b>Introduction</b>	<b>1</b>
<b>2.0</b>	<b>Background Information on Adaptive Filters</b>	<b>4</b>
<b>3.0</b>	<b>Fundamentals of Adaptive Interference Cancellation</b>	<b>7</b>
3.1	Basic Concepts	7
3.2	Error-Performance Surface and the Wiener Filter	9
3.3	Single Reference Channel Adaptive Interference Canceler	12
3.4	The LMS Algorithm	17
3.5	Multiplier Reference Adaptive Interference Cancellation	19
3.6	The Notch Filter Phenomenon	21
3.7	Adaptive Beam Formation and Sidelobe Cancellation	22
3.8	Finite Precision Errors	24
3.9	Estimated Performance of the Adaptive Canceler	27
<b>4.0</b>	<b>Simulations of a Multiple Reference Interference Canceler</b>	<b>28</b>
4.1	Simulator and Platform	28
4.2	Description of Adaptive Canceler System and Input Signals	28
4.3	Overall Canceler Performance	29
4.4	Investigation #1: Performance Vs. Adaptation Step Size	33
4.5	Investigation #2: Performance Vs. Number of Reference Channels	35
4.6	Investigation #3: Performance Vs. Primary Channel Noise Power	36
4.7	Investigation #4: Performance Vs. Reference Channel Noise Power	36
<b>5.0</b>	<b>Conclusions</b>	<b>40</b>
	<b>Appendix</b>	<b>41</b>
	<b>List of Symbols</b>	<b>50</b>
	<b>Bibliography</b>	<b>53</b>

## 1.0 Introduction

An increasing amount of precious radio frequency spectrum in the VHF, UHF, and microwave bands is being utilized each year to support new commercial and military ventures. Advances in both very large scale integration (VLSI) and monolithic RF (MMIC) technology has spurred a plethora of new applications, including improved point-to-point communications, wireless computer communications, and the ever-growing popularity of inexpensive cellular telephones; all have the potential to interfere with radio astronomy observations. Furthermore, the sky is being cluttered with earth-orbiting satellites supporting direct broadcast television, global personal communications, global positioning systems, and other services. Signals from satellites even occasionally leak into the designated radio astronomy bands. The increasing congestion of the radio spectrum has made astrophysical research in radio and microwave bands more difficult to pursue.

Some radio spectral lines of astronomical interest occur outside the protected radio astronomy bands and are unobservable due to heavy interference. One example, the initial motivation behind this work, is the hyperfine transition of hydrogenated buckminsterfullerene ( $\text{HC}_{60}$ ), that is predicted to fall in the 90 - 100 MHz band (Morton et al., 1993). This band, which is part of the FM broadcast band that spans 88 - 108 MHz, contains FM channels that are spaced 200 kHz apart, and even in a remote radio astronomy site such as Green Bank, WV, nearly the entire band exhibits interference, as shown in Fig. 1. These signals are frequency modulated carriers that are also influenced by propagation effects between the transmitter and the receiver; the statistics of the interference signals vary as a function of time. A glance at Fig. 1 reveals that it is impossible to observe in this band without highly effective interference excision.

Over the past several years, scientists and engineers concerned with such interference have organized special workshops and conference sessions to share ideas on ways to manage this growing problem. The more conventional approaches being discussed at these meetings include the following: 1) legislation to designate regions as radio quiet areas such as the National Radio Quiet Zone (NRQZ) around Green Bank,

investigate new approaches to interference excision that have the potential to improve upon the shortcomings of these conventional techniques.

One concept of interference excision that has not been used before in radio astronomy is adaptive interference cancellation which makes use of adaptive filters and high speed digital technology. This report, for the first time, describes the basic concept of adaptive cancellation in the context of radio astronomy instrumentation and estimates the canceler effectiveness on several radio telescopes. The results of system simulations based on FM broadcast signals as interferers is also presented. The report concludes with a summary of the important issues to consider when attempting to use this approach in radio astronomy applications.

that is equal to the reciprocal of the unknown process; 3) Prediction, in which the adaptive filter provides the best prediction of the present value of a random signal, where the actual present value is the desired response; and 4) Interference Canceling, in which the adaptive filter is used to cancel unknown interference contained alongside the information bearing signal component in the primary channel, with the cancellation being optimized in some sense. It is in this latter category that the adaptive filter will be used in the context of radio astronomy interference excision.

Early work on adaptive interference cancellation was limited to narrow audio bandwidths. Around 1965, an adaptive echo canceler for telephone lines was developed at Bell Telephone Laboratories (Sondhi, 1967). Also in 1965, an adaptive line enhancer (ALE) was built to cancel 60 Hz interference at the output of an electrocardiographic (ECG) amplifier and recorder (Widrow et al., 1975). In 1972, a group of students at Stanford University used adaptive filtering to cancel the maternal ECG in fetal electrocardiography, where the mother's heartbeat has an amplitude from two to ten times stronger than the fetal heartbeat (Widrow et al., 1975). Over the past twenty years, such audio interference cancellation systems have been developed for many diverse applications from speech enhancement for communications in noisy environments to the reduction of harmful noise in harsh work environments. There is even a company, Noise Cancellation Technologies Corporation, that specializes in noise reducing audio systems for portable radio telephone applications (Goldberg, 1995)!

Extending the adaptive filtering concept to wideband applications above a few hundred kilohertz has required advances in the digital hardware. Operation up to a few megahertz can now be performed using modern digital signal processing chips such as the Logic Devices Inc. LMA1009 12 x 12 bit multiplier-accumulator chip (Logic Devices, 1995). The development of the Acoustic Charge Transport (ACT) programmable transversal filter (Fleisch et al., 1991) permits limited precision operation up to about 100 MHz. Bullock (1990) describes a wideband adaptive filter which uses the ACT to remove narrowband interference. The system input, which contains both the desired (wideband) and reference (narrowband) signals, is processed by a decorrelation delay that separates the two components (Widrow et al., 1975). The adaptive filter is then used to suppress

### 3.0 Fundamentals of Adaptive Interference Cancellation

In this section, we present the theory of adaptive interference cancellation. For a more complete description, see Widrow et al. (1985). The section begins with a look at the overall system concept and then we describe the performance of the system for a single channel adaptive interference canceler in the presence of stationary inputs (Wiener solution). Next, we describe the algorithm for the adaptation process. The basic concept is then extended to include multiple reference inputs, and we compare this system with adaptive beamforming. This section closes with a brief note on finite precision errors and an estimate of canceler performance on several radio telescopes.

#### 3.1 Basic Concepts

An ideal adaptive interference canceling system for use on a radio telescope is depicted in Fig. 2. All of the signals are digitized with a constant sampling period, giving rise to discrete time sequences indexed by  $n$ . The telescope receiver, located at the prime focus, forms the primary input to the canceler. This input consists of the desired astronomical signal,  $s(n)$ , entering through the main beam, as well as undesired interference,  $i_p(n)$ , entering through the telescope sidelobes. We assume here that the power density of the interference will preclude astronomical observing, but will not be strong enough to "overload" the receiver (overloading occurs when the amplitude of the signal causes the amplifiers to operate outside of their linear range, resulting in the generation of spurious signals). A second receiver connected to an omni-directional antenna forms the reference input,  $x(n)$ , to the canceler. This input consists of only the interference,  $i_x(n)$ , which is uncorrelated with the astronomical signal, but correlated in some unknown way with the interference in the primary channel. Here we assume that the desired astronomical signal does not contribute to the reference input. In the reference channel, the interference is filtered to produce the output,  $y(n)$ , that is a close replica to  $i_p(n)$ . This filter output is subtracted from the primary input,  $s(n) + i_p(n)$ , to produce the system output,  $\varepsilon(n)$ . It is important to note that no prior knowledge of  $s(n)$ ,  $i_p(n)$ , or  $i_x(n)$  or their interrelationships, either statistical or deterministic, is required.

$$\varepsilon(n)^2 = s(n)^2 + (i_p(n) - y(n))^2 + 2s(n)(i_p(n) - y(n)) \quad (1)$$

Taking expectations of both sides and noting that  $s(n)$  is uncorrelated with  $i_p(n)$  and  $y(n)$ , yields

$$E[\varepsilon(n)^2] = E[s(n)^2] + E[(i_p(n) - y(n))^2] \quad (2)$$

The total signal power,  $E[s(n)^2]$ , will be unaffected as the filter is adjusted to minimize  $E[\varepsilon(n)^2]$ . The minimum total output power is therefore

$$E_{\min}[\varepsilon(n)^2] = E[s(n)^2] + E_{\min}[(i_p(n) - y(n))^2] \quad (3)$$

When the filter is adjusted so that  $E[\varepsilon(n)^2]$  is minimized,  $E[(i_p(n) - y(n))^2]$  is therefore also minimized. The filter output,  $y(n)$ , is a best least-squares estimate of the primary interference  $i_p(n)$ . Hence, *minimizing the total output power minimizes the output interference power*, and since the signal in the output remains constant, minimizing the total output power maximizes the output signal-to-interference ratio (SIR).

Two special cases are worth noting. From (3), the smallest possible output power is  $E[s(n)^2]$  when  $E[(i_p(n) - y(n))^2] = 0$ . In this case, minimizing the output power causes the output signal to be perfectly free of interference. Now consider the case when the reference input is completely uncorrelated with the interference in the primary input. The filter will turn itself off and will not increase output power. In this case,  $y(n)$  is uncorrelated with the primary input so that

$$E[\varepsilon(n)^2] = E[(s(n) + i_p(n))^2] + E[y(n)^2] \quad (4)$$

Maximizing the output power requires that  $E[y(n)^2]$  be minimized, which is accomplished by making the filter coefficients zero, bringing  $E[y(n)^2]$  to zero.

### 3.2 Error-Performance Surface and the Wiener Filter

Figure 3 shows the classic single-input, single-output Wiener filter, constructed using a transversal filter (also known as a tapped-delay line), and a linear combiner. The transversal filter is used in almost all interference canceling applications since it has a

$$E[\varepsilon(n)^2] = E[p(n)^2] + W(n)^T E[X(n)X(n)^T] W(n) - 2E[p(n)X(n)^T] W(n) \quad (7)$$

The signals  $x(n)$  and  $p(n)$  are not generally independent. The elements that make up (7) are all constant second-order statistics when the vector  $X(n)$  and  $p(n)$  are stationary, so the error performance surface,  $\xi = E[\varepsilon(n)^2]$ , defined by (7) is quadratic, forming a hyperparaboloid that is concave upward and therefore has a unique minimum. Knowing that the correlation function,  $\phi$ , is equivalent to the expected value function for a stationary process, and expanding the matrix operations, the error performance surface becomes

$$\xi = \phi_{pp}(0) + \sum_{l=-\infty}^{\infty} \sum_{m=-\infty}^{\infty} w(n)_l w(n)_m \phi_{XX}(l-m) - 2 \sum_{l=-\infty}^{\infty} w(n)_l \phi_{XP}(-l) \quad (8)$$

which is constant for stationary processes.

The minimum point on this surface corresponds to the optimum weight vector,  $W_{opt}$ . The values of  $W_{opt}$  can be found by setting the derivatives of  $\xi$  with respect to the weights equal to zero. Thus

$$\frac{\partial \xi}{\partial w(n)} = 2 \sum_{l=-\infty}^{\infty} w(n)_l \phi_{XX}(n-l) - 2 \phi_{XP}(-n) = 0 \quad (9)$$

and therefore the Wiener-Hopf equation is obtained,

$$\sum_{l=-\infty}^{\infty} w_{opt\ l} \phi_{XX}(n-l) = \phi_{XP}(n) \quad (10)$$

Taking the  $z$  transform of (10), the convolution on the left side becomes a product and, defining  $W_{opt}(z) = z$  transform of  $[w_{opt}(n)]$ ,

$$W_{opt}(z) = \frac{\Phi_{XP}(z)}{\Phi_{XX}(z)} \quad (11)$$

The  $z$  transform of the optimum impulse response is the ratio of the cross power spectrum between the input to the transversal filter,  $x(n)$ , and the primary input,  $p(n)$ , to the power spectrum of  $x(n)$ . This result represents the unconstrained, noncausal

The reference input to the canceler is  $m_x(n) + i_x(n)$ . The primary input, is  $s(n) + m_p(n) + i_p(n)$ . The error signal,  $\epsilon(n)$ , is the canceler output. Assuming that the adaptive filter has converged, and the minimum-mean-square-error solution has been found, the adaptive filter is equivalent to the Wiener filter discussed in the previous section. The optimal unconstrained transfer function,  $W_{opt}(z)$  of the filter can be found from the power spectra ratio of (11). The spectrum of the filter input,  $\Phi_{xx}(z)$ , can be expressed in terms of the spectra of two mutually uncorrelated additive components, the spectrum of the

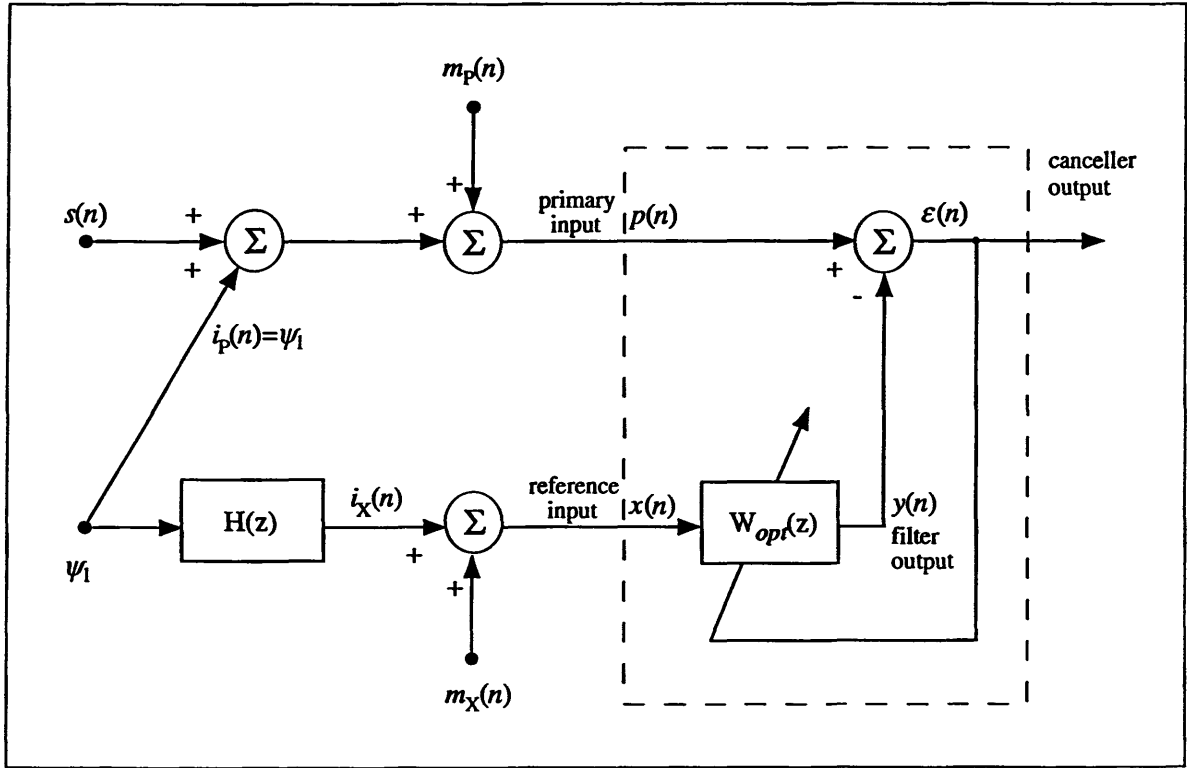


**Figure 4** Model of the system shown in Fig. 2. The model includes the noise temperatures of the primary and reference receivers and the channel transfer functions for the interference paths.

noise  $m_x(n)$  and that of the interference  $\psi_1 = i_p(n)$  arriving via  $H(z)$ ,

$$\Phi_{xx}(z) = \Phi_{m_x m_x}(z) + \Phi_{i_p i_p}(z) |H(z)|^2 \quad (12)$$

The cross power spectrum between the reference input and the primary input depends only on the mutually correlated components, and is given by

which results from the propagation of  $i_p(n)$  through two paths, one via the primary channel and the other through the reference channel. Substitution of equation (17) into (18) gives the interference attenuation as

$$IA(z) = [INR_{ref}(z) + 1]^2 \quad (19)$$

A plot of the interference attenuation as a function of  $INR_{ref}(z)$  is shown in Fig. 5. The magnitude of the attenuation for moderate values of  $INR_{ref}(z)$  can be quite substantial since it is proportional to the square of the reference channel INR. Note that the interference attenuation is frequency dependent, since all quantities are a function  $z$ .

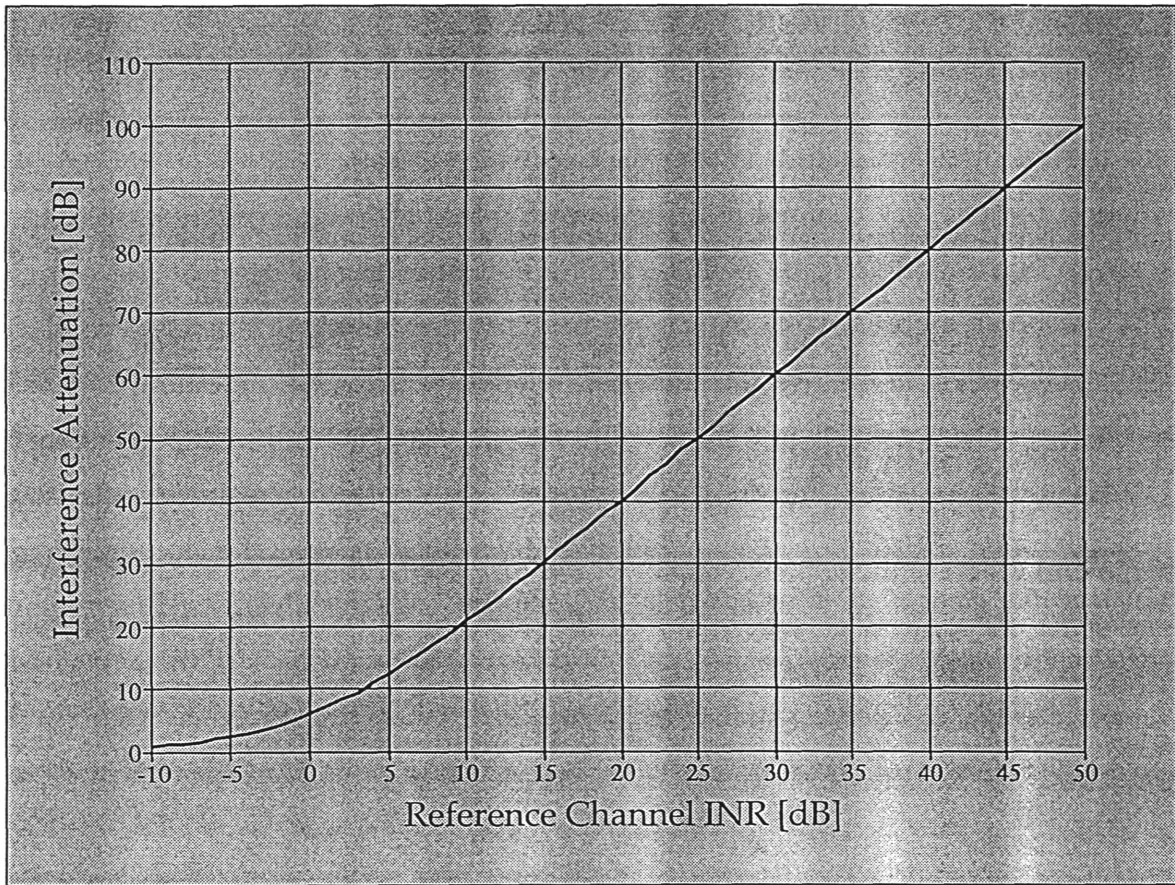


Figure 5 Graph of the Interference Attenuation (IA) as a function of reference channel INR.

Because the reference channel noise is not zero, some noise will be added to the output of the canceler. The residual noise ratio, which provides a measure of this noise

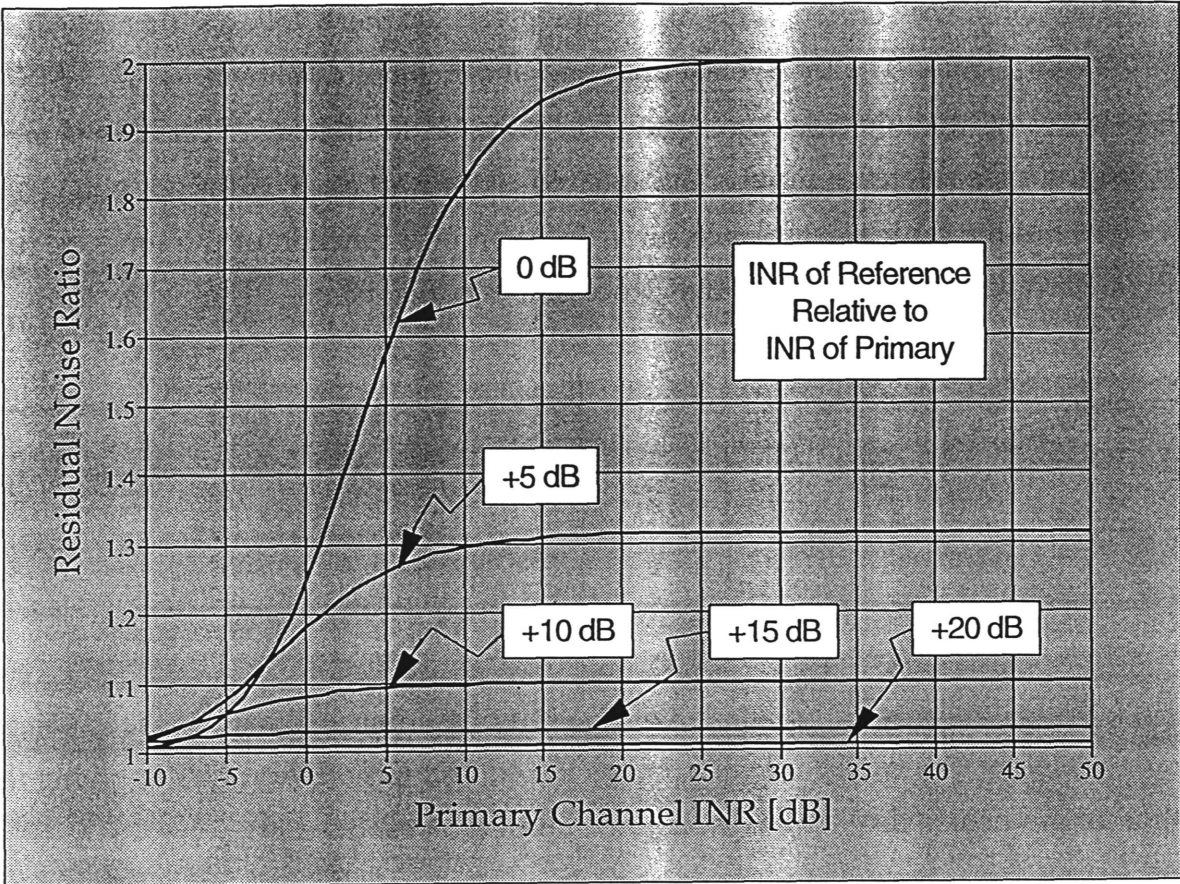


Figure 6 Graph of residual noise ratio as a function of primary channel INR for various values of reference channel INR (relative to the primary channel INR).

### 3.4 The LMS Algorithm

In this section, we introduce the Least-Mean-Square (LMS) algorithm for descending on the performance surface. This algorithm uses a special estimate of the gradient that is closely tied with the structure of the transversal filter. As a result, the algorithm requires a minimal amount of computing and is therefore easy to implement in hardware. There are many other algorithms offering improvements over LMS, examples include the Recursive Least-Squares (RLS) algorithm (Haykin, 1996) which requires off-line gradient estimations, and the newly proposed Higher-Order Statistics (HOS) algorithm (Shin, 1994) which uses higher (greater than 2) order cumulants to mitigate narrowband and wideband interferences but involves greater computational

$$0 < \mu < \frac{1}{(L+1)(E[x^2(n)])} \quad (24)$$

Since  $E[x^2(n)]$  is the reference signal power, the optimum value of  $\mu$  for best convergence is anticipated to be a function of interference power. We explore this in the simulations.

Another important issue in adaptive filters is the misadjustment,  $M_{ADJ}$ , which is defined as the ratio of the excess mean-square error to the minimum mean-square error, and is a measure of how closely the adaptive process tracks the true Wiener solution. It can be shown (Widrow et al., 1985) that the misadjustment for the LMS process is

$$M_{ADJ} \approx \mu \operatorname{tr}(E[X(n) X^T(n)]) = \mu \operatorname{tr}[R(n)] \quad (25)$$

where  $\operatorname{tr}$  indicates the trace operation on the *input correlation matrix*,  $R(n) = E[X(n)X^T(n)]$ . There is a trade-off between misadjustment and rate of adaptation, i.e, a smaller value of  $\mu$  gives a smaller misadjustment, but the algorithm will take much longer to converge. Again, we explore this trade-off in the simulations.

### 3.5 Multiple Reference Adaptive Interference Canceling

When more than one interference signal must be canceled, the single reference channel adaptive system lacks the necessary degrees of freedom to eliminate both signals adequately, and so the result is far from optimum. The effectiveness of the cancellation can be improved substantially by increasing the number of adaptive filter reference inputs to equal or exceed the anticipated number of interference signals that are likely to be encountered. The reference inputs could also include orthogonal spatially-polarized elements. A model of the multiple reference system is shown in Fig. 7 (Widrow et al., 1975). This model shows  $M$  mutually uncorrelated sources of interference,  $\psi_1$  through  $\psi_M$ . The transfer functions,  $G_i(z)$  represent the propagation paths from these sources to the primary inputs. The transfer functions,  $F_{ij}(z)$  similarly represent the propagation paths to the reference inputs and allow for cross-coupling.

$$[\Phi_{XX}(z)] = [F(z^*)]^T [\Phi_{\Psi\Psi}(z)] [F(z)] \quad (27)$$

where

$$[F(z)] = \begin{bmatrix} F_{11}(z) & \dots & F_{1N}(z) \\ \vdots & & \vdots \\ F_{M1}(z) & \dots & F_{MN}(z) \end{bmatrix} \quad (28)$$

The cross-spectral vector from the reference inputs to the primary input is given by

$$[\Phi_{XP}(z)] = [F(z^*)]^T [\Phi_{\Psi\Psi}(z)] G(z) \quad (29)$$

From (27) and (29), the set of optimal weight vectors,  $W_{opt 1}$  through  $W_{opt N}$  becomes the matrix

$$\begin{aligned} [W_{opt}(z)] &= [\Phi_{XX}(z)]^{-1} \Phi_{XP}(z) \\ &= [[F(z^*)]^T [\Phi_{\Psi\Psi}(z)] [F(z)]^{-1} [F(z^*)]^T [\Phi_{\Psi\Psi}(z)] [G(z)] \end{aligned} \quad (30)$$

Equation (30) can be used to derive steady-state optimal solutions to the multiple-interference, multiple-reference canceler. We explore the performance as a function of the number of reference channels in the simulations.

### 3.6 The Notch Filter Phenomenon

An interesting phenomenon will occur in the behavior of the adaptive filter if the reference channel encounters a narrow bandwidth RF carrier (approaching a sinusoid) and if a 90 degree phase shift occurs between two filter tap weights of a single transversal filter or between two channels of a multiple reference canceler system. When presented with this configuration, the canceler behaves like a high-Q notch filter. It can be shown (Widrow et al., 1975) that the poles and zeros of the filter transfer function have almost the same angle and are separated by a distance of approximately  $\mu A^2$ , where  $\mu$  is the step size and  $A$  is the amplitude of the sinusoid. The bandwidth,  $B_{notch}$  of the

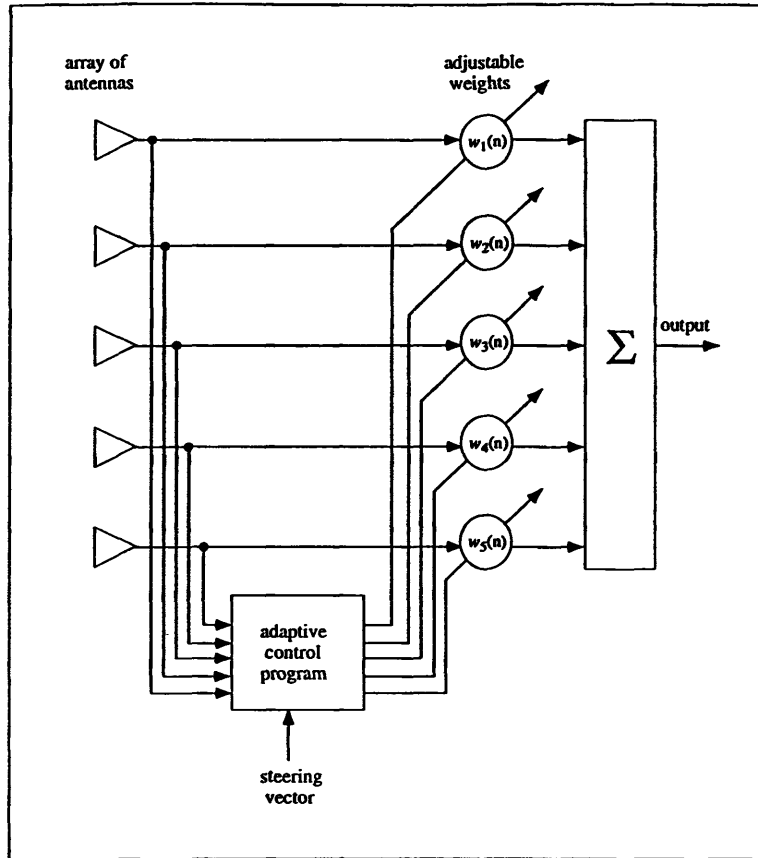


Figure 8 Block diagram of the basic adaptive beam forming system.

For wide bandwidth operation, the single complex weights must be replaced by transversal filters so that the amplitude and phase can be adjusted as desired at a number of frequencies over the band of interest. If the weight temporal spacing (delay) is sufficiently small, this network approaches the ideal filter that would allow complete control of amplitude and phase over the entire passband. Figure 10 shows the a block diagram of the adaptive canceling system which now performs both spatial and temporal canceling. This system is identical to the multi-channel canceler described in Section 3.5.

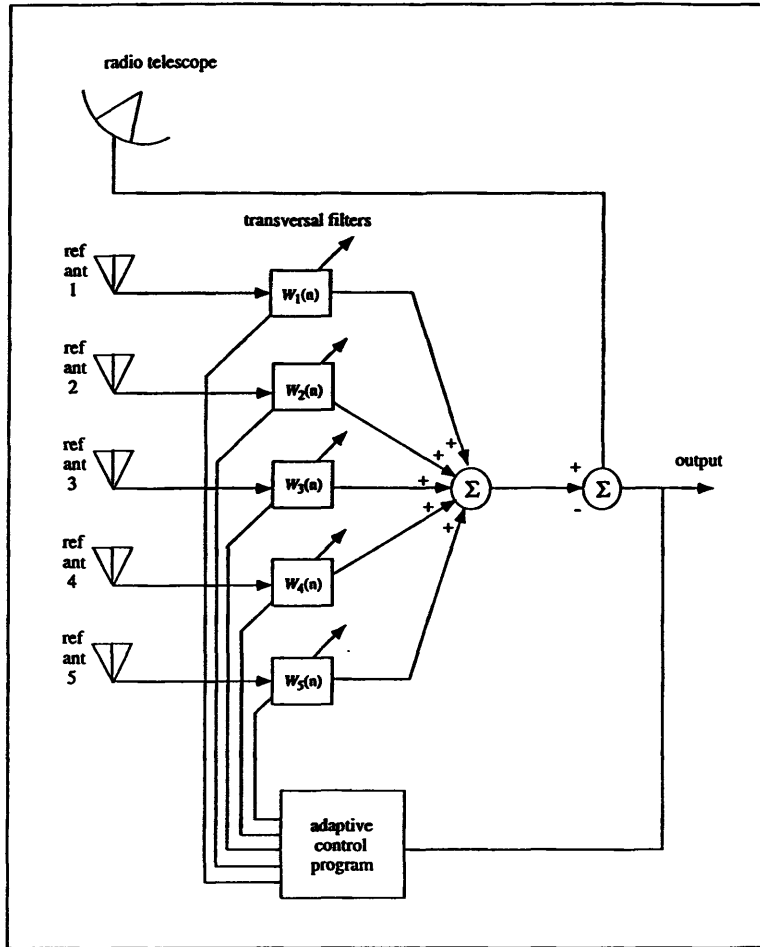


Figure 10 Block diagram of the temporal-spatial interference canceler.

In the digital implementation of an adaptive filter, there are two sources of quantization error: *analog-to-digital (A/D) conversion* and *finite word-length arithmetic*. Analog-to-Digital conversion, using fine quantization levels, results in the generation of white noise with zero mean and a variance determined by the quantizer step size,  $\delta = 2^{-b}$  where  $b$  is the number of digital bits used to represent a given quantity,

$$\sigma_q^2 = \int_{-\delta/2}^{+\delta/2} \frac{1}{\delta} \eta^2 d\eta = \frac{2^{-2b}}{12} \quad (32)$$

and it is assumed that the quantizer input is properly scaled to lie in the interval

### **3.9 Estimated Performance of the Adaptive Canceler**

The performance of the adaptive interference cancellation system was estimated for the following radio telescopes: 1) the Green Bank 140 foot telescope operating at 100 MHz and 1 GHz, 2) the Green Bank Telescope (GBT) operating at 100 MHz and 1 GHz, 3) a VLA antenna operating at 1 GHz, and 4) the Arecibo 1000 foot telescope operating at 100 MHz and 1 GHz. Details are presented in the Appendix.

Figure 11 shows the input signals for the primary channel and two of the four reference channels. The abscissa of each graph is the baseband frequency in kilohertz and the ordinate shows relative power in decibels. There are three frequency-modulated interference signals (modulated with random audio tones) in both the primary and reference channels, one at 300, 550, and 800 kHz. White noise is also included in each channel to represent the system noise temperatures. The characteristics of these signals are shown in Table I. There is also a narrow band test signal, located at 300 kHz, with a power level that is 15 dB below the interference power level at that frequency.

**Table I** Interference signals in the primary and reference channels and estimated canceler performance.

Interference Signal in Baseband [kHz]	Bandwidth [kHz]	$INR_{pri}$ [dB]	$INR_{ref1 \& 2}$ [dB]	Interference Attenuation [dB]	Residual Noise [%]
300	100	30	37	74	20.0
550	100	22	37	74	3.2
800	25	22	37	74	3.2

### 4.3 Overall Canceler Performance

The adaptation process was initiated and the LMS algorithm, with step parameter  $\mu = 0.00015$ , was allowed sufficient time to converge to an optimal solution; the results for 2000 samples (1 block) are displayed in Fig. 12. For comparison, Fig. 12 also contains the perfect interference-free solution which contains only the white noise component. The statistics of the two waveforms are highly correlated in frequency as one would expect if the cancellation is good since the random variables are the same for both cases. Overall, the interference is reduced substantially and the test signal at 300 kHz is visible above the noise floor.

Since the  $INR_{ref}(z)$  is finite, it is expected that the three interference signals will not be canceled completely, and a residual noise component will remain. The interference attenuation is approximately 74 dB for each interference signal. The residual noise, although frequency dependent, will not affect the noise RMS value, but it will affect the baseline structure at the frequency where the interference is located. Upon comparing the  $INR_{ref}(z) / INR_{pri}(z)$  ratio shown in Table I with the graph of Fig. 6, the residual will be on the order of 20 percent for the 300 kHz signal and about 3 percent for the signals at 550 and 800 kHz. Figure 13 shows the canceler output after averaging over 4000 blocks of data. Again, the perfect interference-free solution is included for comparison. The residual noise at 550 and 800 kHz have nearly vanished and the noise RMS value is the same as the in the idealized output. As expected, the residual near 300 kHz is most apparent (maximum about 0.8 dB), manifesting itself as a double sloping baseline, which follows the curve in Fig. 6. The test signal that was 15 dB below the interference power level is now 14 dB above the noise floor. The notch filter phenomenon is present at 800 kHz due to the narrow bandwidth of the interference there and the choice of  $\mu$ . (see Section 3.6). These results form a framework for the investigations that follow.

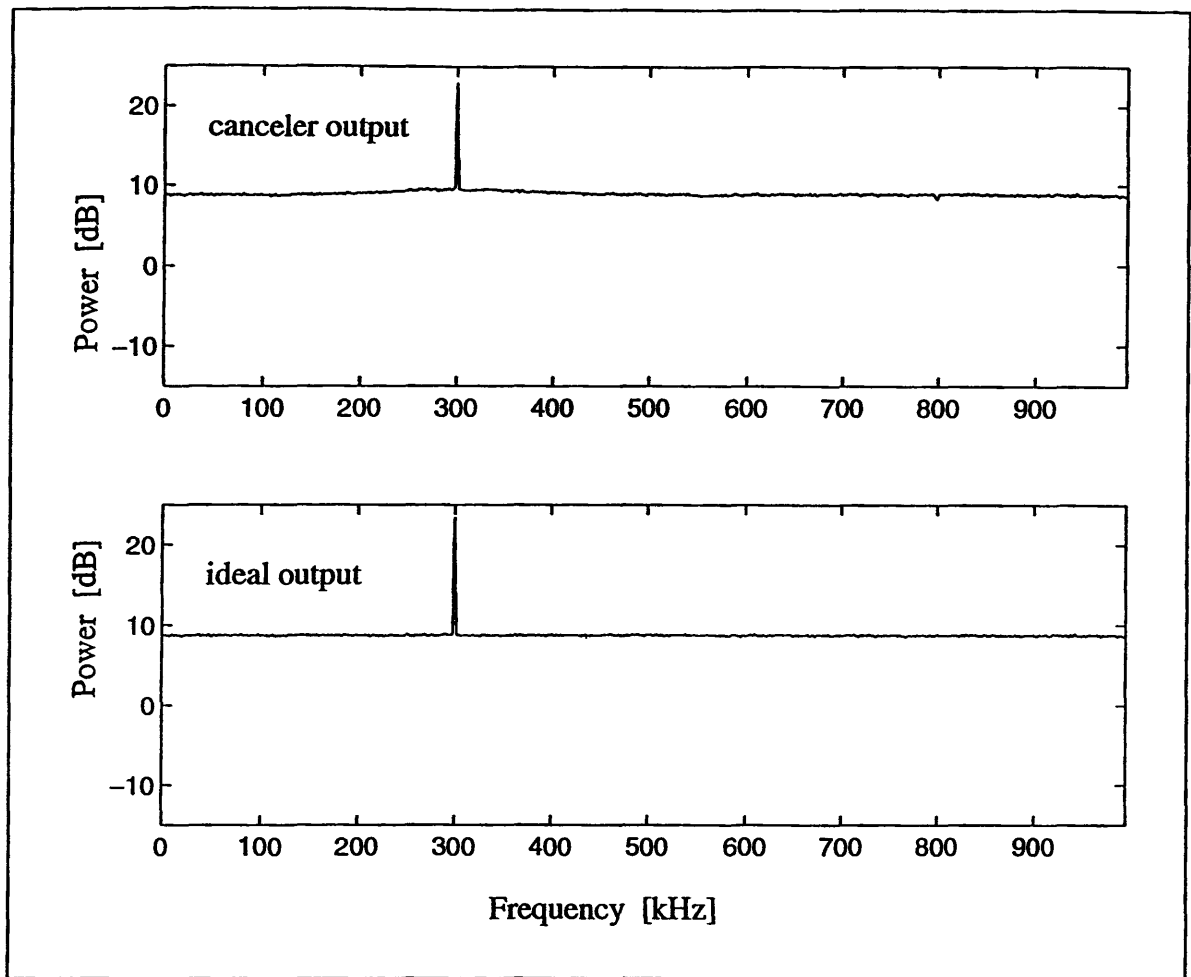


Figure 13 Simulation of a four reference channel adaptive canceler after 4000 block average of the output data. The perfect interference-free solution is shown below.

#### 4.4 Investigation #1: Performance vs. Adaptation Step Size

With the canceler system as described in Section 4.2, we used the simulator to examine the effects of the step size parameter,  $\mu$ . Figure 14 shows the averaged canceler output data for three values of  $\mu$ . The smallest value,  $\mu = 0.000005$ , yields fair performance, yet the baseline contains some structure due to the very slow adaptation time. The notch filter phenomenon is not present in the output when  $\mu$  is relatively small. As described in Section 3.8, a small value of  $\mu$  can result in a large added noise component due to the quantization of the transversal filter tap-weights. This component, which can be significant, is not analyzed in these simulations.

As shown in Fig. 14, the adaptation process resulting from larger values of  $\mu$  suffer from two problems: 1) the notch bandwidth, as described by equation (31), is very large thus causing significant distortion in the passband, and 2) the misadjustment becomes large causing a jitter-type movement toward and around the minimum in the error performance surface as described by equation (25). This jitter movement results in increased noise at the canceler output. Equation (25) also indicates that the misadjustment is a function of the reference signal power (proportional to the trace of the input correlation matrix). *In order to maintain proper operation over a wide dynamic range of interference signals powers, it is recommended that the value of  $\mu$  be fixed and either an automatic gain control be used on all reference channels, or after A/D conversion the reference channels should be scaled by a factor inversely proportional to the interference power in that channel.*

#### 4.5 Investigation #2: Performance vs. Number of Reference Channels

We examine the performance of the canceler as a function of the number of reference channels having interference signals and noise spectrum as outlined in Table I. Averaged canceler output data is shown in Fig. 15 for the case of one, two, and four reference channels. The perfect interference-free solution is also included for comparison. A system having only one reference channel shows uncanceled interference components at all three interference frequencies. These residuals are due to the transversal filter being of finite length and therefore a transfer function with enough resolution to cover the entire operating range cannot be formed. Having two reference channels makes a sizable improvement, particularly at 550 and 800 kHz, and going to four reference channels improves the cancellation further to the point where the overall operation is now limited by the interference-to-noise ratios in the primary and reference channels. The notch filter phenomenon is present only when four reference channels are used, which is consistent with the discussion in Section 3.6.

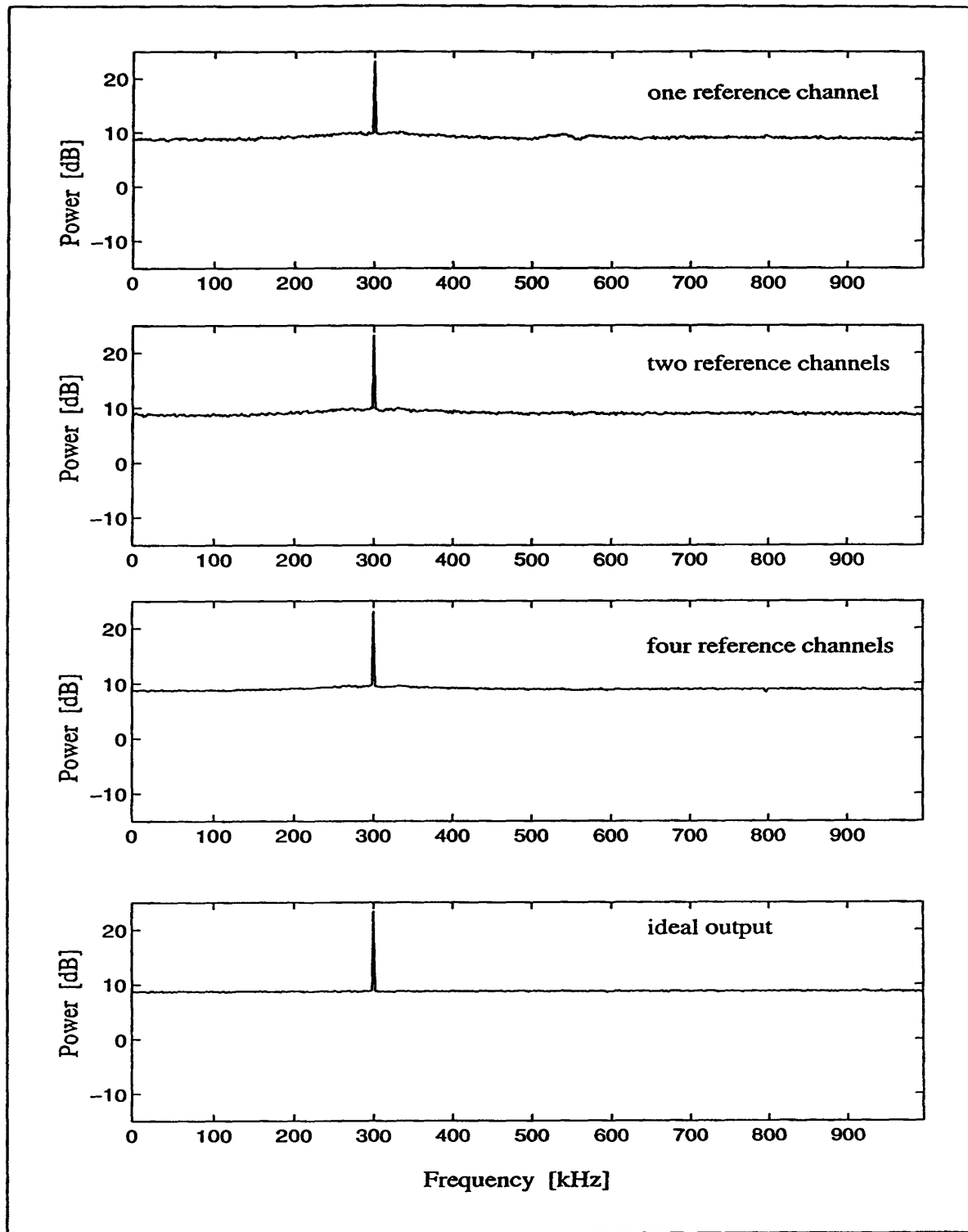


Figure 15 Averaged canceler output data for simulated adaptive interference cancelers having one, two, and four reference channels. Canceler input is described in Fig. 11 and Table I.

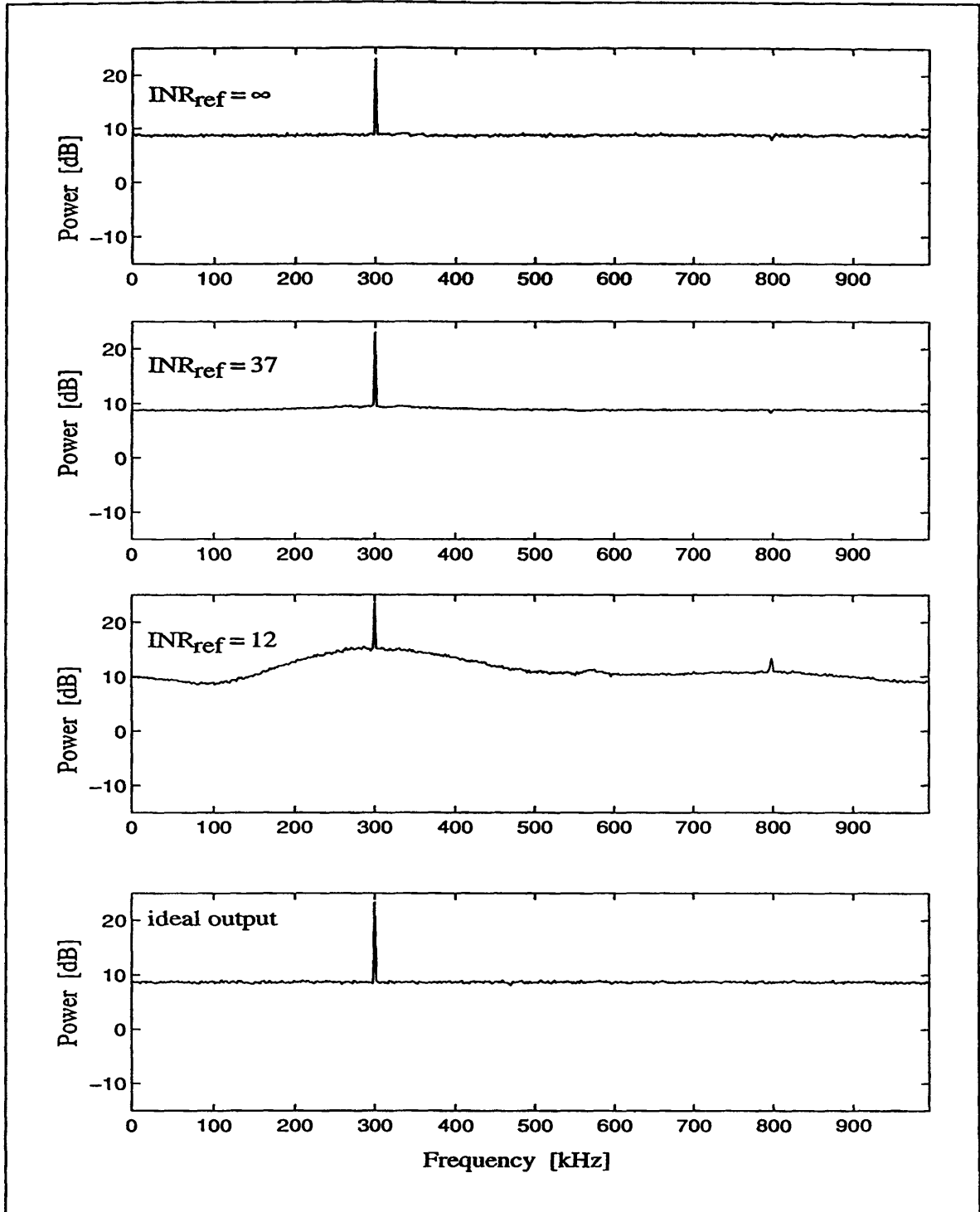


Figure 17 Simulation of a four reference channel adaptive interference canceler. The parameter under investigation is the  $INR_{ref}$ . The perfect interference-free output is shown below.

## Appendix

### Estimate of Adaptive Interference Canceler Performance on Several Radio Telescopes

The effectiveness of the adaptive interference canceling system for reducing interference during astronomical observations is estimated. Four radio telescopes are considered: 1) the Green Bank 140 foot telescope operating at 100 MHz and 1 GHz, 2) the Green Bank Telescope (GBT) operating at 100 MHz and 1 GHz, 3) a VLA antenna operating at 1 GHz, and 4) the Arecibo 1000 foot telescope operating at 100 MHz and 1 GHz. The performance will be estimated from rough calculations of  $INR_{ref}(z)$  and  $INR_{pri}(z)$  for each of the canceler-telescope systems. We assume that the interference levels at both frequencies are -97.5 dBm, which is based on measurements made at 93.5 MHz in Green Bank (see Fig. 1).

The following assumptions are made in order to simplify the calculations: All of the radio telescopes are symmetrical paraboloids and that the interference is in the far-field of the telescope radiation pattern.  $T_{sys P}$  at 100 MHz and 1 GHz depends on the radiometers used with each telescope, but is assumed to be independent of elevation angle.

The type of reference antenna chosen for the canceler will depend on the operating frequency. For 100 MHz operation, a dual-polarized, 5-element yagi antenna is chosen so that a beam with 10 dB of gain over an isotrope is pointed along the horizon in the direction of the interference source, located at azimuth angle  $\alpha_{\psi}$ .  $T_{sys X}$  at 100 MHz is taken to be 750 K for ambient temperature operation. Similarly, at 1 GHz, a dual-polarized horn antenna is chosen so that a beam with 20 dB of gain over an isotrope is pointed along the horizon in the direction of the interference source at  $\alpha_{\psi}$ .  $T_{sys X}$  at 1 GHz is taken to be 300 K. In both cases, knowledge of the direction of the interference is assumed in order to simplify the calculations.

The telescope main beam gain,  $G_{main}$ , is estimated by the well-known equation (Stutzman et al., 1981),

# Green Bank 140 Foot - 100 MHz

*Interference:*

Power Level at Antenna [dBm]: -97.5  
 Bandwidth [kHz]: 100

*Telescope:*

Aperture Diameter [meters]: 43  
 Main Beam Gain [dB]: 30.9  
 Main Beam Half Width [deg]: 2.6  
 System Temp. [K]: 750  
 Noise Power [dBm]: -119.9

Horizon Sidelobe Gain:

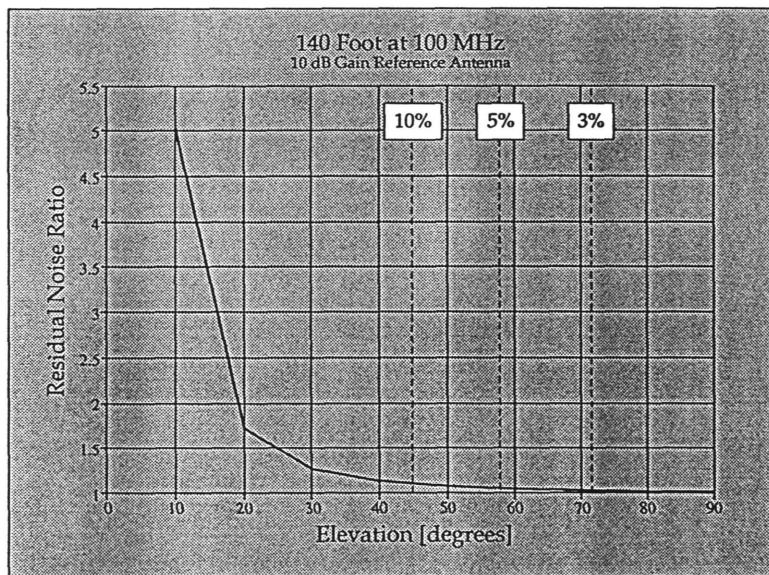
Elev. [deg], Gain [dB]:	90	-7.6
	50	-1.3

Interference-to-Noise:

Elev. [deg], $INR_{pri}$ [dB]:	90	14.7
	50	21.1

*Reference:*

Antenna Gain [dB]: 10  
 System Temperature [K]: 750  
 Noise Power [dBm]: -119.9  
 $INR_{ref}$  [dB]: 32.4



**PERFORMANCE:**

Interference Attenuation [dB]: 64.7

Residual Noise Ratio:

Elev. [deg], Ratio [dB]:	90	1.017
	50	1.075

# GBT - 100 MHz

## Interference:

Power Level at Antenna [dBm]: -97.5  
 Bandwidth [kHz]: 100

## Telescope:

Aperture Diameter [meters]: 100  
 Main Beam Gain [dB]: 38.2  
 Main Beam Half Width [deg]: 1.1  
 System Temp. [K]: 300  
 Noise Power [dBm]: -123.8

## Horizon Sidelobe Gain:

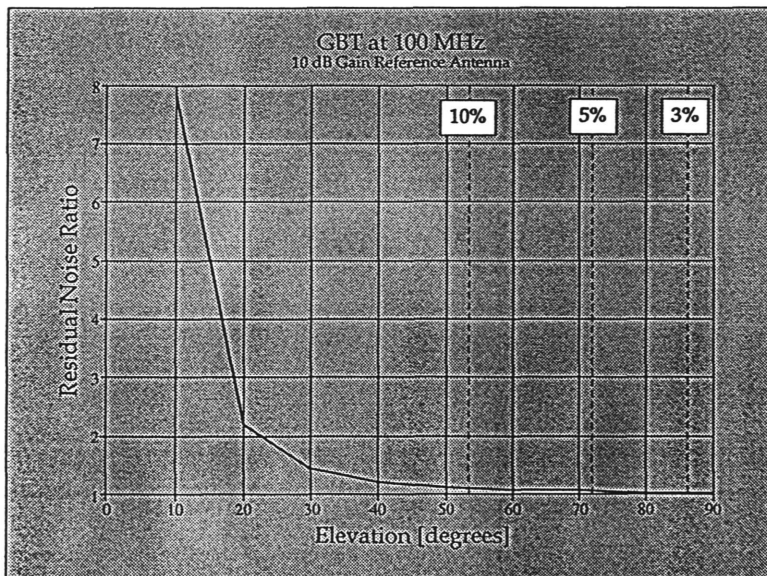
Elev. [deg], Gain [dB]:	90	-9.5
	50	-3.1

## Interference-to-Noise:

Elev. [deg], $INR_{pri}$ [dB]:	90	16.9
	50	23.2

## Reference:

Antenna Gain [dB]: 10  
 System Temperature [K]: 750  
 Noise Power [dBm]: -119.9  
 $INR_{ref}$  [dB]: 32.4



## PERFORMANCE:

Interference Attenuation [dB]: 64.7

### Residual Noise Ratio:

Elev. [deg], Ratio [dB]:	90	1.0282
	50	1.12275

# VLA - 1 GHz

**Interference:**

Power Level at Antenna [dBm]: -97.5  
 Bandwidth [kHz]: 100

**Telescope:**

Aperture Diameter [meters]: 23  
 Main Beam Gain [dB]: 45.4  
 Main Beam Half Width [deg]: 0.49  
 System Temp. [K]: 50  
 Noise Power [dBm]: -131.6

**Horizon Sidelobe Gain:**

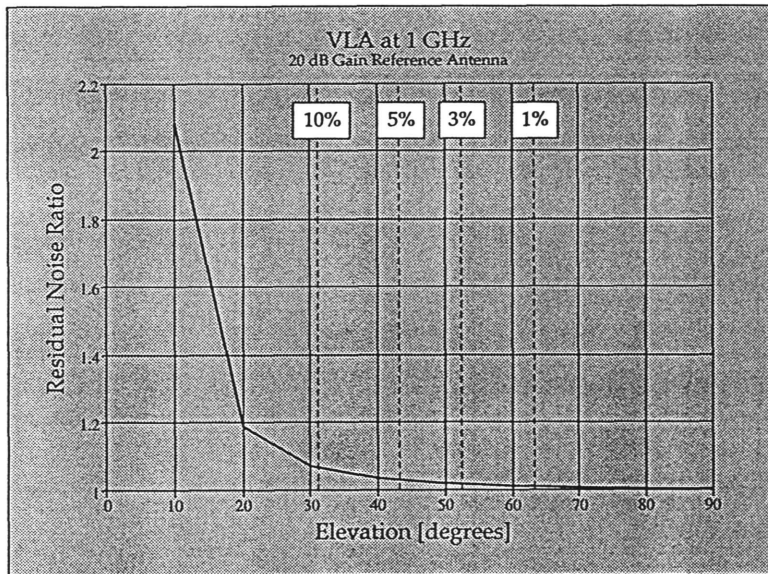
Elev. [deg], Gain [dB]: 90 -11.3  
 50 - 4.9

**Interference-to-Noise:**

Elev. [deg],  $INR_{pri}$  [dB]: 90 22.8  
 50 29.2

**Reference:**

Antenna Gain [dB]: 20  
 System Temperature [K]: 300  
 Noise Power [dBm]: -123.8  
 $INR_{ref}$  [dB]: 46.3



**PERFORMANCE:**

Interference Attenuation [dB]: 92.7  
 Residual Noise Ratio:  
 Elev. [deg], Ratio [dB]: 90 1.00447  
 50 1.01943

# Arecibo - 1 GHz

*Interference:*

Power Level at Antenna [dBm]: -97.5  
 Bandwidth [kHz]: 100

*Telescope:*

Aperture Diameter [meters]: 305  
 Main Beam Gain [dB]: 67.9  
 Main Beam Half Width [deg]: 0.04  
 System Temp. [K]: 50  
 Noise Power [dBm]: -131.6

*Horizon Sidelobe Gain:*

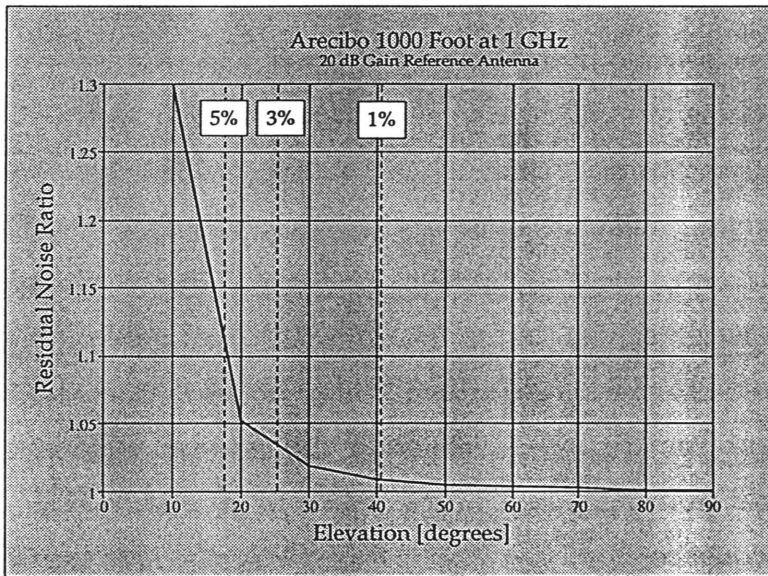
Elev. [deg], Gain [dB]: 90 -16.9  
 50 -10.5

*Interference-to-Noise:*

Elev. [deg],  $INR_{pri}$  [dB]: 90 17.2  
 50 23.6

*Reference:*

Antenna Gain [dB]: 20  
 System Temperature [K]: 300  
 Noise Power [dBm]: -123.8  
 $INR_{ref}$  [dB]: 46.3



**PERFORMANCE:**

Interference Attenuation [dB]: 92.7

**Residual Noise Ratio:**

Elev. [deg], Ratio [dB]: 90 1.00123  
 50 1.00534

## List of Symbols

-- continued --

$s(n)$	Desired signal
$SIR$	Signal-to-interference ratio
$T$	Noise temperature
$T_{sys P}$	Primary channel system noise temperature
$T_{sys X}$	Reference channel system noise temperature
$W(n)$	Tap weight vector which includes the set of $w_i(n)$
$w_i(n)$	Transversal filter tap weight
$W_{opt}$	Vector containing the set of optimum tap weights
$W_{opt}(z)$	Optimum filter transfer function (z-transform of $W_{opt}$ )
$X(n)$	Vector containing delayed versions of the reference input
$x(n)$	Reference channel input (also transversal filter input)
$y(n)$	Transversal filter output
$z^{-1}$	Unit delay
$\alpha_\psi$	Azimuth angle of interference
$\beta$	Elevation angle
$\delta$	Quantizer step size
$\varepsilon(n)$	Interference canceler output and error feedback signal
$\theta_0$	1/2 the beamwidth at the half-power points
$\kappa$	Aperture efficiency
$\lambda$	wavelength
$\mu$	Step size parameter
$\xi$	Error performance surface or mean-squared error
$\xi_{min}$	Minimum mean-squared error
$\pi$	pi, 3.14159
$\sigma_q^2$	Variance of the white noise due to quantization
$\Phi_{ii}$	Signal power spectrum
$\Phi_{ij}$	Cross power spectrum
$\Phi_{io io}$	Interference power spectrum at the canceler output

## Bibliography

- Bullock, S., (1990). "High Frequency Adaptive Filter," *Microwave J.*, vol. 33, Sept., pp. 97+.
- Cariscos, C. and B. Liu (1984). "A Roundoff Error Analysis of the LMS Algorithm," *IEEE Trans. on Acoust. Speech & Signal Process.*, vol. ASSP-32, pp. 34-41.
- Erickson, W. (1982). "Excision of Terrestrial Interference from Meter-Wavelength Radio Data," *Proc. of the Interference Identification and Excision Workshop*, Green Bank, WV, National Radio Astronomy Observatory, pp. 78-90.
- Fisher, J. R. (1982). "An Impulse Noise Suppress and Other Thoughts on Interference Reduction," *Proc. of the Interference Identification and Excision Workshop*, Green Bank, WV, National Radio Astronomy Observatory, pp. 100-111.
- Fleisch, D. A and G.C. Pieters, (1991). "The ACT Programmable Transversal Filter," *Microwave J.*, vol. 34, May, pp. 284+.
- Gerard, E. (1982). "A Radar Blanker at Stockert Observatory," *Proc. of the Interference Identification and Excision Workshop*, Green Bank, WV, National Radio Astronomy Observatory, p.63.
- Goldberg, L. (1995). "Adaptive-Filtering Developments Extend Noise-Cancellation Applications," *Electronic Design*, vol. 43, Feb. 6, pp. 34+.
- Haykin, S. (1996). Adaptive Filter Theory, 3rd ed., Prentice-Hall, Upper Saddle River, New Jersey.
- Howells, P. W. (1976). "Explorations in Fixed and Adaptive Resolution at GE and SURC," *IEEE Trans. on Antennas and Propag.*, vol. AP-24, Special Issue on Adaptive Antennas, pp. 753-763.
- Korvin, W. and R. W. Kreutel (1971). "Earth Station Radiation Diagram with Respect to Interference Isolation Capability: A Comparative Evaluation," *AIAA Progress in Astronautics & Aeronautics: Communications Satellites for the 70's: Technology*, vol 25, M.I.T. Press, Cambridge, MA. pp. 535-548.
- Lin A. and R Monzello, (1992) "An Interference Cancellation System for EW Applications Using an ACT Device," *Microwave J.*, vol. 35, Feb., pp. 118+.
- Logic Devices Inc. (1995). Digital Signal Processing Databook, Sunnyvale, CA., p. 4-45.
- Moffet, A. (1982). "JPL Work on Superconducting Filters," *Proc. of the Interference Identification and Excision Workshop*, Green Bank, WV, National Radio Astronomy Observatory, pp. 91-95.
- Morton, J. R., K. F. Preston, P. J. Krusic, and L. B. Knight Jr. (1993). "The Proton Hyperfine Interaction in  $\text{HC}_{60}$ , Signature of a Potential Interstellar Fullerene," *Chem. Phys. Lett.*, vol. 204, no. 5, 6, March 26, pp. 481-485.
- Oppenheim, A. V. and R. W. Schafer, (1989). Discrete-Time Signal Processing, Prentice- Hall, Englewood Cliffs, NJ.



# The 2 cm Survey of Compact Radio Sources

J.C. Armstrong

10 October 1996

## 1 Introduction

The ability of Very Long Baseline Interferometry (VLBI) to render high resolution images of distance celestial objects greatly amplifies the capabilities of the astronomer. As the technology associated with VLBI has developed, including advancements in receiver technology and the construction of dedicated arrays like the VLBA, the most distant objects of the universe have come under closer and closer scrutiny. The study of these objects allows us to probe deep into the early universe, as the brightest radio sources tend to be quite far away. Regardless of these advances, the process of producing maps of radio sources on the large scale has been arduous and time consuming to say the least. In the past, this has kept surveys limited to a small number of sources. Recently, however, a number of surveys have been performed using automated mapping techniques in an effort to extend the range of existing surveys.

## 2 Some History of Radio Surveys

One of the early large surveys of compact radio sources was the Pearson and Readhead (PR) survey of 1988. The survey consisted of some 65 sources observed at the 6 cm wavelength with VLBI, with additional 20 cm VLA observations for some sources. Although the survey produced high angular resolution (approximately 0.001 arcmin on 37 of the sources), the sample was severely flux limited.

The Caltech-Jodrell Bank Flat Spectrum Survey (CJF) of 1995 was an effort to improve upon the PR survey. This survey contributed additional 6 and 18 cm observations of 135 sources (totaling 200 with PR). The survey extended the flux density limit of the PR survey, going down to 0.7 Jy, with a dynamic range of about 500:1. This greatly improved the database for maps of compact radio sources.

## 3 The 2 cm Survey

The 2 cm survey, conducted by Anton Zensus and Ken Kellermann of NRAO, collaborating with Rene Vermeulen and Marshall Cohen of Caltech, is designed to

improve upon past surveys and refine a procedure for automated mapping. The smaller wavelength will improve angular resolution, while the use of the VLBA will improve the dynamic range. Also, by working with automated mapping techniques, the survey is easily extendible to a large number of sources, with the limiting factor being the computer time involved in reducing the data. During the past summer, Dr. Kellermann, Dr. Zensus, and I have improved the mapping routines and attempted to model source behavior in an effort to extend the database of compact radio sources.

## **4 Goals of the 2 cm Survey**

There are several goals to the 2 cm survey project. First, the survey will advance the efforts of previous surveys. That is, the data acquired for the 2 cm survey will be used to classify sources, provide a large sample for statistical analysis, and provide a sample in which one can search for gravitational lenses. The 2 cm survey will also achieve a higher dynamic range (3x that of other surveys) and better resolution (10x that of other surveys). Also, many of the sources have never been observed at 2 cm. This could lead to new discoveries and modifications of old classification schemes. Finally, the results will be made available on the World Wide Web in an effort to distribute the information for readily.

## **5 Observations and Analysis**

### **5.1 Source Selection**

The 2 cm survey, as with all surveys, is flux limited to some extent. The sources consist of the 130 brightest sources in the sky. However, since many sources have not been imaged at 2 cm, it is possible they are not brightest at this wavelength. Attention was also paid to galactic latitude by choosing sources outside of the galactic plane. Also, there is some intentional overlap between the 2 cm survey and the PR/CJF surveys.

### **5.2 Observations**

The survey is designed to employ the VLBA in what is known as "Snapshot Mode". This consists of approximately four minute scans taken over twelve hours, which are then combined later during the imaging process. Observations to date include for epochs: April 1995, December 1995, May 1996, and July 1996.

### **5.3 Data Reduction**

The data reduction process includes several factors. First, in collaboration with Marshall Cohen of Caltech, a source database is being constructed. This will

include background data and information on all the sources in the survey. The idea behind this is to have an extensive research base for the analysis of the data.

Secondly, with the help of Rene Vermeulen (also of Caltech), automated mapping procedures have been developed using the mapping routine DIFMAP. The idea behind this is to automate as much of the imaging process as possible. Although it cannot be automated completely, this process can reduce the time per source to a few minutes rather than a few hours.

The reduction process consists of calibration, mapping, and model fitting. The calibration process is conducted in AIPS, using standard VLBA reduction techniques for which the software was developed. Next, the data are imported to DIFMAP, where the automated script attempts to clean and transform the raw data (u,v) data into (x,y) maps. This process is surprisingly robust. However, it is still necessary to touch up each map. In some cases, with sources at low declination and/or poor (u,v) coverage, it is necessary to re-map the source entirely. After the sources have been mapped, they are modeled using simple Gaussian components. It is necessary to view each image and choose components to be modeled, and this process has not been successfully automated. The modeling, however, produces a wealth of data concerning motion of the source components. These data can be used for statistical analysis of sources and searches for superluminal motion.

## 6 Results

The results to date are summarized below:

First Epoch: 130 uniformly weighted maps, 130 naturally weighted maps, and Gaussian component models for each source.

Second Epoch: 60 naturally weighted maps.

Third Epoch: 33 naturally weighted maps.

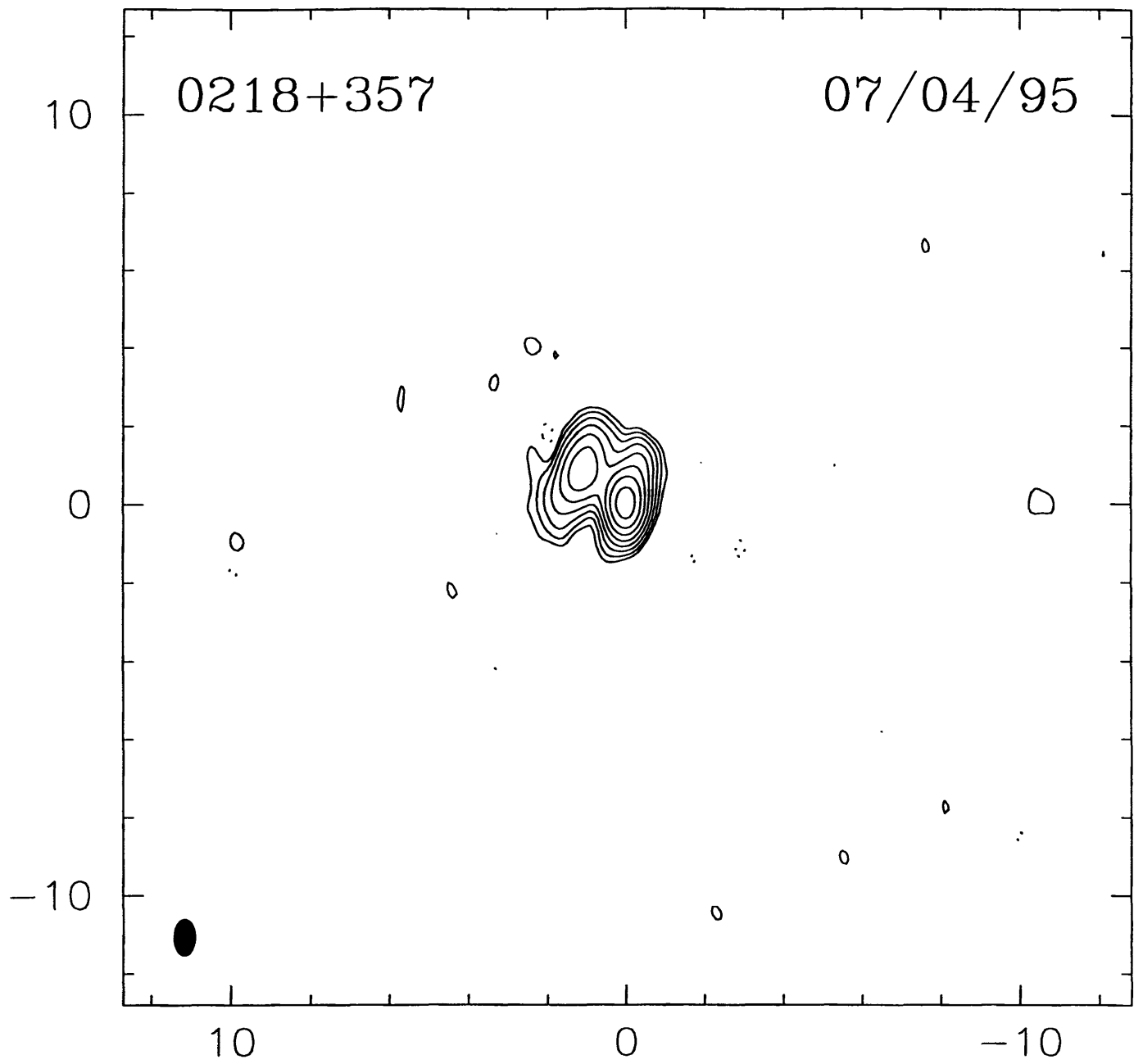
Fourth Epoch: 27 naturally weighted maps.

See attached for examples of finalized maps.

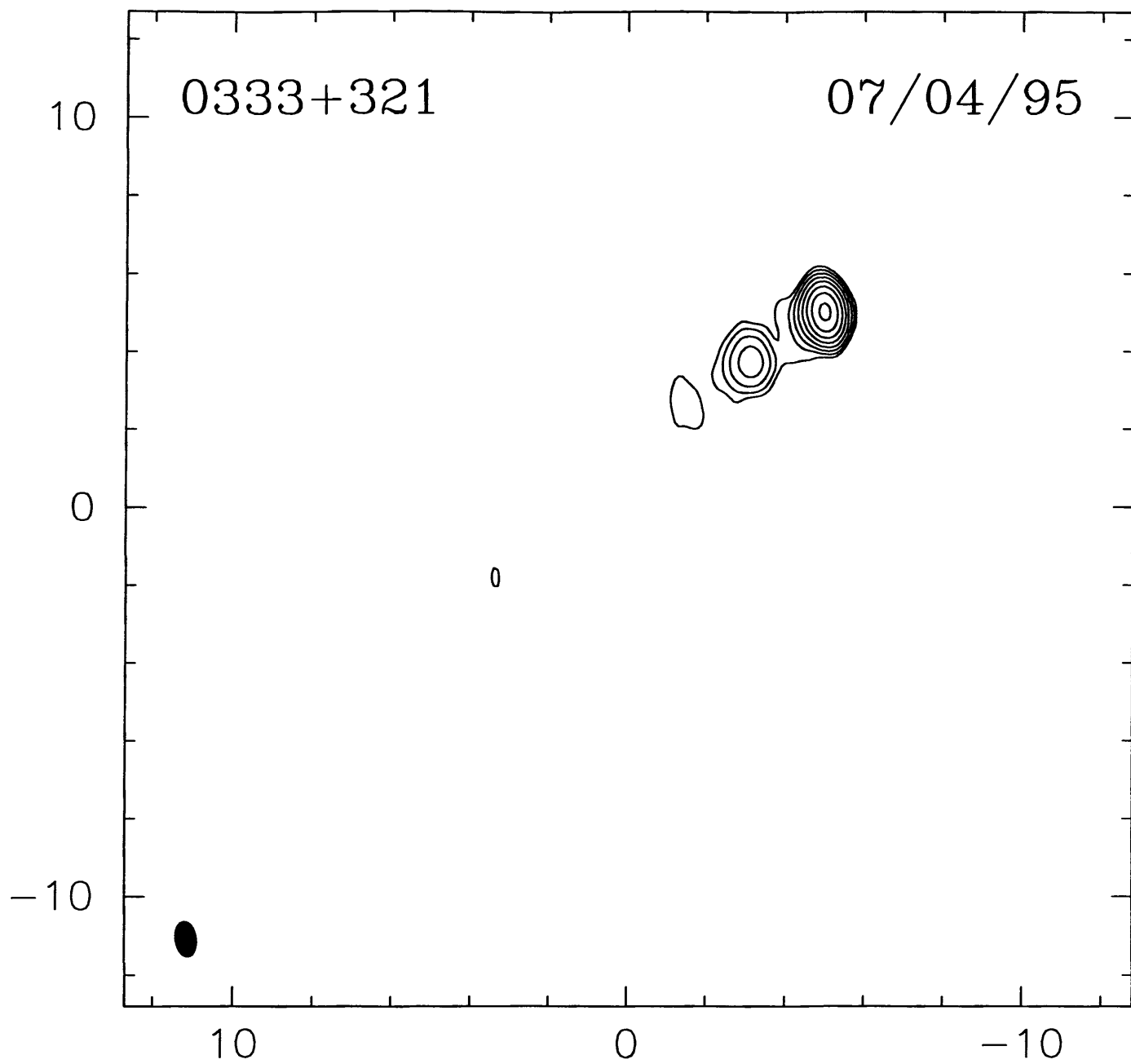
## 7 Future Study

Future goals for this study include expanding the source list, conducting a multi-wavelength study, and creating a less limited source sample. With luck, I will not only have the opportunity to continue with the survey, but be able to use the data collected to conduct a more in-depth study of these sources.

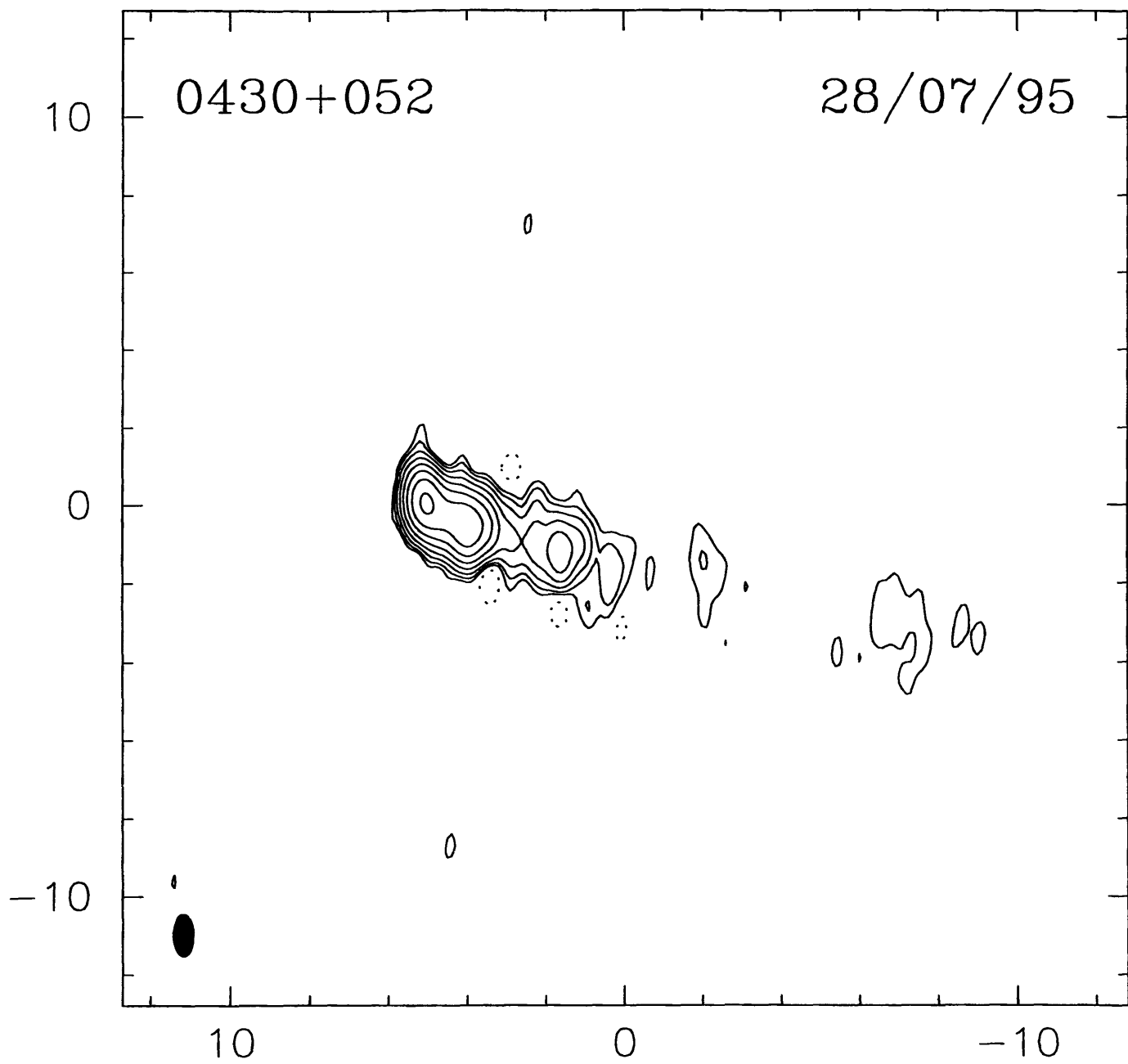
max=0.436651, bot=0.00219418



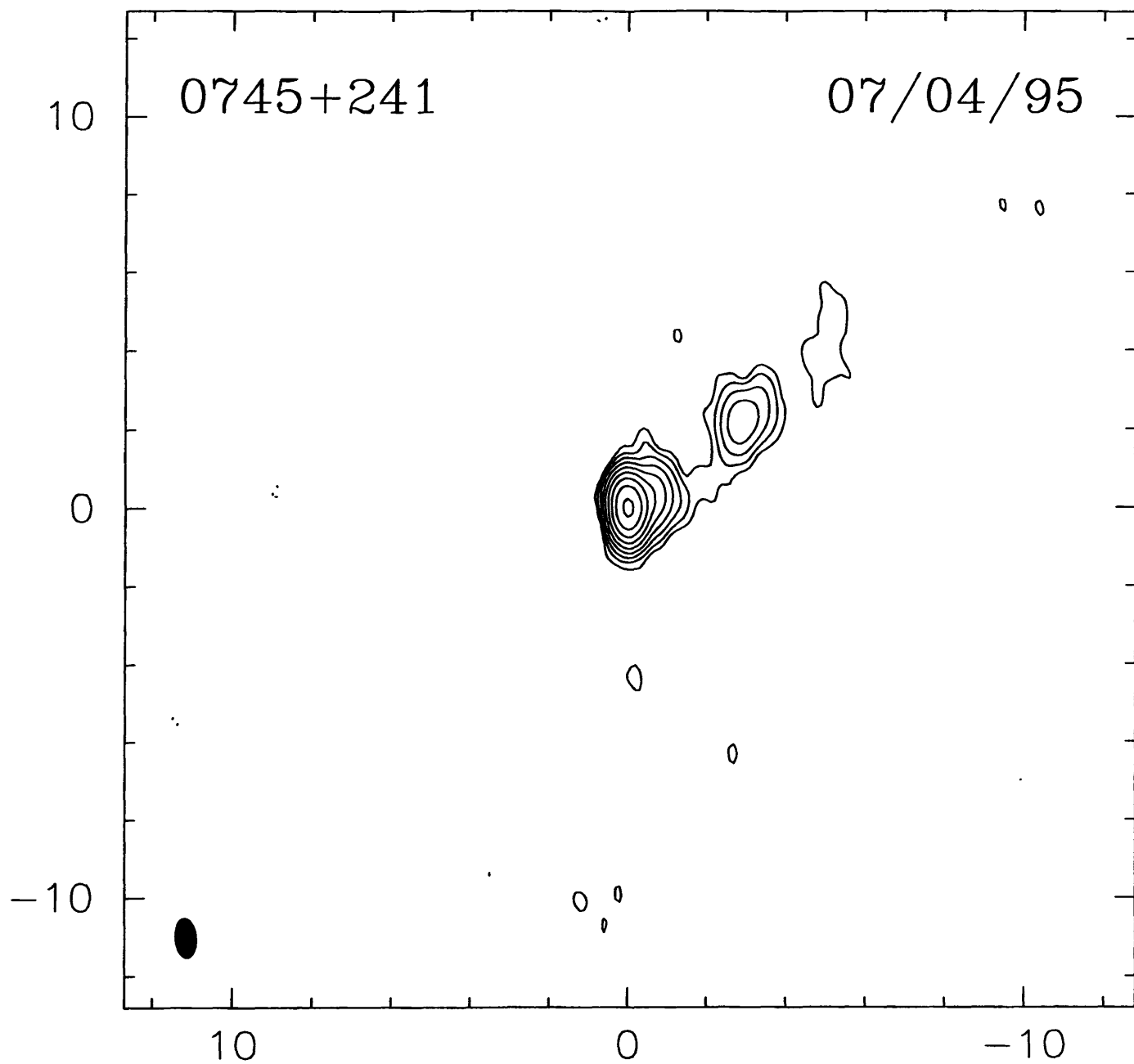
max=1.11565, bot=0.00729144



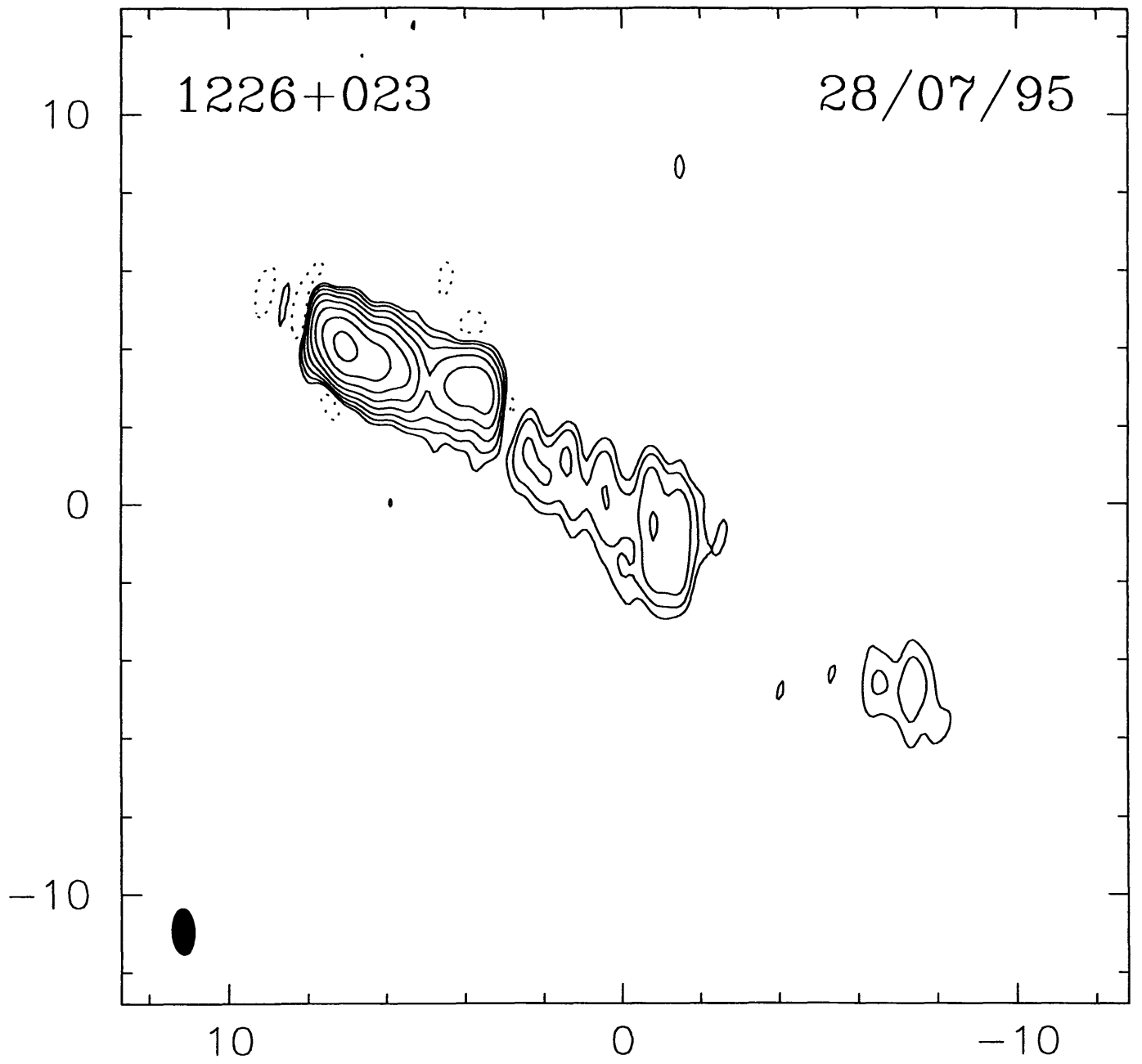
max=0.730574, bot=0.00489552



max=0.630394, bot=0.00214672



max=6.92286, bot=0.0425919



**The Large Scale Effects of Outflows from Young Stars on the  
Dense Molecular Material in Orion**

~VLA Maps of Ammonia~

Mary E. Putman and Jennifer Wiseman

First of all, thank you very much for funding my summer research at the National Radio Astronomy Observatory. I had a very educational and enjoyable summer. The project I worked on explored the structure of Orion, in particular the Orion BN-KL region. I mapped the large scale structure of this region using the (1,1) and (3,3) inversion transition lines of ammonia, as observed with the Very Large Array. My advisor for this project was Jennifer Wiseman, who led me in interpreting the results of this data and understanding the many peculiarities of AIPS.

The Orion BN-KL core is an active star forming region which has been studied by a wide range of astronomers. We had a somewhat different approach to observing this region by looking at the area surrounding the BN-KL core at high spatial resolution. The process of star formation remains much of a mystery and in order to understand it, studies such as this one must continue to probe into star formation regions. The basic star formation scenario which led us to study this region in this way begins with a massive molecular cloud like the Orion Cloud. The structure within this cloud seems to be made up of a series of clumps and filaments. A star begins to form when something causes one of these clumps to begin to gravitationally collapse. Likely culprits could be either an internal magnetic field diffusing out of the region or outside pressure from supernova shocks or outflows causing the clump to collapse. This non-suspecting clump continues to collapse and due to its rotation, a flattened circumstellar disk forms about the clump (we will now officially call the clump a protostar). The protostar spins more and more rapidly as it continues to collapse inwards. In order for this protostar to grow up and form a stable star it must find some way of shedding the excess angular momentum and thus allow the disk material to accrete onto the central core. The solution to the angular momentum problem appears to be some type of combination of magnetic braking and bipolar outflows. The bipolar outflows send huge amounts of mass out from the poles of the young star at high velocities (100-500 km/sec); thus greatly disrupting the surrounding environment. The protostar is then able to continue to accrete material and grow up into a full-fledged star. The series of collapsing clumps and bipolar outflows within the molecular cloud, as well as the dense gas being pushed by the outflow can then

be mapped by looking at various molecular transition lines such as ammonia. The structure within the cloud ultimately appears to take on a filamentary structure.

The ammonia molecule is a symmetric top and the inversion motion of the nitrogen molecule between the triangle of hydrogen atoms results in the transition lines at approximately 23 GHz which we used to map this region. Cleaning the maps from the VLA which contained our low-signal to noise inversion line data was a challenge. When calibrating the data, almost all of the data was usable, with the (3,3) line data being of somewhat higher quality. Cleaning maps full of filaments is difficult, as the filamentary structure results in deep negative trenches and our signal to noise was only approximately five. We used IMAGR within AIPS to clean the maps and attempted many different methods of cleaning the data. Natural weighting was used over uniform weighting and the maps were generally cleaned with a 20-40 kilolambda taper, which weights down data from the longest baselines. Zerospacing was introduced in an attempt to reduce the bowl shape of our data which confuses the clean when looking for real sources. A clean box was used on some of the fields to tell the clean where to look for the source, but there is some concern that this may bias the clean, so this was not used in the final clean. The clean was also slowed down, completing less iterations with each cycle. Each method attempted resulted in a somewhat different quality of clean. The final maps were generally cleaned with a 30 kilolambda taper and approximately 2000 iterations. All of the fields were slowed down by a factor of .3 and the gain was set to 0.05.

After finding the best method to resolve the structure, we took each of the fields observed with the VLA and made a mosaic of the cleaned maps, thus giving us lovely, detailed maps of Orion BN-KL and the surrounding region. Referring to the maps following this summary we can see that the large scale structure within the cloud takes on a filamentary structure, as has also been shown through maps of other molecules. The velocity distribution of the filaments indicates that they may actually form a cone of material about the central outflow from Orion-KL. Since the ammonia transition lines trace material which is at a somewhat higher temperature, we are able to see specific areas of dense and heated material within the filaments. The heated clump seen at a significant distance from the central core region as seen in the (3,3) line data could be a

sign of an embedded young protostar. There is also a ratio plot, the (3,3)/(1,1), within these plots which shows regions which are not particularly dense yet are very hot. These hotspots exist at locations near the edges of the Orion KL core which indicate they may be tracing the outflow from this region. This is also indicated when you look at the map of the bipolar outflow in this region as mapped in CO. Another indicator of the ammonia tracing the outflow is the high velocity wings seen in the (3,3) spectral lines in the core region. The velocity versus position plots also show this blue-shifted material as well as the presence of several different core components within the main core. It also shows the beginning of each of the filaments, one at 8km/sec and the other at 10km/sec. The high velocity blue-shifted wings found in the ammonia lines indicate that the dense molecular material in this region is being pushed away from the core. The outflow appears to also affect the large scale environment of the cloud, as seen in the series of filaments and clumps in this region. There may be a cone of dense material forming about the central outflow and this outflow may also be triggering the formation of new stars with the clumpy filaments. Further work needs to be done to truly understand the relevance of all of the maps which we have been created and to understand the star formation process within these molecular clouds.

Plot file version 10 created 30-AUG-1996 15:27:38

GREY: ORION12 IPOL OR3/1 3F.10CH.1

CONT: ORION12 IPOL ORN1,1 25-35.BLNK.1

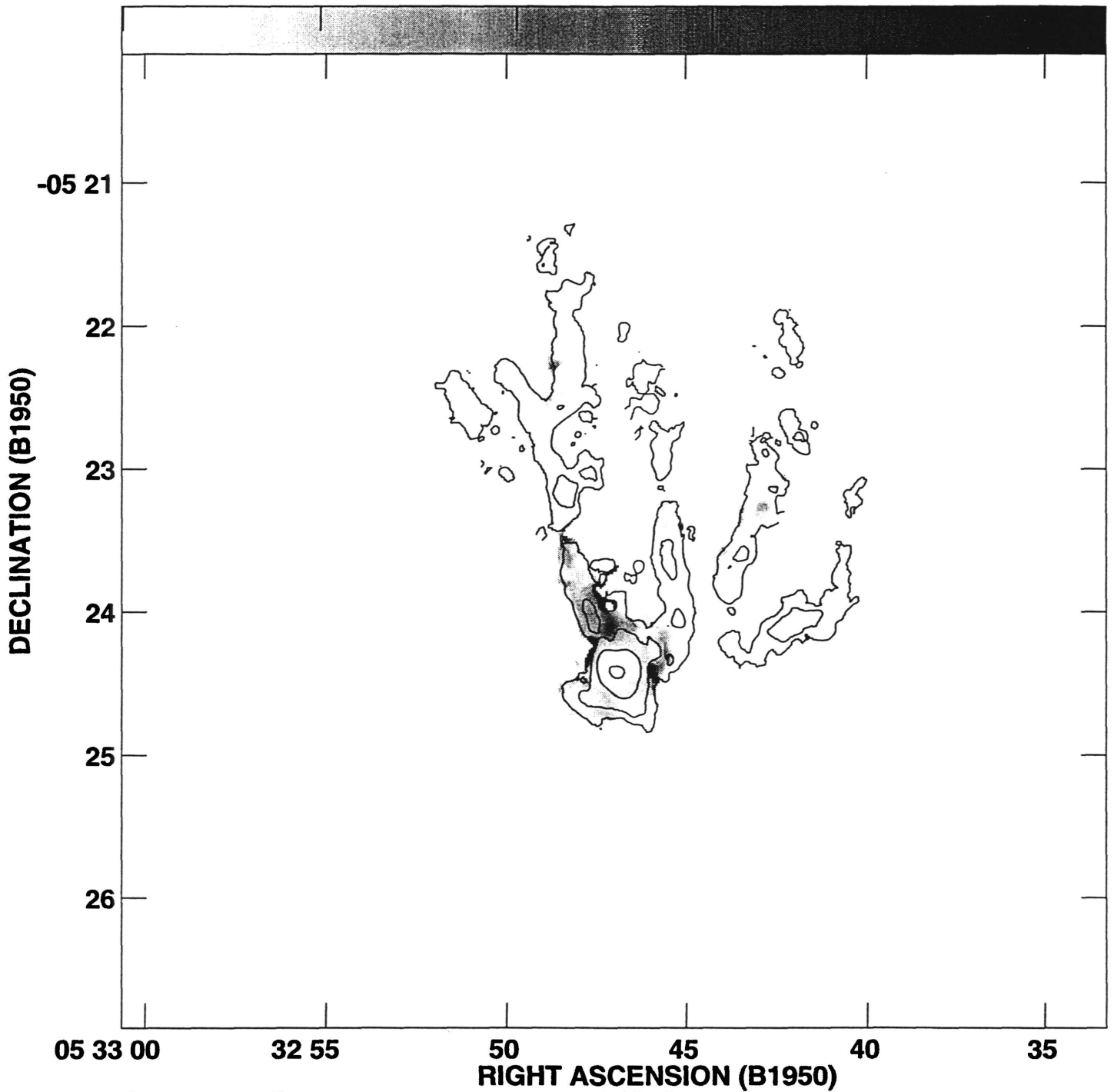
0

1

2

3

4



Grey scale flux range= .000 5.000 RATIO

Peak contour flux = 7.2107E+03 RATI\*M/S

Levs = 1.0000E+01 \* ( 5.000, 25.00, 125.0,  
625.0, 3000.)

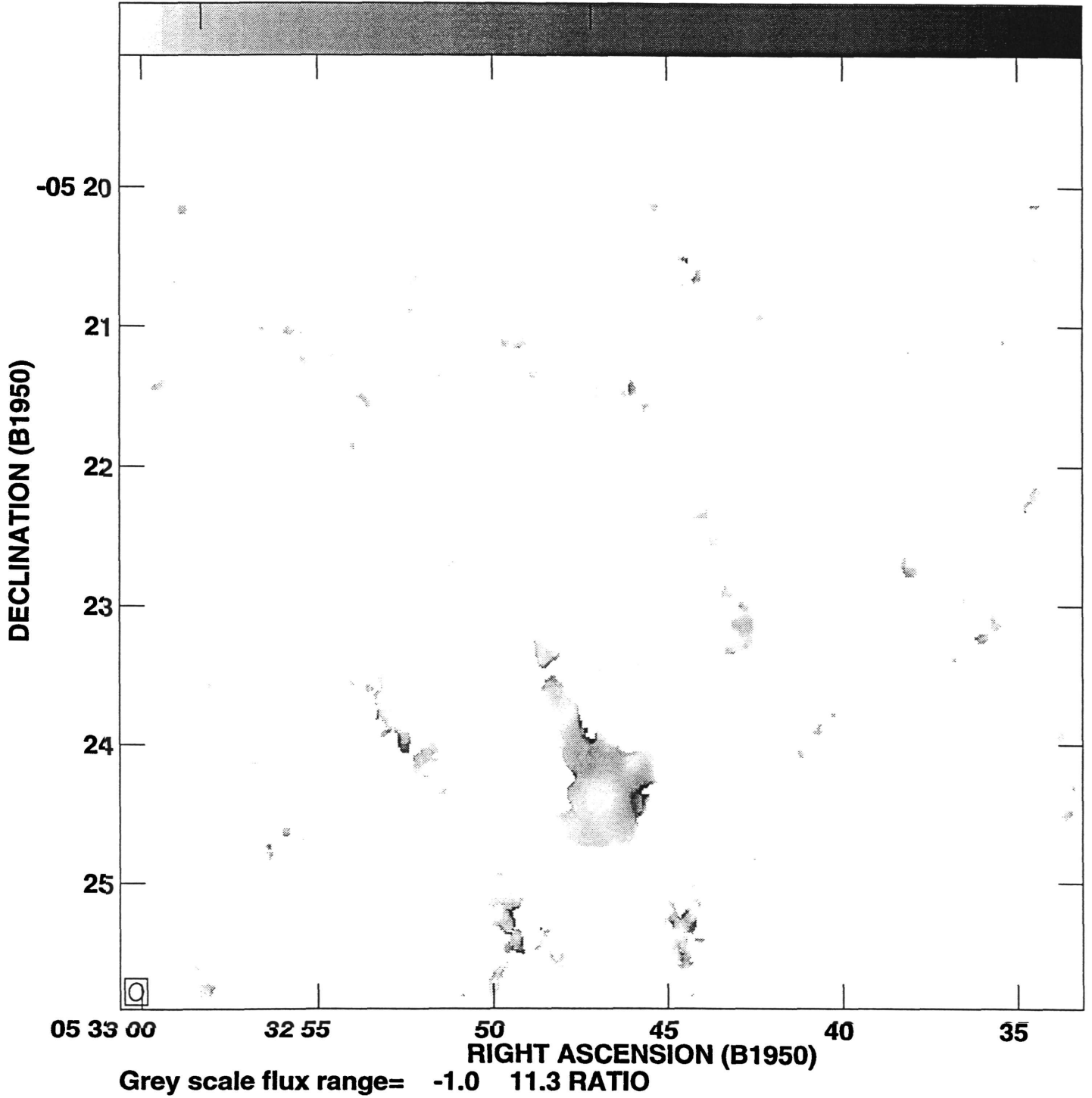
Plot file version 1 created 01-AUG-1996 08:54:11

GREY: ORION8 IPOL ORN 3,3/1,1.RATIO.1

0

5

10



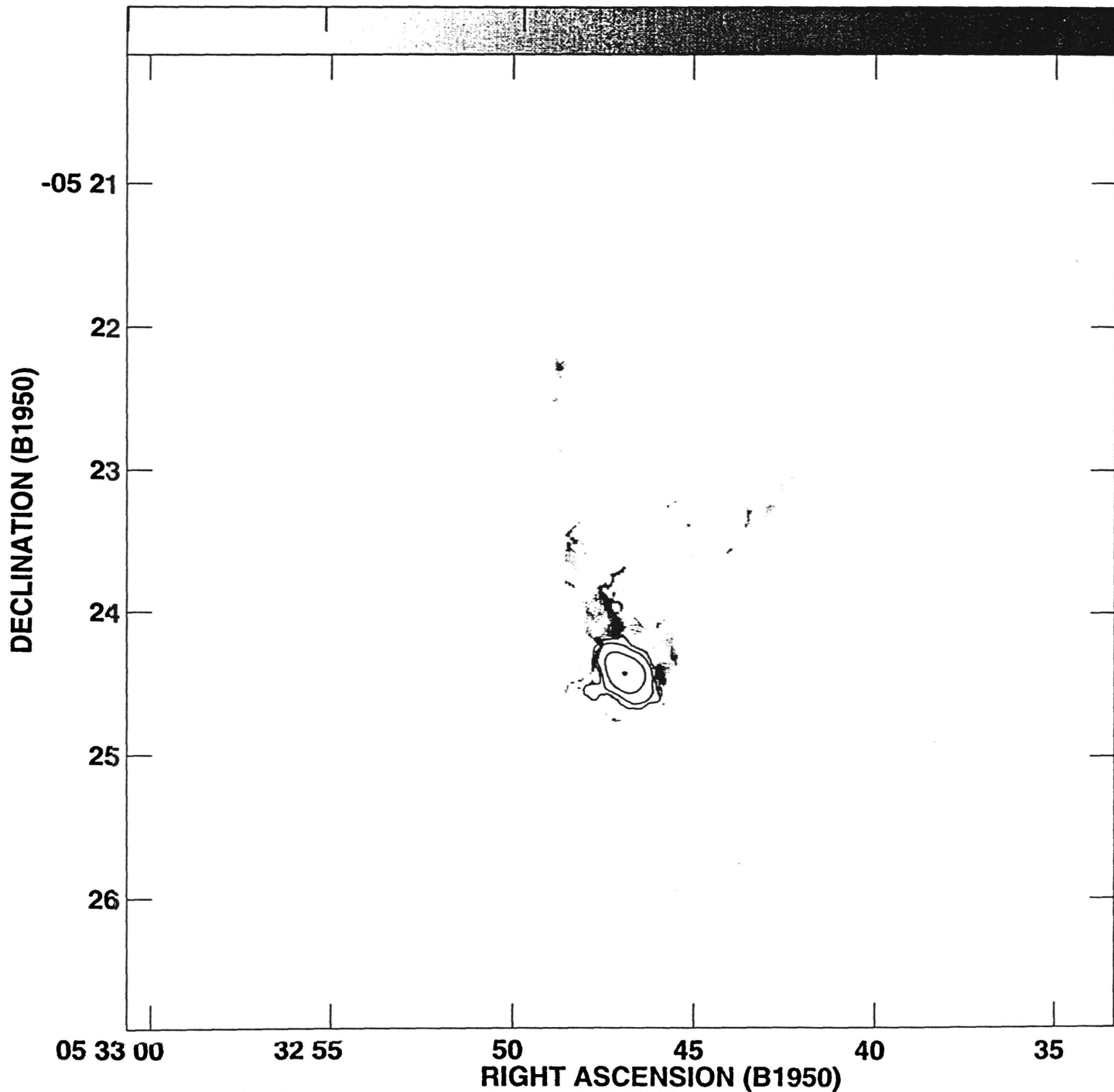
Grey scale flux range= -1.0 11.3 RATIO

Plot file version 11 created 30-AUG-1996 15:33:40

GREY: ORION12 IPOL OR3/1 3F.10CH.1

CONT: ORION15 IPOL ORN3,3 16-25.BLNK.1

0 1 2 3 4



Grey scale flux range= .000 5.000 RATIO

Peak contour flux = 6.3643E+03 RATI\*M/S

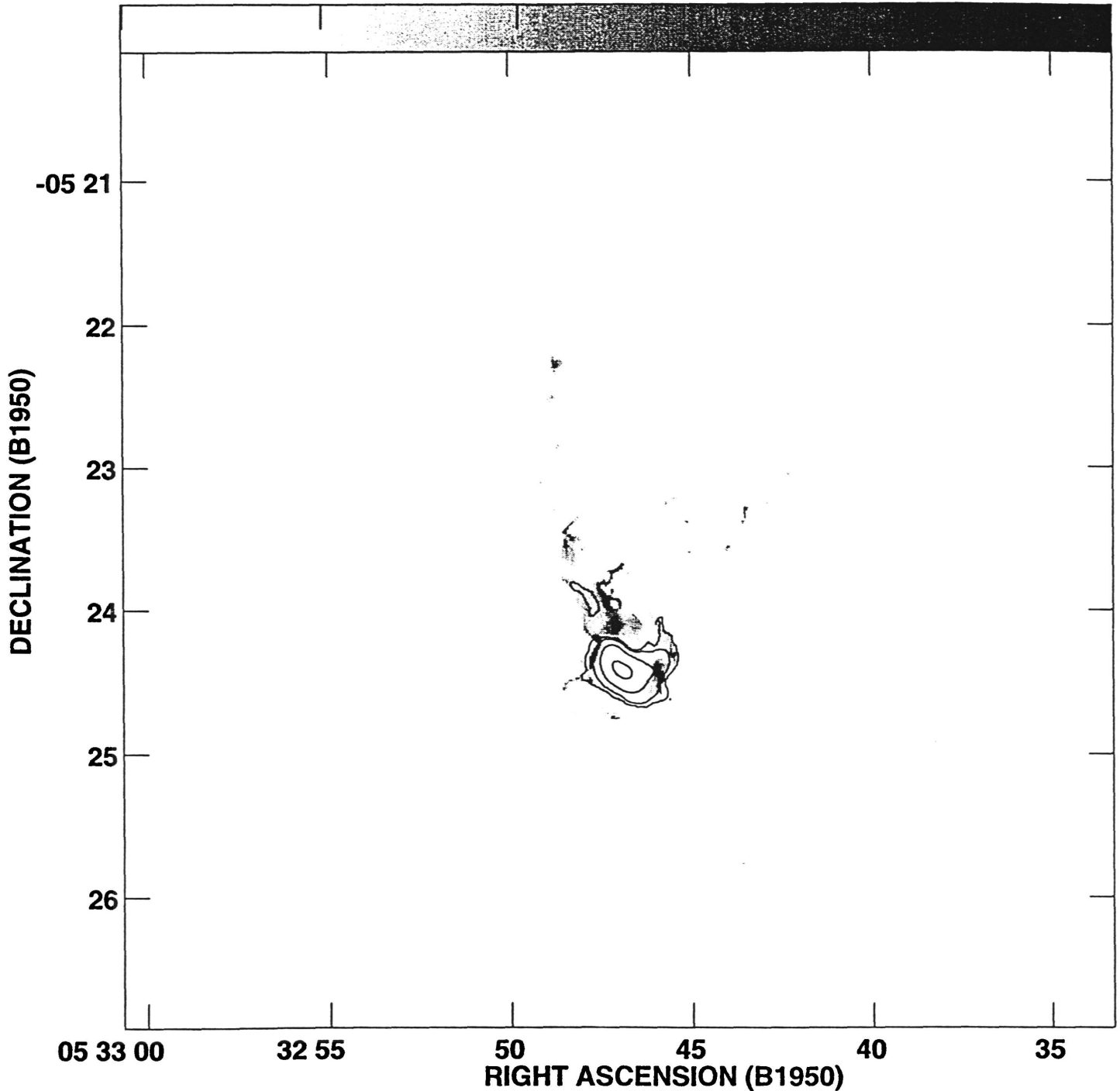
Levs = 1.0000E+01 \* ( 5.000, 25.00, 125.0, 625.0, 3000.)

Plot file version 9 created 30-AUG-1996 15:24:45

GREY: ORION12 IPOL OR3/1 3F.10CH.1

CONT: ORION15 IPOL ORN3,3 36-45.BLNK.1

0 1 2 3 4



Grey scale flux range= .000 5.000 RATIO

Peak contour flux = 8.1853E+03 RATI\*M/S

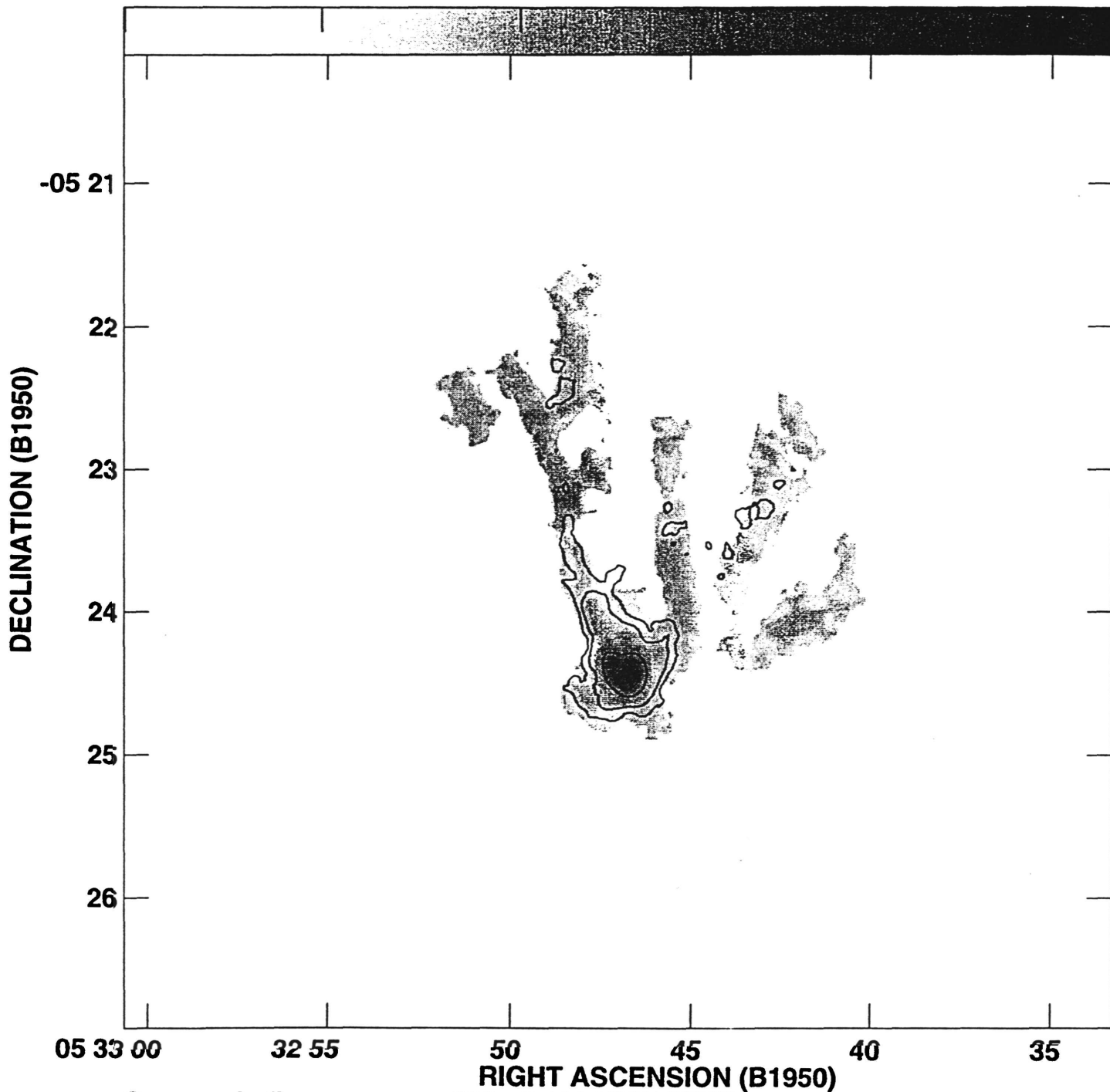
Levs = 1.0000E+01 \* ( 5.000, 25.00, 125.0, 625.0, 3000.)

Plot file version 1 created 30-AUG-1996 16:27:53

GREY: ORION12 IPOL ORN1,1 25-35.LOG.2

CONT: ORION12 IPOL ORN3,3 25-35.BLNK.1

0 1 2 3 4



Grey scale flux range= .000 5.000 UNDEFINE

Peak contour flux = 3.8778E+03 RATI\*M/S

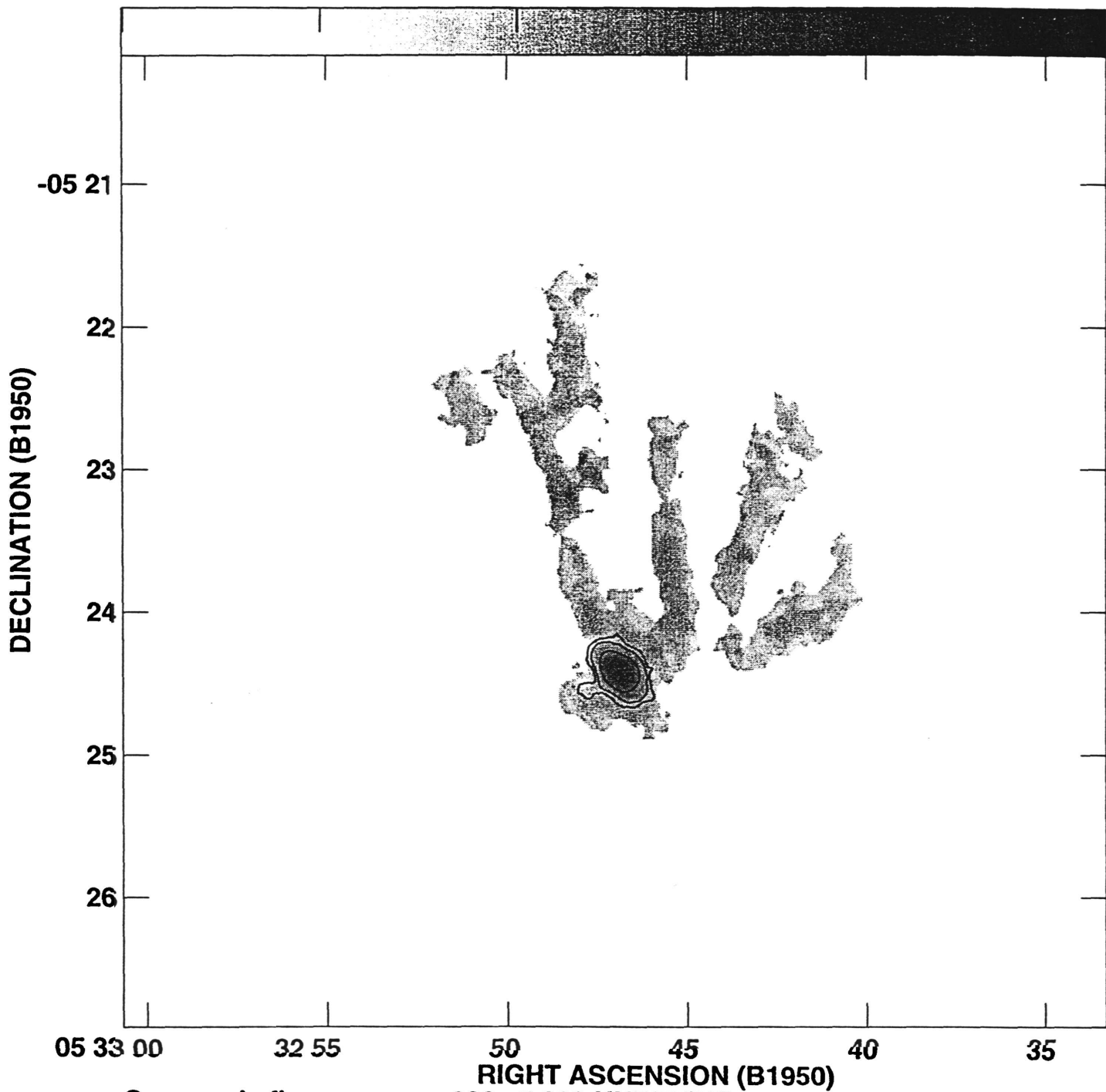
Levs = 1.0000E+01 \* ( 5.000, 25.00, 125.0,  
625.0, 3000.)

Plot file version 3 created 30-AUG-1996 16:32:19

GREY: ORION12 IPOL ORN1,1 25-35.LOG.2

CONT: ORION15 IPOL ORN3,3 16-25.BLNK.1

0 1 2 3 4



Grey scale flux range= .000 5.000 UNDEFINE

Peak contour flux = 6.3643E+03 RATI\*M/S

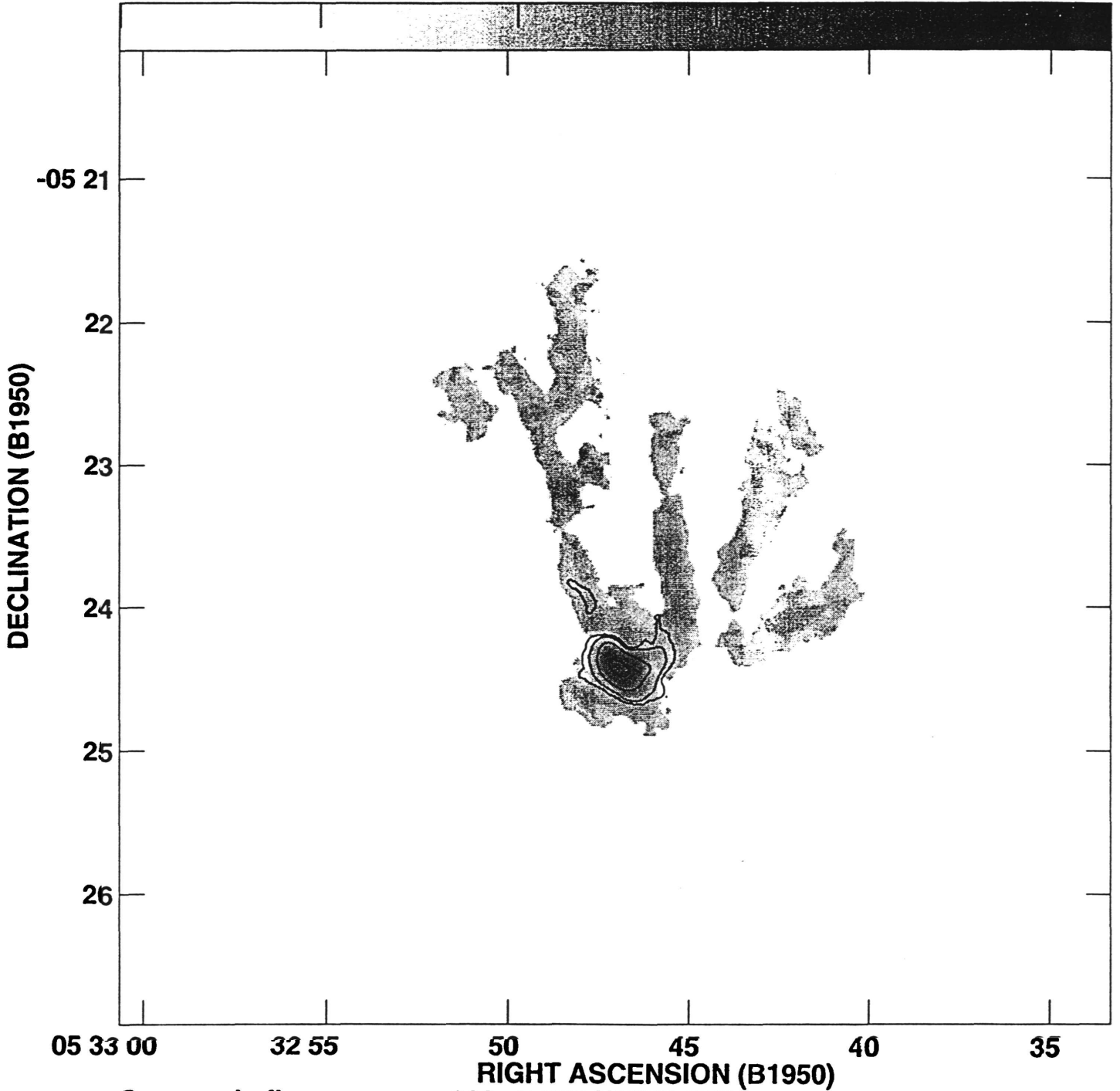
Levs = 1.0000E+01 \* ( 5.000, 25.00, 125.0, 625.0, 3000.)

Plot file version 2 created 30-AUG-1996 16:31:31

GREY: ORION12 IPOL ORN1,1 25-35.LOG.2

CONT: ORION15 IPOL ORN3,3 36-45.BLNK.1

0 1 2 3 4



Grey scale flux range= .000 5.000 UNDEFINE

Peak contour flux = 8.1853E+03 RATI\*M/S

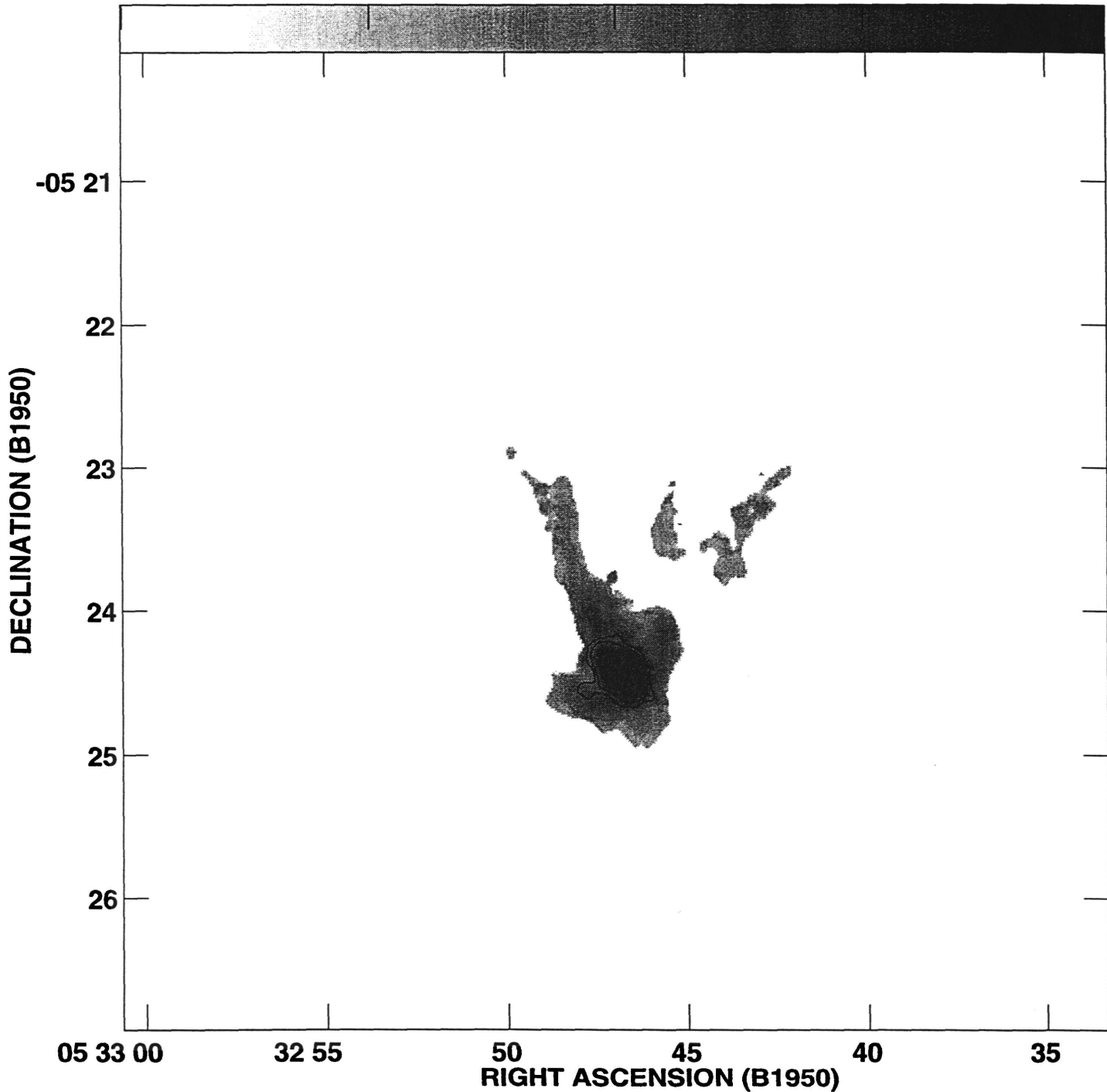
Levs = 1.0000E+01 \* ( 5.000, 25.00, 125.0,  
625.0, 3000.)

Plot file version 1 created 30-AUG-1996 16:47:56

GREY: ORION15 IPOL ORN3,3 25-35.LOG.1

CONT: ORION15 IPOL ORN3,3 16-25.BLNK.1

0 1 2 3



Grey scale flux range= .000 3.984 UNDEFINE

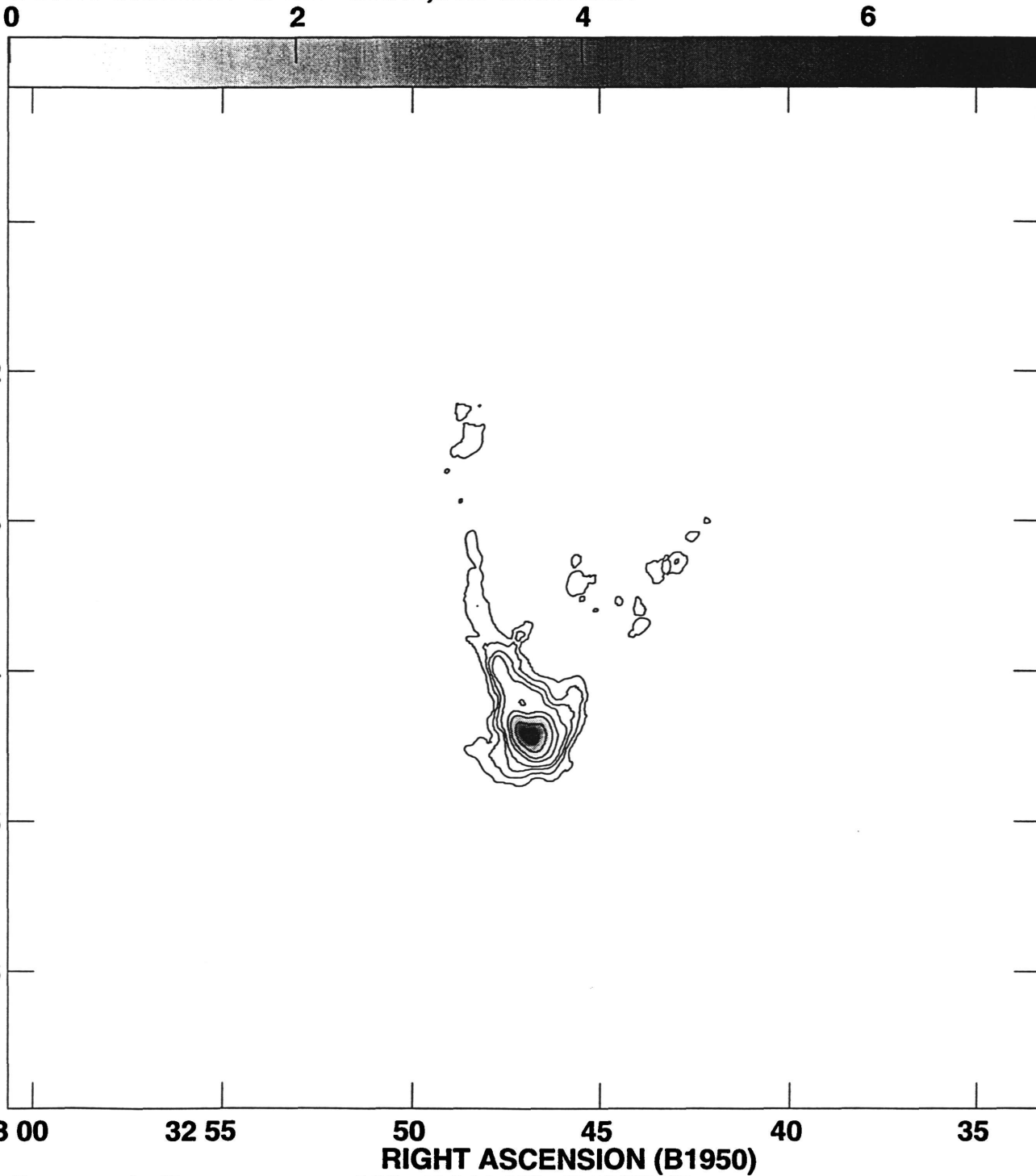
Peak contour flux = 6.3643E+03 RATI\*M/S

Levs = 1.0000E+01 \* ( 5.000, 25.00, 125.0, 625.0, 3000.)

Plot file version 8 created 30-AUG-1996 12:02:03

GREY: ORION12 IPOL ORN1,1 25-35.BLNK.1

CONT: ORION12 IPOL ORN3,3 25-35.BLNK.1

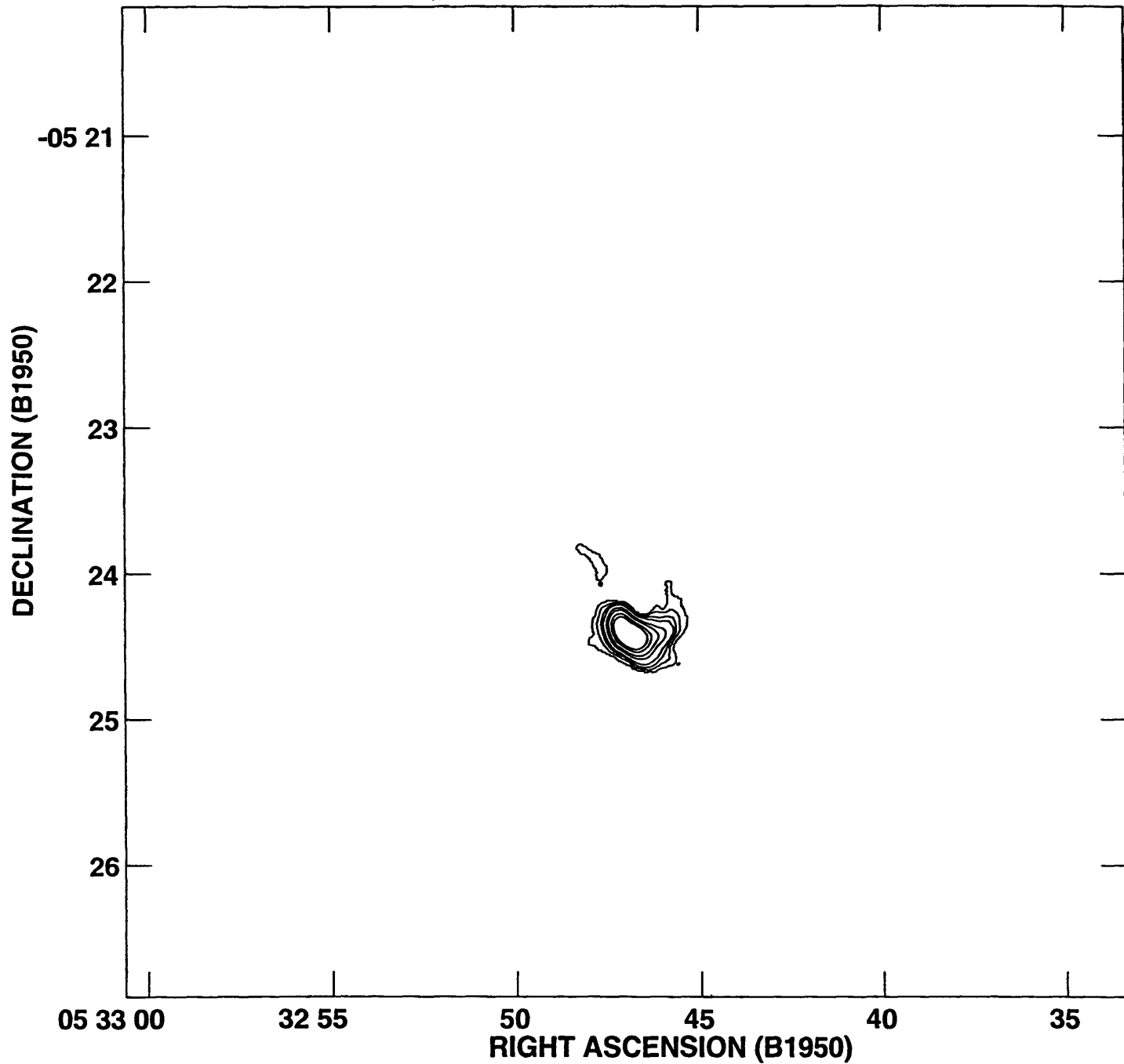


Grey scale flux range= .000 7.211 Kilo RATI\*M/S

Peak contour flux = 3.8778E+03 RATI\*M/S

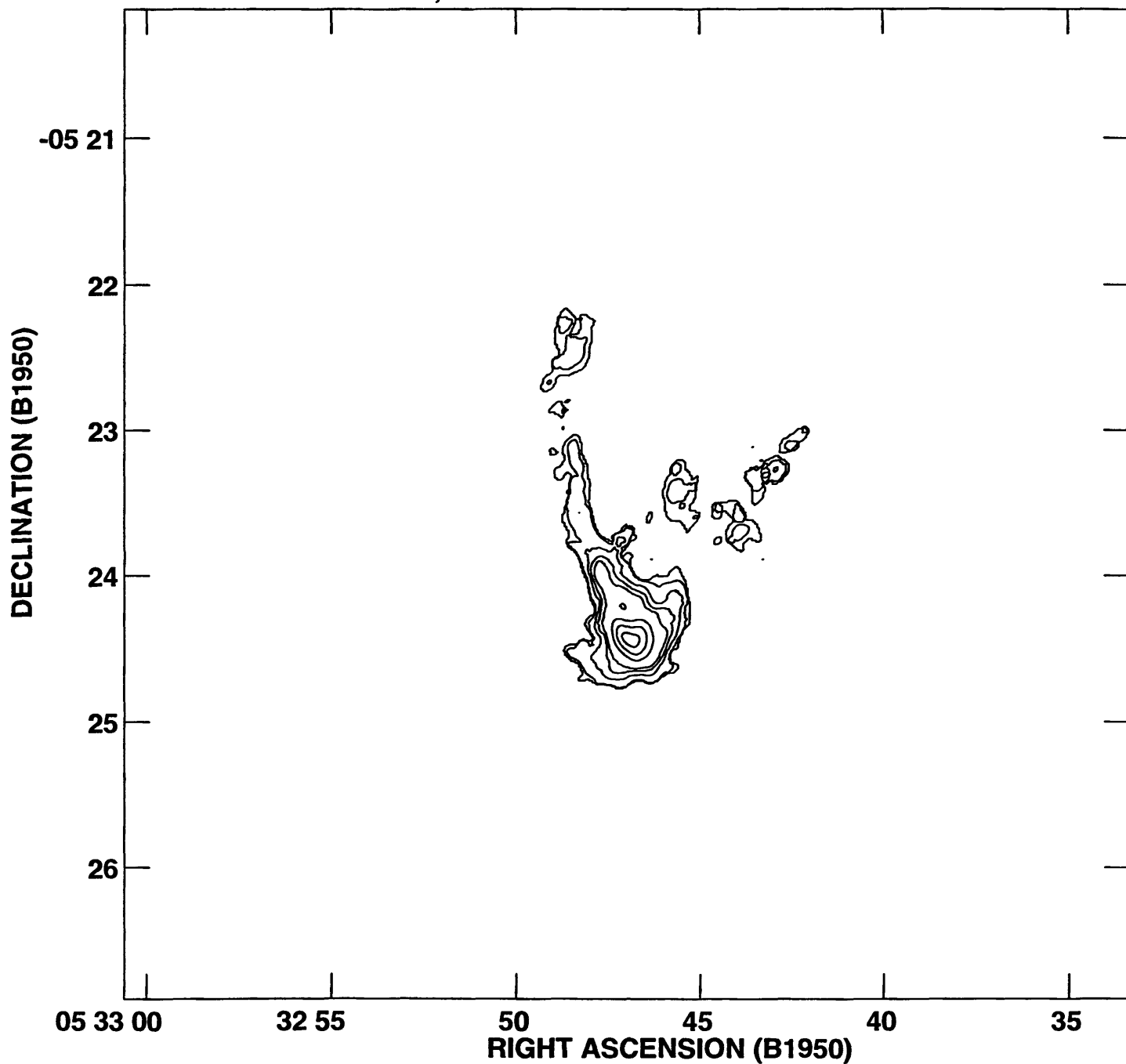
Levs = 2.000E+01 \* ( 2.000, 8.000, 16.00,  
25.00, 50.00, 75.00, 125.0, 175.0)

PLot file version 1 created 30-AUG-1996 14:23:21  
ORION15 IPOL ORN3,3 36-45.BLNK.1



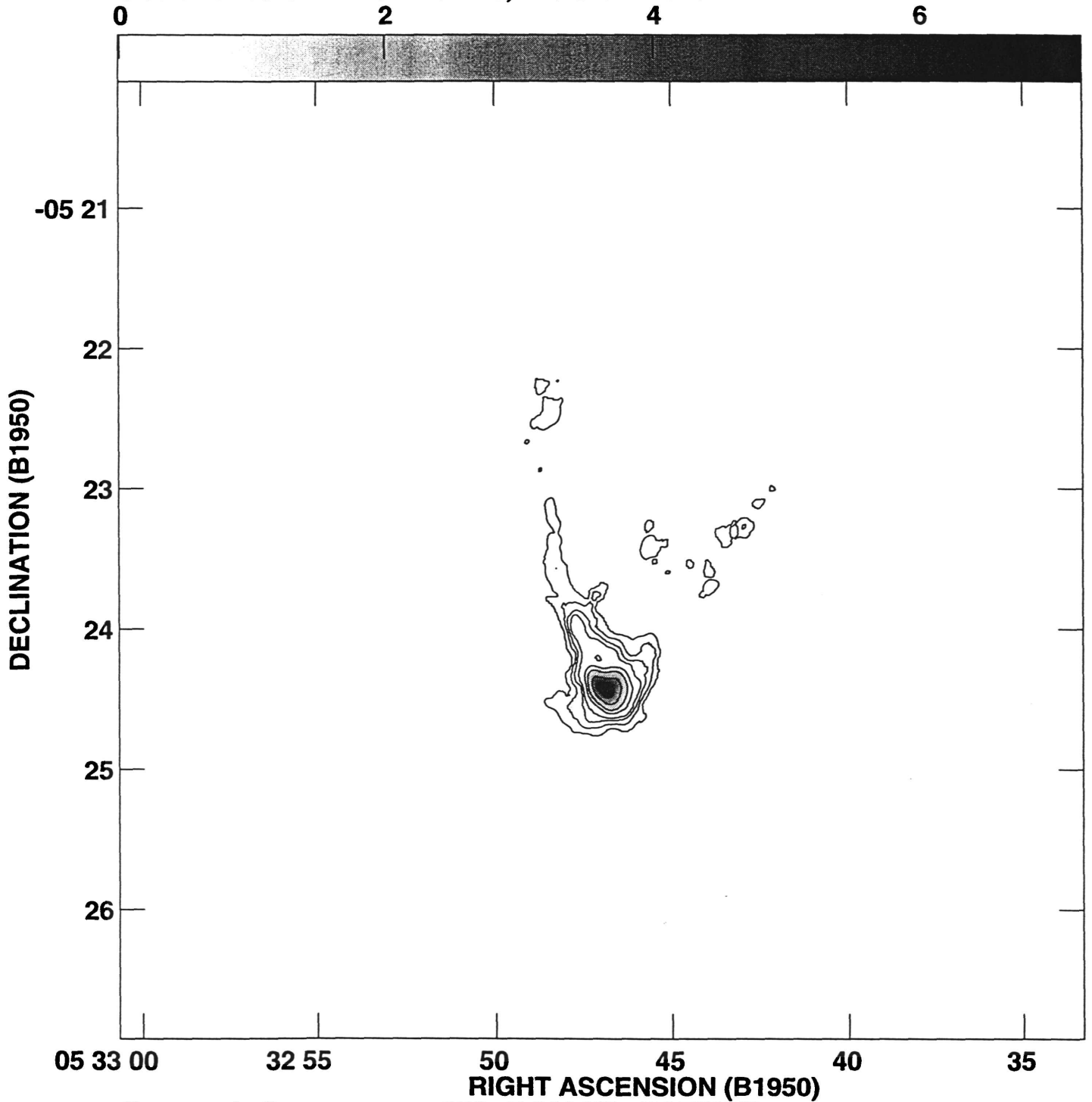
Peak flux = 8.1853E+03 RATI\*M/S  
Levs = 2.000E+01 \* ( 2.000, 8.000, 16.00,  
25.00, 50.00, 75.00, 125.0, 175.0)

PLot file version 1 created 30-AUG-1996 10:07:31  
ORION12 IPOL ORN3,3 25-35.BLNK.1



Peak flux =  $3.8778E+03$  RATI\*M/S  
Levs =  $2.0000E+01$  \* ( 1.000, 2.000, 8.000,  
16.00, 25.00, 75.00, 125.0, 175.0)

Plot file version 17 created 30-AUG-1996 14:02:52  
GREY: ORION12 IPOL ORN1,1 25-35.BLNK.1  
CONT: ORION12 IPOL ORN3,3 25-35.BLNK.1



Grey scale flux range= .000 7.211 Kilo RATI\*M/S  
Peak contour flux = 3.8778E+03 RATI\*M/S  
Levs = 2.0000E+01 \* ( 2.000, 8.000, 16.00,  
25.00, 50.00, 75.00, 125.0, 175.0)

Plot file version 3 created 30-AUG-1996 14:59:50

GREY: ORION12 IPOL ORN1,1 25-35.LOG.1

CONT: ORION15 IPOL ORN3,3 36-45.BLNK.1

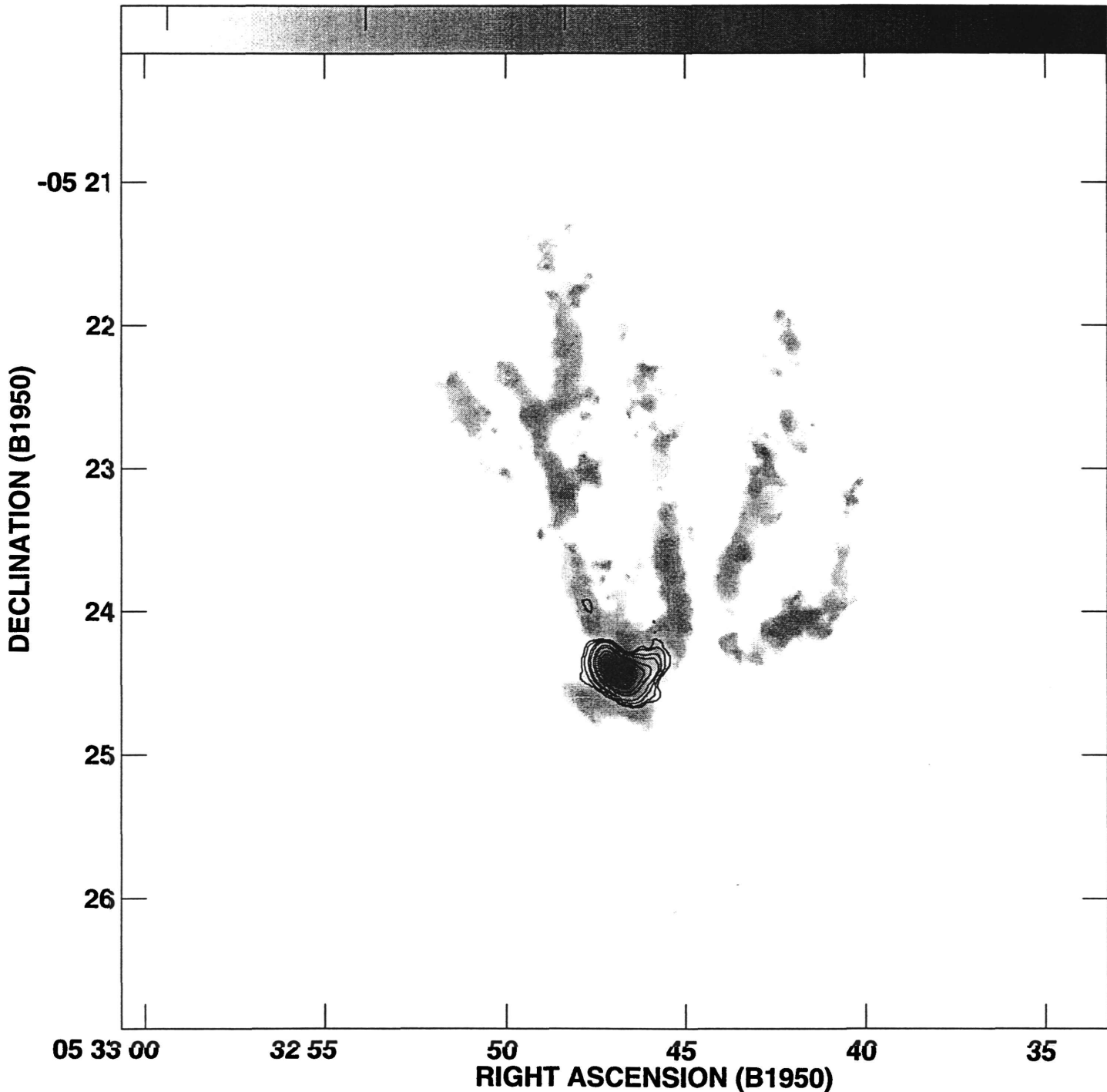
1.5

2.0

2.5

3.0

3.5



Grey scale flux range= 1.388 3.858 UNDEFINE

Peak contour flux = 8.1853E+03 RATI\*M/S

Levs = 2.0000E+01 \* ( 4.000, 8.000, 16.00,  
25.00, 50.00, 75.00, 125.0, 175.0)

Plot file version 1 created 30-AUG-1996 15:07:14

GREY: ORION15 IPOL ORN3,3 36-45.LOG.1

CONT: ORION15 IPOL ORN3,3 16-25.BLNK.1

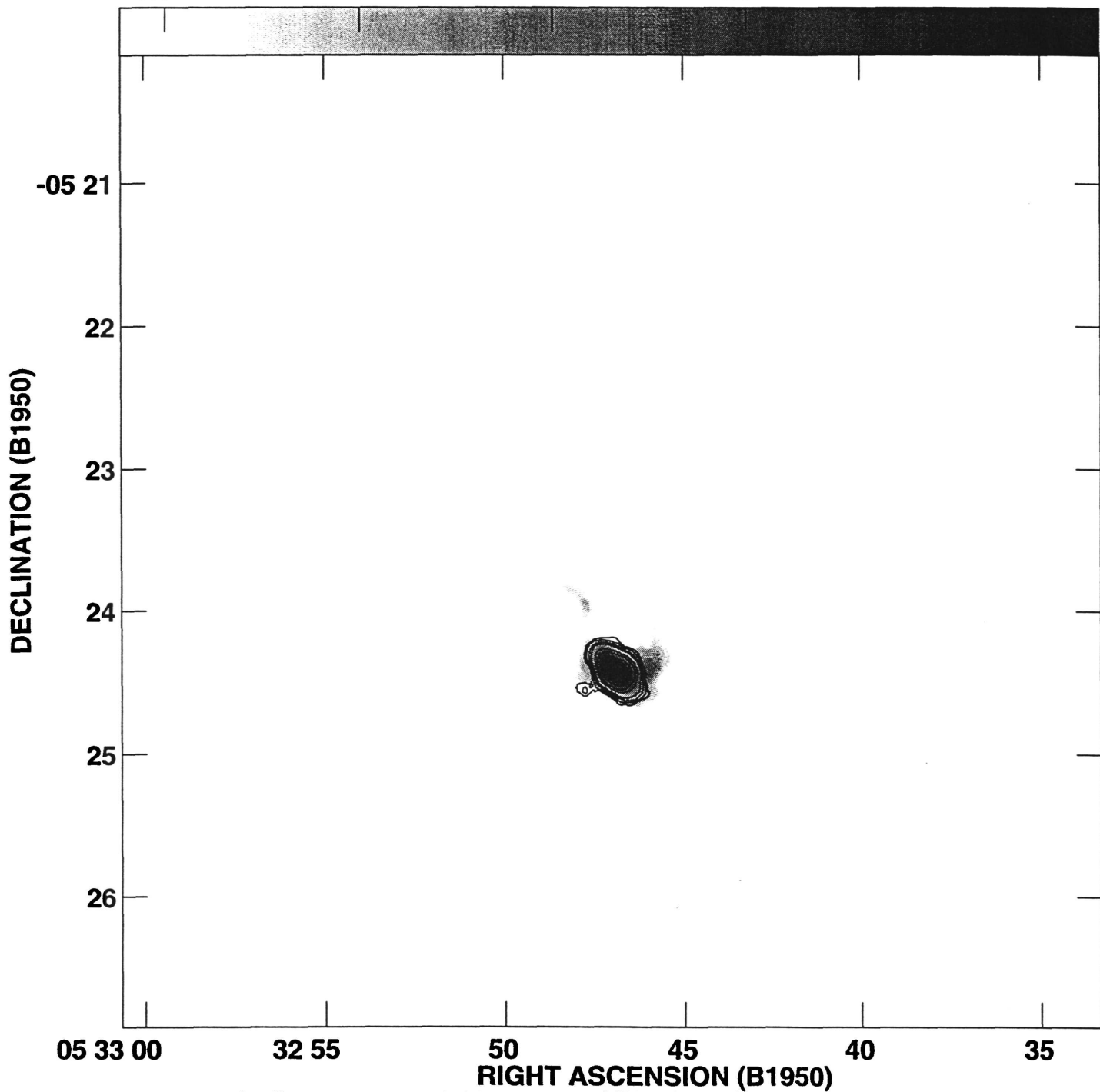
1.5

2.0

2.5

3.0

3.5



Grey scale flux range= 1.388 3.913 UNDEFINE

Peak contour flux = 6.3643E+03 RATI\*M/S

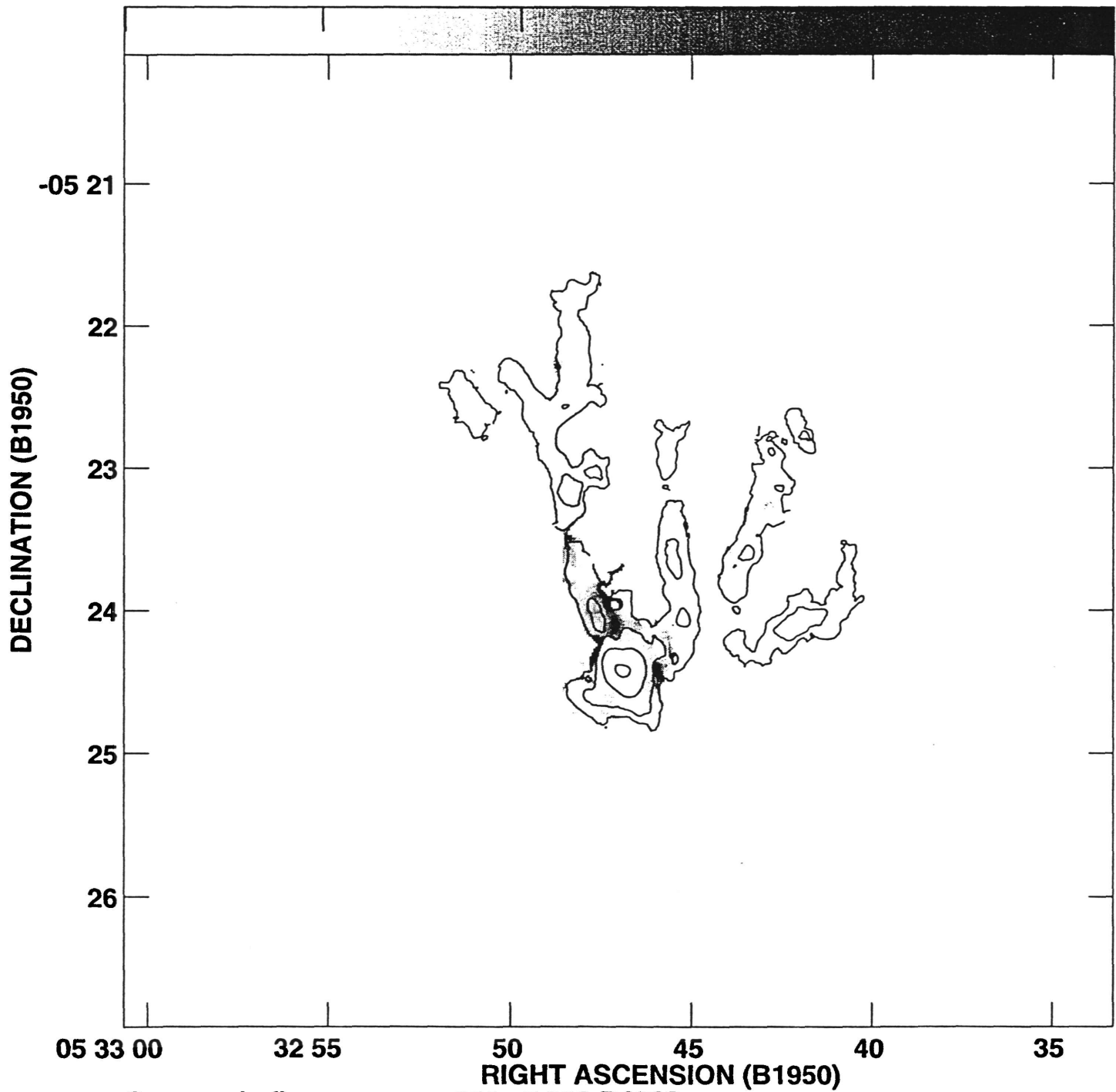
Levs = 2.0000E+01 \* ( 4.000, 8.000, 16.00,  
25.00, 50.00, 75.00, 125.0, 175.0)

Plot file version 12 created 30-AUG-1996 16:22:26

GREY: ORION12 IPOL OR3/1 3F.10CH.1

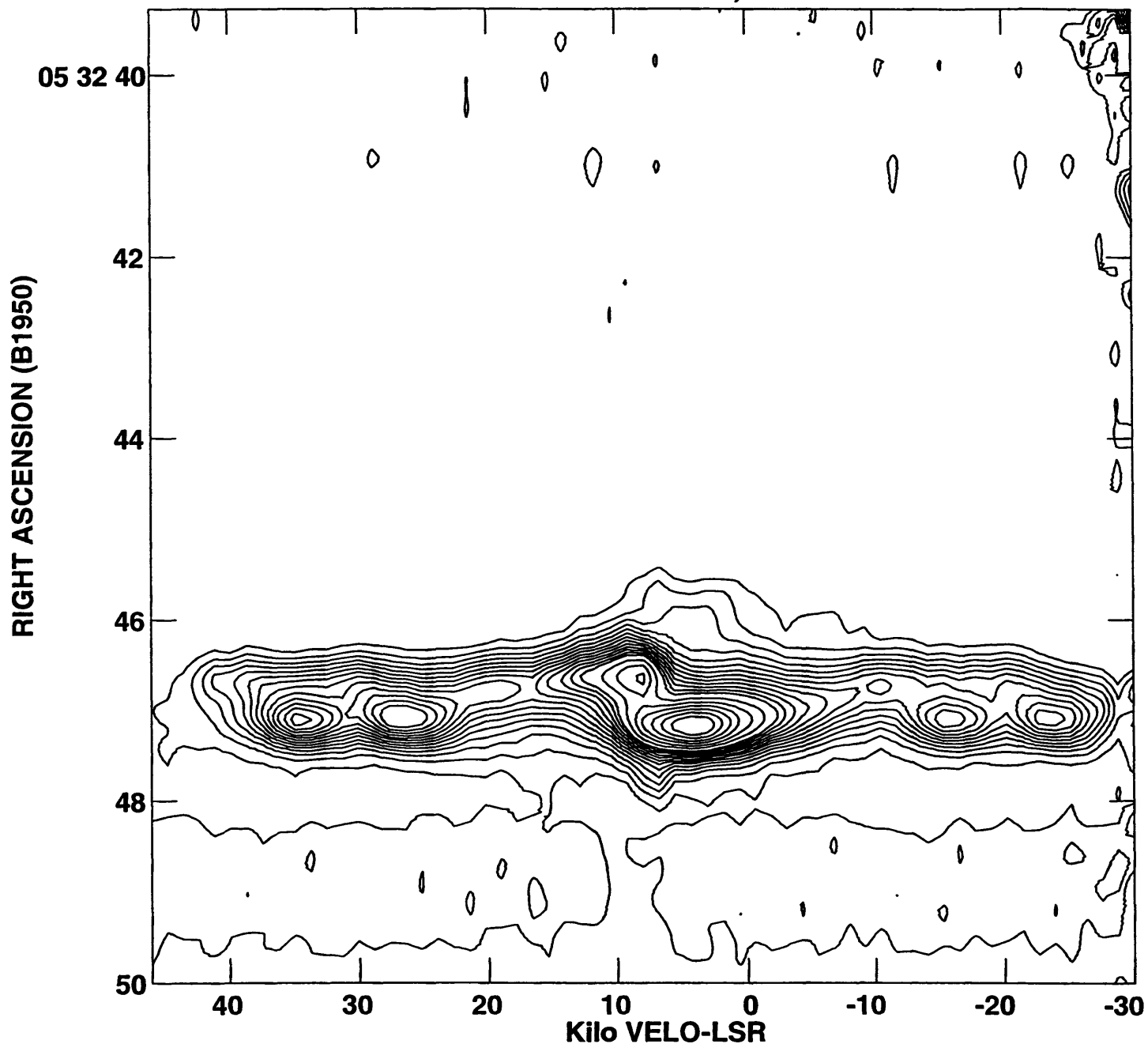
CONT: ORION12 IPOL ORN1,1 25-35.BLNK2.1

0 1 2 3 4



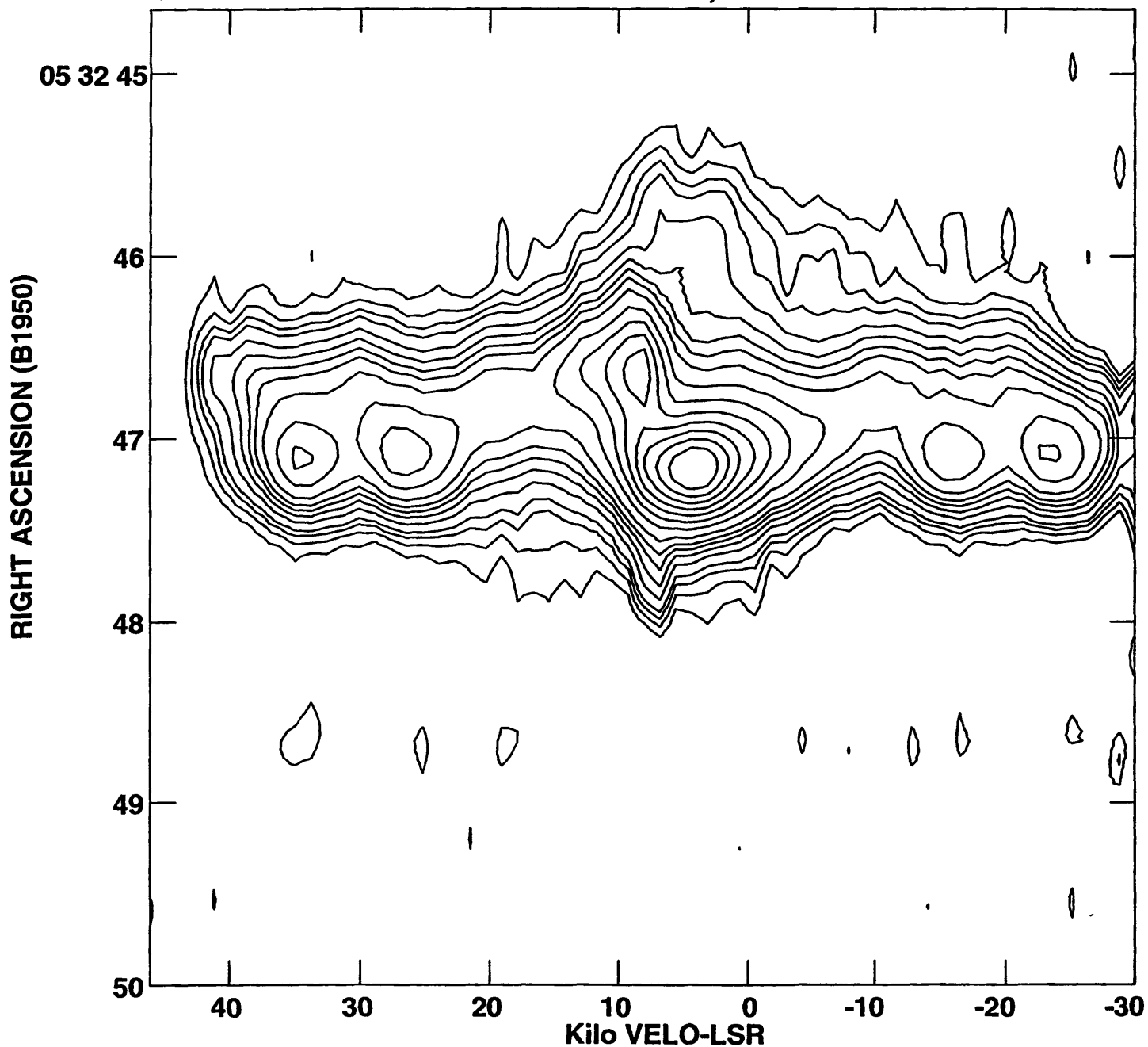
Grey scale flux range= .000 5.000 RATIO  
Peak contour flux = 7.2107E+03 RATI\*M/S  
Levs = 1.0000E+01 \* ( 5.000, 25.00, 125.0,  
625.0, 3000.)

PLot file version 2 created 16-AUG-1996 10:58:09  
ORION15 DEC -05 24 22.00 IPOL ORION3,3.VRDCUB.1



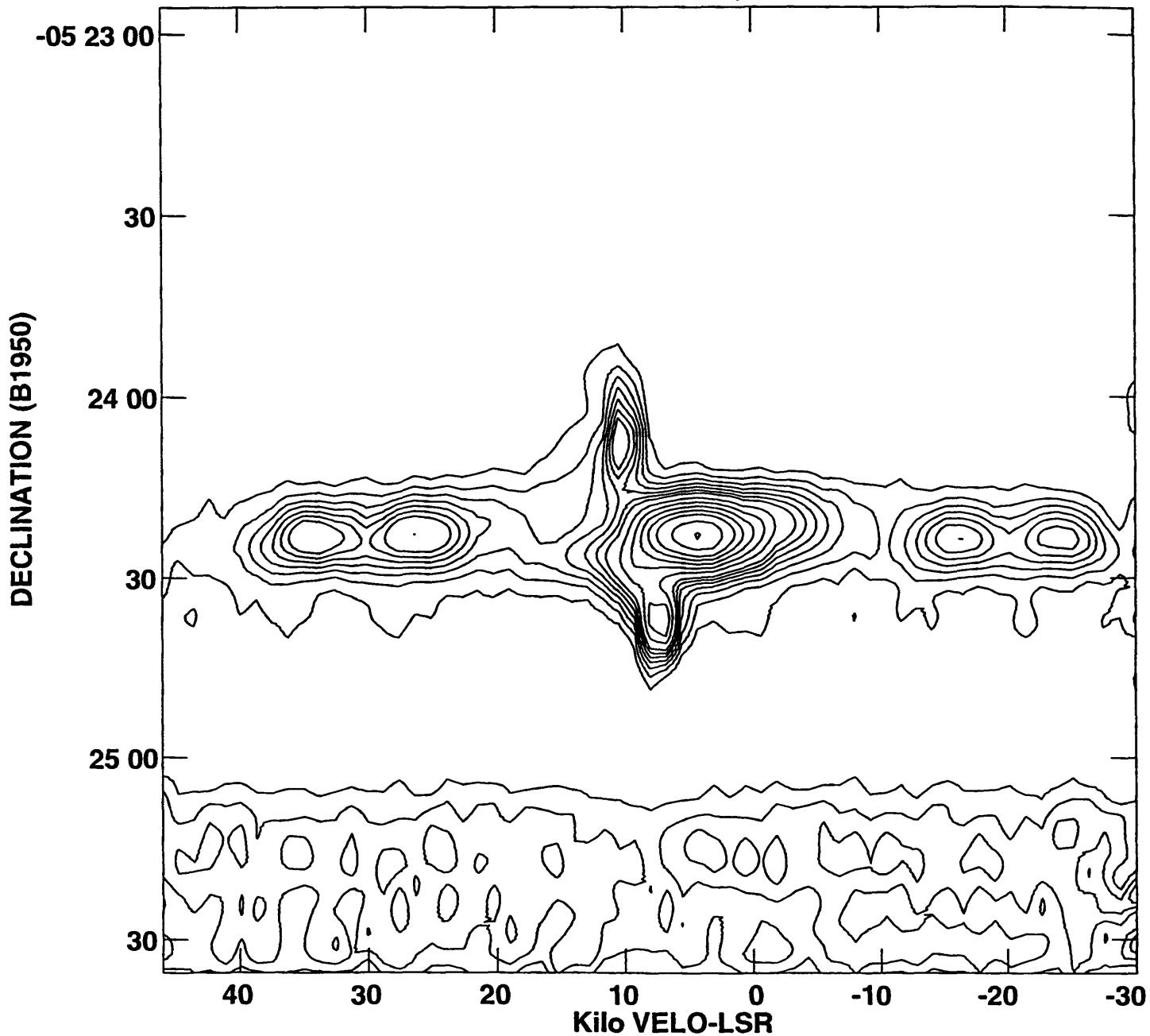
Peak flux =  $-1.1334\text{E}+01$  JY/BEAM  
Levs =  $2.0000\text{E}-02$  \* ( 2.000, 4.000, 6.000,  
8.000, 10.00, 12.00, 14.00, 16.00, 18.00,  
20.00, 22.00, 24.00, 26.00, 30.00, 34.00,  
38.00, 42.00, 46.00, 50.00)

PLot file version 2 created 26-AUG-1996 15:47:50  
ORION15 DEC -05 24 22.00 IPOL ORN3,3 NOCON.VRDCUB.1



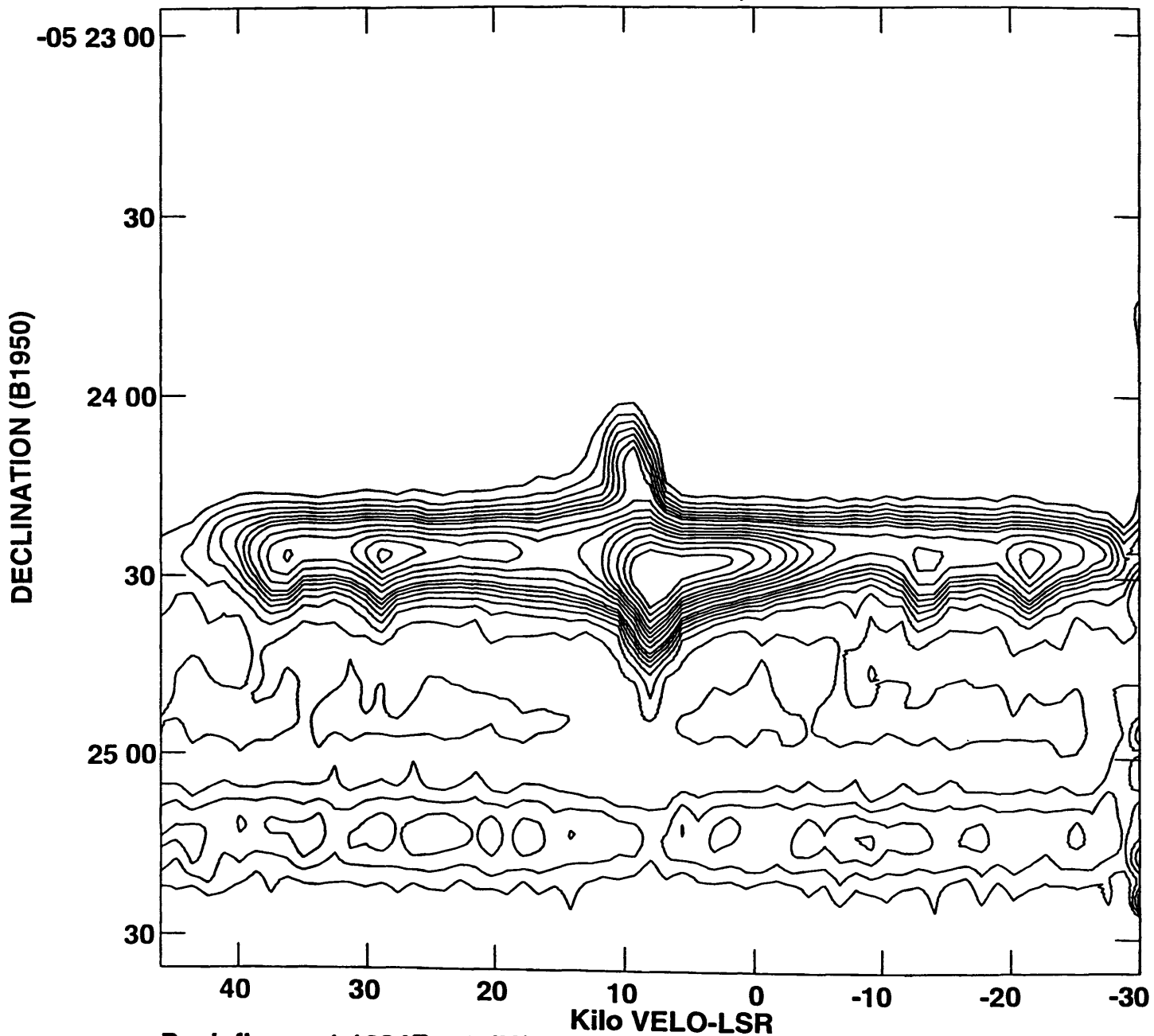
Peak flux =  $-1.2883 \times 10^1$  JY/BEAM  
Levs =  $1.0000 \times 10^{-2} * ( 2.000, 4.000, 6.000,$   
 $8.000, 12.00, 16.00, 20.00, 24.00, 30.00,$   
 $40.00, 50.00, 60.00, 70.00, 80.00, 90.00,$   
 $100.0)$

PLot file version 5 created 16-AUG-1996 10:30:33  
ORION15 RA 05 32 47.321 IPOL ORION3,3.VDRCUB.1



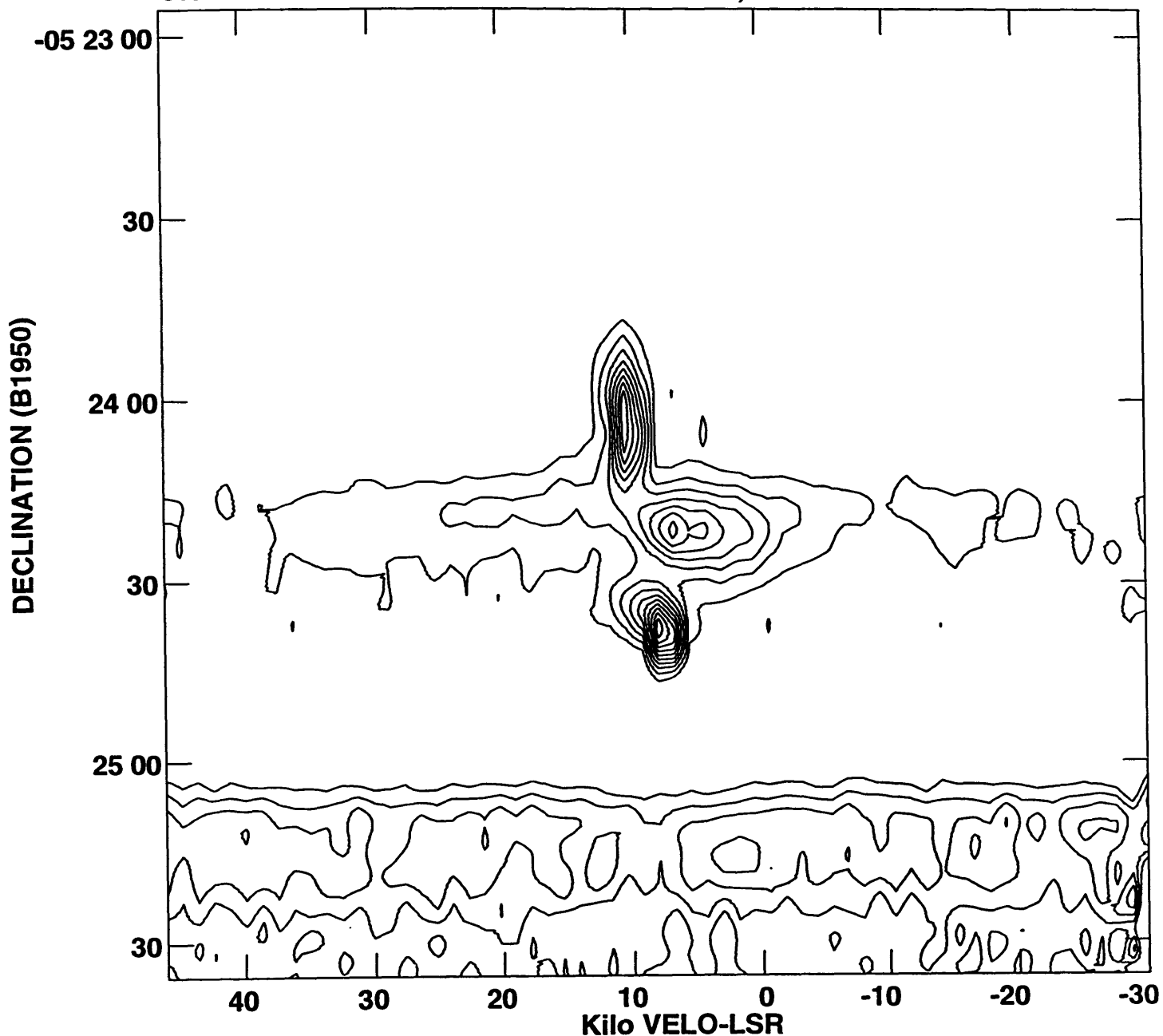
Peak flux =  $-1.1334E+01$  JY/BEAM  
Levs =  $2.0000E-02 * ( 2.000, 4.000, 6.000,$   
 $8.000, 10.00, 12.00, 14.00, 18.00, 22.00,$   
 $26.00, 30.00, 34.00, 40.00, 46.00, 52.00)$

PLot file version 3 created 16-AUG-1996 10:27:55  
ORION15 RA 05 32 46.786 IPOL ORION3,3.VDRCUB.1



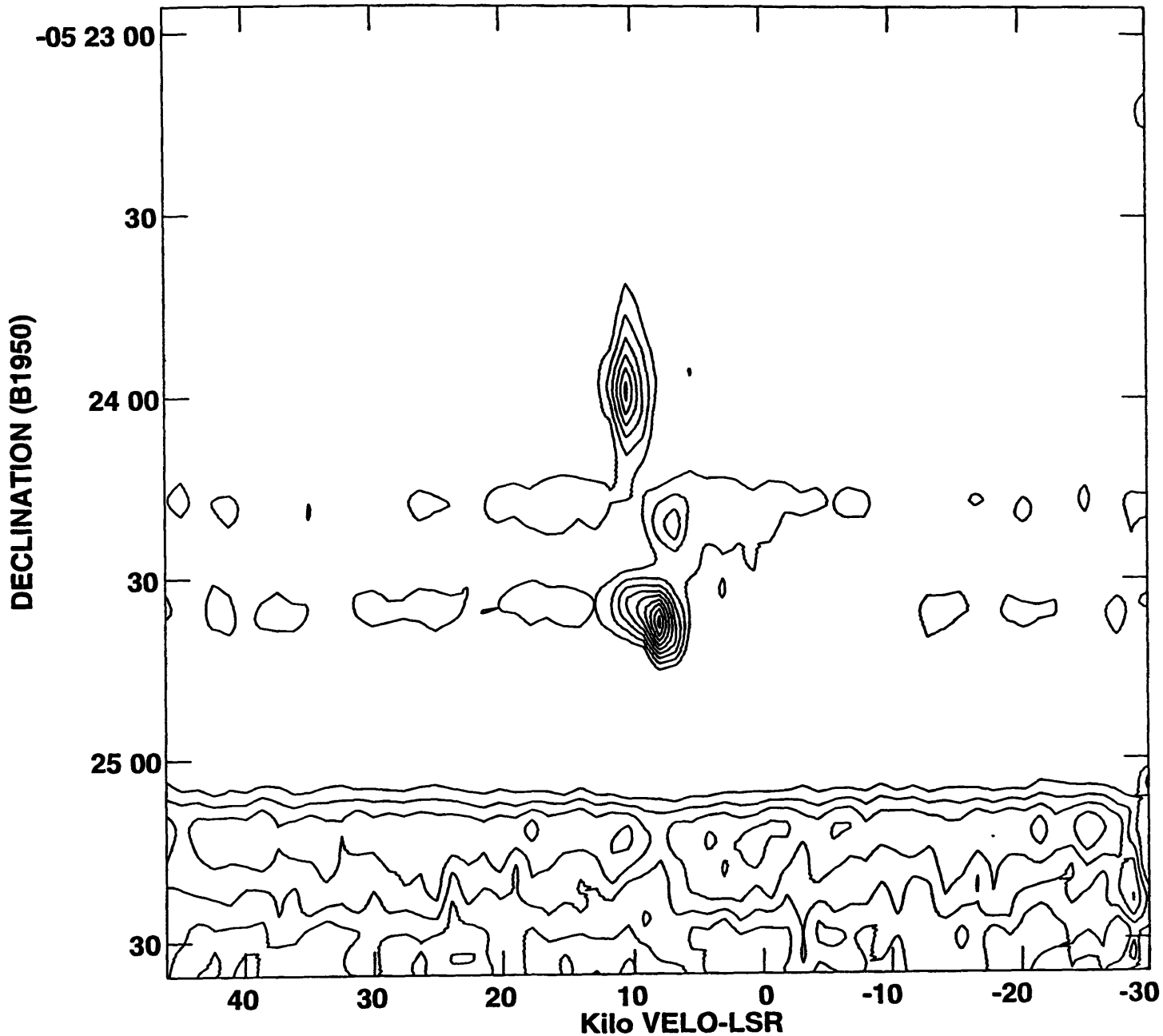
Peak flux =  $-1.1334 \times 10^1$  JY/BEAM  
Levs =  $2.0000 \times 10^{-2} * ( 2.000, 4.000, 6.000,$   
 $8.000, 10.00, 12.00, 14.00, 18.00, 22.00,$   
 $26.00, 30.00, 34.00, 40.00, 46.00, 52.00)$

PLot file version 7 created 16-AUG-1996 10:34:25  
ORION15 RA 05 32 47.589 IPOL ORION3,3.VDRRCUB.1



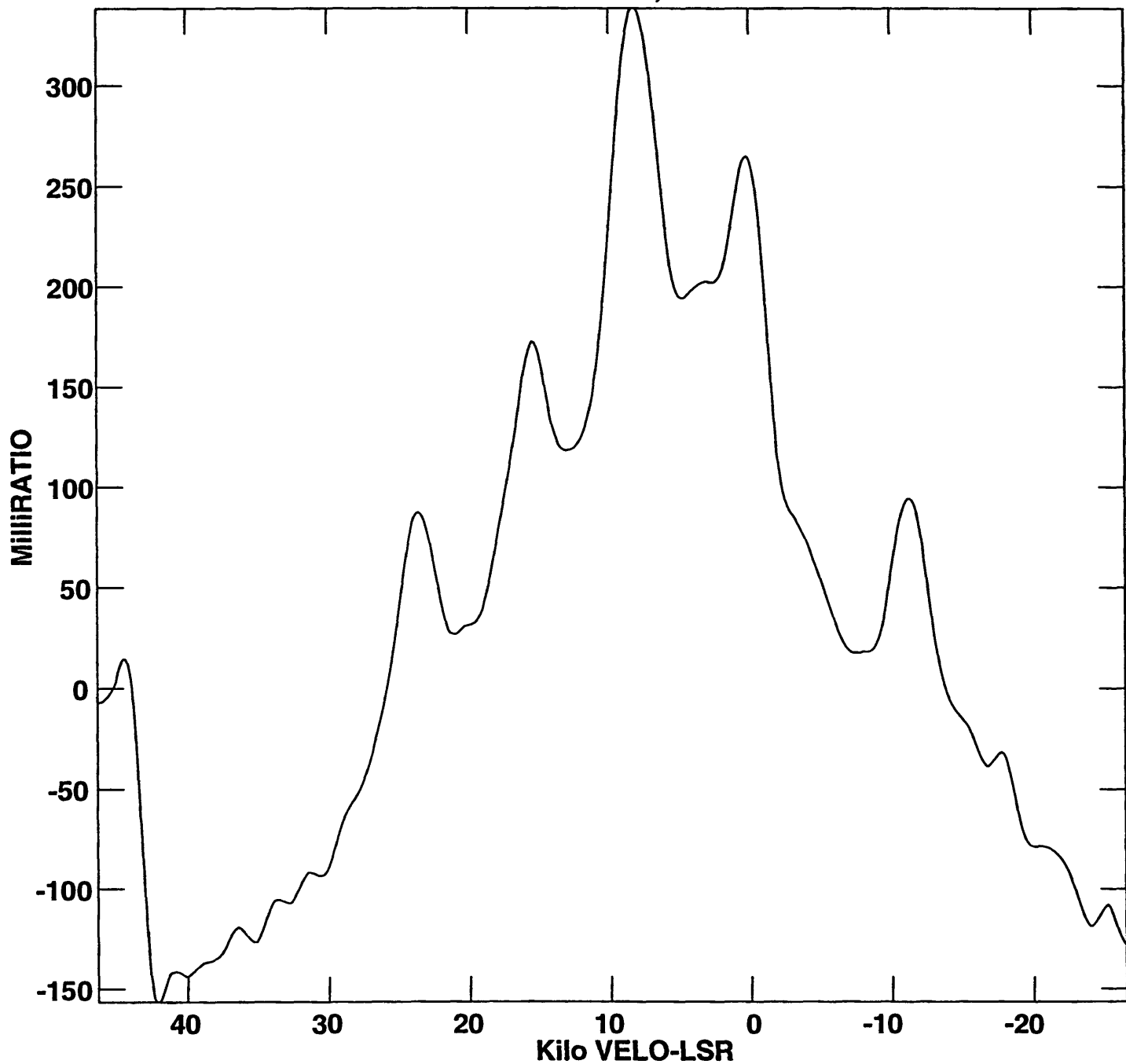
Peak flux =  $-1.1334E+01$  JY/BEAM  
Levs =  $2.0000E-02 * ( 2.000, 4.000, 6.000,$   
 $8.000, 10.00, 12.00, 14.00, 16.00, 18.00,$   
 $20.00, 22.00, 24.00, 26.00, 30.00, 34.00,$   
 $38.00, 42.00, 46.00, 50.00)$

PLot file version 8 created 16-AUG-1996 10:35:44  
ORION15 RA 05 32 47.857 IPOL ORION3,3.VDRCUB.1



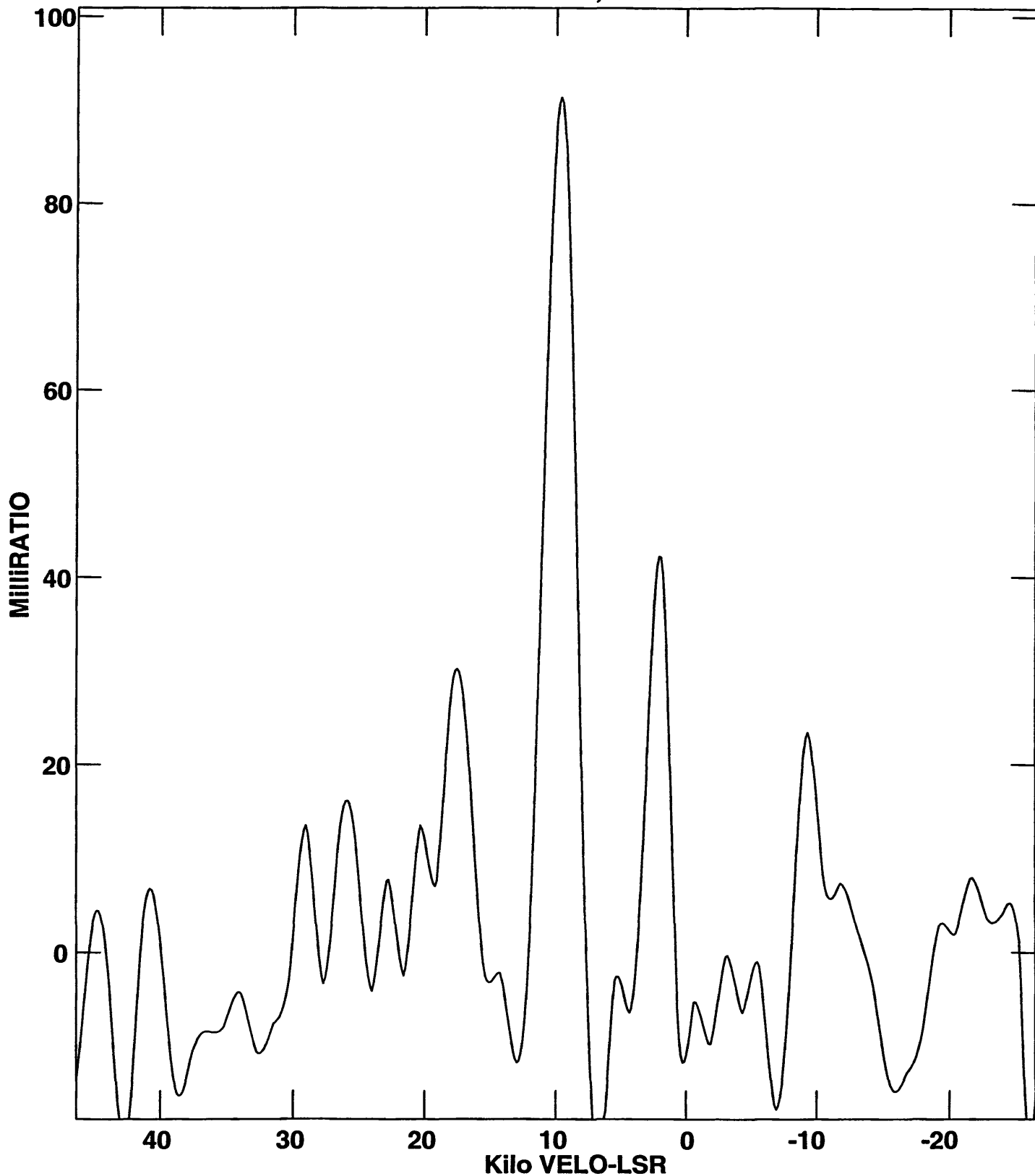
Peak flux =  $-1.1334 \times 10^1$  JY/BEAM  
Levs =  $2.0000 \times 10^{-2} * ( 2.000, 4.000, 6.000,$   
 $8.000, 10.00, 12.00, 14.00, 16.00, 18.00,$   
 $20.00, 22.00, 24.00, 26.00, 30.00, 34.00,$   
 $38.00, 42.00, 46.00, 50.00)$

Plot file version 6 created 29-AUG-1996 10:11:57  
ORION12 DEC -05 24 28.40 IPOL ORN1,1 4FNOC.VRDST.1



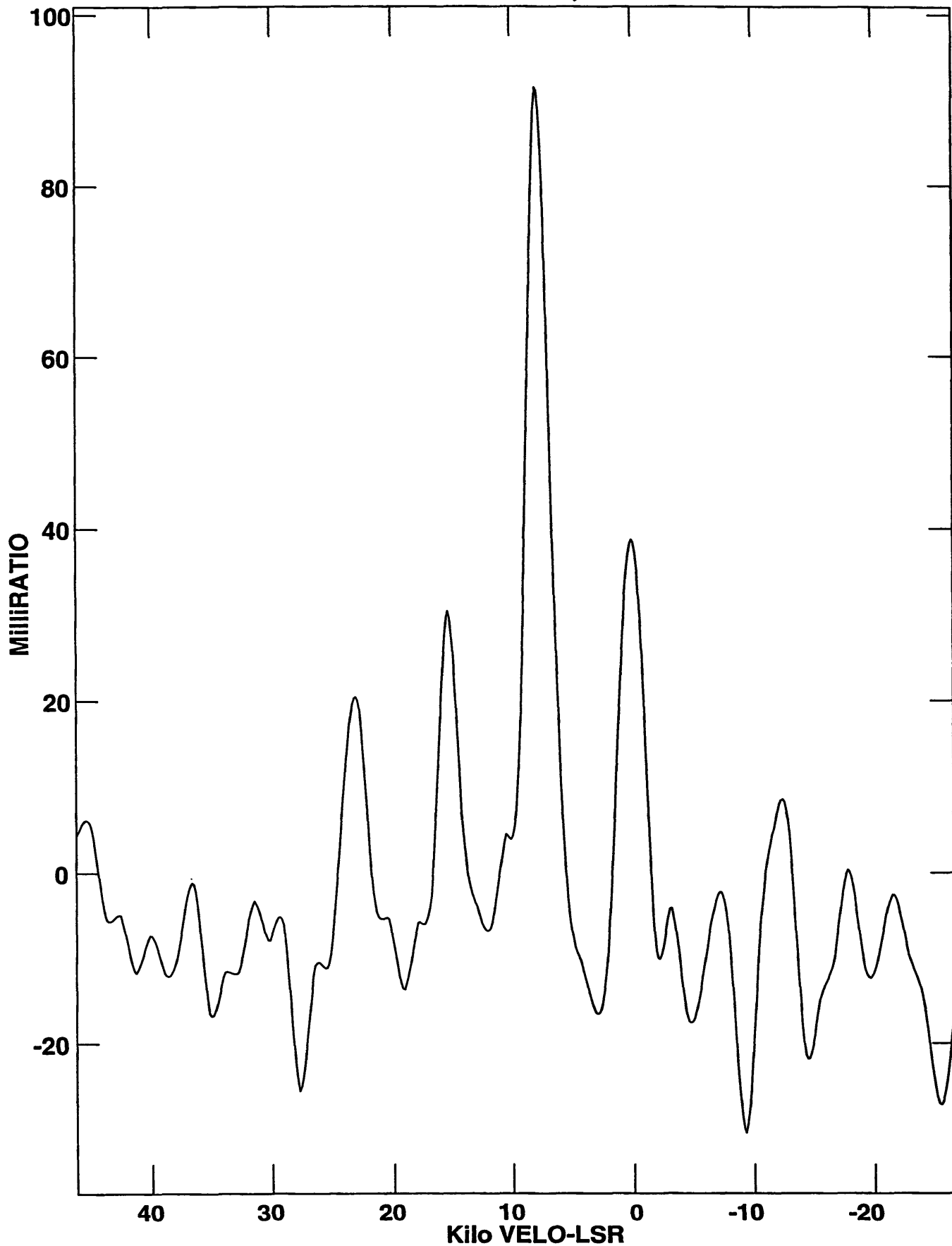
Center at RA 05 32 46.679

Plot file version 5 created 29-AUG-1996 10:10:21  
ORION12 DEC -05 24 07.60 IPOL ORN1,1 4FNOC.VRDST.1



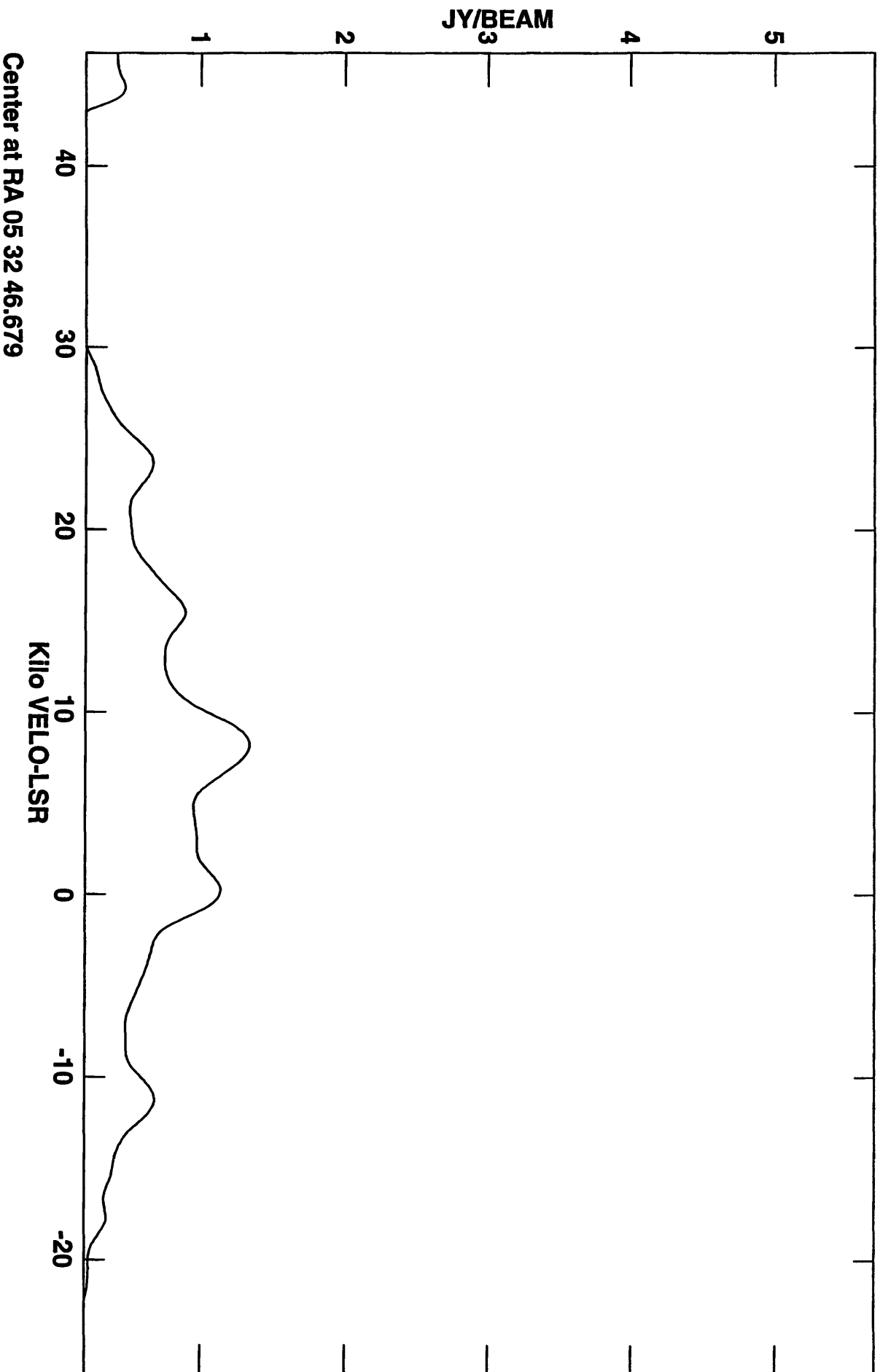
Center at RA 05 32 46.679

Plot file version 10 created 29-AUG-1996 10:22:52  
ORION12 DEC -05 24 37.20 IPOL ORN1,1 4FNOC.VRDST.1

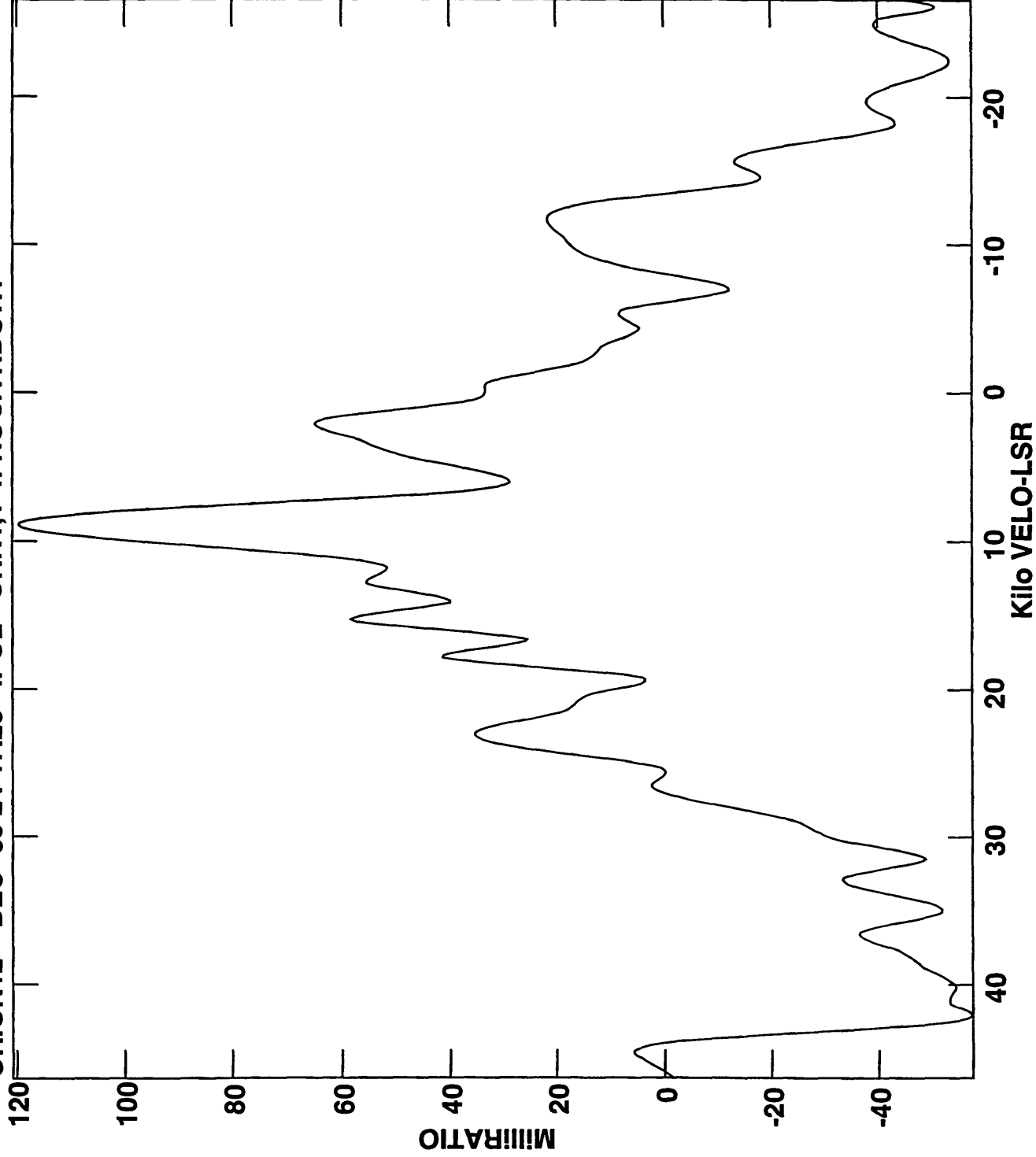


Center at RA 05 32 47.750

Plot file version 10 created 29-AUG-1996 09:41:19  
ORION12 DEC -05 24 28.40 IPOL ORN1,1 4F\*:VRDCUB.1



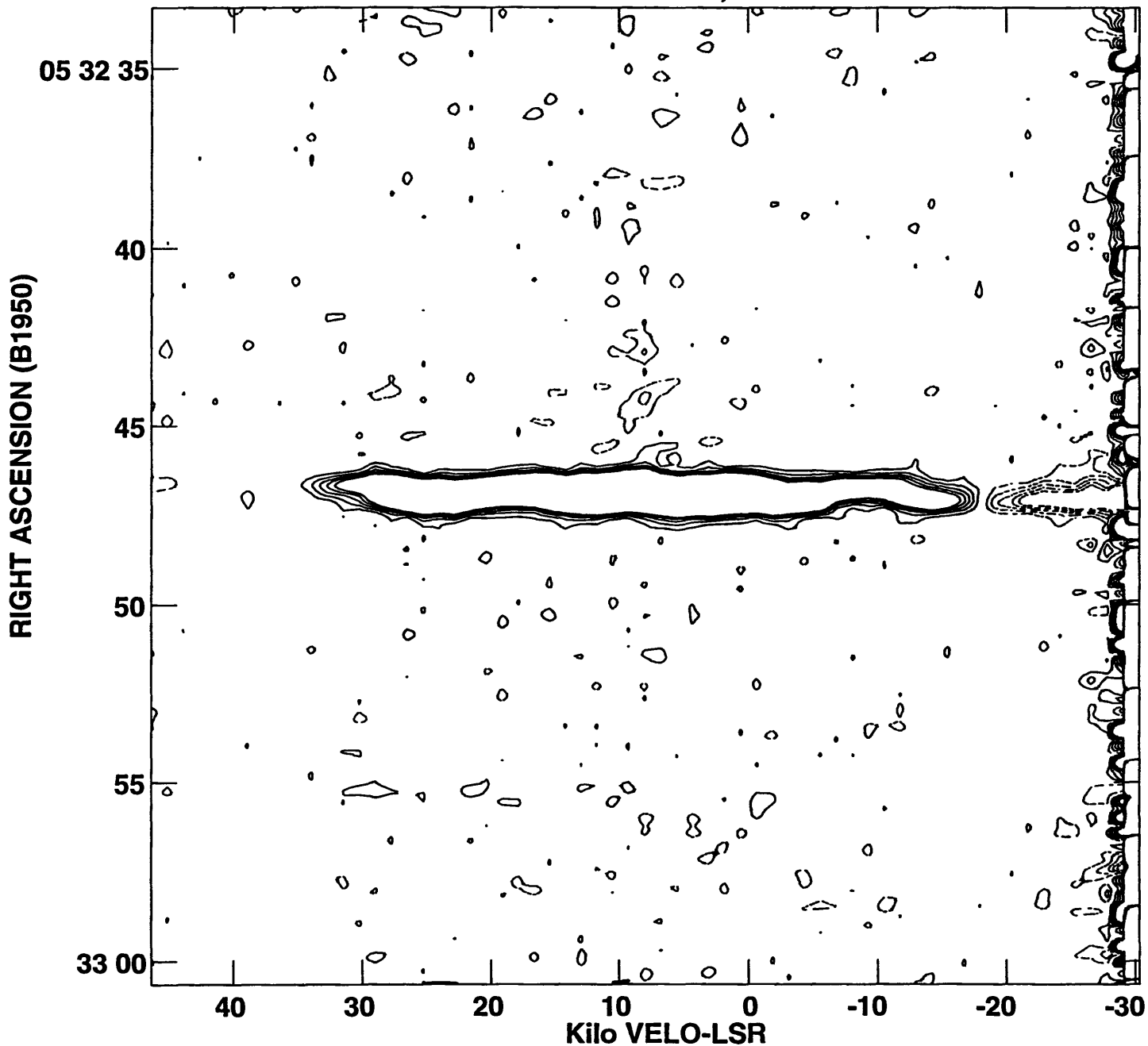
Plot file version 7 created 29-AUG-1996 10:19:32  
ORION12 DEC -05 24 17.20 IPOL ORN1,1 4FNOC.VRDST.1



Center at RA 05 32 46.839

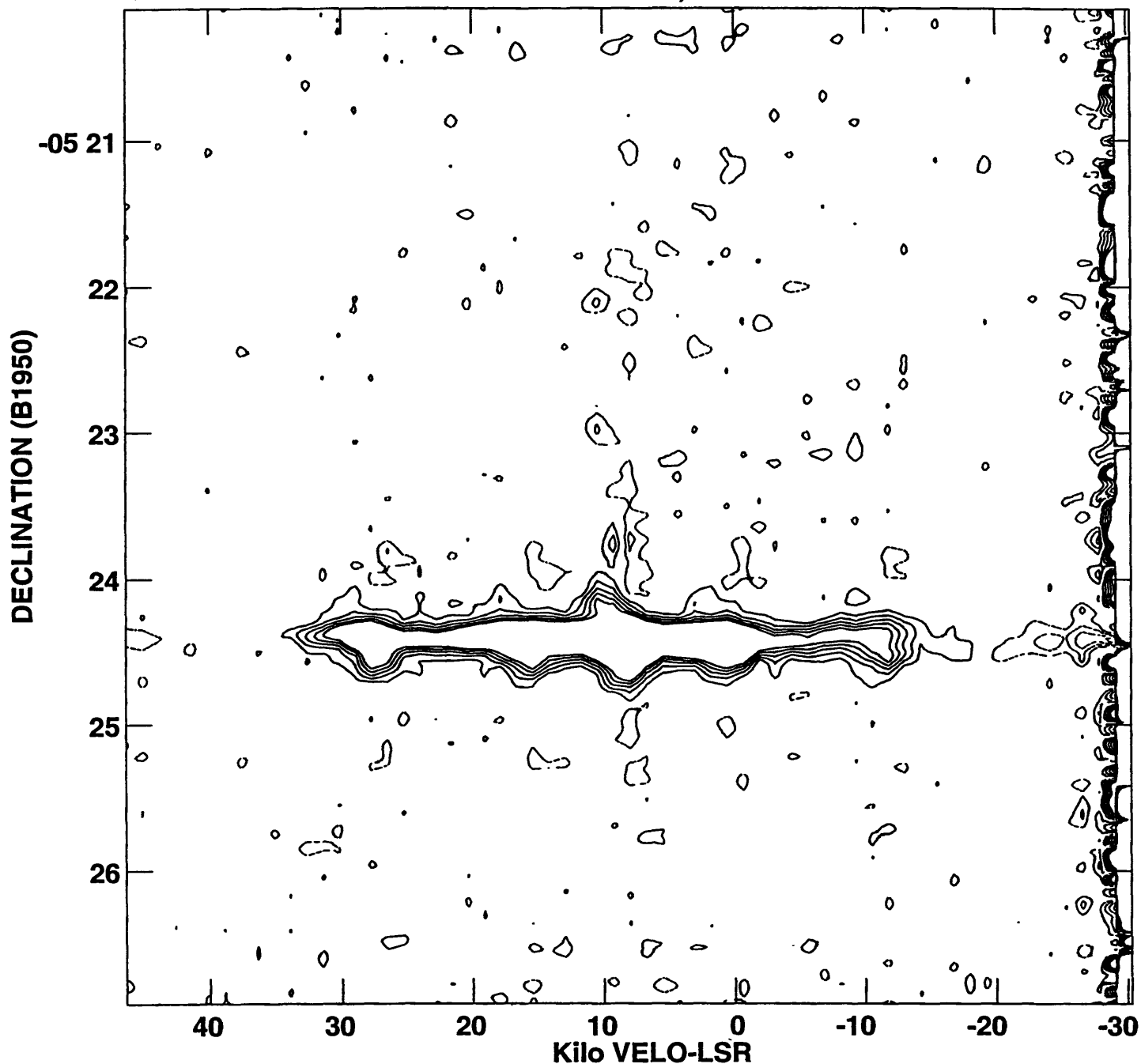
Vel. vs. RA for the (1,1) line  
(location on map specified below)

PLot file version 1 created 29-JUL-1996 16:00:30  
ORION11 DEC -05 24 22.00 IPOL OR111,163CH.VRDCUB.1



Peak flux = 1.2986E+01 JY/BEAM  
Levs = 1.0000E-02 \* ( -10.0, -8.00, -6.00,  
-4.00, -2.00, 2.000, 4.000, 6.000, 8.000,  
10.00)

PLot file version 1 created 29-JUL-1996 15:34:25  
ORION11 RA 05 32 46.518 IPOL OR111,163CH.VDRCUB.1



Peak flux = 1.2986E+01 JY/BEAM  
Levs = 1.0000E-02 \* ( -10.0, -8.00, -6.00,  
-4.00, -2.00, 2.000, 4.000, 6.000, 8.000,  
10.00)

## **GENERAL HARDWARE**

### Declination Indicator

Declination dial indicator on the motor control drawer was tested for accuracy. The following procedure was used for this 'pointing' experiment:

- set telescope declination to a chart read value of a  $\geq 40$ Jy source
- as object crosses the meridian, the signal increases and the strip chart recorder pen is deflected
- adjust telescope's declination slightly North [South]
- does slope of strip-chart line increase?
  - if YES, then the declination SHOULD have been more North [South]
  - if NO, then adjust back to original declination and check the opposite direction

After several tests on Cassiopeia A, it was determined that the declination the dial should be positioned to is the actual declination minus 37minutes, instead of subtracting a full 1degree as before (apparently due to an erroneous, but non-critical position indicator).

### Motor Control Box

In the motor control box, a  $300\Omega$ , 20W resistor was placed in parallel with a  $250\Omega$ , 20W to increase voltage across safety relay RY2 (see the motor control box schematic either with this documentation or in the 40' Technical Manual) Also, a  $350\Omega$ , 10W resistor was replaced with a  $350\Omega$ , 20W resistor to ensure that each resistor had  $\leq 1/2$  the specified wattage. In the past, this relay had switched, then switched back into position immediately when the telescope was in motion in one direction, then switched manually to the other. This produced an arc on the mechanical switching arm inside the relay that had been observed to, at times, melt and fuse, bypassing the north and south safety limit-switches and causing the telescope to move (either north or south) until it could physically move no further, in the process severing cables and causing great motor and structural strain. This problem has apparently been remedied, as it has not occurred since.

### Internal Interference

Severe interference was found after the repeated use of a frequency counter, specifically the HP 5343A Microwave Frequency Counter. This produced at least three constant, large peaks in the telescope's IF band, 10 - 80Mhz, observed on the

HP 8558B Spectrum Analyzer 0.1-1500Mhz with Channel A as the input. The interference only occurs during the time in which the monitor is turned on, the purpose of which is to monitor the local oscillator (LO) frequency, which must be kept at a very stable 1350Mhz.

#### External Interference

Another source of interference was found to emanate, ironically, from the interference monitoring trailer located behind the 40' antenna. The simple action of opening the door will leak out an extreme spike as seen on the spectrum analyzer. Unfortunately, it is not yet known what is broadcasting this signal inside the trailer (as this matter has not been followed up), but the simple solution is to make sure the door is shut tight during observation, as it is thickly shielded.

#### IF Drawer

Two new (but used) RF switches (model TTSL211, 28VDC, ser-no: 73-15) were mounted in the IF drawer so that a simple front-mounted switch could be used to select either a continuum or a broad-band scan.

#### Miscellaneous

Other minor changes, such as recabling--including new computer control cables, a new power supply for Channel B in the front end, and the introduction of a one-turn logarithmic potentiometer for the motor control box for finer adjustments of the declination.

## DIGITAL INTERFACE BOX

### Protocol Converter Box

A protocol converter box (PCB) was introduced to the digital interface, between the computer and the digital control box. This box contains a fully functional, though nearly inaccessible, IBM compatible AT computer, complete with two serial ports of its own. It performs the simple function of switching parity (as necessary) on the control bytes sent from the computer to the standard interface board (SIB). One port of the PCB can be attached to the serial connection from the computer (the 9pin connector, COM1) and the other port of the PCB to the 25pin connector on the back panel of the motor control box. The PCB will be useful for continued MS-Windows based control software, as it has proven difficult to switch parity in midstream in the Windows environment (without the use of a Virtual Device Driver, or VxD), but is a relatively easy task for a DOS based application, such as the old (current) Pascal control software. The PCB requires a 9600 baud link with the computer and a 57600 baud link with the SIB. Hence, a new SIB is needed, and must be used if the PCB is to be used (the old SIB and Pascal software communicate with each other at only 1200 baud).

### Resources

The digital interface box currently employs an older model SIB, the PDSET 5. The most useful documentation available is the VLBA Technical Report No. 12, entitled "VLBA Standard Interface Board Manual" by Wayne Koski and David Weber, July, 1991. Wayne Koski can be reached directly in Socorro, New Mexico (the VLA) at 505-835-7208, or more reliably by email at [wkoski@nrao.edu](mailto:wkoski@nrao.edu). Excerpts from this manual can be found in the 40' Computer Hardware Manual, but the official manual is a must. Another valuable document is the 'VLBA Cheat Sheet' compiled by Tim Weadon, and should be included with this documentation.

### Old vs. New SIB

PDSET 5 communicates at 1200 baud. To use the protocol converter box (PCB) and as a general upgrade to the aging 40' interface, a newer SIB, PDSET 9, is to be used as a replacement for the old (but still functional) SIB. The pin-outs are exactly the same for these two boards, but PDSET 5 is single-ended, accepting analog inputs (from Channels A and B) as referenced to ground. PDSET 9, however, is differential, and expects an analog input that is the voltage difference between the two conductors of a coaxial cable. Therefore, to ensure compatibility and proper

functioning, pins 18 through 25 on the 50pin female, wire wrapped connector attached to the SIB should be grounded (actually, only 18 and 19 need to be grounded out, as there are only two inputs, Ch. A and B but all should be done for completeness). Also, PDSET 5 does not require the use of an ID-byte, and is found in the firmware of the board. The newer SIB's poll external circuitry for the ID-byte.

### Computer Interface Card

This external circuitry has been added to the computer interface card, complete with a DIP switch to set the default ID-byte (currently a '1') for the device (there is only one device--one computer interface card). This circuitry has been proven to work, through a test program written in Delphi, IOTEST.PAS. This test employs the PCB, the new RS-232 to RS-422 converter, and the new SIB. The program was able to move the telescope north, fire each Cal., and toggle the power on the motor control box.

### Incompatibility

Unfortunately, this new circuit does not appear to be compatible with the old SIB, PDSET 5. So, the chip that would normally send the ID-Byte, the 74LS244 has been removed, and must be replaced in its proper position when the new SIB is used.

### Undocumented Circuits

There seems to be undocumented circuitry on the computer interface card (the wire-wrap board) which may only be an additional register for the board, but has yet to be determined (see the 40' Computer Hardware manual for schematics).

### Timing

There are very strict timing diagrams relating to the flow of messages to and from the computer and SIB (pg. 8, VLBA SIB Manual). These show that all five bytes which must make up one command or data request to the SIB are received within 1ms. However, it has been demonstrated with an SIB test box that the board will respond with as much as 1ms *gaps* between each of the five bytes (a total time of over 5ms).

### Alternative to a New SIB

A possibility of making the newer Windows based control software function without installing a new SIB or attempting to write a VxD (which could be used to bypass the protocol converter box), is to reprogram the PCB. It would need to be programmed so that it outputs at 1200baud instead of 57.6kbaud. This can be done by simply editing one line of the C program stored in an EEPROM on the protocol converter card, inside the box, and recompilation (the Borland C++ 3.0 compiler has been demonstrated to work well). The process of reloading the EEPROM with the new program is not quite as straightforward, but is documented in the "MicroPC 5012 Control Card Users Manual" from Octagon Systems. This documentation, support disks, and technical help contacts are available at the 40' or from Frank Ghigo, who has worked with this system before. A 10-line multi-colored ribbon cable with a rectangular 10pin connector on one end (for COM1 or J4 connector on the PCB) and a DB-9 connector (9pin for COM1 on the computer) has already been made just for this purpose, but has not been attempted.

### RS-232 / 422 Converter

The original RS-232 to RS-422 converter has been replaced by a smaller module from B&B Electronics, which performs the same function. However, the pin-outs differ from the old and an adapter cable was needed and made (but needs to be redone--see the 'suggestions' section). This converter also requires an external power supply, which comes from a small plug in the side of the converter and runs to a 12VDC power converter plugged in the wall.

### *Summary:*

- the MCB interface is confusing--the protocol converter box itself was a result of the realization of this difficulty (and each one cost about \$1800)
- the PCB was only intended (at the 40') to be used for a Windows application, where parity switching in midstream (especially at a high baud rate) is difficult
- an SIB test box can be obtained from Tim Weadon to rule out failure of the SIB
- the C program that came with the PCB has proven to be a good test (when running on the controller computer) as to if the SIB is responding properly, and also to emulate the PCB during debugging and testing of the code in case the PCB is to be reprogrammed

Changes to the 40' Telescope  
Greg Holsclaw  
1996 NRAO Summer Student

- as of now, the old Pascal software cannot be recompiled (for reasons unknown) for working use at a higher baud rate (e.g. 57.6kbaud), so the SIB cards (PDSET 5 and 9) will need to be swapped out if an interface with the PCB is desired

## **SOFTWARE**

### Current Software (written in Turbo Pascal)

The old Pascal software can, in fact, be compiled given the following restriction (for reasons unknown): it does not use or call procedures in the file TESTTASK.PAS. The main routine, 40.PAS only calls procedures from this file twice. If these two lines are commented out (lines 185 and 186), and TESTTASK is eliminated from the include block (line 128--a space after the beginning brace will do), the entire program can be compiled. This was tried using the Borland Turbo Pascal 7.0 compiler (two things need to be done before compilation: set 'var-string checking' to RELAXED and 'numeric processing' to 8087). Of course, this means that the task-file capability of the program will not be functional, and will eventually need to be remedied, but it is a good starting point in the debugging or upgrading of this code.

### New Software (written in Delphi)

The new Delphi software appears to have been written from the top down (in a previous summer to this one). That is, from the user interface down to the low-level serial communication. When serial communication was then attempted, many problems were encountered. The entire file MCBIO.PAS will probably need to be rewritten, using the new serial component which was found on the internet (as Delphi does not come with any default serial objects). It is this same serial communications object (found in C:\DELPHI\SERLCOMM\, but should already be installed on the Delphi Component Palette) that is used in the I/O test program, IOTEST (located in C:\DELPHI\NOTEST\). This can be used to make sure the software is working as expected, in addition to checking that the hardware is responding correctly. Another excellent method of checking communications is to borrow a digital oscilloscope, and put one channel on the Tx (transmit) line and one channel on the Rx (receive) line of the of the RS-232 connection.

## SUGGESTIONS

### Hardware

- The SIB will need to be mounted on some insulated spacers, as it is now just laying on the chassis of the motor control box, and some of the printed circuit board traces may come into contact and short out.
- A new adapter cable should be made, running from the output of the RS-232 / RS-422 converter to the cables from the SIB. Since it is a differential input (RS-422) the signal lines Tx+ and Tx- will need to be twisted together. So will the pair, Rx+ and Rx-. There are cables made just for this purpose, all pre-twisted and includes a ground line.
- It will be useful for later work if the undocumented circuitry on the computer interface card is traced out and documented.

### Software

- Despite the success of the Delphi test program in controlling the telescope, the old software should probably be worked on so that it is compatible with the new hardware (specifically the new SIB, but probably not the PCB).
- However, the test program revealed that Delphi, the PCB, the new SIB, and the ID-Byte circuit can all work together to control the telescope. Now it will only be a matter of integrating the new serial component and these hardware changes into the already existing Delphi control program, TMACS40.
- This integration will take effort, but is certainly not unreasonable. The new software has many benefits, including an attractive user interface, reliability, and a high potential for improvements/upgrades.

# **North Pole Transient Search**

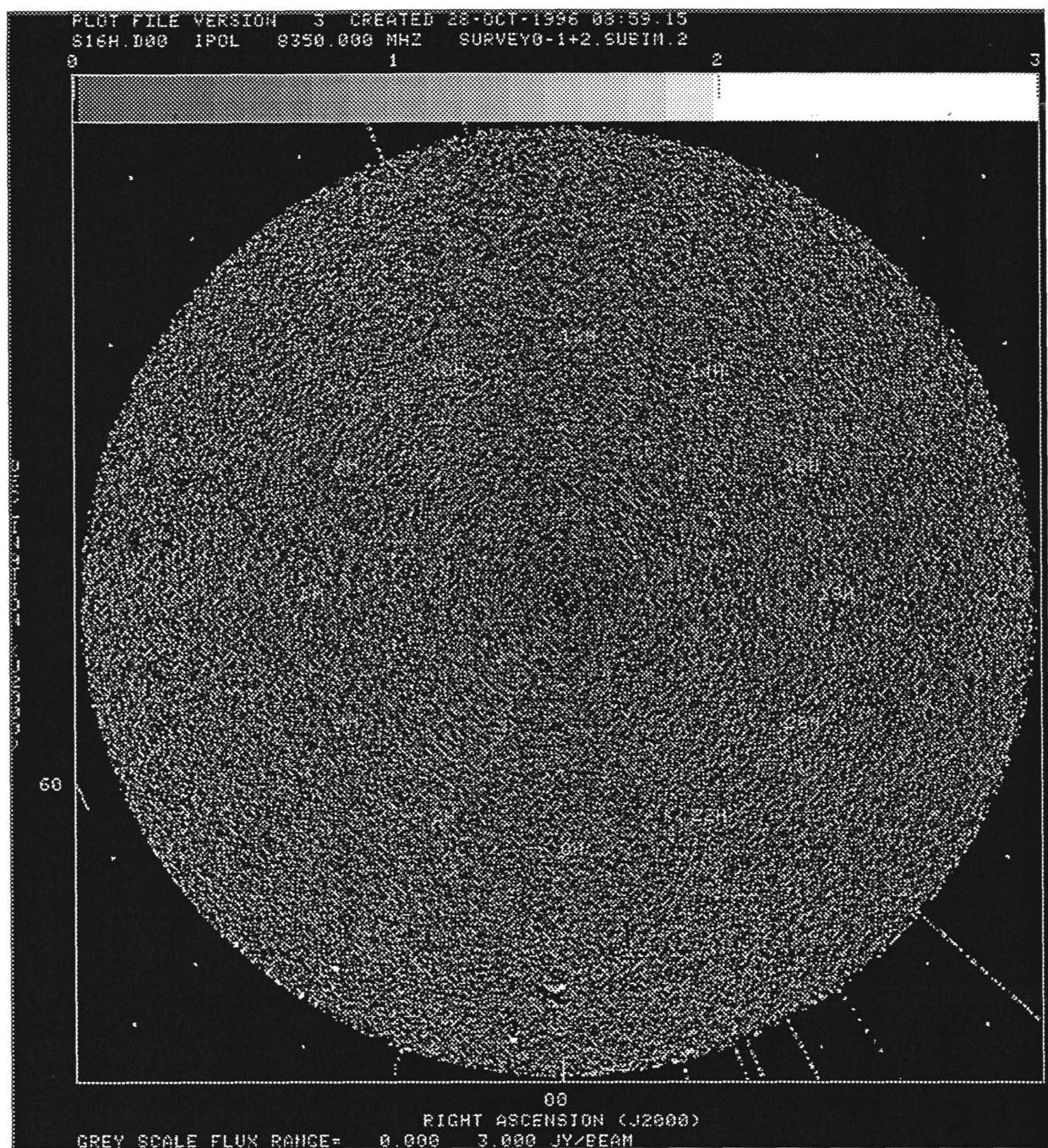
**Julie Zuber, Oberlin College**

**Glen Langston, NRAO**

## **Abstract**

During 1996 May, June and July, we monitored the sky north of 62 degrees declination at 8.35 GHz, searching for transient radio sources. After extensive editing to reject data taken during bad weather, a total of 119 hours of observations were obtained. During these times all sources brighter than 11.4 Jy were detected (10 sigma limit). A total of 3 known radio sources are found in this region, and 5 transient radio source candidates were detected. The nature of these sources is discussed.

## Introduction



The first radio source surveys have shown that the universe is evolving (Ryle 1968 and references therein). It is well known that although the radio sky is mostly constant, some radio sources vary on short time scales. It is observed that sources vary earlier and to greater degree at higher frequencies (Kellerman and Pauliny-Toth 1968, Clements et al. 1995). However, the duration of extragalactic radio sources variations observed is much longer and smaller in magnitude than is seen in higher energy events, such as gamma-ray bursts. Detection of bright but short lived, non-repeating, astronomical radio transient sources is limited by primarily by weather and by man-made interference. Reliable detection of transient events requires careful examination of the data to exclude a wide variety of man made effects.

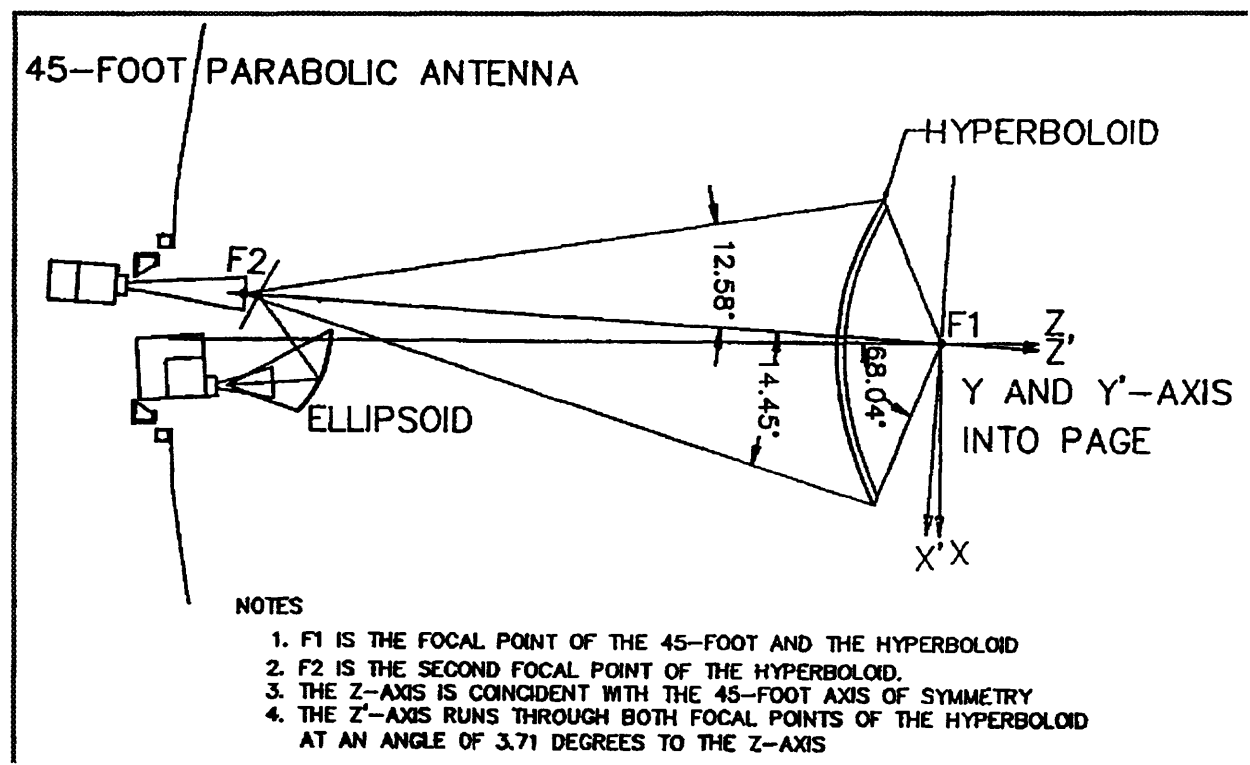
We have started a series of observations intended to place limits of the number of short lived radio transients. The north polar region of the first survey is shown in the figure above. The SVA survey presented here is the first of a series of all northern sky surveys to detect sources variable on the time scale of weeks. The SVA survey is also the first complete survey of the northern sky at 8.35 GHz (X-Band), 14.35 GHz (Ku-Band) flux densities are given for sources detected at

X-Band. This survey uses the NRAO/NASA/JPL Green Bank Earth Station, recently re-ferbished to track space radio telescopes, as a part of a orbiting VLBI (OVLBI) network. The tracking station in Green Bank is funded by NASA, to support the Japanese VSOP and Russian RadioAstron satellites to be launched in 1997/1998 (Hirabayashi, 1995, Burke, 1995). Initially, it was planned that the SVA survey would report flux densities at both X and Ku bands simultaneously, however bad weather and hardware problems have made it difficult to obtain simultaneous Ku data for all times when X band data were obtained.

## ANTENNA and OPTICS

D'Addario et al. (1992), described the design of the the OVLBI Green Bank Earth Station (GBES). Here, the properties relevant to astronomical surveys are described. The GBES is required to support satellite links in both X- and Ku-band in support of the Radioastron and VSOP missions. The tracking station utilizes cryogenically cooled front ends with dual circularly polarized feed horns at both X- and Ku-bands. The antenna optics are arranged to allow simultaneous observations at both bands of a single location on the sky.

The optics geometry is sketched in the figure 2, below.



The primary reflector is a 13.7m parabola (M1), the secondary is a hyperbolic subreflector of approximately 2m diameter (M2). The X-band feed horn illuminates the subreflector directly; ideally all its energy passes through the tilted Frequency Selective Surface (FSS, labeled M3) which is placed in front of it. The Ku-band horn illuminates the subreflector via a double reflection off of an offset ellipsoid (M4) and the FSS.

The magnification (M) parameter of a Cassegrain antenna relates the focal length of the primary reflector to the equivalent focal length of the Cassegrain system. The relatively high value of  $M=5.70$ , in the optics system reduces spurious beam squint to a negligible level.

The radome sits above the vertex ring, and encloses the feeds, FSS, and ellipsoid. The radome is a sheet metal hexagon with an outer diameter of approximately 1 meter. The top of the radome is covered with a sheet of woven-Teflon based radome material. Due to the fact that there are four surfaces that could get wet, the ellipsoid, FSS, and the two horn windows, it was decided that a radome covering of the optics would provide many benefits. First, loss will be reduced in wet

weather conditions, since there will be only one layer of water for the signal to pass through. The loss is not comparatively worse in dry conditions, since the radome material can be made thin and have extremely low-loss ( $< 0.01$  dB). Also, Teflon-based radome laminates are naturally hydrophobic, so the effect of rain will be lessened. Finally, enclosing the vertex optics has the benefit of allowing environmental control, which reduces the effects of temperature on the FSS and ellipsoid.

## OBSERVATIONS

The observations presented here were made during between 96 May 01 and 96 June 30, but were frequently interrupted due to weather and development work in preparation for the space VLBI mission. The survey observations are carried out with the telescope in "transit mode", with azimuth near 0 or 180 degrees from north. The sky is scanned in a "raster mode" common for single dish surveys (eg. Langston et al. 1990), taking data while moving the antenna up or down in elevation.

The declination range is scanned continuously moving the telescope in elevation at a constant rate of  $28^\circ$  per minute north and south. At the end of each 1 minute scan, 1.5 seconds are used for calibration of the system gain. The second declination range is scanned in 2 days, again taking data in 1 minute scans, while scanning moving the antenna in elevation at a rate of  $26.8^\circ$  per minute. The start local sidereal time of the scans two days are offset by 30 seconds, so that regions missed in one day are scanned in the next. The third declination range is observed in 7 days, with the antenna at 180 degrees azimuth. Each scan in the third region has a duration of 160 seconds, with calibration performed when the antenna is pointed near zenith. During all scans in all declination ranges, the antenna moves slightly in azimuth, to follow a constant right ascension for each scan. Data are recorded every 0.125 seconds for sky frequencies of 8.35 and 14.35 GHz for both left and right circular polarization. The intensities were measured. for 500 MHz bandwidths.

## CALIBRATION AND ANALYSIS

The data are written in "RAW archive" FITS format tables at the end of each scan. The raw data recorded are the azimuth, elevation, local sidereal time, and 4 channels of antenna temperature in Kelvins. The "RAW archive" table also records the offset between station and GPS time, and weather information. The data were written to FITS files in 1 hour segments. The raw archive data intensities were recorded in Kelvins of system temperature as a function of antenna elevation. The system temperature measurements were calibrated by injecting a calibration signal into the front ends, and synchronously detecting this signal at the detectors.

After a day of observations, the "Raw archive" data are calibrated and the angular coordinates are converted to Right Ascension and Declination (J2000). The calibration process also includes extensive data flagging, to remove the

- (1) sun and moon,
- (2) jumps in the baseline data due to intermittent hardware problems,
- (3) tests on the sky and system temperature values to reject bad weather and,
- (4) rejection of entire scans if the RMS signal level exceeded tolerances.

The process of removing the sky and system temperature contributions to the measured signal is illustrated in figures [3](#), [4](#), [5](#). The raw X band LCP signal level for a scan containing radio source 3C58 is shown in figure [3](#). The sky and system temperature were removed from the input data by fitting a simple system temperature plus sky model to the raw data and subtracting that model from the data. The fit was made for each band and polarization separately. The result of subtracting the sky model is shown in figure [4](#). Next, for all data in each scan, the median was

calculated for all data points with 30 arc minutes of the central point. This median was subtracted from the data. The result of this processing was to leave a nearly flat scan of the sky with occasional radio sources, as is shown in figure 5.

A number of attempts were made to automatically flag data. The entire scan was discarded if the RMS noise in the scan exceeded 0.01 Kelvins after this processing. If the sky + system temperature value in any data point in a scan exceeded 100 Kelvins, the data point was discarded.

Antenna pointing corrections are calculated offline. During the data calibration process, the data are converted into "Single Dish FITS" format so that further processing may be done using the Astronomical Image Process System (AIPS).

Each day of observation is gridded onto a image using the AIPS task SDGRD, which allows a variety of image projections and data convolution options. The SVA data were grided onto images with 3.4 square arcminute pixels, using a Gaussian convolving function with 7.46 arcminute full width at half maximum.

The data are visually examined for uniform quality; bad weather data are easily recognized by "stripes" of high noise along strips of declination. If any data were bad in a one hour segment, that segment was discarded.

After all one hour segments of the survey are completed, the final images were produced. These images were examined by eye in AIPS to select all sources with flux density per beam greater than 11.4 Jy. A Gaussian fit is made to each maxima in the images and the coordinates and peak flux densities are recorded. The flux density scale was set by observations of the bright radio source 3C286, with a Baars et al. flux density of 5.20 Jy at 8.35 GHz.

After the source list was completed, the sources were identified by comparison with an updated version of the Dixon (1970) source list and Becker et al. 1991 source list based on the Condon et al. 1989 survey of the sky at 6cm.

For all sources detected in this manner, the raw data scans were examined for baseline problems and other signs of hardware problems. Sources were kept only if they visible in both X and Ku bands and both Left and Right circular polarizations of these bands. Otherwise the data for the entire hour was discarded.

## SOURCE LIST

The SVA source list consists of 6 columns, (1) Source Name, (2) Right Ascension, (3) Declination (J2000), (4) Flux Density (Jy) at 8.35 GHz and (5) Notes.

If the source is previously detected in the 3CR, Westerhout (1958), or Dixon (1970) catalogs, that source name is listed. If the source is unidentified, the source is given the IAU style, name with the prefix SVA.

The sources are identified based on their location measured in the SVA survey being within 9 arc minutes of a published radio source location. For a few sources near the galactic plane, when the source appeared extended, the angular distance criteria was extended to 15 arc minutes.

RA (J2000)	DEC (J2000)	Intensity (Jy)	Name	Date/Type (DDMMYY)	Note
00 00 40.605	67 24 58.70	28.1	W1		HII region
00 25 18.797	64 09 10.63	26.1	3C10	SNR	Remnant of 1572
02 05 44.950	64 47 33.45	49.4	3C58	SNR	Remnant of 1181
09 33 38.405	87 34 33.94	29.5	SV=155.3	280596	Transient
10 48 22.903	74 02 14.35	18.3	SV=96.5	240596	Transient

10	56	39.065	76	50	48.39	12.3	SV=64.8	310596	Transient
22	33	55.976	82	52	19.04	23.8	SV=125	040596	Transient
23	13	5.111	75	06	13.38	79.2	SV=417	110596	Transient

## Transient Events

During the SVA survey observations, a large number of transient events were detected, but few events met all selection criteria. No events were selected unless the events were detected in both X and Ku band, and unless the events showed similar brightnesses in both polarizations of each band. This selection criteria should remove all known satellites and many types of hardware errors intrinsic to the tracking station electronics.

All events were rejected unless the data were taken during good weather, and all scan data taken immediately before and after the events were of good quality.

Initially it was planned that all transient events would be rejected unless the measured points of the event within the scan were well matched to the antenna beam shape, as would be expected for transient radio sources which varied slowly during the 1 second the antenna beam crossed the source. However, this criteria rejects very rapidly varying sources and sources seen in the near sidelobes of the antenna beam. Since the sidelobes cover a few times the angular area that primary beam covers, it is much more likely to detect a short lived transient source in a sidelobe than in the main beam.

## DISCUSSION

The first large area survey of the sky at 8.35 GHz has been presented. The data from this survey is useful for placing limits on the number of short lived radio sources. Several intriguing transient radio sources were also detected in this survey. Further observations are needed to determine the nature of these sources. The requirement that the sources be detected in both polarizations and both bands strongly suggests the sources are external to the antenna and electronics. However a number of terrestrial explanations are possible. These include birds, planes or satellites. Assuming that the 5 transients represent an upper limit to the number of transient radio sources, then transient rate for sources with total time duration of 1 day is  $N(S > 11.4 \text{ jy}, \tau = 24 \text{ hours}) < 1.34 / \text{str/day}$ .

This research was supported by the National Radio Astronomy Observatory operated by Associated Universities Incorporated under a cooperative agreement with the National Science Foundation. This research has made use of data obtained through the High Energy Astrophysics Science Archive Research Center Online Service, provided by the NASA-Goddard Space Flight Center.

## REFERENCES

Baars, J. W. M., Genzel, R., Pauliny-Toth, I. I. K., and Witzel, A. 1977, *A&A*, **61**, 99.

Becker, R. H., White, R. L., Edwards, A. L. 1991, *A&J*, **75**, 1

Burke, B. F. 1995, *A&A*, **27**, 850.

Clements, S. D., Smith, A. G., Aller, H. D., and Aller, M. F. 1995, *A&J*, **110**, 429.

Condon, J. J., Broderick, J. J. and Seielstad, G. A. 1989, *A&J*, **97**, 1064.

D'Addario, L. R., Hudson, R., Meinfelder, E., Shillue., W., and Varney, D. 1992, ``The Green Bank Earth Station Project: Report on the Detailed Design Phase", NRAO, Green Bank, WV.

Dixon, R.S. 1970, \apjs, {\bf 20}, 1.

Hirabayashi, H. 1995, \baas, {\it 27}, 850.

Kellerman, K. I., and Pauliny-Toth, I. I. K. 1968, \araa, {\bf 6}, 417.

Langston, G. I., 1990, \apjs, {\bf 72}, 621.

Ryle, M. 1968, \araa, {\bf 6}, 249.

Shillue, B. 1992, ``Measurement Results of Sandwich FSS," NRAO OVLBI Memo \#26.

Westerhout, G 1958, Bulletin of the Astronomical Institutes of the Netherlands, {\bf 14}, 215.



# REU '96 Summer Work Report

Ryan McCowan

August 2, 1996

In this report, I will detail my work with the GBT laser metrology project. I will describe problems and their resolutions, discuss experimental results, and offer suggestions for software improvement. I would like to thank the Observatory for giving me the opportunity to work on this challenging and innovative project.

After researching and correcting a number of hardware problems, experimentation began at the 140-foot telescope. In summary, it was a success and denoted good progress. In the longest test period, the four laser rangers scanned five retroreflectors at various locations over an eleven hour period from noon to late evening. The test included determining the feasibility of using a long path length to a reflector for use as a refractometer.

Each laser unit measures a short reference path inside the instrument to calibrate slow drift of the zero point due to heat and other factors affecting the phase of the oscillation electronics. Typically, this drift is proportional to and varies directly with temperature, at least to a first-order approximation. The data from ZY10 (Fig. 1) and ZY11 (Fig. 2) bear this out. However, an unusual and unexplained phenomenon was observed in the data from ZY12 (Fig. 3) and ZY13 (Fig. 4). Both showed a sharp increase

in the reference signal phase at approximately the same time. It is speculated that this could be caused by the position of the sun or the shade of the telescope creating a large temperature gradient between the pairs of laser units. The cause of this change could likely be found with ease by simple observation of the site at the time in question.

By measuring the same path with two different lasers, one can determine the instrument-to-instrument consistency of measurements. This was performed with ZY10 and ZY13, over a path length of approximately 93.9 m. The instruments exhibited satisfactory consistency, with both of the distance measurements changing in sync with each other and inversely proportional to the temperature (again, to a first-order approximation). Data from this experiment are shown in Figs. 5 and 6. Measurements of this type can also be used in refractometry to determine the index of refraction of the atmosphere on a local scale, but noise and other interfering factors would be a greater hindrance to accurate measurement, producing a higher degree of error than would be exhibited by a longer path length. It would be difficult to account for extremely local changes in atmospheric condition caused by the position of the telescope and shading from the structure or main reflector.

For the long-path refractometer, the results were very encouraging. However, ZY10 was the only instrument that could reliably get return energy from the reflector, situated on a hillside almost 1000 m away (Fig. 7). Because of their position, ZY11 and ZY12 do not have a clear line of sight to the refractometer reflector. After manual intervention and testing, ZY13 was able to get a return from the reflector in subsequent tests (Fig. 8). These results are encouraging because the instruments have demonstrated the ability to measure distance accurately over a long path length and the results from this long path length are consistent with theoretical models. The lower noise (as a proportion of actual distance) and “low-pass filtering” of the long distance produce a smooth curve which can be used to produce an accurate, instantaneous index of refraction for the atmosphere with regard to local conditions. Using this measurement would be preferable to using an index of refraction calculated from weather instruments. The refractometer

measurement is an instantaneous indicator of the index of refraction; the weather instruments exhibit a delay in reflecting actual weather information because the mass of sensor probes has a dampening effect on their measurements, limiting the rate at which they can change. In contrast, the refractometer calculates an index of refraction by measuring the wavelength of the modulated laser signal, which changes instantaneously with atmospheric conditions.

In summary, the operational tests at the 140-foot are encouraging. They represent progress and help solidify the previous proof-of-concept experiments, and have also provided valuable insight on installation and start-up concerns.

This summer's testing also provided an opportunity to evaluate the design and reliability of the ZIY control software. It gained a number of new features, including the ability to point any number of laser units in unison, useful for checking calibration and verifying survey data.

A formidable task lies in processing the large amount of data collected in these experiments. Useful processing of the data, which requires importing the data into a spreadsheet, formatting it, and generating charts, often requires a full man-day or more. A way to read the experimental data directly into the spreadsheet is being developed. It would allow the visual representation of the numerical data in near real-time, which would give the experimenter a method of easily correlating changes in the data with current observed atmospheric conditions.

Another aid to processing experimental data is reliable, real-time weather data. This would also help the experimenter relate data trends with atmospheric conditions and have the added advantage of simplifying data processing. This is a feasible and relatively straightforward programming task; it has not been implemented because of other, higher priority tasks, like the automation of data analysis.

Possibly due to pointing errors and any number of possible calibration errors, the lasers did not consistently see optimum return signal amplitude. An additional survey of the laser monuments around the 140-foot telescope is scheduled to determine if the unusually harsh winter changed the positions or orientations of the monuments from ground freezing and heaving. A “raster scan” function in the ZY or ZIY software to “home in” on the strongest return in a specified area would be useful to gather information on possible pointing and surveying errors.

The laser ranging program has made good progress this summer; I am glad that I could be a part of it. The experimental results are encouraging and continue to support our theories and provide us with ideas and methods for improvement. These suggestions should improve the usability and usefulness of the software for experimental purposes – it is planned that for the actual use on the GBT much if not all of the laser ranging functions will be completely automated with minimal operator interaction. I have enjoyed working on this project – it has been a challenging endeavor and has given me valuable experience in solving real-world engineering problems.

Fig. 1 Reference retroreflector for ZY10

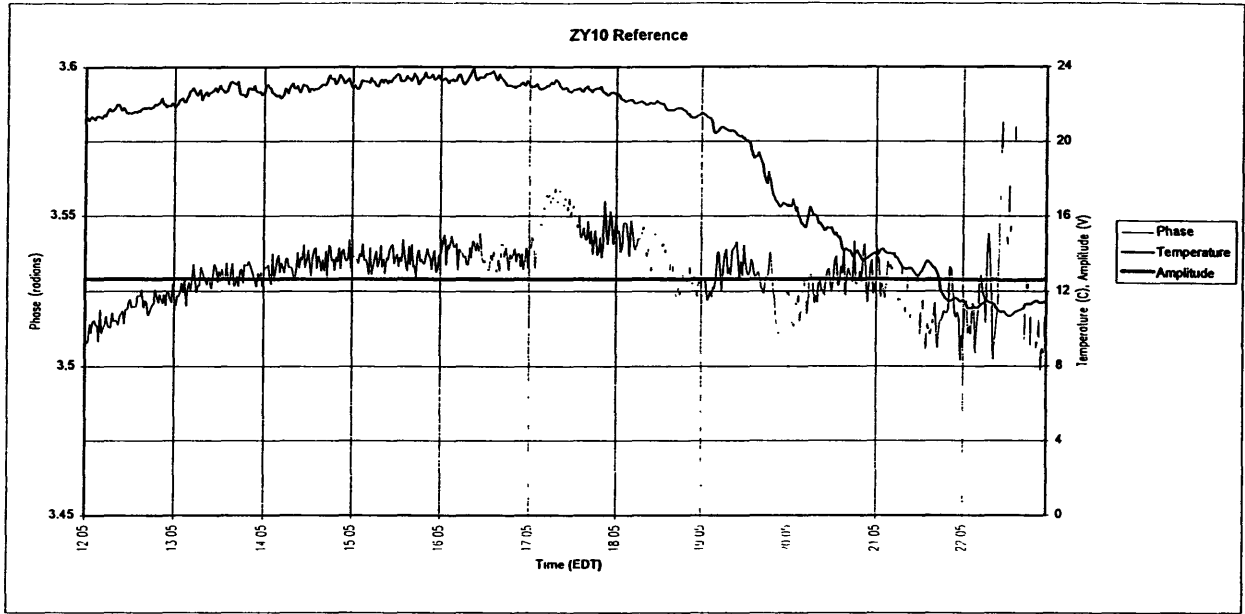


Fig. 2 Reference retroreflector for ZY11

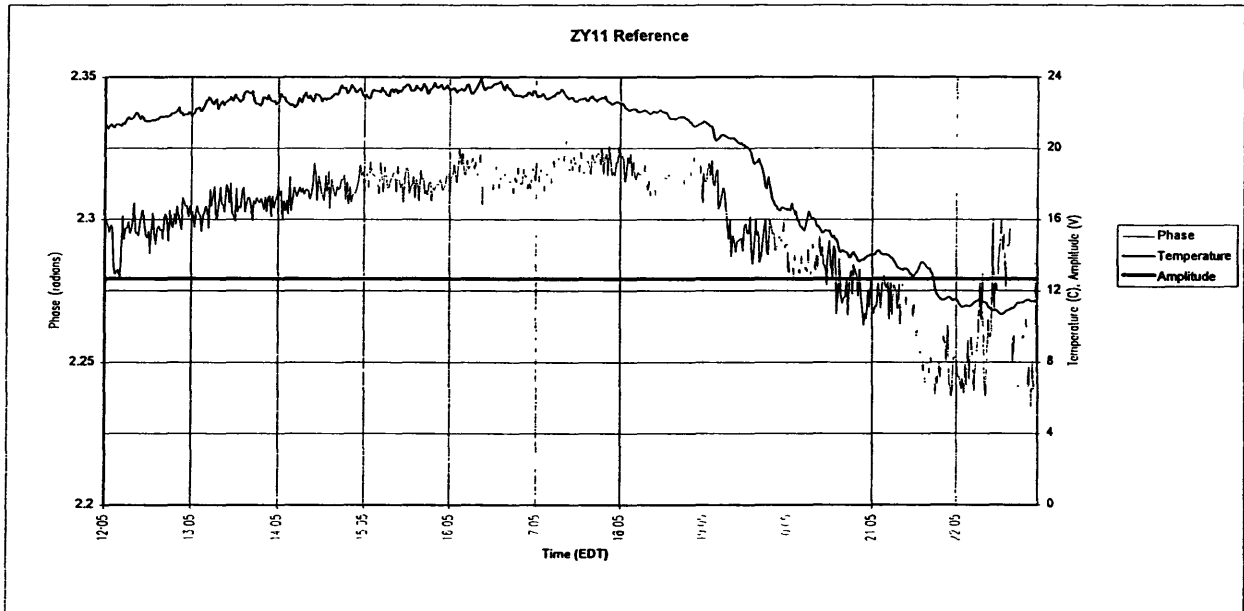


Fig. 3 Reference retroreflector for ZY12

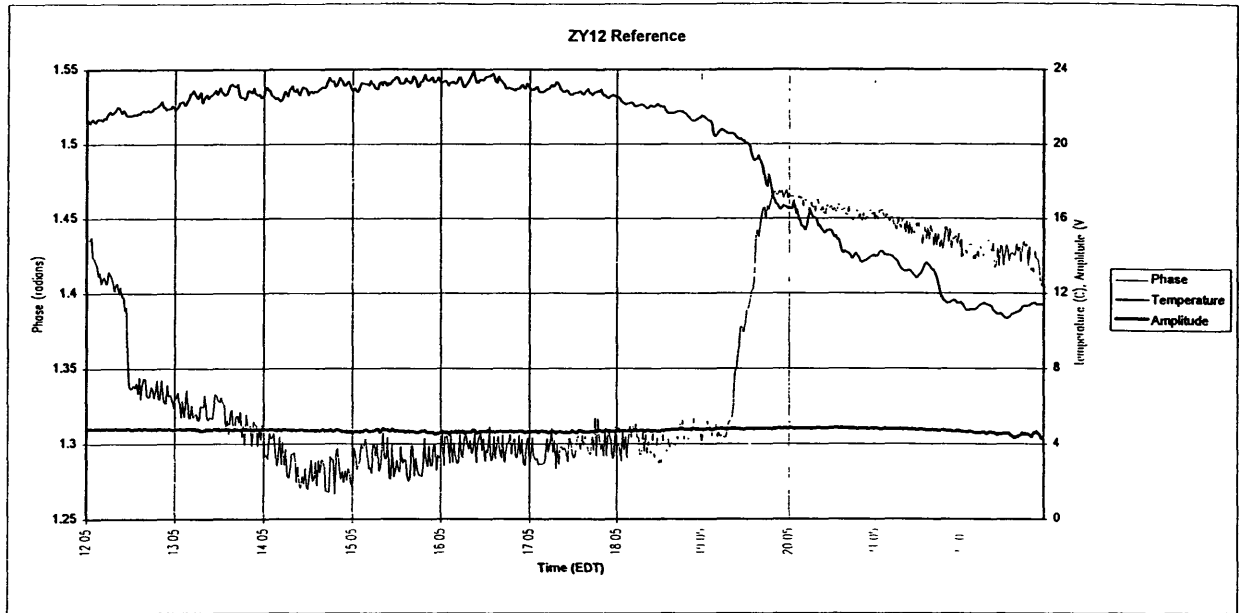


Fig. 4 Reference retroreflector for ZY13

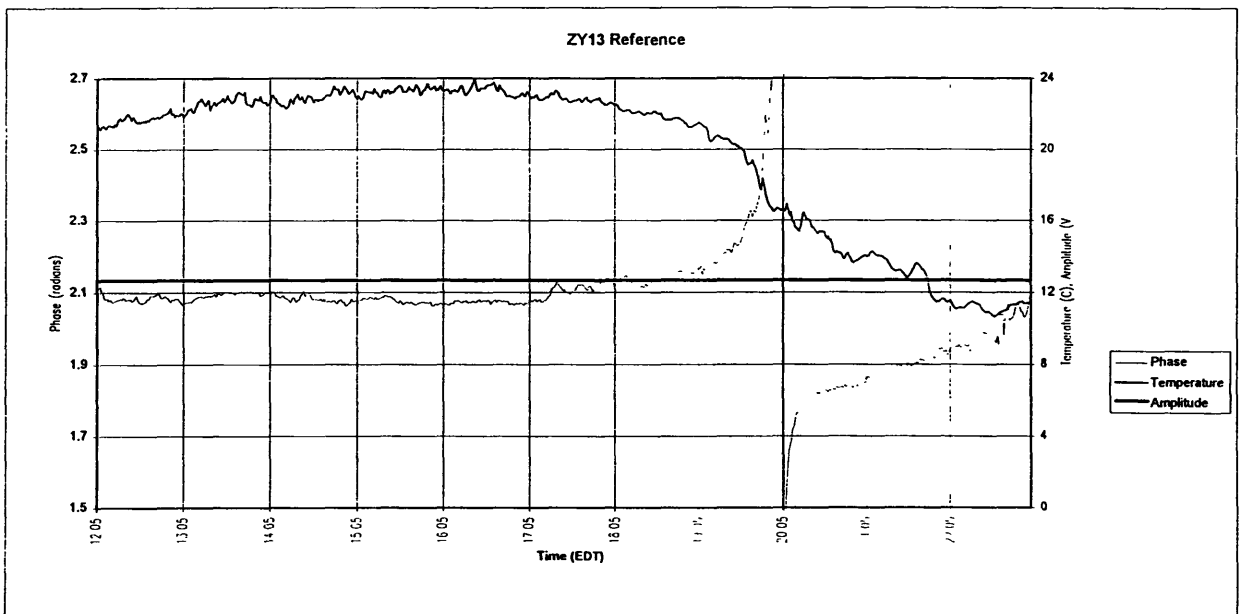


Fig. 5 laser ZY10 to retroreflector on ZY13

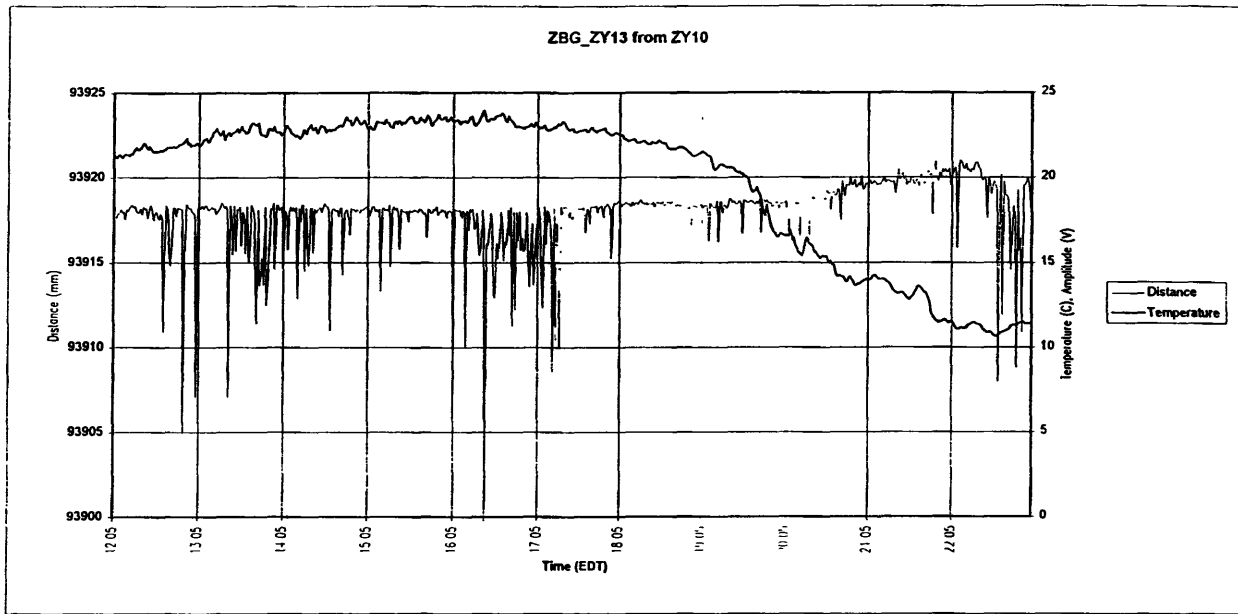


Fig. 6 laser ZY13 to retroreflector on ZY10

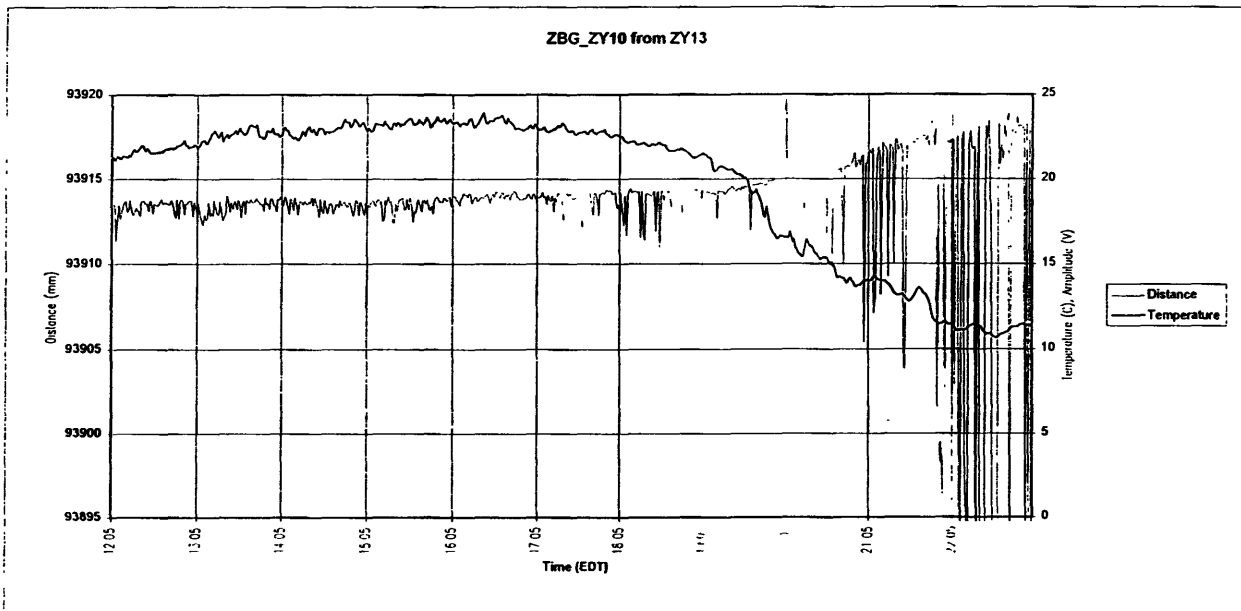


Fig. 7 Refractometer retroreflector from ZY10

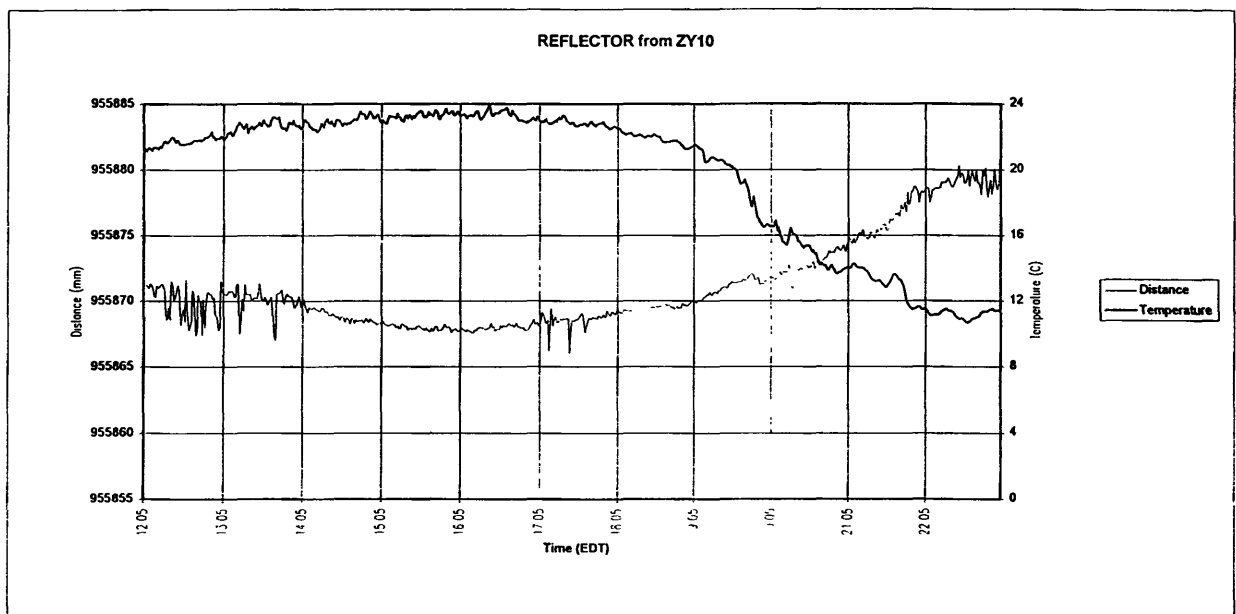
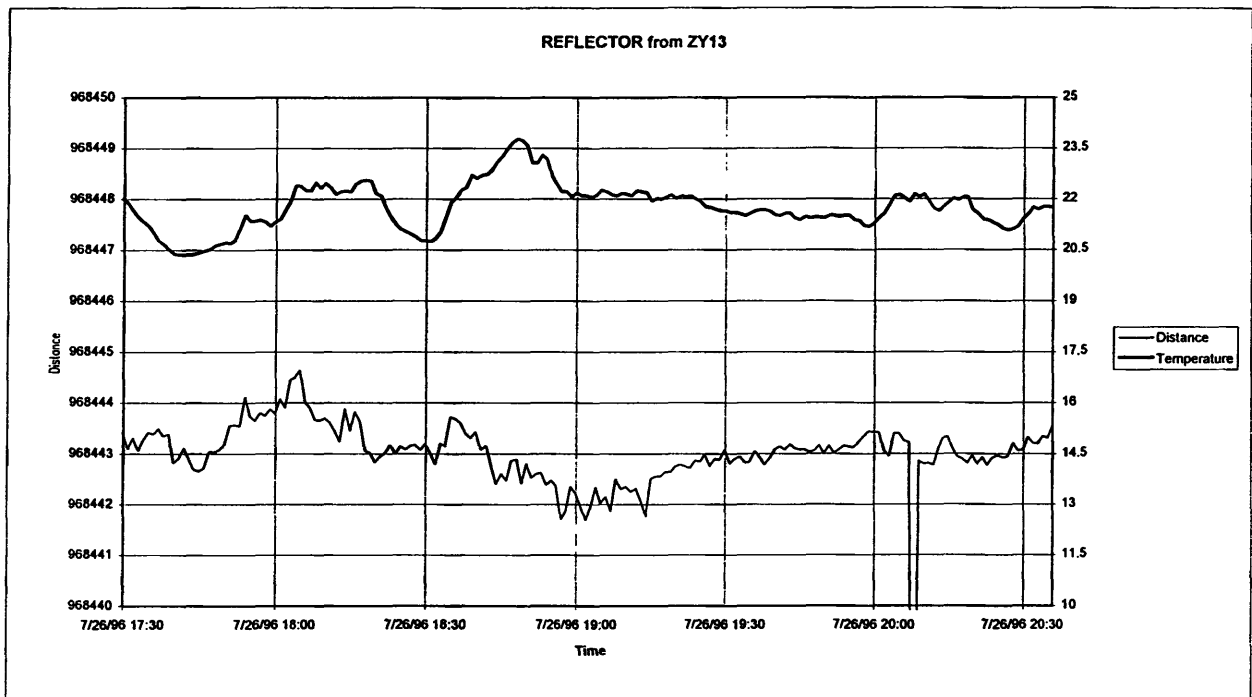


Fig. 8 Refractometer retroreflector from ZY13





# H66alpha Observations of M17-UC1

Olivia Johnson, Vassar College

Miller Goss, NRAO

Chris DePree, Agnes Scott College

## Abstract

We have observed the H66alpha line towards the ultracompact HII region M17-UC1 and toward the nearby arc-shaped structure to the east with an angular resolution of approximately 1". Toward the ultracompact source, we detect an unusually broad radio recombination line (RRL) with a full width at half maximum of approximately 47 km/s. We have integrated the H66alpha emission over several regions in the arc and have found that to within our errors the observed parameters of the line are constant throughout the arc. We have derived the physical parameters of the ultracompact source and the arc-shaped structure and we compare them with the values of Felli, *et al.* (1984, hereafter denoted as FCM). We discuss the source as an example of shock induced star formation consisting of a hot young massive star surrounded by ionized material resultant of a stellar wind outflow. We compare M17-UC1 with six other sources known to have unusually broad RRL emission.

## Introduction

M17-UC1 was first reported by Felli *et al.* (1980) as an "unusual point source in M17" with an estimated mean electron density exceeding  $10^6 \text{ cm}^{-3}$  and electron temperature exceeding 25,000 K. The source is found in the upper portion of M17's southern bar, lying between molecular material to the near west and an arc-shaped ionized structure to the east. Assuming a distance to the nebula of 2.2 kpc, the diameter of the nearly spherical ultracompact HII region is approximately 0.006 pc. It is positioned approximately 0.2 pc from the concave edge of the arc. Emission from the arc at 1.3 cm is well defined over an area ranging approximately 0.04 pc in the northwest direction and 0.01 pc from east to west, though extended arc emission is observed by FCM over an area of 0.96 x 0.16 pc. These features reside in an environment dense with maser emission and other compact source objects; an OH maser (Knowles *et al.* 1976), an H<sub>2</sub>O maser (Genzel and Downes 1976), a 10.6 micron compact source (Harper *et al.* 1976), and a 5 GHz compact source (Matthews *et al.* 1979) are all within approximately 0.4 pc. A multiwavelength (1.3, 2, 6, and 21 cm), high resolution study of M17 was carried out by FCM in which significant attention was paid to the UC1/Arc region. They determined the continuum spectrum to continuously rise, with a spectral index of approximately 1.1, between 1.5 and 23 GHz. The conclusion of their investigation modeled UC1 as a shell type HII region fueled by outflow from a young massive star. FCM further postulated that the arc structure was an edge-on ionization front (I-front) heated by a heavily obscured star cluster 0.7 pc to the northeast (Beetz, *et al.* 1976) and that the shape of this I-front focused its preceding shock front at the position of UC1, inducing the formation of the hot young star which ionizes the ultracompact source.

Over the past decade a handful of radio sources have been identified which exhibit unusually broad radio recombination line (RRL) profiles (DePree *et al.* 1996a; Gaume *et al.* 1995; Shepard *et al.* 1995; DePree *et al.* 1996b). While average RRL linewidths have full width at half maximum (FWHM) ranging from about 20 to 30 km/s, these broad line sources have FWHM ranging from about 45 to 180 km/s. Additionally, the majority of the sources known exhibit continuously rising continuum spectra with spectral indices ranging from 0.6 to 2. As pressure broadening is negligible at high frequencies, these broad lines are indicative of kinematic phenomena; the rising spectral indices further support the interpretation of the broad lines as signifiers of large scale motion of ionized material, such as stellar wind outflow from massive star. Indeed, most broad line sources appear to be, with varying degrees of certainty, caused by ionized outflow from young high mass stars. This paper provides the first RRL data on M17-UC1, identifies it as a broad line source of the type described above, and applies this new data to discussion of both its origin and its relation to other broad line sources.

### Observations and Data Reduction

A total of 11 hours of observations in two Very Large Array (VLA) configurations were used to image UC1 and the arc in the H66alpha line and in the 1.3 cm continuum. Parameters of these observations are presented in Table 1. Our continuum data sets were flagged individually, combined, and phase self-calibrated using the AIPS software package of the National Radio Astronomy Observatory (NRAO). These calibrations were then applied to composite line data set. Continuum subtraction was achieved by fitting channels free of line emission and subtracting the continuum thus formed from the line data. The UV data were then imaged with the IMAGR task. The parameters of these images are listed in Table 2.

Table 1. Observational Parameters

VLA Array	Observation Dates	Total Observation Time
DnC	24, 26 Jan. '95	11
C	24 Mar. '96	2
R.A. (1950) = 18:17:31.39		
Dec. (1950) = -16:12:58		
LSR Central Velocity = 18 km/s		
Total Bandwidth = 25 MHz		
Number of Channels = 16		
Channel Separation = 1562.5 kHz		
Velocity Resolution = 21.3 km/s		
Rest Frequency = 22364.167630 MHz		
Flux Density Calibrator: 3C286		
Phase Calibrator: NRAO 530 (1730-130)		

Table 2. Image Parameters

FWHM of synthesized beam = 1.24" x 0.98"  
Position Angle = 16 deg.  
Continuum RMS Noise = 3.7 mJy/beam  
Line RMS Noise = 0.91 mJy/beam

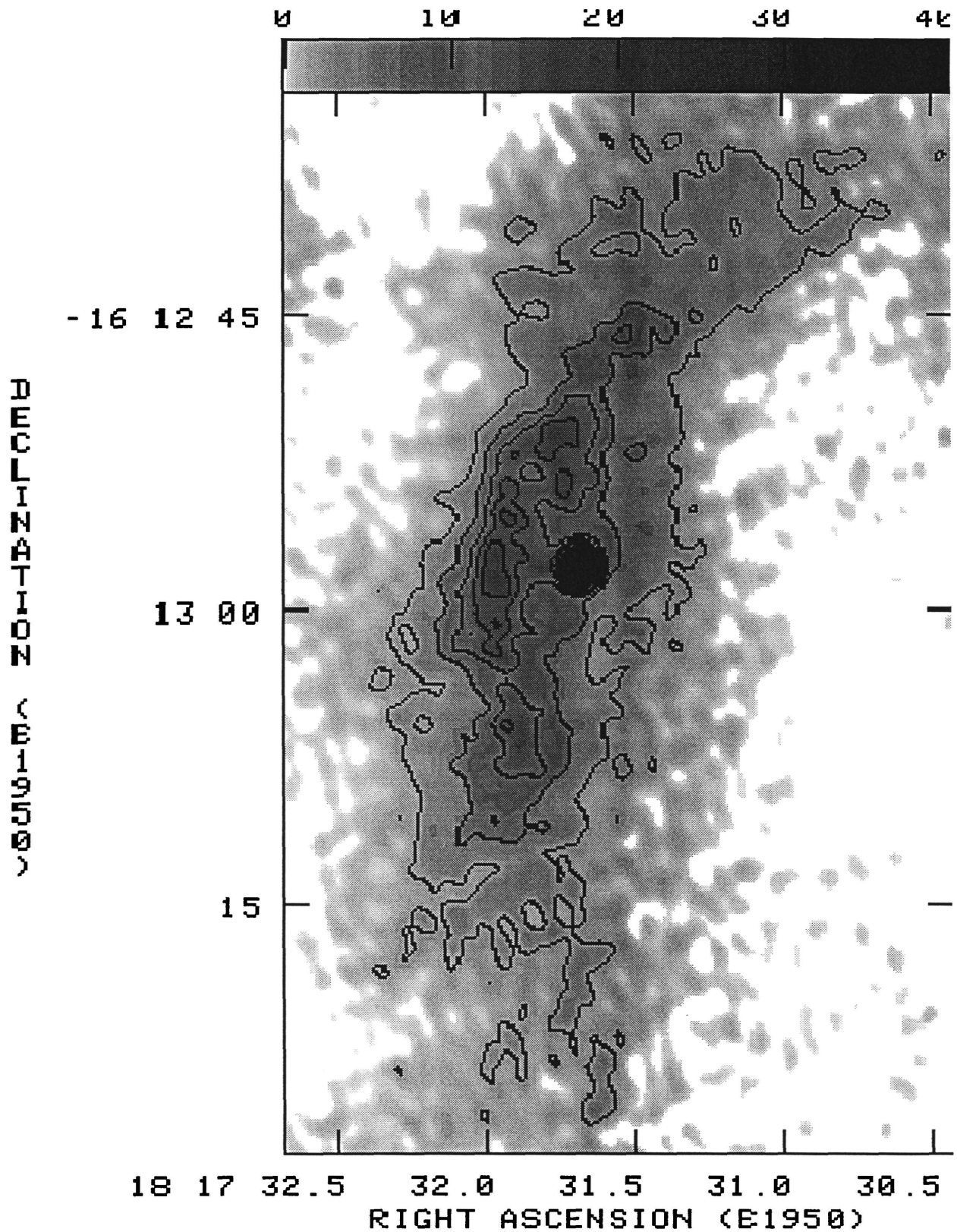
Integrated H66alpha line to continuum profiles and Gaussian fits to these profiles were made using the PROFIL and PROFIT tasks of the Groningen Image Processing System (GIPSY). Parameters of these fits appear in Table 3 .

Table 3. Gaussian Fits to H66alpha Line to Continuum Profiles

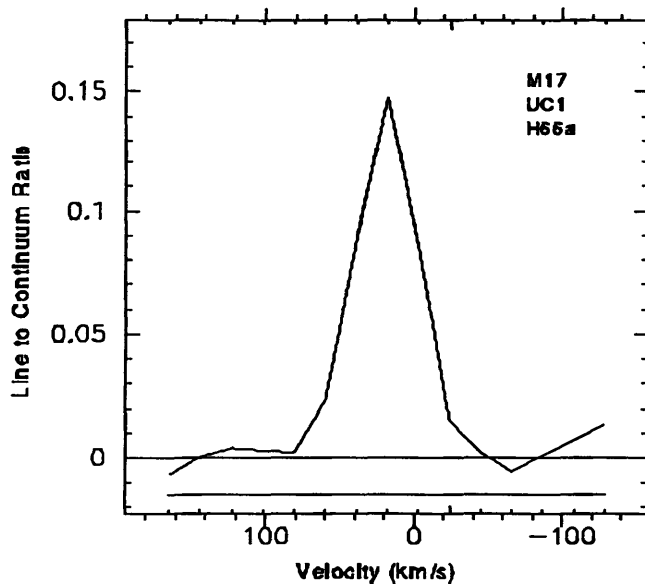
Structure	Tl/Tc	VLSR (km/s)	$\Delta V$ (km/s)	continuum flux (Jy)
UC1	0.146 +- 0.009	18.7 +- 0.82	47 +- 2.1	0.24 +- 0.007
ARC	0.17 +- 0.02	16 +- 1.2	36 +- 2.5	0.616

## Results

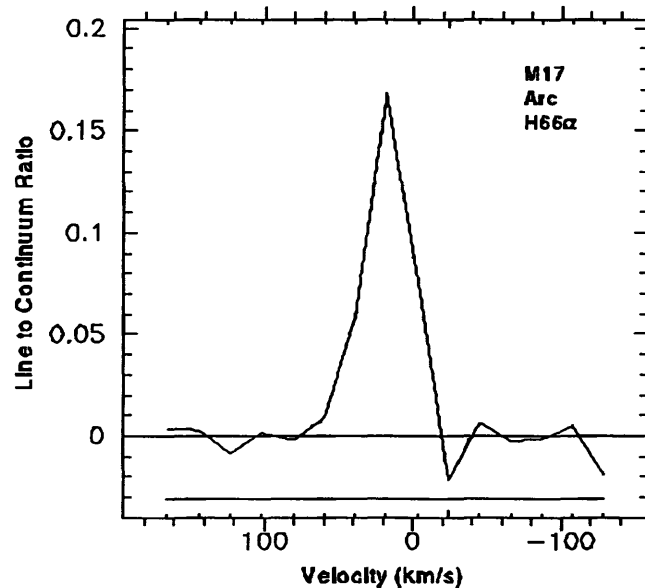
A 1.3 cm greyscale map of UC1 and the arc is presented in Figure 1 . The beam size is 1.24 x 0.98" (PA = 16 deg.). Gaussian fits to the integrated H66alpha line to continuum ratio profiles are shown for UC1 ( Figure 2a ) and the arc ( Figure 2b ). Parameters for both structures derived from the continuum and RRL data are given in Table 4 which lists total flux density ( $S_{\nu}$ ), linear



**Figure 1** 1.3 cm continuum image of UCL and the Arc structure, with a resolution of 1.24" by 0.98" (PA = 16°). Peak flux is 189 mJy/beam, with contours at 18.9 \* (0.2, 0.4, 0.6, 0.8, 1.0, 1.6, 3.2, 6.4, 12.8) mJy/beam.



size, continuum optical depth ( $\tau_c$ ), emission measure (EM), mean electron density ( $n_e$ ), LTE electron temperature corrected for continuum opacity effects ( $T_e^*$ ), non-LTE electron temperature further corrected for non-LTE effects ( $T_e$ ), excitation parameter ( $U$ ), and the number of ionizing photons ( $N_{Ly\alpha}$ ). From the derived  $N_{Ly\alpha}$ , we have calculated the type of the ionizing star for UC1 to be between B0 and B0.5 (Panagia 1973). The calculations followed the methods of Wood and Churchwell (1989), Mezger and Henderson (1967), and Roelfsema and Goss (1992). The values of  $b_n$  and  $1 - \beta_n$  were selected from the tabulation of Walmsley (1990).



Spatially integrated profiles of the H66alpha line were also examined for eight boxes of equal dimensions along the length of the arc, the positions of which are shown in Figure 3 overlaid on 1.3 cm continuum flux contours.

## Discussion

### UC1

Our VLA D array data has a continuum spatial resolution of approximately 1". A single component Gaussian fit to continuum emission from UC1 in this data set (made with the AIPS tasks IMFIT and JMFIT) describes the ultracompact source as a fairly uniform, nearly spherical object with a mean diameter of  $0.6'' \pm 0.04''$ . The calculated hydrogen mass of a

**Figure 2** Spatially integrated continuum weighted profiles for (a) UC1 and (b) the Arc. H66alpha line to continuum ratios are plotted versus LSR velocity.

sphere of pure ionized hydrogen of constant density the size of UC1, assuming  $n_e = n_H$ , is approximately  $1.5 \times 10^{28}$  kg (approximately  $7.5 \times 10^{-3} M_\odot$ ). In contrast, the total main sequence mass output due solely to stellar wind outflow from a B0.5 type star is approximately  $9.44 \times 10^{23}$  kg ( $4.7 \times 10^{-7} M_\odot$ ), assuming a main sequence wind energy of  $8.5 \times 10^{48}$  ergs. At the derived density of UC1 this mass would fill a sphere of radius approximately 1/12th that of UC1. Earlier data taken in the VLA A configuration with a spatial resolution of approximately 0.1" measures the diameter of UC1 to be  $0.4'' \pm 0.01''$  and begins to reveal a shell structure which is extended slightly to the NW in which the outer regions are about a factor of two brighter than the inner region (FCM). FCM's model of the shell source, which best fit their data with input electron

temperature and mean electron density in good agreement with those quoted in Table 4 , predicts a still smaller outer radius of 0.21". Yet, as FCM note, even accepting the lowest values for the radius, speculations that UC1 be solely due to massive ionized outflow from a high mass star (Simon *et al.* 1983) are effectively ruled out because the size of such an object would be an order of magnitude smaller than UC1.

Utilizing the formulations of DePree *et al.* (1995), we find an age for UC1, assuming a temperature of  $10^4$  K, a number of ionizing photons of  $10^{46}$ , and a ambient density of  $10^5$ , of approximately 100 years. Adopting a higher density, as DePree *et al.* suggest may be more appropriate for most UCHIIs, the age is recalculated to be approximately  $2 \times 10^3$  years. It seems unlikely that either age estimation is correct, and that calculation of the true age of UC1 may be complicated by other effects, such as which can extend the life of an UCHII. Our calculations do suggest however, that it is very likely that UC1 formed in an environment of density greater than  $10^5$ .

Our lower resolution continuum observations show no hint of the shell structure seen in FCM's image, nor is the signal to noise good enough, on a pixel to pixel basis to see any variation in line parameters across the ultracompact object.

#### Arc

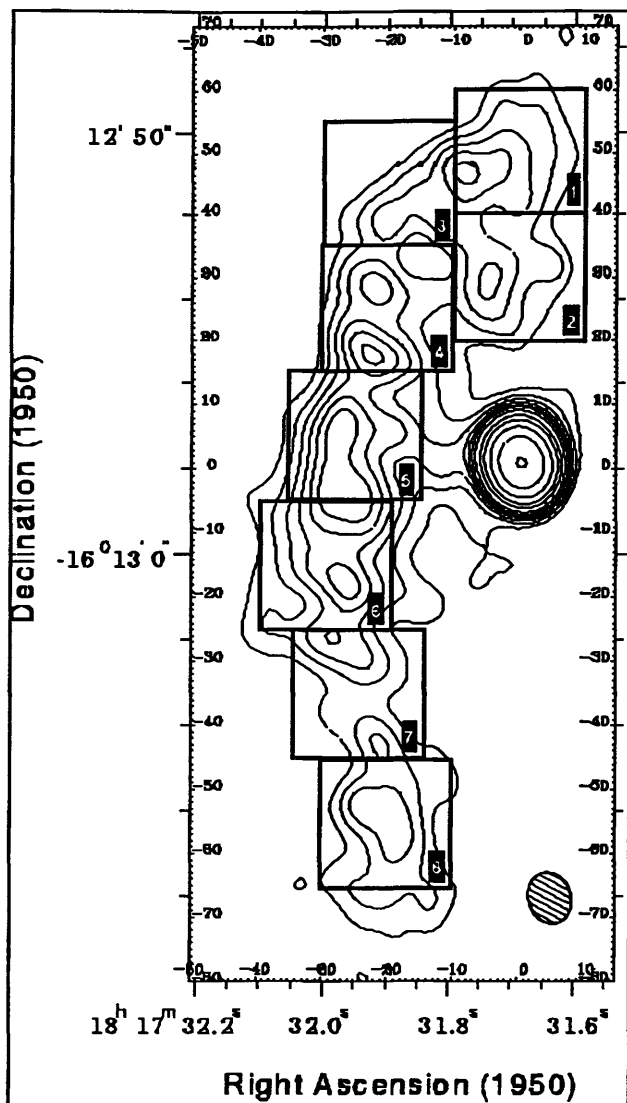
In the 1.3 cm continuum image, the arc appears as a irregular elongated structure which is brightest within approximately 0.02 pc of UC1. This region, where flux values are between 10 and 20 mJy, rests on a much more extended area of fainter, more diffuse emission. The H66alpha emission in the region has a FWHM of  $36 \pm 2.5$  km/s, a central velocity of  $16 \pm 1.2$  km/s, and a peak line to continuum ratio of  $.17 \pm 0.02$ . Perhaps the most remarkable aspect of the RRL data on the arc is the surprising constancy of these parameters across this extended source, which are tabulated in Table 5. Errors in the amplitude of the line/continuum ratio profile are on the order of 0.01, while those of the central velocity are typically approximately 3 km/s and those of the FWHM are approximately 7 km/s. Either there is no structure in the arc feature, which seems unlikely as it is so extensive, or any mass motion which would affect these observed line parameters occurs at a significant angle to our line of sight.

Table 4. Derived Physical Parameters

Structure	Sv	$\tau_c$	EM	ne	$T_e^*$	$T_e$	U	$N_{Lyc}$
UC1	8000?	0.28	4.4E8	3.3E5	12300?	11400	14.3	9.3E46
ARC	??	0.05	8.0E7	5.2E4	11000?	10500	35	1.3E48

#### The relation between UC1 and the Arc

FCM suggested that the arc region is an edge-on ionization front, powered by



**Figure 3** The arc regions for which spatially integrated H66alpha line to continuum profiles were generated. Each box is 20 pixels on a side, containing a region in M17 which is approximately  $0.009 \text{ pc}^2$ . The parameters of Gaussian fits to these profiles are tabulated in Table 3. The underlying contours are of 1.3 cm continuum flux and are at 10, 12, 14, 16, 18, 20, 24, 42, 62, 102, and 184 mJy/beam.

and 2. The two exceptions are NCG 7538 and G25.5+0.2, both of which have linewidths in excess of 150 km/s. NGC 7538 also has a turnover frequency near 1.3 cm, while G25.5+0.2 has a flat spectrum. These objects have eluded detection due partially to their high continuum opacity at low frequencies. Augmenting this difficulty is the fact that, for many objects, pressure broadening effects would be so great at lower frequencies that the line observed would be broadened off the observing bandpass, becoming invisible. High resolution, high frequency observations are needed if more broad line sources are to be identified. Figure 4 shows a fit to the spectrum of M17-UC1, yielding a spectral index of 1.1.

a heavily obscured star cluster 0.7 pc to the NW and providing the shock to induce star formation at the position of UC1. They consider it unlikely that the star central to UC1 contribute significantly to the ionization of the arc as the very sharp boundary between them suggests that a neutral retaining medium exists there. In the same paper, FCM investigate the clumpy structure of the North and South bars and conclude that neutral clumps on the order of tens of pc are contained within ionized shells of thickness approximately  $10^{-5} \text{ pc}$  and densities on the order of  $10^5 \text{ cm}^{-3}$  and they note the similarity of these values to those derived for the arc. Further, they apply the model of Lada and Elmegreen (1977), showing that the separation between UC1 and the arc corresponds well to that theorized between the I-front and the shock-front and that the predicted density matches derived density values well.

#### UC1 as a broad line source

Summarized in Table 6 are the seven objects recognized as broad line sources to date. The RRL measured, the FWHM linewidth in km/s, a linearly fit spectral index,  $\alpha$ , and the frequency range in GHz over which this fit is valid are listed. All references are to the author who first discussed the source's unusually broad RRL profile. Broad line sources generally have FWHM RRL linewidths of 45-100 km/s and continuously rising spectral indices with a between 0.6

Table 5. Parameters of Gaussian fits to Spatially Integrated H66alpha Profiles for Arc Regions

Box Number	Line/Continuum Ratio	Central Velocity	Linewidth (FWHM)
1	.22 +- .05	19 +- 2.7	30 +- 4.4
2	.16 +- .03	19 +- 2.7	34 +- 5.3
3	.15 +- .05	16 +- 4.2	34 +- 8.1
4	.14 +- .02	19 +- 2.1	39 +- 4.6
5	.18 +- .02	13 +- 1.4	33 +- 3.2
6	.18 +- .03	18 +- 1.9	36 +- 3.8
7	.18 +- .02	20 +- 1.5	30 +- 2.6
8	.18 +- .04	17 +- 2.8	31 +- 4.8

Table 6. Broad Line Sources

Source	RRL	FWHM Linewidth (km/s)	Spectral Index (a)	Frequency Range (Ghz)
NGC 7538 (a)	H66alpha	180	(f)	na
G25.5+0.2 (b)	H42alpha	161 +- 25	(g)	na
Sgr B2 F (c)	H66alpha	80	.95	1.4-22.5
W49 A A (d)	H66alpha	50	.6	8.3-43
W49 A B (d)	H66alpha	60.0 +- 8.1	1.1	8.3-43
W49 A G (d)	H52alpha	45	2	22-43
M17-UC1 (e)	H66alpha	47 +- 2.1	1.1	1.5-22

(a) Gaume et al. 1995

(b) Shepard et al. 1995

(c) DePree et al. 1996a

(d) DePree et al. 1996b

(e) this paper

(f) turnover frequency near 1.3 cm

(g) flat spectrum

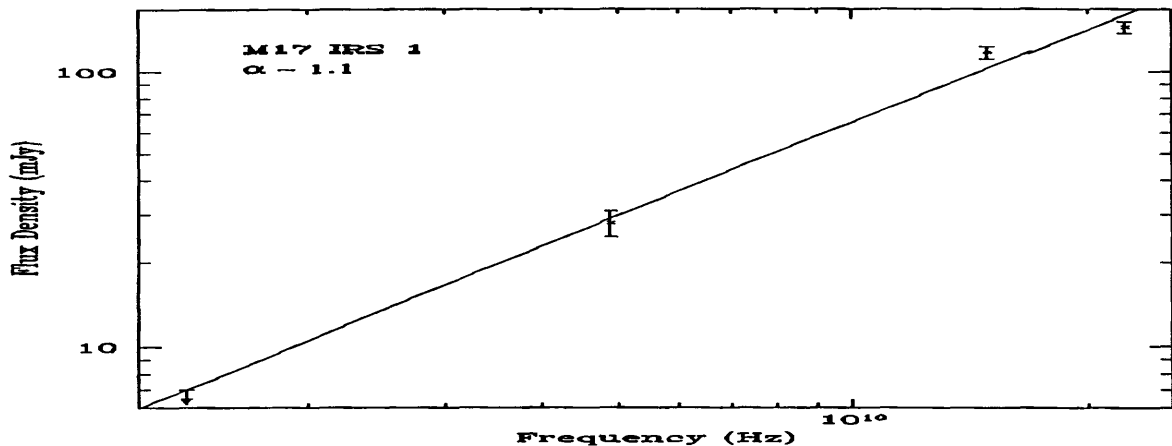


Figure 4 Log flux density (mJy) versus log frequency (Hz) for UC1 with the best linear fit to the data indicating an  $\alpha$  ( $S_\nu$  proportional to  $\nu^\alpha$ ) of approximately 1.1.

The physical properties of these objects are also generally quite similar, many with derived electron temperatures on the order of  $10^5$  and derived mean electron temperatures of approximately  $10^4$  K. Furthermore, with differing levels of certainty, all but one of the sources identified seems most likely to be a case of stellar outflow from a young hot star.

NGC 7538 IRS 1 is described by Gaume *et al.* (1995) as "stellar wind outflow along with photoevaporation from a clumpy distribution of neutral material." DePree *et al.* (1996a) conclude that Sgr B2 F involves outflow from a very young source. All three objects in W49 A are also thought, preliminarily, to be due to massive stellar winds (DePree *et al.* 1996b). The exception is G25.5+0.2, which seems to be resultant of outflow from a much older star, perhaps of the Ofpe/WN9 class (Shepard *et al.* 1995).

Perhaps the most exciting result of the discovery and homogeneity of broad line sources, is that they provide a way to observe energetic phenomena generally thought to be associated with low mass stellar objects, in high mass star environments. DePree *et al.* (1995) note that an O star typically remains embedded in a molecular cloud for 10 to 20 percent of its main sequence life (Mezger and Smith 1975) and that Wood and Churchhill (1989) have recognized the correlation of this estimate to the percentage of O stars found in UCHII phase of their lives in the solar neighborhood. As more broad line sources are identified, we can begin to have a statistical and observational tool with which to probe the early stages of massive stars.

## Conclusions

- (1) We have observed H66alpha RRL emission from M17-UC1 and from the nearby arc structure. The RRL profile from UC1 is unusually broad at 47 km/s, identifying UC1 as the seventh such object known.
- (2) RRL profile parameters are surprisingly constant over the arc to within 10 percent in  $T_l/T_e$ , within approximately 3 km/s in central velocity, and within approximately 7 km/s in FWHM.
- (3) Derived values of  $T_e$ , mean  $n_e$ , and EM are comparable to those obtained by the Felli *et al.* (1984) multifrequency continuum study. Our observations support their model of UC1 as a shell type HII resultant of stellar outflow from a star of type near B0.5.
- (4) Age estimates for UC1 range from approximately 100 yrs to approximately 2000 years, dependant on density. From these estimates it seems likely the star formed in an environment of density higher than approximately  $10^5$ .
- (5) A summary of the seven broad line sources known suggests that most of these types of objects are resultant of stellar outflow from massive stars.

## Acknowledgements:

We thank D. Mehringer, P. Palmer, and M. Claussen for help with various aspects of this study.

## REFERENCES

- Beetz, M., H. Elsasser, C. Poulakos, and R. Weinberger, 1976, *A&A*, 50, 41.
- DePree, C. G., R. A. Gaume, W. M. Goss, and M. J. Claussen, 1996a, *ApJ*, 464, 788.
- DePree, C. G., D. M. Mehringer, and W. M. Goss, 1996b, in press.
- Felli, M., K. J. Johnston, and E. Churchwell, 1980, *ApJ Lett*, 242, L157.
- Felli, M., E. Churchwell, and M. Massi, 1984, *A&A*, 136, 53.
- Gaume, R. A., W. M. Goss, H. R. Dickel, T. L. Wilson, and K. J. Johnston, 1995, *ApJ*, 438, 776.
- Genzel, R., and D. Downes, 1977, *A&AS*, 30, 145.
- Harper, D. A., F. J. Low, G. H. Rieke, and H. A. Thronson Jr., 1976, *ApJ*, 205, 136.
- Knowles, S. H., J. L. Caswell, and W. M. Goss, 1976, *MNRAS*, 175, 537.
- Matthews, H. E., R. J. Harten, and W. M. Goss, 1979, *A&A*, 72, 224.
- Mezger, P. G., and A. P. Henderson, 1966, *ApJ*, 147, 471.
- Panagia, N., 1973, *AstronJ*, 78, 929.
- Roelfsema, P. R., and W. M. Goss, 1992, *A&A Rev*, 4, 161.
- Shepard, D. S., E. Churchwell, and W. M. Goss, 1995, *ApJ*, 448, 426.
- Simon, M., M. Felli, L. Cassar, J. Fischer, and M. Massi, 1983, *ApJ*, 266, 623.
- Wood, D. O. S., and E. Churchwell, 1989, *ApJS*, 69, 831.

# Investigating the Calibration of the Q-band Receiver at Three Observing Bands

by:  
**Andrew W. Kerr**  
**August 9, 1996**

## Introduction

The forty-three gigahertz, seven mm receiver system on the VLA has been around for about two years. However, a lack of solid data has kept the forty-three gigahertz system from being used to its full potential. It is the goal of this paper to alleviate that problem by presenting accurate Q-band noise calibration data for each antenna equipped with the system, as well as tipping scan data. These values are essential for determining opacity and antenna efficiency. After a description of the process and calculations, the data from each of the thirteen Q-band antennas will be presented. These values, presented across three observing bands should further the knowledge of the characteristics of the Q-band receivers.

## Hot-Sky Loads and Tipping Scans

From the stowed position, hot load and sky (and/or liquid nitrogen) tests are one of two ways, the other being a tipping scan, of gaining values for  $T_{sys}$  and  $T_{cal}$ . These values are derived from taking measurements of the synchronous detector voltages with a hot load covering the feed horn and with the feed horn looking at open sky. These values are then used to determine the system and calibration temperatures.

The tests are performed at three frequencies by making a record of  $V_{sd}$  on each channel at each frequency. The frequencies for each band are given by table 1 . The first series of tests is performed at the middle band, approximately 43 GHz. This can be accomplished by setting the F5 to manual mode and setting the dial to 067260. The sixes are the Q-band designations, while the 72 is used to set the observation frequency. In this case, it represents 17.2 on the F3, which according to the equation:

$$(1) \text{ Sky Frequency} = 3 * F3 \text{ frequency} - F12 \text{ frequency} + L6 \text{ freq.} + IF \text{ freq.} ,$$

sets the observing frequency to 43.365 or 43.315 GHz, depending on the IF and local oscillator frequency. For these tests, the F12 frequency is 13.0 GHz, the L6 frequency is the local oscillator frequency, and the IF frequency is 1.025 GHz. Next, using the command simulator in the b rack, the

**Table 1. Sky Frequencies and Instrument Settings**

<b>IF AC(Sky)</b>	<b>IF BD(Sky)</b>	<b>F3</b>	<b>F12</b>	<b>L6(AC)</b>	<b>L6(BD)</b>
41.065	41.015	16.4	13.0	3.840	3.790
43.365	43.315	17.2	13.0	3.740	3.690
49.065	49.015	19.1	13.0	3.740	3.690

local oscillators (see tables 1 and 2 ) can be set as well as the subreflector at the focus point of the dish (see table 3 ). Now, measurements may be taken directly from the IF's themselves from a voltmeter, or may be read off the data tap using table 4 . The Vsd values for each of the antennas can be found in appendix A .

At this point, a tipping scan may be performed at the band for which the hot and liquid nitrogen loads have been completed. This is accomplished by manually adjusting the elevation of the antenna from the pedestal room. Values for each of the IF's can be read from the data tap at each of 4 positions, 90 degrees, 30 degrees, 19 degrees, and 15 degrees. In this paper, tipping scans were performed only for the mid band. Appendix B contains the raw data for the three scans performed at the stationary antennas 4, 8, and 27. Combining hot-liquid nitrogen tests with the tipping scans, values may be obtained for Tatm as well as Tsub. Tsub is the added temperature of the subreflector, while Tatm is temperature added by the atmosphere. These two values both are part of the system temperature.

Next, data from the low and high bands must be calculated. The same procedure is followed as in the case of mid band, substituting 066460 for the low band F5 setting and 069160 for the high band F5 setting. Also, each L6 must be changed to the appropriate settings as seen on tables 1 and 2 . The raw data for these bands can also be found in appendix A .

## Calculations Using the Raw Data

Several equations were used in the preparation of these results. The theory behind each of these can be found in the RF Radiometer Handbook. These equations allow the raw data, in the form of Vsd to be transformed into the various values necessary to define the system. The first equation is common to all phases of processing, the rest will be explained as necessary. For a description of the symbols, please refer to table 5 .

$$(2) \text{Vsd}_c / \text{Vsd}_h = Y$$

The next two equations were used to determine the calibration and system temperatures of the receiver. These equations are associated with hot and sky load testing.

$$(3) T_{\text{sys}} = (T_h - T_c) / (Y-1)$$

$$(4) T_{\text{cal}} = [(\text{Vsd}_c) * (T_{\text{sys}})] / 45$$

In the tipping scan, these equations were used to find the associated Tsys, which was then graphed against the total atmosphere the signal had to go through. Tatm and Tsub were then calculated from the graph.

$$(5) T_{\text{rx}} = (T_h - Y * T_{\text{ln}}) / (Y-1)$$

$$(6) T_{\text{cal}} = [(T_{\text{rx}} + T_{\text{ln}}) * \text{Vsd}_{\text{ln}}] / 45$$

$$(7) T_{\text{sys}} = (45 * T_{\text{cal}}) / \text{Vsd}_{\text{ts}}$$

$$(8) T_{\text{atm}} = T_{\text{sys}}(1) - T_{\text{sys}}(0)$$

**Table 2. Command Simulator Settings**

<b>Band</b>	<b>DSA</b>	<b>MUX</b>	<b>Setting</b>	<b>Comments</b>
All Bands	4	320	00000060	Sets F12
Noise Cals	4	322	00000000	Turns off noise cals (Used to find Vsd0)
Noise Cals	4	322	01403006	Turns on noise cals
Mid	2	350	00007152	Sets L6
Mid	2	352	00007234	"
Low	2	350	00007316	"
Low	2	352	00007400	"
High	2	350	00007153	"
High	2	352	00007234	"

**Table 3. Q-band Subreflector Settings (\*)**

<b>Antenna</b>	<b>Subreflector Setting</b>
3	?
4	00032147
6	00032610
8	00032421
11	00032514
12	00037015
13	00037014
14	00033016
16	00032706
20	00032002
22	00032712
25	00000155
27	00031700

(\*) Command Simulator Settings: DSA: 3 Mux: 330

**Table 4. Data  
Tap Settings to  
read Vsd**

<b>DSA</b>	<b>MUX</b>	<b>IF</b>
1	0	A
1	4	B
1	20	C
1	24	D

$$(9) T_{sub} = T_{sys}(0) - T_{rx}$$

## Results

Appendix C contains the results of the above calculations. The first page lists  $T_{cal}$  by antenna, band, and IF, with values for  $T_c$  of 33 K, 38 K, and 70 K for low, mid, and high bands respectively. These values were obtained from the hot and sky load testing. This is not the same temperature as the atmospheric temperature, which will be discussed later. The most stable antenna across the three bands was antenna eight. The least stable was antenna four, which spans a temperature range of almost twelve Kelvin from mid to high band. It is also important to notice the x's in the results. These values were not obtained due to poor data, possibly caused by the receiver itself. Notice that in all four cases, the  $T_{cal}$ 's are missing in the high band.

The next series of results are the  $T_{sys}$  values obtained from the hot and sky load testing. The x's correspond to the same locations as the  $T_{cal}$  values. The mid band values span the range from 74.53 K to 227.82 K (antennas 11 and 12). For most of the antennas though, the highest  $T_{sys}$  values are found in the high band.

A very important question about the values of  $T_{cal}$  deals with stability. Over the span of almost two months, each of the three stationary antennas were monitored six times. This affords the opportunity to monitor  $T_{cal}$  versus time for this period, a good measure of stability. One immediately noticeable point is found in the mid band of antenna four. This point was taken on a day when the sky was covered with dense clouds. Otherwise, for the other eight graphs,  $T_{cal}$  varies by no more than 12.5%, and generally varies by no more than 5%. So, on a clear day, the average  $T_{cal}$  will be a accurate representation of this figure. However, on a cloudy day, Q-band is not the best choice of observing bands.

Another important question deals with the effects of temperature on the receivers. As evidenced in an interoffice memo from Paul Lillie, at least one of the noise diodes varies significantly with temperature. In two in-lab tests with receivers, however, the change was not as noticeable. The graphs showed each receiver's noise diode at ambient temperature, and then at an elevated temperature (approximately 42 °C) for RCP and LCP. The higher temperature was achieved by placing a resistor in contact with the noise diode and applying voltage across the resistor. In these graphs, there is very little difference between the  $T_{cal}$  line before heat and after the heat, but enough to show that temperature does have some effect on the value of  $T_{cal}$ .

Finally, the tipping scans ( Appendix B ) also provided some information about the forty-three gigahertz system as well. Looking at the values for  $T_{atm}$  and  $T_{sub}$ , one thing immediately stands out, the discrepancy between antenna 4 and the other two in the values. This can be explained very simply; the tipping scan was performed into a forming thunderhead. Therefore, the data from antennas 8 and 27 are likely to be more accurate for clear days. These values also support the use of a value between 15 K and 20 K as sky temperatures. The clear day values range from about 15 to 17 K, and the cloudy day temperature shows that the effective temperature of the sky can be slightly higher on various days. Also, it shows that a good estimate of the subreflector temperature is from 20 to 25 K.

## Conclusions

**Table 5. Definition of Abbreviations**

<b>Abbreviation</b>	<b>Definition</b>
Vsdc	Cold load voltage
Vsdh	Hot load voltage
Y	Y factor
Th	Hot temperature
Tc	Cold temperature
Tsys	System temperature
Tcal	Calibration temperature
Trx	Receiver temperature
Tln	Liquid nitrogen temperature (77 K)
Vsdln	Liquid nitrogen voltage
Vsdts	Tipping scan voltage
Tsys(0)	System temperature with no atmosphere (from graph)
Tsys(1)	System temperature straight up
Tatm	Atmosphere temperature
Tsub	Subreflector temperature

The Q-band system on the VLA offers exciting possibilities for new areas of exploration. The values presented in this paper should make the system easier and more accurate to use. Q-band calibration has proved to be consistent with time and partially consistent with temperature. However, since all of these measurements were completed during the summer, the system should be investigated during the winter or any time with lower temperatures to test how consistent the receivers stay in ambient temperature. Weather also plays a big factor, with clear days allowing the most accurate observations. However, despite its faults, the Q-band system still has the capability to become a large contributor to the field of radio astronomy.

## References

Evans, G., McLeish, C. W., RF Radiometer Handbook, Artech House, Dedham, Mass., 1977

Vsd values for single checked antennas					Trial 2				
Ant. band	IF A	IF B	IF C	IF D		IF A	IF B	IF C	IF D
3 mid Vsd	2.965	2.789	3.061	3.081		2.946	2.802	3.084	3.1
Th=299K Vsdh	1.015	0.97	1.005	1.02	Th=300K	1.006	0.951	1	1.00
3 low Vsd	4.027	3.937	4.23	4.25		3.99	3.9	4.2	4.25
Th=301K Vsdh	1.33	1.27	1.25	1.24	Th=301K	1.33	1.26	1.24	1.24
3 highVsd	3.16	2.99	2.73	2.69		3.16	3	2.73	2.69
Th=303K Vsdh	1.23	1.24	1.18	1.13	Th=303K	1.25	1.23	1.16	1.12
6 mid Vsd	4.23	4.3	4.34	3.89		4.21	4.29	4.33	3.88
Th=297K Vsdh	0.93	0.94	1	0.88	Th=298K	0.96	0.97	1.02	0.91
6 low Vsd	3.47	3.44	4.08	3.67		3.47	3.44	4.08	3.67
Th=300K Vsdh	0.81	0.8	0.97	0.86	Th=301K	0.79	0.79	0.95	0.86
6 highVsd	1.62	1.62	1.57	1.53		1.6	1.62	1.58	1.52
Th=302K Vsdh	0.61	0.6	0.66	0.59	Th=302K	0.57	0.58	0.64	0.57
11 mid Vsd	5.05	4.64	3.1	3.18		5.01	4.6	3.09	3.18
Th=297K Vsdh	1.126	1.066	0.801	0.828	Th=297K	1.122	1.041	0.785	0.82
11 low Vsd	3.704	3.457	2.173	2.113		3.713	3.483	2.173	2.13
Th=298K Vsdh	0.906	0.863	0.591	0.576	Th=298K	0.912	0.867	0.595	0.57
11 highVsd	2.332	2.162	xxxxxx	xxxxxx		2.332	2.173	xxxxxx	xxxx
Th=298K Vsdh	0.73	0.682	xxxxxx	xxxxxx	Th=298K	0.729	0.713	xxxxxx	xxxx
12 mid Vsd	1.738	1.735	2.852	2.809		1.736	1.723	2.844	2.80
Th=296K Vsdh	0.818	0.825	0.961	0.927	Th=297K	0.809	0.794	0.944	0.93
12 low Vsd	2.351	2.303	3.191	3.245		2.357	2.298	3.197	3.25
Th=299K Vsdh	0.809	0.789	0.985	0.985	Th=301K	0.801	0.795	0.963	0.98
12 highVsd	xxxxxx	xxxxxx	1.708	1.741		xxxxxx	xxxxxx	1.705	1.74
Th=302K Vsdh	xxxxxx	xxxxxx	0.645	0.676	Th=303K	xxxxxx	xxxxxx	0.639	0.68
13 mid Vsd	4.084	3.869	3.462	3.193		4.068	3.867	3.453	3.20
Th=300K Vsdh	0.999	0.993	0.838	0.812	Th=301K	0.967	0.937	0.837	0.78
13 low Vsd	3.36	3.266	3.02	2.889		3.352	3.264	3.025	2.88
Th=302K Vsdh	0.837	0.821	0.789	0.733	Th=303K	0.832	0.818	0.787	0.72
13 highVsd	3.536	3.287	2.901	2.8		3.517	3.27	2.893	2.79
Th=303K Vsdh	0.836	0.805	0.721	0.716	Th=304K	0.858	0.799	0.705	0.69
14 mid Vsd	3.541	3.736	2.263	2.41		3.722	3.891	2.321	2.46
Th=297K Vsdh	0.843	0.886	0.648	0.701	Th=298K	0.89	0.903	0.695	0.71
14 low Vsd	2.864	2.812	3.223	3.187		2.847	2.823	3.223	3.17
Th=299K Vsdh	0.885	0.856	0.888	0.887	Th=300K	0.895	0.869	0.892	0.87
14 highVsd	xxxxxx	xxxxxx	1.183	1.338		xxxxxx	xxxxxx	1.203	1.32
Th=301K Vsdh	xxxxxx	xxxxxx	0.607	0.655	Th=302K	xxxxxx	xxxxxx	0.592	0.64
Ant. band	IF A	IF B	IF C	IF D		IF A	IF B	IF C	IF D
16 mid Vsd	5.51	5.56	4.48	4.21		5.48	5.65	4.46	4.22
Th=299K Vsdh	1.48	1.52	1.26	1.23	Th=300K	1.47	1.54	1.26	1.22
16 low Vsd	5.82	5.53	6	5.27		5.8	5.48	6	5.26

Th=299					Th=300				
Vshc	5.36	5.17	2.36	2.21	Vshc	5.19	4.98	2.28	2.14
Vsdh	1.84	1.78	0.77	0.74	Vsdh	1.92	1.82	0.77	0.73
Th=296					Th=296				
Vsdc	5.35	5.12	2.37	2.26	Vsdc	5.35	5.1	2.35	2.27
Vsdh	1.87	1.75	0.73	0.73	Vsdh	1.82	1.73	0.76	0.75
Th=302					Th=302				
Vshc	5.54	5.29	2.48	2.37	Vshc	5.51	5.28	2.48	2.37
Vsdh	1.83	1.73	0.76	0.75	Vsdh	1.82	1.72	0.75	0.75
Th=303					Th=303				
Vsdc	5.54	5.28	2.45	2.33	Vsdc	5.45	5.22	2.42	2.31
Vsdh	1.82	1.75	0.78	0.74	Vsdh	1.88	1.8	0.76	0.74
Th=298					Th=299				
Vshc	5.32	5.1	2.4	2.29	Vshc	5.28	5.06	2.36	2.27
Vsdh	1.84	1.71	0.75	0.75	Vsdh	1.81	1.71	0.75	0.74
Th=304		(thin clouds)			Th=304		(thin clou)		

Ant band	IF A	IF B	IF C	IF D	IF A	IF B	IF C	IF D	
4 high									
Vsdc	4.79	4.62	2.63	2.86	Vsdc	4.81	4.65	2.63	2.88
Vsdh	1.93	1.8	0.93	1.08	Vsdh	1.89	1.81	0.96	1
Th=298					Th=299				
Vsdc	4.73	4.6	2.62	2.84	Vsdc	4.7	4.58	2.57	2.77
Vsdh	1.89	1.8	0.97	1.04	Vsdh	1.89	1.82	1.01	1.04
Th=296					Th=296				
Vsdc	4.67	4.51	2.63	2.85	Vsdc	4.66	4.53	2.64	2.84
Vsdh	1.9	1.79	0.91	1.04	Vsdh	1.88	1.75	0.93	1.09
Th=302					Th=302				
Vsdc	4.85	4.67	2.76	3.01	Vsdc	4.83	4.67	2.76	3.01
Vsdh	1.87	1.79	0.9	0.97	Vsdh	1.85	1.77	0.92	0.97
Th=303					Th=304				
Vsdc	4.76	4.61	2.67	2.93	Vsdc	4.78	4.63	2.69	2.94
Vsdh	1.85	1.8	0.98	1	Vsdh	1.85	1.81	0.97	1.01
Th=299					Th=299				
Vsdc	4.63	4.48	2.62	2.86	Vsdc	4.6	4.45	2.63	2.85
Vsdh	1.88	1.76	0.89	1.03	Vsdh	1.85	1.76	0.92	1.01
Th=304		(thin clouds)			Th=304		(thin clou)		
8 mid									
Vsdc	2.535	2.553	4.2	4.23	Vsdc	2.52	2.53	4.17	4.2
Vsdh	0.68	0.68	1.12	1.14	Vsdh	0.67	0.69	1.12	1.15
Th=298					Th=298				
Vsdc	2.375	2.387	3.97	4.017	Vsdc	2.373	2.387	3.97	3.97
Vsdh	0.657	0.658	1.119	1.12	Vsdh	0.697	0.667	1.143	1.12
Th=297					Th=298				
Vsdc	2.364	2.351	3.925	3.953	Vsdc	2.338	2.341	3.927	3.94
Vsdh	0.658	0.681	1.112	1.138	Vsdh	0.662	0.687	1.112	1.14
Th=295					Th=295				

Th=297 (thin clouds)					Th=297 (thin clou				
Ant band	IF A	IF B	IF C	IF D	IF A	IF B	IF C	IF D	
27 high	Vsdc 1.664	1.55	0.78	0.763	Vsdc 1.675	1.535	0.775	0.75	
	Vsdh 0.58	0.535	0.307	0.32	Vsdh 0.586	0.537	0.31	0.32	
	Th=305				Th=306				
	Vsdc 1.595	1.46	0.773	0.744	Vsdc 1.593	1.464	0.764	0.74	
	Vsdh 0.596	0.54	0.328	0.325	Vsdh 0.594	0.543	0.327	0.32	
	Th=298				Th=298				
	Vsdc 1.563	1.442	0.746	0.735	Vsdc 1.55	1.436	0.755	0.74	
	Vsdh 0.583	0.532	0.315	0.319	Vsdh 0.587	0.532	0.321	0.32	
	Th=301				Th=301				
	Vsdc 1.61	1.48	0.76	0.76	Vsdc 1.61	1.48	0.77	0.75	
	Vsdh 0.57	0.51	0.31	0.31	Vsdh 0.58	0.52	0.32	0.31	
	Th=302				Th=302				
	Vsdc 1.67	1.53	0.8	0.78	Vsdc 1.68	1.53	0.8	0.79	
	Vsdh 0.59	0.53	0.34	0.32	Vsdh 0.6	0.53	0.33	0.32	
	Th=298				Th=298				
	Vsdc 1.59	1.46	0.77	0.75	Vsdc 1.58	1.45	0.77	0.75	
	Vsdh 0.58	0.53	0.32	0.33	Vsdh 0.59	0.54	0.32	0.33	
	Th=298	(thin	clouds)		Th=298	(thin	clou		

## Appendix B. Tipping Scan Data

### Antenna 4, Mid Band

Degrees	Vsd A	Vsd B	Vsd C	Vsd D
90	2.75	2.59	3.82	3.93
30	2.35	2.22	3.16	3.28
19	2.00	1.87	2.68	2.76
15	1.68	1.63	2.20	2.32

### Antenna 8, Mid Band

Degrees	Vsd A	Vsd B	Vsd C	Vsd D
90	2.54	2.54	4.22	4.25
30	2.17	2.18	3.60	3.62
19	1.88	1.90	3.11	3.13
15	1.68	1.68	2.80	2.82

### Antenna 27, Mid Band

Degrees	Vsd A	Vsd B	Vsd C	Vsd D
90	2.88	2.89	2.33	2.41
30	2.52	2.54	2.00	2.07
19	2.23	2.23	1.74	1.80
15	2.03	2.03	1.57	1.62

Tcal	values	for	all	Q-band	antennas		
Antenna	Band		IF A		IF B	IF C	IF D
3	mid		8.9355		8.48512	8.646	8.7655
	low		11.849		11.113	10.527	10.42
	high		10.557		10.8814	10.630	10.060
4	mid		7.1245		6.7016	9.0918	9.6342
	low		16.741		15.813	6.5672	6.5204
	high		15.946		14.994	7.4729	8.1428
6	mid		7.0190		7.0925	7.5886	6.7113
	low		6.1893		6.1518	7.4637	6.6718
	high		4.7935		4.7895	5.7070	4.8259
8	mid		5.3561		5.3102	8.9575	8.9851
	low		5.5367		5.5086	9.1061	9.2653
	high		4.3938		4.2888	8.5211	7.9557
11	mid		8.3302		7.8572	6.1351	6.4244
	low		7.0931		6.7748	4.8037	4.6398
	high		5.3857		5.2125	xxxxxx	xxxxxx
12	mid		8.7940		8.7619	8.2246	7.9996
	low		7.2558		7.1668	8.3144	8.3753
	high		xxxxxx		xxxxxx	5.3112	5.7400
13	mid		7.5589		7.50377	6.44625	6.1795
	low		6.6515		6.55312	6.38437	5.8640
	high		5.7892		5.50993	4.91076	4.8864
14	mid		6.5643		6.7342	5.4848	5.7787
	low		7.654		7.3542	7.2839	7.2043
	high		xxxxxx		xxxxxx	6.2082	6.5275
16	mid		11.716		12.222	10.185	10.038
	low		12.297		11.589	12.414	11.448
	high		7.1801		7.4106	4.0127	3.9440
20	mid		6.8600		6.3405	7.5911	7.1221
	low		6.9124		6.5469	5.8955	6.5234
	high		4.9875		4.6844	xxxxxx	xxxxxx
22	mid		6.2623		6.0742	5.9779	5.7852
	low		5.1064		4.3068	4.3863	4.1665
	high		2.7311		2.5780	2.4572	2.6062
25	mid		8.8427		9.1505	10.978	10.8409
	low		9.3615		9.6237	11.665	11.426
	high		4.4103		4.3659	4.8582	5.1084
27	mid		6.8272		6.6801	4.7321	4.9251
	low		7.0825		6.5110	4.7404	4.8341
	high		4.7129		4.2368	2.8084	2.8729

Tsys	values	for	all	Q-band	antennas		
Antenna	Band		IF A		IF B	IF C	IF D
3	mid		136.22		136.61	126.66	127.61
	low		133.01		127.62	112.37	110.29

33.0035	1.0270967741935	1.0178326474623	1.0202224469161
40	0.96387096774194	0.97942386831276	0.98483316481294
40.0035	1.0193548387097	0.97942386831276	0.96966632962588
42	1.0051612903226	1.0246913580247	0.98988877654196
42.0035	0.99354838709677	1.0452674897119	0.9726996966633
47	0.96774193548387	0.96296296296296	0.98483316481294
47.0035	0.9858064516129	0.96296296296296	1.0091001011122

Normal values for Tcal on Ant 4 low band

Average 17.87 16.88 7.01

Time	IF A (15K)	IF B (15K)	IF C (15K)
0	1.029658645775	1.0065165876777	0.98145506419401
0.0035	0.99384443200895	1.0325829383886	0.96861626248217
12	0.98041410184667	1.0065165876777	1.0199714693295
12.0035	1.0665920537213	1.0586492890995	1.0356633380884
33	1.0263010632345	1.0023696682464	0.9586305278174
33.0035	0.98433128147734	0.98815165876777	1.0228245363766
40	0.97761611639619	0.9739336492891	1.0014265335235
40.0035	0.97202014549524	0.96682464454976	0.98002853067047
42	0.95579182988248	0.9739336492891	1.0271041369472
42.0035	1.0128707330722	1.0272511848341	1
47	1.011751538892	0.97985781990521	1
47.0035	0.988248461108	0.98222748815166	1.0057061340942

Normal values for Tcal on Ant 4 high band

Average 19.76 18.58 9.26

Time	IF A (15K)	IF B (15K)	IF C (15K)
0	1.0298582995951	0.9962325080732	0.97624190064795
0.0035	0.99746963562753	1.0059203444564	1.0302375809935
12	0.99645748987854	0.99085037674919	1.0388768898488
12.0035	0.99696356275304	1.0129171151776	1.1252699784017
33	1.0323886639676	1.0182992465016	0.95788336933045
33.0035	1.0161943319838	0.97793326157158	0.98812095032397
40	0.98785425101215	0.9989235737352	0.92116630669546
40.0035	0.9752024291498	0.98439181916039	0.95680345572354
42	0.96811740890688	1.0037674919268	1.0583153347732
42.0035	0.96609311740891	1.008073196986	1.0356371490281
47	1.0308704453441	0.9989235737352	0.93628509719222
47.0035	1.0035425101215	1.005382131324	0.98056155507559

Normal values for Tcal on Ant 8 mid band

Average 5.83 5.78 9.75

Time	IF A (15K)	IF B (15K)	IF C (15K)
0	1.0017152658662	1.0103806228374	0.98461538461538
0.0035	0.98456260720412	1.0311418685121	0.98871794871795
20	0.97770154373928	0.98442906574394	1.0010256410256
20.0035	1.0668953687822	1.0069204152249	1.0369230769231
35	0.97427101200686	1.0328719723183	0.98974358974359
35.0035	0.98627787307033	1.0449826989619	0.99076923076923
42	0.95368782161235	0.93944636678201	0.96512820512821
42.0035	0.97770154373928	0.96539792387543	0.98358974358974
43	0.99313893653516	0.96020761245675	0.99487179487179

Normal values for Tcal on Ant 27 low band

Average	7.56	6.95	5.06
Time	IF A (15K)	IF B (15K)	IF C (15K)
0	0.99470899470899	0.99136690647482	0.98221343873518
0.0035	0.94708994708995	0.9568345323741	0.95454545454545
23	1.0145502645503	1.0287769784173	0.9901185770751
23.0035	1.026455026455	1.031654676259	1.00395256917
37	1.0185185185185	1.0143884892086	1.0316205533597
37.0035	1.0198412698413	1.0230215827338	1.0098814229249
43	0.99470899470899	1.0028776978417	0.97826086956522
43.0035	0.98412698412698	1.0057553956835	1.00395256917
44	1.0224867724868	0.99712230215827	1.0276679841897
44.0035	1.0066137566138	0.97841726618705	1.00395256917
51	0.99074074074074	0.99568345323741	1.0237154150198
51.0035	0.98015873015873	0.97985611510791	0.99802371541502

Normal values for Tcal on Ant 27 high band

Average	5.84	5.25	3.48
Time	IF A (15K)	IF B (15K)	IF C (15K)
0	0.98116438356164	1.0019047619048	0.9367816091954
0.0035	0.99657534246575	1.0171428571429	0.95977011494253
23	1.0222602739726	1.0285714285714	1.0258620689655
23.0035	1.0205479452055	1.032380952381	1.0316091954023
37	1.0119863013699	1.0209523809524	0.99425287356322
37.0035	1.0291095890411	1.0228571428571	1.0201149425287
43	0.96575342465753	0.94666666666667	0.95977011494253
43.0035	0.98801369863014	0.97142857142857	1
44	0.98287671232877	0.96952380952381	1.0718390804598
44.0035	1.0051369863014	0.96952380952381	1.0172413793103
51	0.98458904109589	1	0.98563218390805
51.0035	1.0119863013699	1.0285714285714	0.98563218390805

Ant. 4	Tipping	Scan	Results	Date	6/14/96
Atm	Tsys A	Tsys B	Tsys C	Tsys D	Average
1	116.75	115.19	111.15	111.58	Tatm 28.3825 K
2	136.63	134.39	134.36	133.7	Tsub 6.6175 K
3.072	160.54	159.55	158.42	156.89	
3.864	191.12	183.04	192.99	189.02	

Regression Output:		A	Regression Output:	
Constant		88.316851452294	Constant	89.5
Std Err of Y Est		5.9445366480666	Std Err of Y Est	3.25
R Squared		0.97705292778521	R Squared	0.99
No. of Observations		4	No. of Observations	
Degrees of Freedom		2	Degrees of Freedom	
X Coefficient(s)		25.339431782491	X Coefficient(s)	23.5
Std Err of Coef.		2.7459110835254	Std Err of Coef.	1.50
Tatm=	28.43 K		Tatm=	25.67 K
Tsub=	5.82 K		Tsub=	10.29 K

Regression Output:		C	Regression Output:	
Constant		80.592832074725	Constant	82.7
Std Err of Y Est		6.7927055721674	Std Err of Y Est	6.10

Tatm= 15.5 K  
Tsub= 19.75 K

Tatm= 14.97 K  
Tsub= 22.75 K

Regression Output:

Constant  
Std Err of Y Est  
R Squared  
No. of Observations  
Degrees of Freedom

C  
73.588677573093  
0.59024691217716  
0.99932182381071  
4  
2

Regression Output:

Constant 72.6  
Std Err of Y Est 0.52  
R Squared 0.99  
No. of Observations  
Degrees of Freedom

X Coefficient(s)  
Std Err of Coef.

14.801257015663  
0.27264791759523

X Coefficient(s) 14.8  
Std Err of Coef. 0.24

Tatm= 15.06 K  
Tsub= 22.19 K

Tatm= 15.16 K  
Tsub= 21.93 K



# Modeling HI In Interacting Galaxies Using 3-Body Simulations

Lauren Herold, Princeton University  
Summer 1996

## Introduction

This summer I worked with Min Yun on debugging and providing a user friendly graphical interface for software which maps the perturbation of HI in interacting galaxies using 3-body simulations. The goal of the project was to create a program with a good graphics display and versatility so that it can be used to examine the orbital details of two or more interacting galaxies quickly and easily, without having to do any full N-body calculation.

## Process

The initial debugging of the existing code took the majority of the summer, mostly consisting of translating the unfriendly graphical interface of GAG to the more widely used PGPlot library and eliminating what seemed to be ever present precision inaccuracies. Once that was completed to the point where we could view the interaction of galaxies, we modeled three companion galaxies, M81, M82, and NGC3077 to refine the code even more. M81 is possibly the most famous spiral galaxy and its two companion galaxies do not seem to be interacting with it at all in the optical light. However, at 21cm there are clear signs of tidal interactions between the three galaxies. One can see tidal tails, bridges, and even some spiral arm structure when HI is mapped in this interacting system.

The code is an example of a type of numerical simulation known as 3-body simulations which is believed to be a good first order approximation to full N-body simulations. The entire simulation can be done in a few minutes on Sun workstations. This has clear advantages to the user who wishes to know whether his parameters are reasonable before attempting the full N-body simulation. We assumed that each galaxy is represented by a point mass (with some softening parameter) and test particles are perturbed by the gravitational potential set up by the three point masses. The user must input the galaxy's position on the sky, line of sight velocity, the ellipticity of its orbit, its perigalactic distance, and its mass. The program then finds its orbit and perturbs the test particles as they follow this orbit around its companion.

The final part of the process consisted of producing a movie which would show these three galaxies perturbing one another as they followed the orbits computed by the program. The galaxies each start as a

disk of particles, and the whole system is then projected onto the plane of the sky. In the movie yellow dots represent HI particles in M82, magenta represents M81, and green represents NGC3077.

[Click here to see the movie](#), but be warned, it's somewhat large [50K]).

## **Conclusions**

With working, user friendly code we have been able to successfully model three well understood interacting galaxies. The interactions have also indicated that interactions between galaxies might be another formation mechanism for spiral arm structure (beside the traditional spiral density wave). In the future we hope to generalize the code to take any two or three galaxies the user wishes to perturb and output the results of their interaction. If we can model a number of galaxies using this type of simulation, there is a lot to be learned about the evolution of HI, spiral arm structure, and other aspects of galactic morphology.

# **20 cm VLA Observations of Uranus and Neptune**

**Todd Konkel, Rice University**

**Bryan Butler, NRAO**

## **Objective**

The primary goal of this project was to obtain disk-averaged brightness temperatures for Uranus and Neptune at 20 cm. Previous studies of Uranus at a wavelength of 20 cm were conducted in 1988 by Imke de Pater and Samuel Gulkis. Previous studies of Neptune at 20 cm were conducted in 1989 by de Pater and Michael Richmond. The aim of this project was to combine the results of multiple observations in order to obtain smaller error measurements than those obtained in previous studies. This would allow us to place a tighter constraint on the 20 cm region of the planets' brightness temperature spectra, thus constraining possible models for each planet's atmospheric composition.

## **Background**

Thomas Spilker (1995) did a study of the radio spectra of the giant planets in which he described the "H<sub>2</sub>S/NH<sub>3</sub> problem." Basically, unlike those of Jupiter and Saturn, radiative transfer models of Uranus and Neptune using near-solar NH<sub>3</sub> abundances do not agree with the observed data. Models using 1% solar NH<sub>3</sub> abundances fit the data much better. David DeBoer and Paul Steffes (1994) suggested a superabundance of H<sub>2</sub>S as a possible cause of the apparent NH<sub>3</sub> depletion in Neptune's troposphere.

## **Observations and Data Reduction**

We observed Uranus and Neptune quasi-simultaneously on eight occasions using the VLA at 20 cm. Each set of observations was conducted using a subarray of antennas which were not involved in Q-band tests occurring simultaneously.

The first six sets of observations were obtained between October and December 1995 while the VLA was in B configuration. The last two sets of observations were obtained in February 1996 while the VLA was in C configuration. Unfortunately, the three sets of December data have some problems whose causes we have not yet ascertained. Also, the February data sets were corrupted by confusion sources. Because of time limitations, we were only able to self-calibrate and remove the confusion sources from

the February Uranus data. As a result, we combined 5 of the 8 Uranus data sets and 3 of the 8 Neptune data sets to create master data sets for each planet.

Before combining the data sets from different days, we adjusted the Uranus data sets to a common distance of 20.65 AU and the Neptune data sets to a common distance of 30.56 AU. We also adjusted each data set to a common frequency of 1400 MHz. We then combined the October, November, and February Uranus data into one data set and did the same for the October and November Neptune data.

We estimated the total flux density from a cleaned map of each planet. We took the flux of Uranus out to a radius of 14" and Neptune out to a radius of 10".

## Results

For Uranus, we obtained a total on-disk flux density measurement of  $3.16 \pm 0.11$  mJy, corresponding to a disk-averaged brightness temperature of  $250 \pm 9$  K. For Neptune, we obtained a total on-disk flux density measurement of  $1.68 \pm 0.07$  mJy, corresponding to a disk-averaged brightness temperature of  $307 \pm 12$  K.

The Uranus result agrees with the results obtained by de Pater and Gulkis (1988). The Neptune result is slightly lower than but still within the error of the results obtained by de Pater and Richmond (1989). In both cases, however, our error values are smaller, and this places a tighter constraint on the brightness temperature spectra at 20 cm, thereby better constraining possible models for the tropospheric compositions of Uranus and Neptune.

## Conclusions

The brightness temperature spectrum of Uranus appears to turn over or level out at about 250 K in the 6-20 cm region. One possible explanation for this is a significant increase in opacity sources (NH<sub>3</sub> or H<sub>2</sub>O) at greater atmospheric depths. Another cause might be that Uranus' atmosphere is isothermal below a depth of about 40 bars.

Unlike that of Uranus, the brightness temperature spectrum of Neptune continues to increase with increasing wavelength in the cm region. This is consistent with NH<sub>3</sub> depletion at greater atmospheric depths (Spilker). Thus, if Neptune were to have the same atmospheric composition as Uranus (as is believed), it would require dynamical differences to account for Neptune's different vertical structure.

## Future Work

With more time we might be able to determine the problems with the December 1995 data. We would also self-calibrate the February 1996 Neptune data to remove the confusion sources. Then we would recombine all of the data and calculate new values for the brightness temperature of each planet. Finally, we would develop radiative transfer models that take our results into account, and this would provide us with information about the atmospheric compositions of Uranus and Neptune.

## REFERENCES

- DeBoer, D.R., and P.G. Steffes 1994. Laboratory Measurements of the Microwave Properties of H<sub>2</sub>S under Simulated Jovian Conditions with an Application to Neptune, *Icarus* 109, 352-366.
- de Pater, I., and S. Gulikis 1988. VLA Observations of Uranus at 1.3-20 cm, *Icarus* 75, 306-323.
- de Pater, I., and M. Richmond 1989. Neptune's Microwave Spectrum from 1 mm to 20 cm, *Icarus* 80, 1-13.
- Spilker, T. 1995. NH<sub>3</sub>, H<sub>2</sub>S, and the Radio Brightness Temperature Spectra of the Giant Planets, Earth, Moon, and Planets 67, 89-94.



# Monitoring of Gamma-Ray Bursters

and

## Measuring the Motion of the Pulsar 1257+12

**Craig Heinke**

For several years, Dale has been looking for time-variable radio counterparts to gamma-ray bursts. He takes images of the locations of previous gamma-ray bursts several times a year, looking to detect radio emission on time scales of months to years. This summer, I took data from the past year off tape and made images of 11 GRB locations over several months, looking for time variability. People have been looking for counterparts for these strange beasts for more than twenty years, and none has had any luck. We also did not detect any new or time-variable sources, and by compiling all the maps from one source together, we can place a limit of 60 microJanskys on the strength of any time-variant sources during our observations.

The other project was the pulsar. The discovery of planets around the pulsar was made by analyzing the timing data, the variations in the period of the pulses from the pulsar. These variations are caused by the motion of the pulsar, and the motion of the earth. If the exact position and proper motion of the pulsar are known, the earth's motion can be taken out of the equation. Then any remaining residuals are due to something--in this case planets-- pulling back and forth on the pulsar. The timing method, given a reasonably accurate position for the pulsar, looks for a least-squares fit to the data to find the most likely exact position and proper motion. But it might not contain all the data--so we wanted to check the pulsar's position and motion with the Very Large Array.

A minor task was to deal with the position. The original position quoted by Dale and the timing position were .7 arcseconds away, with much smaller error bars. This was a problem. But later timing measurements, taken in an improved planetary ephemeris system and taking into account a third planet, agreed with our measurements. Plus, our measurements of the pulsar position in later epochs agreed with our earlier measurement to within the absolute position errors. Problem goes away. My part in this was to determine the accuracy of our position measurements by examining short term variations in the phase information.

Proper motion measurement was a much more difficult task. This pulsar was by far the faintest pulsar anyone has ever tried to take a proper motion measurement of--ranging down to .2 mJys but more often at .5 to .7 mJys. Also, the first epoch (1992) was not suitable for proper motion studies due to being taken in continuum mode, causing chromatic aberration in sources far from the center of the field (where

the pulsar was). So we had only two epochs, 1.123 years apart, to work with.

We did the measurements of proper motion by a differential method. We essentially subtracted the overall average motion of an extragalactic reference frame from the pulsar's motion, arriving at our estimate. Sources with low flux levels can have their positions determined to less certainty. Therefore, we weighted the sources' apparent motions according to  $1/\sigma^2$ , where  $\sigma$  is the uncertainty in this case derived from noise over peak flux.

After Dale found all the bright point sources in the field and made subimages of them, I used the AIPS process IMFIT (and later JMFIT) to determine their apparent position at each epoch by fitting a Gaussian curve to the flux density map. Any extended sources were judged unsuitable as background sources because a Gaussian could not be fitted to them. This left us with 22 sources.

Our first results were extremely encouraging. Using a program I built up from Dale's idea, I found the pulsar proper motion to be in almost exactly the same direction and of the same magnitude as the timing proper motion. The initial errors were small enough to justify claiming a significant result.

But then we noticed problems. Using the same errors, based on signal-to-noise criteria, the background sources were also moving--impossible because the background sources are extragalactic. We tried a variety of improvements to the data, but the motions did not go away completely.

These motions could be separated into two groups. Those sources significantly fainter than the pulsar, with a signal-to-noise of 5 or so, could not be pinned down--their motion was often a fifth of the synthesized beam. We decided that the fitting algorithm was failing for signals so low, and discarded the 13 sources significantly fainter than the pulsar.

However, the sources as bright or brighter than the pulsar were also moving with a much larger scatter than expected for a normal distribution around our errors. This was a definite problem, and questioned the validity of our detection.

I eventually came up with three partial solutions to this problem. One was the empirical observation, at this time without a firm theoretical basis, that it is impossible with the VLA to measure source positions, no matter how high their signal-to-noise ratio, to better than about 15 milliarcsecond precision. With this minimum position error, added in quadrature to the signal-to-noise errors as it was assumed that they were independent, the brightest sources in the field no longer were moving beyond their estimated errors. It was then possible to believe that they were stationary.

A second one was to use a newer version of the Gaussian-fitting program, JMFIT, rather than the old one IMFIT. With the new program, it was possible to analyze the fits more carefully and determine the fitted positions to greater accuracy. Careful analysis showed that the sources approximately as bright as the pulsar were actually not moving as significantly as they had seemed.

The final step was to use the errors generated by the Gaussian-fitting task rather than the signal-to-noise criterion we had been using. These new errors better fit the distribution of background source motion. However, we do not claim to fully understand the theoretical basis for how to correctly calculate these errors, and so we feel the need for more work on this matter.

The results we eventually get are that the pulsar is moving  $+28 \pm 42$  milliarcseconds a year in right

ascension, and  $-98 \pm 27$  milliarcseconds a year in declination. This agrees well with the  $46.4 \pm 6$  mas/year in RA and  $-82.9 \pm 9$  mas/year given by the timing measurements. The errors quoted are the signal-to-noise errors which we do understand, rather than the Gaussian-fitting errors which we do not understand as well but seem to be more empirical.

The final solution to the pulsar question is to measure its position against the background sources at a 1996 or 1997 epoch, giving the apparent displacement of the pulsar a fourfold increase. Another observation is planned, which should verify the significance of the proper motion.





This page contains material being prepared into a paper. Unauthorized use of any of this material is strictly forbidden!



# The rotation-measure structure of OQ172 at 2 mas resolution

Patricia Udomprasert, Princeton

Greg Taylor, NRAO

Tim Pearson, Caltech

David Roberts, Brandeis

## Introduction

Compact steep spectrum (CSS) sources are a class of extragalactic radio objects loosely defined as those having subgalactic size  $< 15 h^{-1}$  kpc, and a steep radio spectral index,  $\alpha < -0.5$  (where  $S_\nu$  is proportional to  $\nu^\alpha$ ) (Kapahi 1981; Peacock and Wall 1982). CSS's make up roughly 50% of sources that have been determined from single dish studies to have anomalously high Faraday rotation measures (RMs), exceeding  $1000 \text{ rad m}^{-2}$ . Faraday rotation is the change in plane of polarization of an electromagnetic wave that occurs when it travels through a magnetoionic medium. Faraday rotation exhibits a characteristic wavelength squared dependence according to the equation:

$$X = X_0 + \text{RM} * l^2, (1)$$

where  $X$  is the observed position angle,  $X_0$  is the intrinsic position angle,  $l$  is the wavelength of the emitted radiation, and RM is the rotation measure given in  $\text{rad m}^{-2}$  by:

$$\text{RM} \sim 812 * n * B * L. (2)$$

$$RM \sim 0.12 n_e B_{\parallel}^2 L \quad (2)$$

Here  $n_e$  is the electron density in  $\text{cm}^{-3}$ ,  $B_{\parallel}$  is in microGauss, and  $L$  is in kpc.

The high RM radio sources of large angular extent, the FRI and FRII radio galaxies such as Hydra A and Cygnus A, have been studied extensively with instruments such as the VLA, and it has been determined that a good candidate mechanism for producing such high RMs in these sources is hot X-ray emitting cluster gases and cooling flows (Taylor et al. 1994). Higher resolution observations were necessary to determine whether the high RMs in CSS sources resulted from a similar cluster-scale phenomenon, or whether they are generated on smaller galactic or sub-galactic scales.

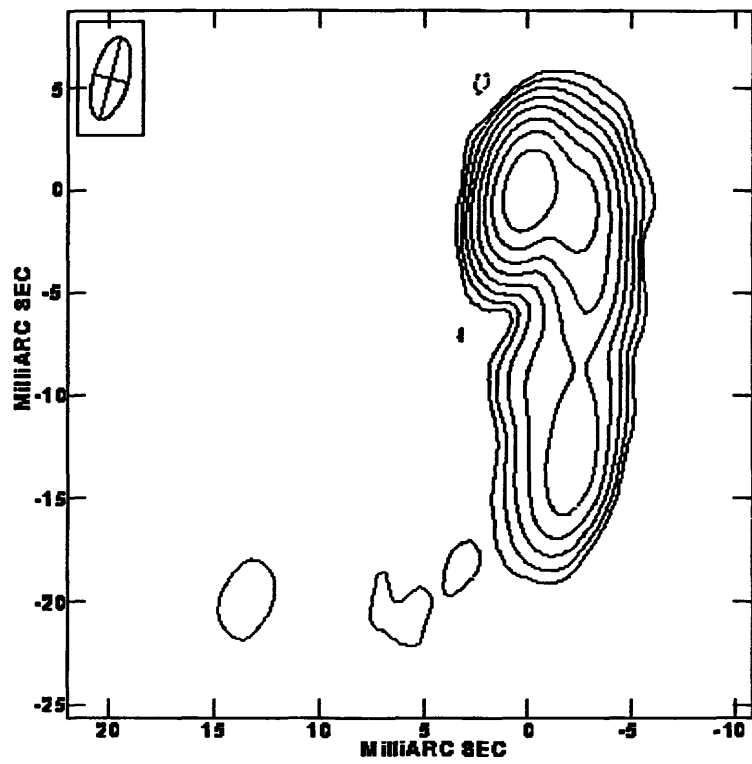
The quasar OQ172 is one of the CSS sources that has been observed with single dish measurements to have an anomalously high RM. While the source has been mapped on the mas scale (Dallacasa et al. 1995; Gurvits et al. 1994), previous polarimetry had not been done. Here we present polarimetric VLBA observations used to determine the RM structure of OQ172 at 2 mas resolution. Osmer et al. (1994) have calculated the redshift of OQ172 to be:  $z = 3.52$ . If we assume  $H_0 = 50 \text{ km s}^{-1} \text{ Mpc}^{-1}$  and  $q = 0.5$ , then  $1 \text{ mas} = 6.81 \text{ pc}$ .

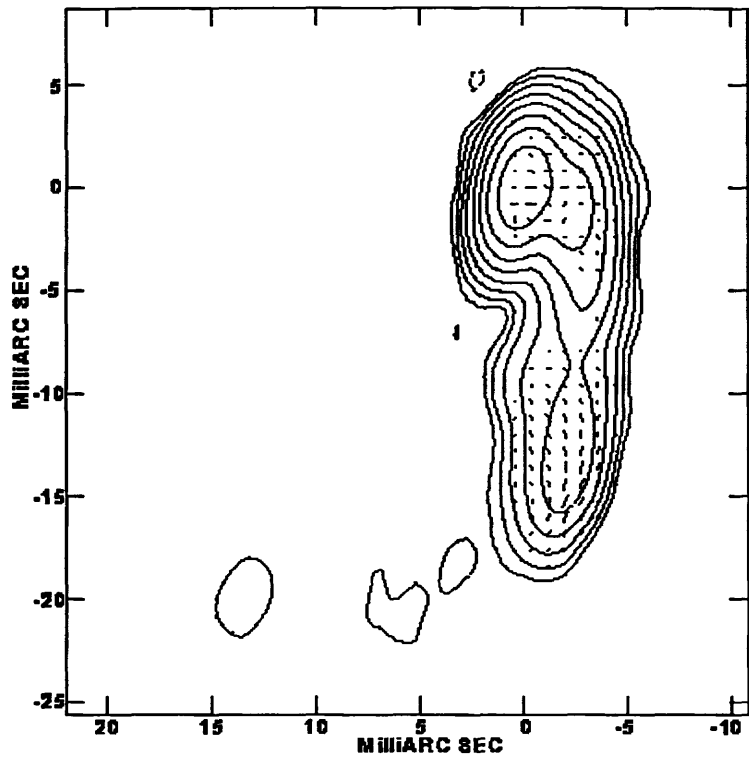
## Observations and Data Reduction

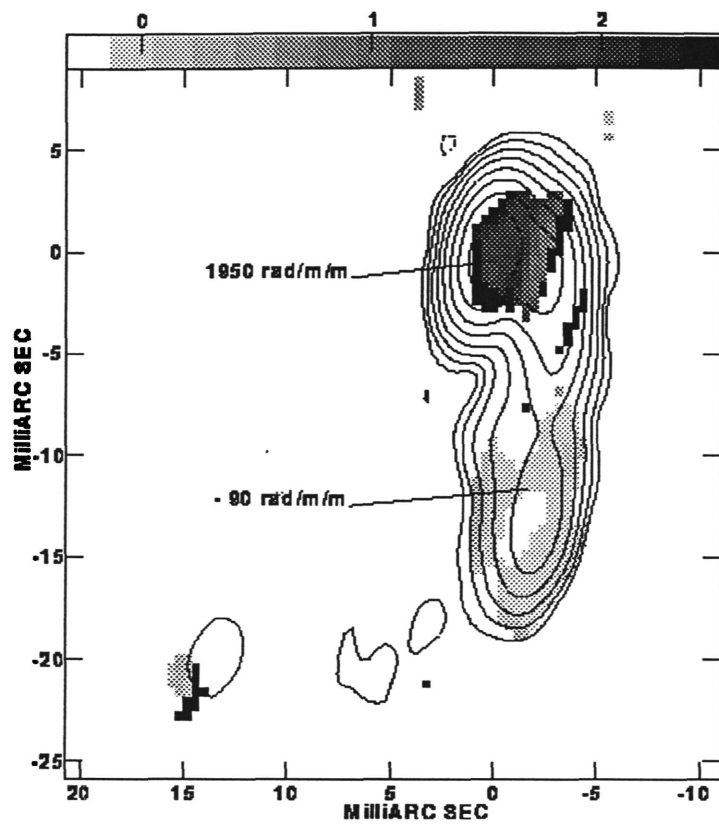
The observations, performed on 1995 June 4, were carried out at four frequencies in the 6 and 18 cm bands (as listed in Table 1) using the 10 element VLBA and one element of the VLA. The VLA and VLBA were built and are operated by the National Radio Astronomy Observatory, which is a facility of the National Science Foundation operated under cooperative agreement by Associated Universities, Inc. Eleven scans, each of 8.5 minutes duration, were obtained on OQ172. At each frequency, both right and left circular polarizations were recorded using 1 bit sampling across a total bandwidth of 8 MHz. The VLBA correlator produced 16 frequency channels in each 4 second integration. Problems with the VLA resulted in the loss of all crosshand data from that antenna, and parallel hand data were obtained at only 3 frequencies, 1664, 1672, and 4854 MHz.

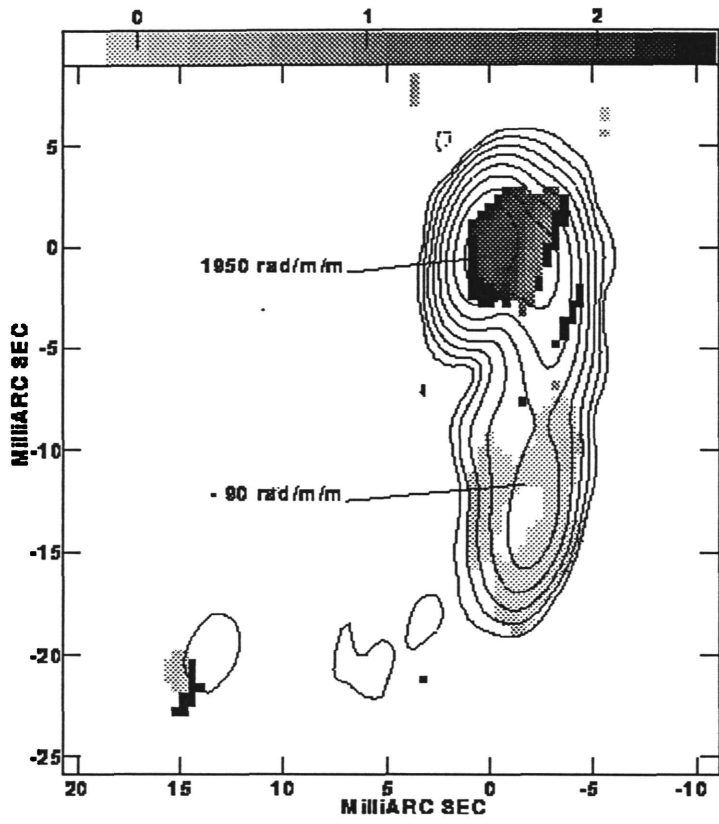
Amplitude calibration for each antenna was derived from measurements of the antenna gain and system temperature during each run. In addition, observations of the strong calibrator OQ208 were used to refine the amplitude calibration. The polarization calibration was performed following a procedure suggested by Cotton (1992). Following correlation, a correction was made to remove the effects of parallactic angle. Global fringe fitting was performed using the AIPS task FRING, an implementation of the Schwab & Cotton (1983) algorithm. The fringe fitting was performed using a solution interval of 4 minutes, and a point source model was assumed. Next, a short segment of the cross hand data from the strongly polarized calibrator 3C345 was fringe fitted in order to determine the right-left delay difference, and the corrections obtained were applied to the rest of the data. Once delay and rate solutions were applied, the first and last channel were omitted, and the data were averaged in frequency over the remaining 7 MHz. The data from all sources were edited and averaged over 30 second intervals using "difmap" (Shepherd, Pearson & Taylor 1994, 1995) and then were subsequently self-calibrated within AIPS.

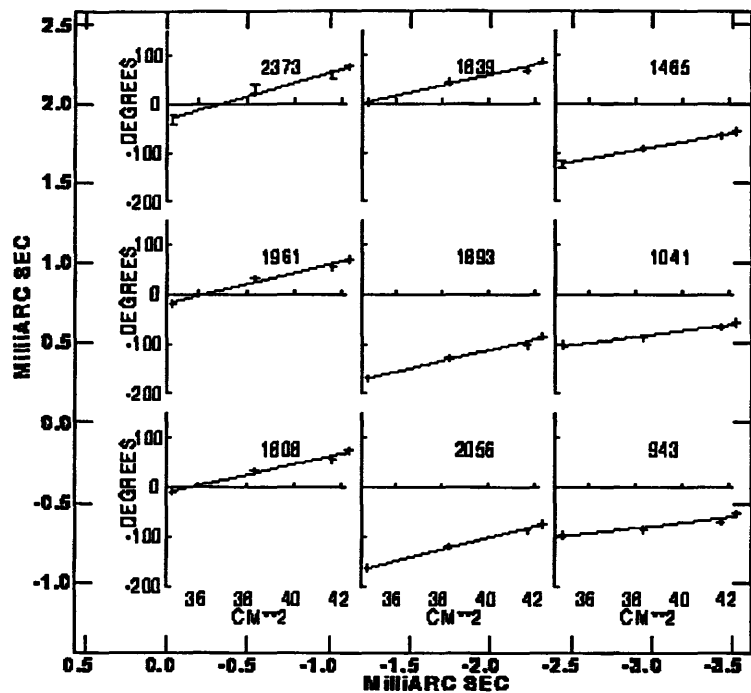
Next, the calibrator OQ208 was used to determine the feed polarizations of the antennas using the AIPS task PCAL. We assumed that the VLBA antennas had good quality feeds with relatively pure

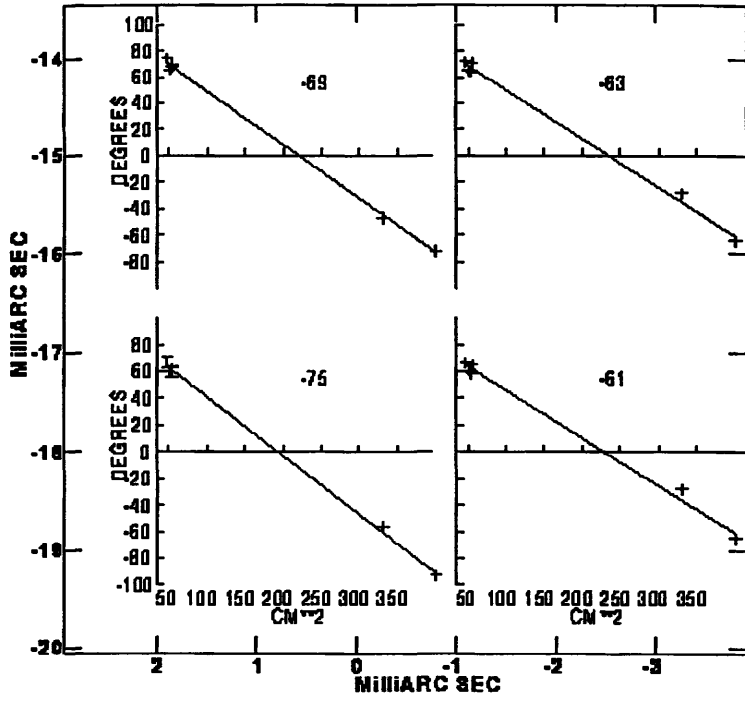












polarizations, which allowed us to use a linearized model to fit the feed polarizations. Once these were determined, the solutions were applied to the calibrator 3C345, whose magnetic field component has been observed to lie parallel to the jet axis at 6cm (Cawthorne et al 1993). We expected this to remain the case over time, and we used this information to correct for the instrumental polarization by rotating the observed position angle of the calibrator's E field vector to lie perpendicular to the jet, at a position angle of  $29^\circ$ . We compared our result to that given by the University of Michigan Radio Astronomy Observatory and found it to be within  $16^\circ$ . A single correction was then applied to the right-left phase difference for all 6cm frequencies of OQ172. Of prime importance to this experiment are the relative angles among the 6cm frequencies, and these are preserved by applying a constant correction to all the frequencies. Since previous polarimetry of 3C345 had not been done at 18cm, we calculated its approximate position angle at 18cm using the formula:

$$X_1 - X_2 = RM * (l_1^{-2} - l_2^{-2})$$

where  $X$  is the position angle in radians,  $l$  is the wavelength of the radiation in meters, and  $RM$  is the rotation measure in  $\text{rad m}^{-2}$ . We used a value of  $RM = 22 \text{ rad m}^{-2}$  (Simard-Normandin et al. 1981) and obtained a value of  $X_{18 \text{ cm}}$  of approximately  $70^\circ$ . A single correction was made to the R-L phase difference for the four 18cm frequencies.

## Results

### Total Intensity Images at 6 and 18 cm

Four 6cm frequencies were combined to create a total intensity map of OQ172, using a restoring beam of  $4.2 \times 1.7 \text{ mas}$ , at  $PA = -14.7^\circ$  ( Figure 1). Positions are given in mas relative to the core, which is located at RA(J2000) 14:45:16.465 and Dec(J2000) 09:58:36.072. The naturally weighted image has a dynamic range of 1700, and the rms noise in the image is 0.25 mJy/beam, which is a factor of about 1.5 above the thermal noise. At this resolution, OQ172 shows the typical core and jet structure of a CSS quasar, but it is slightly unusual in that the jet turns through almost  $180^\circ$ . The jet emission extends from the central core in a southwest direction and almost immediately bends southward. About 20 mas south of the core, it turns again, about  $90^\circ$ , and continues east.

A similar map was made from the four 18cm frequencies, and a dynamic range of 2250 was achieved. Since the resolution was decreased by a factor of 3, the core and jet are not as well resolved. However, more of the eastern jet emission is detected at the lower frequencies.

### Polarized Structure and Rotation Measures

The polarization properties of OQ172 were investigated through analysis of the Stokes Q and U maps made at each of the four 6cm frequencies. The rms noise of these maps ranged from 0.25 mJy/beam to 0.36 mJy/beam. A map of the projected B field vectors was made after correcting for the rotation measures as described below, and it is shown overlaid on the 6cm total intensity image ( Figure 2 ). While there seems to be little ordered structure at the core, the B field parallels the southern jet quite

nicely, as is generally found for quasars (Roberts et al. 1989).

The RM structure of OQ172 was examined by combining the position angle maps of the four 6cm frequencies and determining the change in PA with respect to wavelength squared for each pixel. The RM map is shown in Figure 3 . A pixel was blanked if the error in PA exceeded  $20^\circ$  for any particular frequency. No corrections have been made for the redshift of the observed emission, so if the RMs are being produced in the region of the source, the values in the rest frame of OQ172 are larger by a factor of  $(1+z)^2$ , or 20. As Figure 3 shows, there is a distinct difference in RM between the core and the jet. Typical RM values at the core are extremely high, ranging from 1000 to 2000  $\text{rad m}^{-2}$ , with a slight downward gradient of about  $-445 \text{ rad m}^{-2} \text{ mas}^{-1}$  toward the southwestern jet, while the values in the southern jet area are only about  $-200$  to  $-60 \text{ rad m}^{-2}$ .

Figure 4 shows sample fits to the position angle vs. wavelength squared for a group of pixels in the core region. The plots show that the fits agree well with the  $l^2$  law in the core. In the jet, the lower rotation measures yield a much smaller change in position angle over this range of frequencies, so more caution is needed in the analysis of those fits since the errors in the angle measurements become fractionally more significant. Figure 5 shows sample fits from the jet with the 18cm data added to increase the range of frequencies, yielding better fits.

## Discussion and Conclusions

The most striking result obtained from the RM maps at this resolution is the observed non-uniformity in RM between the core and the jet. The lower RMs observed in the jet can be explained as being Galactic in origin, as they are comparable to RM values obtained from single dish measurements of objects at similar Galactic latitude (Simard-Normandin et al. 1981), and we do not consider them further. However, something peculiar to the nuclear environment is producing the anomalously high RMs in the core of the quasar. When the redshift in wavelength is taken into account, the values obtained for the RMs in the rest frame of OQ172 are 20,000 to 40,000  $\text{rad m}^{-2}$ , values which to our knowledge, are the highest RMs yet observed in any source.

Since these high RMs are observed only in the core and not across the entire source, they cannot be explained by the cluster magnetic fields and cooling flows that cause the high RMs in the larger radio galaxies such as Hydra A and Cygnus A. Something entirely different is occurring either within the nucleus of OQ172 or in the immediate environment surrounding the core. We explored a few possibilities, including internal Faraday rotation, and external Faraday rotation due to the broad line emitting region and the narrow line region associated with active galactic nuclei (AGN), but since so little is known about the nuclear environment of AGNs, it is difficult to say anything conclusive. If some typical AGN phenomenon were the cause of the high RMs in OQ172, one would expect to see such high RMs in other sources as well. Since we don't, we must consider the possibility that OQ172 is simply an extremely unusual quasar, in which case invoking theorized AGN environmental parameters would probably not be helpful anyway. However, it is also possible that we are viewing a normal quasar at some special line of sight, in which case, we would need to perform more high resolution studies of the other high RM CSS sources, as well as other CSSs which don't exhibit these anomalous RMs in order to fully understand what is occurring in their nuclear environments. Perhaps continuing to observe additional objects at this resolution will yield more insight into the structure of AGNs, as well as the nature of CSSs as a class and their relation to other radio sources.

## Acknowledgments

This research has made use of the NASA/IPAC Extragalactic Database (NED) which is operated by the Jet Propulsion Laboratory, Caltech, under contract with NASA. This research has made use of data from the University of Michigan Radio Astronomy Observatory which is supported by the National Science Foundation and by funds from the University of Michigan.

## REFERENCES

- Cotton, W. D., 1995, 'Polarization Calibration of VLBI Data', in the VLBA white book.
- Dallacasa, D., C. Fanti, R. Fanti, R. T. Schilizzi, and R. E. Spencer, 1995, *A&A*, 295, 27.
- Gurvits, L. I., R. T. Schilizzi, P. D. Barthel, N. S. Kardashev, K. I. Kellermann, A. P. Lobanov, I. I. K. Pauliny-Toth, and M. V. Popov, 1994, *A&A*, 291, 737.
- Kapahi, V. K., 1981, *A&AS*, 43, 381.
- Peacock, J. A., and J. V. Wall, 1982, *MNRAS*, 198, 843.
- Roberts, D. H., J. F. C. Wardle, L. F. Brown, D. C. Gabuzda, and T. V. Cawthorne, 1989 in "Parsec-Scale Radio Jets", eds. A. Zensus and T. Pearson, Cambridge, p.110.
- Schwab, F. R., and W. D. Cotton, 1983, *AJ*, 88, 688.
- Shepherd, M. C., T. J. Pearson, and G. B. Taylor, 1994, *BAAS*, 26, 987.
- Simard-Normandin, M., P. P. Kronberg, and S. Buton, 1981, *ApJS*, 45, 97.
- Taylor, G. B., E. J. Barton, and J. Ge, 1994. *AJ*, 107, 1942.



# **Monitoring Radio Frequency Interference**

**Augustus Tucker, Athens State College  
Summer 1996**

## **Introduction**

This summer I worked with Clint Janes on ways to monitor Radio Frequency Interference (RFI) , developing RFI Bulletins for the Very Large Array (VLA) and Vary Long Baseline Array (VLBA) homepage, and work with interference data taken at VLBA sites. The goal of my project was to become familiar with SPAN, process an Amplitude vs Frequency plot using AIPS with interference data taken from VLBA sites, and make available to observers RFI Bulletins for future observations.

The Spectrum Analyzer (SPAN) is an application program that lets you examine the radio frequency spectrum. This program allows you to search for radio frequency interference that may be associated with the antenna or observation runs. SPAN may also be used to search for RFI from a defined direction to try and locate or identify an unknown potential RFI source. With the help of SPAN, I was able to perform radio interference tests on VLBA antennas and potential unknown RFI, generate plots, and observe the PCAL signals strengths at the VLBA sites. SPAN was very helpful in determining if RFI existed at the VLBA antennas or if the RFI existed along the observes line of sight.

Radio frequency interference is a major, growing problem for radio astronomy, especially at lower frequencies such as L Band (near 20 cm) and P Band (near 90 cm). Most radio interference occurs around 1400 Hz and 330 MHZ . By putting the RFI bulletins out on the Internet, observers can easily have access to what type of interference they can expect, at what frequencies to expect it, and at what strength. This way hopefully observers can plan their observations to avoid these types of problems.

NRAO does receive warnings from some of the RFI generators, in addition to spot checking astronomical observations. Before, information in the past has circulated only within the NRAO. Part of my project this summer, was to come up with a standard bulletin document that would make RFI information available for future observations so that observers could plan their observations accordingly.

## **Conclusion**

The search for RFI is an on going process and the RFI department hopes that people will learn to check the RFI bulletins on the Internet routinely before writing Observe files. This will aid in helping the observer avoid as much interference as possible.



# Visualization of Astronomical Images

Jeff Mangum – advisor

Clair Branch – student

December 6, 1996

## 0.1 Introduction

Based on the growing popularity of On The Fly (OTF) observing with the NRAO 12m telescope on Kitt Peak, the astronomical community needed a way to view OTF data more dynamically than with the current two dimensional standards such as AIPS and *aipsview*. Because the data obtained by OTF observing is four dimensional (*i. e.* right ascension, declination, velocity, and intensity), it makes sense to actually observe these images four dimensionally in velocity-space. To fill this void, Clair Branch (University of Michigan) wrote an interface between OTF data in the FITS format and PV-Wave.

As a practical test case for this visualization package, OTF images of the CO emission from a remarkable molecular cloud near the Pleiades star cluster were analyzed. The molecular cloud “visitor” near the Pleiades star cluster presents a unique case of cluster-cloud interaction in the interstellar medium. The cometary structure of this cloud is due to the apparent interaction between the Pleiades and a molecular cloud which has been injected into the region. Since most star-cloud interactions involve HII regions or supernova remnants, the proximity ( $\sim 135$  pc) and unusual nature of the Pleiades cluster-cloud interaction represents a unique environment in which to study the detailed structure within this phenomenon. Using OTF measurements of the CO j21 emission toward this region, the visualization software developed by Clair Branch allowed us to study the physical conditions and dynamics of this interaction region.

## 0.2 The Pleiades Molecular Cloud

The observed continuity between the reflection nebula and the dark nebular filaments in the Pleiades, a feature apparent even in the earliest optical images of this region, have pointed to an interaction between the Pleiades and a dense molecular cloud. There are numerous structures in the interstellar medium which are the result of local processes, such as the interaction between remnant molecular material and nearby HII regions and supernova remnants. The interesting aspect of the cluster-cloud interaction in the Pleiades is that it involves an interaction between stars, that neither ionize hydrogen nor generate powerful stellar winds, and an apparent molecular

cloud interloper. This molecular cloud, located approximately 15' south of the star Merope, was first discovered through its CO j21 emission by Cohen (1975). A later study of the CO j10 emission by Bally & White (1986) revealed a large (1. deg 5 × 1 deg) molecular cloud with a cometary morphology. By combining the available radio, infrared, and optical measurements of this region, White & Bally (1993) proposed a model where the soft-ultraviolet radiation produced by the Pleiades interacts with the ambient gas and dust, which subsequently deflects the inflowing material, leading to the production of a shock and downstream wake near the molecular cloud.

Recent measurements of its CO, <sup>13</sup>CO, and C<sup>18</sup>O j10 and j21 emission, which include OTF images of its CO and <sup>13</sup>CO j10 and CO j21 emission, indicate that this molecular cloud has some unusual properties. Our OTF measurements cover < 40 square arcminutes around the peak emission region (see Figure 1) and reveal a number of interesting structures. Most apparent in our CO j21 map is the incredible amount of substructure in this cloud. Along several lines-of-sight toward these condensations there are two velocity components separated by as much as 13 km s<sup>-1</sup>. Within the shock model of White & Bally (1993), these structures represent pieces of the same parent molecular condensation which has been split by its interaction with the Pleiades. We also find that the peak <sup>13</sup>CO j10 intensity is about 10 K, but the C<sup>18</sup>O vj10 intensity is only about 0.2 K, indicating the presence of moderately dense yet cool gas.

Further analysis of this remarkable region is currently underway. With our images of this region visualized using our PV-Wave interface, we are addressing the following questions:

- How does the spatial distribution of the multiple-component subcondensations in the cloud fit with the picture proposed by White & Bally?
- How do the properties of the molecular cloud condensations constrain the possible acceleration mechanisms giving rise to the cometary morphology?
- What are the densities, masses, and kinetic temperatures of the molecular cloud condensations?

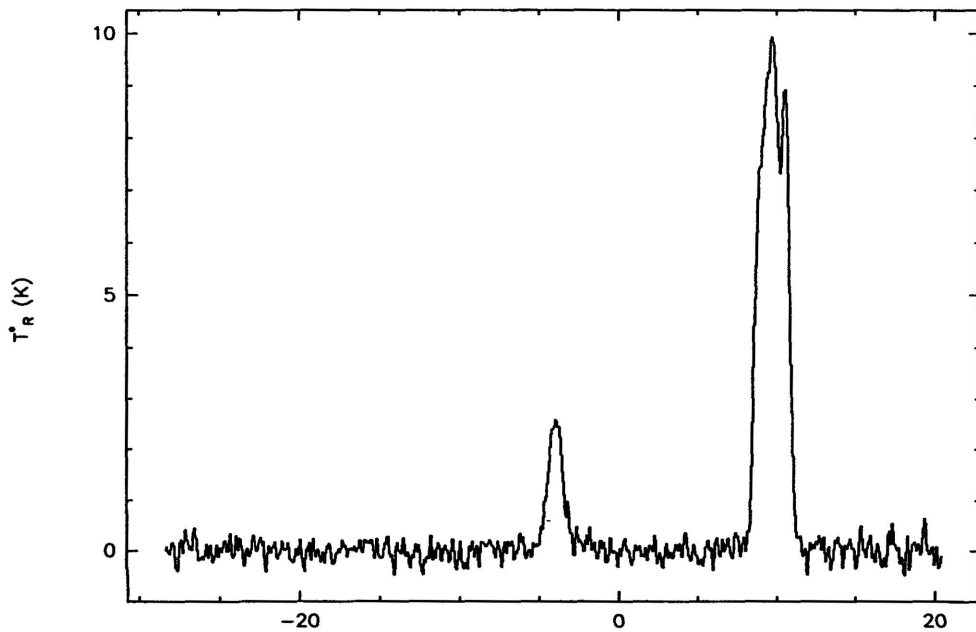
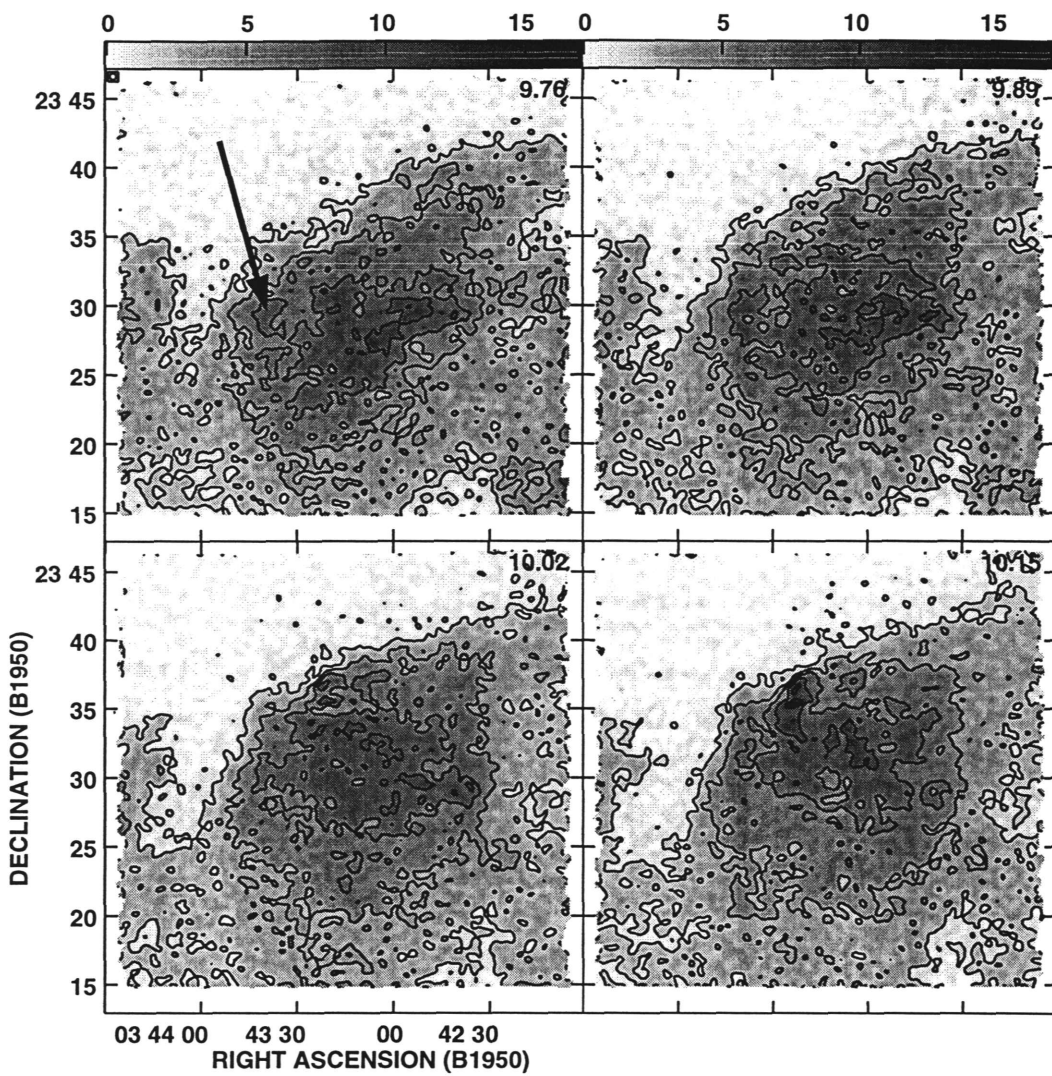


Figure 0.1: Four-panel mosaic of the peak CO  $J=2-1$  emission channels towards the Pleiades molecular cloud. This OTF image was acquired using the single-beam dual-polarization 1mm receiver at the 12m. Since we wanted to sample a rather large region, we scanned at a faster rate than that which would have allowed us to fully recover the information in the map, making interpretation of this data set difficult. The spatial resolution for this map is indicated in the upper left corner of the first panel, while each panel is tagged with its LSR velocity in the upper right corner. The single-channel rms for this data is approximately 0.6 K. The spectrum shown below the grey scale image was measured toward the position indicated by the arrow in the upper left panel of the grey scale image. This spectrum is representative of the velocity-split emission toward several positions in this disrupted molecular cloud.

### 0.3 References

Bally, J. & White, R. E. 1986, in "Proc. Summer School on Interstellar Processes: Abstracts of Contributed Papers", ed. D. J. Hollenbach & H. A. Thronson, Jr. (Washington: NASA TM, 88342), 51

Cohen, R. S. 1975, unpublished data

White, R. E. & Bally, J. 1993, ApJ, 409, 234